UNIVERZA V LJUBLJANI
FAKULTETA ZA MATEMATIKO IN FIZIKO

Rok Pestotnik

Identifikacija pionov, kaonov in protonov v spektrometru HERA-B

DISERTACIJA

MENTOR: PROF. DR. PETER KRIŽAN

Ljubljana, 2001

UNIVERSITY OF LJUBLJANA
FACULTY OF MATHEMATICS AND PHYSICS

Rok Pestotnik

Identification of pions,kaons and protons in the HERA-B spectrometer

DOCTORAL THESIS

SUPERVISOR: PROF. DR. PETER KRIŽAN

Ljubljana, 2001

Abstract

The subject of the present thesis is the identification of particles with the Ring Imaging Cherenkov counter (RICH), which is part of the HERA-B detector at the HERA e-p collider in DESY, Hamburg. The method uses an iterative procedure in order to reduce the background of other overlapping rings. It requires as input, the track information, which should be available from other components of HERA-B. Likelihoods for various particles are assigned to each track using a maximum likelihood method. Efficiencies for identification of different particles are then investigated using Monte Carlo simulated events, as well as data measured during the 2000 data taking periods. From the analysis, it follows that the RICH detector and the data seem to be well understood. Somewhat lower efficiency in some cases could be explained by input track parameter resolutions being below expectations. When the improvements, now in progress, will be implemented, a design value of the RICH efficiency should be reached.

Povzetek

Predmet doktorskega dela je identifikacija delcev z detektorjem Čerenkovih obročev (RICH), ki je del detektorja HERA-B na shranjevalnem obroču e-p na inštitutu DESY v Hamburgu. Metoda uporablja iterativni postopek za zmanjšanje prispevka ozadja prekrivajočih se Čerenkovih obročev. Vstopna informacija so sledi, ki jih priskrbijo druge detektorske komponente detektorja HERA-B. Vsakemi sledi pripišemo funkcijo zanesljivosti na osnovi metode največje zanesljivosti. Izkoristki za identifikacijo različnih delcev so raziskani na Monte Carlo simuliranih dogodkih, kot tudi na podatkih, izmerjenih leta 2000. Iz analize sledi, da RICH detektor in podatke dobro razumemo. Izkoristek, v nekaterih primerih nižji od pričakovanega, lahko razložimo s slabšo ločjivostjo sledi od pričakovane. S pričakovanimi izboljšavami bi moral izkoristek RICHa doseči pričakovano vrednost.

Physics and Astronomy Classification Scheme:

- 20. NUCLEAR PHYSICS
- 29. Experimental methods and instrumentation for elementary particle and nuclear physics
- 29.40.-n Radiation detectors

- 29.40.Ka Cherenkov detectors
- 29.85.+c Computer data analysis

posvečeno Ljubezni in Bobru

Za prijetno delovno vzdušje se zahvaljujem mentorju prof.dr. Petru Križanu, pa tudi vsem ostalim članom ljubljanske raziskovalne skupine HERA-B Samu Korparju, Marku Stariču, Andreju Gorišku in Alešu Stanovniku. Disertacije ne bi bilo brez moje mame, ki me je sooblikovala od plenic naprej. Še posebej pa hvala za vso potrpežljivost, ki jo je imela z mano, moji ženi Špeli.

Contents

1

Introduction

1.1 Motivation

The difference between the properties of matter and antimatter is one of the most intriguing puzzles of nature. Most likely, without this difference the existence of our civilization would be impossible, since the baryons and antibaryons would all have had to annihilate in the early stages of the development of the Universe and there would be no matter left to form the Universe as we know it.

Studies at CP violation proceed in many directions, one of them is the search for the difference in the behavior of beauty particles and their antiparticles. Large accelerators and detectors are being built for this purpose, and important results should soon emerge.

The development of the idea of antimatter started in 1928 when Paul Dirac derived his equation for electrons [1]. Besides having solutions with positive energy, this equation had negative energy solutions. To solve this problem he postulated in 1931 [2] entirely new particles, an anti-electron and an anti-proton. In the same year, C. D. Anderson discovered the anti-electron [3]. This symmetry between the matter and antimatter is known today as charge-conjugation symmetry, or C invariance. The concept of charge-conjugation symmetry is not trivial, since our Universe is highly asymmetric. No indications that the Universe contains an appreciable amount of antimatter have been found up to now. In 1956 T. D. Lee and C. N. Yang predicted mirror symmetry breaking, i.e. the breaking of left-right symmetry [4]. This symmetry is also called P invariance (P for parity). In the same year it was found that the predicted way of parity violation would lead to violation of C invariance as well.

In 1957, C. S. Wu et al. [5] observed parity violation, while R. Garwin et al. [6] discovered charge-conjugation symmetry breaking. Landau, who was extremely opposed to the asymmetry of space with respect to mirror reflection, proposed the hypothesis of invariance with respect to combined inversion, which is now called CP invariance. The symmetry of matter and antimatter was reestablished on a new level.

Many experiments corroborated the CP-invariance hypothesis. However, there were researchers who doubted the validity of this hypothesis and urged experimenters to continue the

Particles	Charge	Baryonic charge	Generations		
			1	2	3
Quarks	$+2/3$	$1/3$	u	c	t
	$-1/3$	$1/3$	d	s	b
Leptons	0	0	ν_e	ν_μ	ν_τ
	-1	0	e	μ	τ

Table 1.1: Fundamental particles in the Standard Model

search for CP violation. In 1964, J. W. Cronin et al. [7], found a violation of CP invariance in decays of K mesons. And in 1967, A. Sakharov demonstrated [8] that to explain the baryon asymmetry of the Universe, i.e. the excess of matter in the Universe, there must be CP violation. Thus, it was realized that CP violation plays a fundamental role in the formation of Matter.

1.2 Mechanism of CP violation

Today we know of three generations of fundamental fermions (see Table 1.1). The first generation consists of the fermions of which the matter surrounding us is built, while the particles of the second and third generations (with the exception of ν_μ and ν_τ) are the heavier unstable particles, which eventually decay to first-generation particles.

1.2.1 The Cabibbo-Kobayashi-Maskawa matrix

In the Standard model (SM) with SU(2) × U(1) as the gauge group of electroweak interactions, both quarks and leptons are assigned to be left-handed doublets and right-handed singlets. The quark mass eigenstates are not the same as the weak eigenstates, and the matrix relating these states was defined for three generations of quarks and given an explicit parameterization by Kobayashi and Maskawa [9].

The Cabibbo-Kobayashi-Maskawa (CKM) matrix V_{CKM}

$$V_{CKM} = \begin{pmatrix} V_{ud} & V_{us} & V_{ub} \\ V_{cd} & V_{cs} & V_{cb} \\ V_{td} & V_{ts} & V_{tb} \end{pmatrix} \tag{1.1}$$

describes the coupling constants of quarks belonging to different generations. For example, the probability of a b quark becoming a c quark depends on the matrix element V_{cb}, and the probability of a b quark becoming an u quark depends on the matrix element V_{ub}. Altogether, in the case of three generations, the CKM matrix has nine complex elements. It can be shown that they all depend solely on four parameters, three angles θ_{12}, θ_{13}, θ_{23} and one phase δ_{13}:

$$V_{CKM} = \begin{pmatrix} c_{12}c_{13} & s_{12}c_{13} & s_{13}e^{-i\delta_{13}} \\ -s_{12}c_{23} - c_{12}s_{23}s_{13}e^{i\delta_{13}} & c_{12}c_{23} - s_{12}s_{23}s_{13}e^{i\delta_{13}} & s_{23}c_{13} \\ s_{12}c_{23} - c_{12}s_{23}s_{13}e^{i\delta_{13}} & -c_{12}s_{23} - s_{12}c_{23}s_{13}e^{i\delta_{13}} & c_{23}c_{13} \end{pmatrix} \tag{1.2}$$

with $c_{ij} = \cos\theta_{ij}$ and $s_{ij} = \sin\theta_{ij}$. In the Standard model, it is this phase that is responsible for the different properties of matter and antimatter. The parameters determining the CKM matrix are the fundamental parameters of the modern theory. They are not predicted by the theory and must be determined from experiments. Often, the CKM matrix is represented by Wolfenstein's approximate parameterization scheme:

$$V_{CKM} = \begin{pmatrix} 1-\frac{\lambda^2}{2} & \lambda & A\lambda^3(\rho - i\eta) \\ -\lambda & 1-\frac{\lambda^2}{2} & A\lambda^2 \\ A\lambda^3(1-\rho-i\eta) & -A\lambda^3 & 1 \end{pmatrix} + O(\lambda^4). \tag{1.3}$$

Since this matrix is unitary, its columns must be orthogonal:

$$\sum_k V_{ki}^* V_{kj} = \delta_{ij}. \tag{1.4}$$

One of the most interesting unitary conditions for the CKM matrix is

$$V_{ud}V_{ub}^* + V_{cd}V_{cb}^* + V_{td}V_{tb}^* = 0. \tag{1.5}$$

where the absolute values of all three terms are of the same order of magnitude. Here the matrix elements V_{ud},V_{cs} and V_{tb} describe the couplings between quarks belonging to the same generation and are approximately equal to unity, while the matrix element $V_{cd} \approx -V_{us} \approx -\lambda$ describes the coupling between quarks of the first and the second generation, and is well known from semileptonic decays of K mesons and hyperons: $|V_{us}| = 0.2196 \pm 0.0023$ [10]. Hence the above expression reduces to a simpler one:

$$V_{ub}^* - \lambda V_{cb}^* + V_{td} \approx 0. \tag{1.6}$$

This relationship between the elements of the CKM matrix allows us to geometrically visualize it as a triangle in the complex plane (Fig. 1.1). This triangle is known as the unitarity triangle. Its sides are equal to the absolute values of the elements of the CKM matrix, while its angles determine the difference in the decays of the B^0 mesons, which consist of ($\bar{b}d$) quarks, and $\bar{B}^0$ mesons.

1.2.2 How to measure the angles?

The three sides of a triangle completely determine the angles in the triangle. Unfortunately these elements are small, and there are uncertainties in the measurements. On the other hand, experimental evidence requires that the angles of the unitarity triangle are large. However, in the Standard Model they are related directly to the asymmetry of the decays of B and $\bar{B}$ mesons. For instance, the asymmetry in the decays of B^0 and $\bar{B}^0$ mesons to $J/\psi K_S^0$ is determined by the angle β.

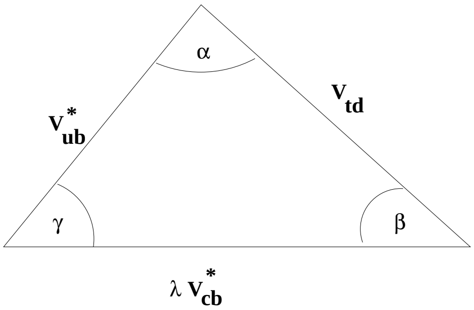

Figure 1.1: The unitarity triangle.

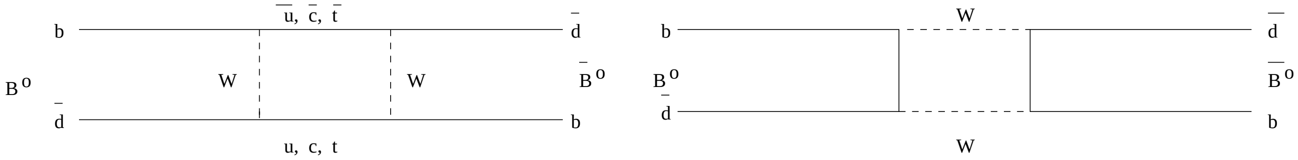

Figure 1.2: Box diagram contributions to B meson mixing.

This asymmetry emerges because a B meson can decay to the final state $J/\psi K^0_S$ directly or first oscillate to the $\bar{B}^0$ meson and then decay to the same final state (Fig. 1.2). The interference of the two amplitudes leads to an asymmetry in the number of decays of the B and $\bar{B}$ mesons to $J/\psi K^0_S$.

For beams of B^0 and $\overline{\mathrm{B}}^0$ mesons the decay rates into J/ψ $\mathrm{K_s}$ are given by [11]

$$\begin{aligned} n(t) &\propto e^{-\frac{t}{\tau}}(1+\sin(2\beta)\sin(x\frac{t}{\tau})) \\ \bar{n}(t) &\propto e^{-\frac{t}{\tau}}(1-\sin(2\beta)\sin(x\frac{t}{\tau})). \end{aligned} \tag{1.7}$$

The observable asymmetry of the time integrated rates is

$$A_{int} = \frac{\int n(t)dt - \int \overline{n}(t)dt}{\int n(t)dt + \int \overline{n}(t)dt} = \frac{x}{1+x^2}\sin(2\beta). \tag{1.8}$$

Here the mixing parameter x is given by the mass difference of the mass eigenstates ΔM and by the neutral B meson lifetime τ,

$$x = \frac{\Delta M c^2 \tau}{\hbar}. \tag{1.9}$$

The discovery of unexpectedly large $B^0\bar{B}^0$ oscillations with $x \approx 0.7$ [12] made it possible to search for CP violation in B mesons. Similarly, as the asymmetry in the decay of B meson to $J/\psi\, K_S$ depends on the angle β of the unitarity triangle, the asymmetry in the decay of B meson to $\pi^+\pi^-$ depends on $\beta + \gamma = \pi - \alpha$. In this case penguin diagrams can contribute significantly and violate the simple relationship between asymmetry and $\sin(2\alpha)$. Nevertheless, the angle α can still be obtained. In addition to the above examples, there is a large number of decays that can be used to determine the angles of the unitarity triangle.

Recently the search for CP violation in the system of B mesons has formed a new avenue of research in elementary particle physics. Two special large accelerators, known as B factories, have been built at KEK (Japan) and SLAC (United States). Also, four specialized detectors are being built: BaBar (SLAC), Belle (KEK), HERA-B (DESY, Germany), and the next generation detector LHC-B (CERN). The search for CP violation in B mesons has been incorporated into the research programs involving the existing CDF and D0 detectors at the $p\bar{p}$ collider at FNAL. Such activity is a reflection of the great interest in the problem. In fact, it may well be that the modern theory of CP violation is either incorrect or incomplete, and instead of a unitarity triangle with matching sides and angles we may find something totally unexpected, the more so that there are strong theoretical indications that the expected level of CP violation in the Standard Model is not sufficient to explain the large baryonic asymmetry of the Universe.

In addition to the parameters of CP violation in the B meson system, also the mixing in the B_S and in D meson systems are a very interesting topic, which is also related to the V_{CKM} matrix. Until now, the problem in the study of mixing in these two systems was too fast oscillations in the B_S meson system and too slow oscillations in the D meson system. With the expected resolution of the today's HERA-B and CDF experiments and the forseen experiments at the Large Hadron Collider in CERN, these measurements become possible.

1.3 Contents of the thesis

This doctoral thesis is devoted to several aspects of particle identification of hadrons, i.e. pions, kaons and protons, in the Ring Imaging Cherekov counter of the HERA-B experiment. The HERA-B spectrometer is situated in the western experimental area of the HERA electron proton ring of the DESY institute in Hamburg. The experiment will study rare decays of B and D mesons to add to the knowledge of the Standard Model.

The layout of the thesis is as follows. In the introductory Section 1 the motivation for the HERA-B experiment is presented with the review of some theoretical background. In Section 2 the structure of all detector components is explained, starting from the target wires, where interactions of interest take place through tracking and identification components to the trigger and data acquisition system. For the identification of hadrons the Ring Imaging Cherenkov Counter is employed. The phenomenon of Cherenkov radiation is explained and types of detectors where it can be applied are presented in Section 3. The iterative method for particle identification in the ring imaging Cherenkov counter is presented in Section 4. The identification algorithm relies on the good reconstruction of the tracks. The important input information for it are the parameters of tracks, i.e. momenta and slopes with estimated errors in the ring imaging Cherenkov counter. In Section 5 the reconstruction chain is explained in some detail, mostly covering the connections with the particle identification algorithm.

Well identified two body decays allow to determine the particle identification efficiency of the iterative method. The study of the efficiencies in the decays $K_S \to \pi^+\pi^-$, $\Lambda \to p\pi^-$, $\phi \to K^+K^-$ and $J/\psi \to \mu^+\mu^-$ is presented in Section 6. The concluding Section 7 is followed by the last section 8, where a summary of the thesis is presented in Slovenian language.

2

The HERA-B experiment

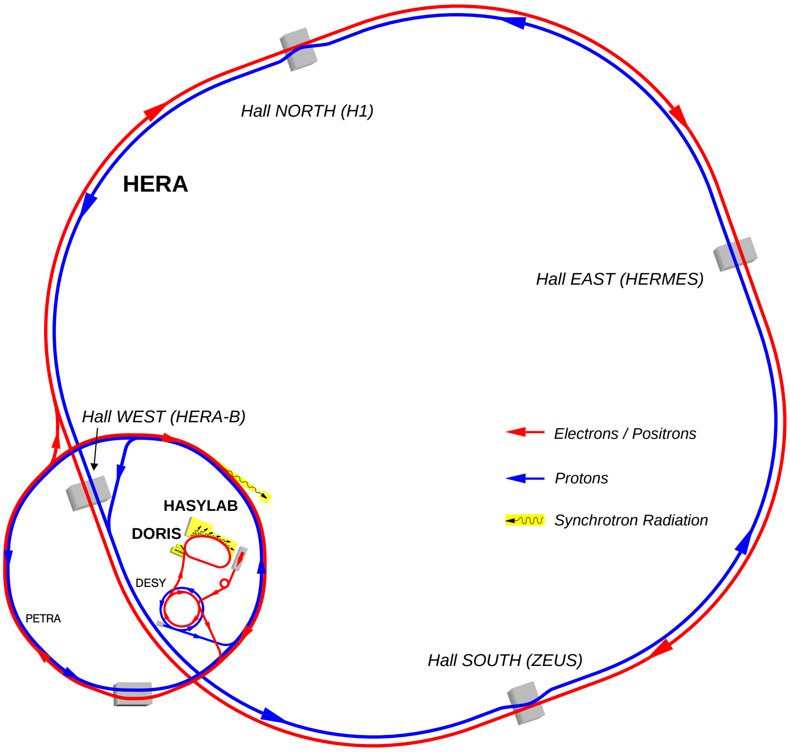

Figure 2.1: Layout of the HERA rings with the location of the four experimental areas.

The Hadron Elektron Ring Anlage (HERA) is a double storage ring at DESY in Hamburg. It is designed for colliding a 920 GeV proton beam with a 30 GeV electron beam. The rings with a length of 6335.8 m, their multi step injector chain and their four interaction regions are shown in Fig. 2.1. The North and the South hall house the collider experiments H1 and ZEUS, while in the other two experimental areas the beams are not brought to collision. The HERMES detector, which is using only the electron beam, is installed in the East hall. Thus the West hall offers space for a fourth experiment, called HERA-B, which is using only the proton beam. The particles in both beams are grouped in 220 bunches. The time between the two consecutive bunches in the proton beam is only 96 ns. These bunches trigger the data acquisition systems of the experiments with the bunch clock rate of more than 10 MHz.

The HERA-B experiment was designed to search for CP violation in decays of neutral B mesons [14]. Since the decay $\mathrm{B}^0 \to \mathrm{J}/\psi\, \mathrm{K_s} \to \ell^+\, \ell^-\, \pi^+\, \pi^-$, with leptons in the final state, is accepted as the best candidate, both theoretically and experimentally, for the study of CP asymmetries [15], the HERA-B spectrometer is optimized to detect such, so called "gold plated " decays. The HERA-B detector also allows to perform a number of valuable physics measurements in particular in the fields of quantum chromodynamics and charm physics [16]. Among the most competitive are the measurements of $\sigma_{b\bar{b}}$ cross-section, measurement of J/ψ, ψ' and χ_c production and decay angular distributions, measurement of the angular distribution of Drell-Yan pairs, measurements of the Υ cross section and decay angular distributions, measurement of the direct photon production at high transverse momenta, improvement of the upper limit on the $D^0 \to \mu^+\mu^-$ branching ratio and accumulation of an open charm sample large enough to allow competitive measurements of the properties of charm decays.

In the HERA-B detector, B and D mesons are produced in interactions of protons with nuclei in thin wire targets surrounding the HERA proton beam, not disturbing other experiments on the storage ring. It is possible to use the protons from the beam halo, which would otherwise be lost. The schematic view of the HERA-B detector is presented in Fig. 2.2. B mesons are produced in the wire target, and the vertices of the B-meson decays are registered by silicon micro-strip detectors. The momenta of the charged particles are measured by drift and gas micro-strip chambers placed inside and behind the magnet. K mesons are identified by a Cherenkov counter, electrons are identified by a transition radiation detector and electromagnetic calorimeter, and muons are registered by a muon identifier. Nearly 600.000 electronic readout channels are used in the device.

The proton energy in the HERA accelerator is 920 GeV. The neutral B meson decaying into the signal channel J/ψ $\mathrm{K_S^0}$ has an average momentum of 120 GeV/c and decays after an average flight distance of about 9 mm. J/ψ further decays into two leptons, either e^+e^-or $\mu^+\mu^-$, while $\mathrm{K_S^0}$ decays after a typical flight distance of about 1.1 m into charged pions of large momentum. The most powerful tagging methods for the beauty content of the decaying neutral B meson make use of the second beauty particle, i.e. charged or neutral meson or baryon. The cleanest tag, although occurring with rather small probability, is provided by the charge of a lepton with high transverse momentum from the semileptonic decays of the associated B meson. Less clean but more frequent is the tag provided by the charge of a kaon, produced in the subsequent charm decay (see Fig. 2.3).

At this energy the production cross-section of B mesons is approximately one million times smaller than the inelastic scattering cross-section. Taking into account the branching fractions of the decays $\mathrm{Br}(\mathrm{B}^0 \to \mathrm{J}/\psi\ \mathrm{K}^0_{\mathrm{S}}) = 5 \times 10^{-4}$, $Br(J/\psi \to l^+l^-) = 0.06$, and $Br(K^0_s \to \pi^+\pi^-) = 0.69$, it appears that there is only one event of interest for every 25000 B mesons. Hence in establishing an effective system for selecting the necessary events, an effective trigger, is the key issue of the experiment. The interaction frequency that is required to collect enough B mesons in a reasonable time of 3 years is 40 MHz. To achieve this extremely high interaction rate there has to be on average four superimposed interactions in a single crossing of proton bunches.

The HERA-B detector system should thus cope with very high interaction rates, where each bunch crossing generates tracks in the detector with extremely high particle densities (see Fig. 2.4). This requires fast track detectors which provide high precision in the decay reconstruction. To achieve the necessary precision, the detector elements with sufficiently high granularity and high rate capabilities are required to be as close as 1 cm from the beam, where they are hit by some $10^7\ \mathrm{particles/cm^2 s}$. Leptons from B decays have to be identified with high purity in order to suppress backgrounds from the ordinary proton nucleus interactions and charm decays. Also the identification of the tagging kaon with its momentum between a few GeV/c and 50 GeV/c should be performed. Due to restricted access to the detector, given by the fact

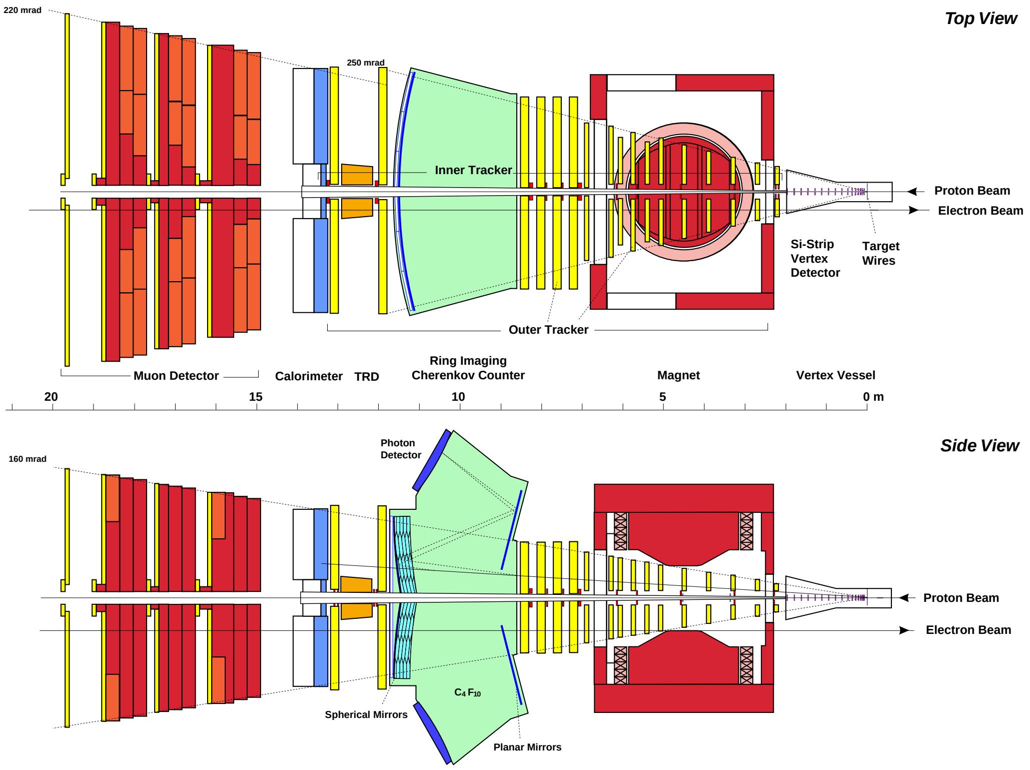

Figure 2.2: Configuration of the HERA-B spectrometer with the silicon vertex detector, the main tracking system with a dipole magnet, transition radiation detector and ring imaging Cherenkov counter for particle identification, followed by the electromagnetic calorimeter and the muon system.

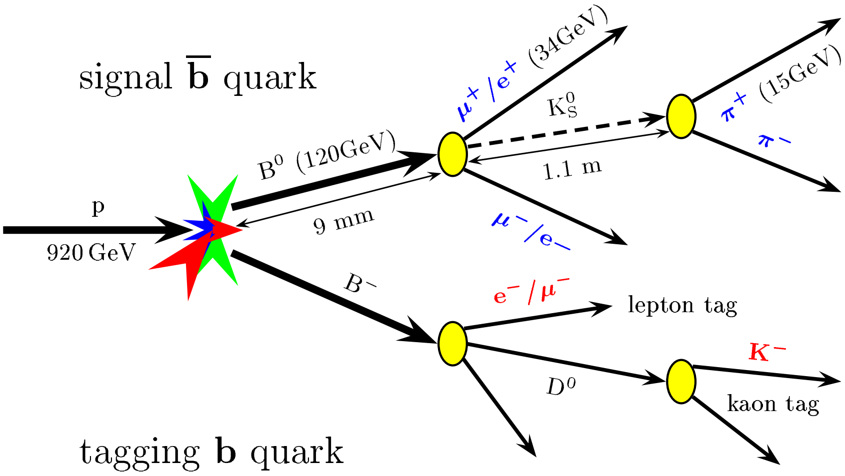

Figure 2.3: The ” gold platted ” $B^0 \to J/\psi\, K_s$ decay with some kinematical quantities at the HERA-B experiment.

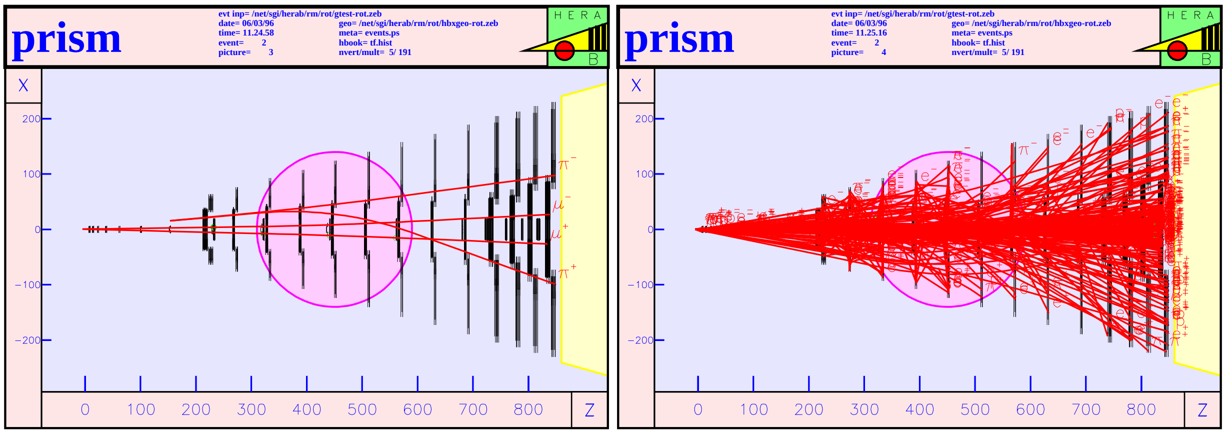

Figure 2.4: Simulated tracks due to one bunch crossing in the HERA-B detector. The golden plated events (left) lay in a huge background of other particles produced in the same event.

that HERA-B is not the main user, it has to be designed such that even the components very close to the beam have a minimum lifetime of about 10^7 seconds operating at full target rate.

All in all the detector has to provide a good B meson decay vertex resolution, lepton and kaon identification, and multiple event reconstruction per bunch crossing. To meet these requirements, the spectrometer consists of several detector subsystems which can be grouped into tracking and particle identification systems according to their tasks. The tracking system consists of the magnet, the vertex detector (VDS), and the inner and outer tracker detectors, while the transition radiation detector (TRD), the ring imaging Cherenkov detector (RICH), the electromagnetic calorimeter (ECAL) and the muon identification system (MUON) compose the particle identification system. The HERA-B spectrometer (Fig. 2.2) reflects the fixed target nature of the experiment, with finer detector granularity for small production angles, where higher particle densities are expected. Its outer dimensions are $9\mathrm{m} \times 7\mathrm{m} \times 20\mathrm{m}$. The acceptance of the detector is from 10 mrad to 160 mrad vertically and from 10 mrad to 220 mrad horizontally. This is equivalent to 90% of the solid angle in the proton nucleus center of mass frame.

The problem of selecting interesting events is solved by using triggers at three levels, and at each level the amount of information per event processed is larger than at the previous level. At the first level, the calorimeter and the muon chambers are used to separate regions in the track system in which a lepton may pass and a search of such tracks is carried out. After the tracks are found, the invariant mass of the l^+l^- pair is calculated, which is matched with the mass of the J/ψ particle. Specially designed processors are used to carry out all these operations in maximal time of 12 μs, suppressing the background by a factor of 200 and yet retaining more than 60% of all the useful events in the process. During the processing of the triggers, the data is stored in the front end electronics pipeline buffers, to avoid dead time, At the second level, information about the secondary vertex is used, which makes it possible to suppress the background by an additional factor of 25. Finally, at the third level, the complete reconstruction of the event is achieved, which decreases the background by an additional factor of 20. In the final analysis, the separation of the $B \to J/\psi K_S^0$ decay is achieved primarily by calculating the invariant mass of the candidate for the B meson and by imposing the requirement that the vertex of the decayed B meson is several millimeters away from the primary vertex. Since for times much shorter than the lifetime of the B meson the CP asymmetry is small (Eq. 1.7), the requirement that the B meson decay length be large (up to $\beta\gamma ct > \beta\gamma c\tau_B$) practically does not affect the accuracy in determining the asymmetry.

To calculate the CP asymmetry (Eq. 1.8), the decays of B^0 and $\bar{B}^0$ mesons must be separated. Since this cannot be done via the final states, which are identical, one must use the information about the second beauty (anti)particle that was produced together with the neutral B meson. This beauty particle can be identified by the charge sign of the leptons and K mesons produced in its decay. It tags the B meson being investigated. Mesons and baryons which contain a b quark decay to positive leptons or K mesons and their anti-particles decay to the respective negative particles. Unfortunately, sometimes leptons and K mesons of the other sign are produced in the decays of beauty particles, which leads to errors in identification. In addition, hadrons can be incorrectly identified as leptons, and π mesons as K mesons. Finally the second beauty particle may oscillate into its own anti-particle, which again results in incorrect tagging of the B meson under investigation.

At HERA-B minimum separation between the primary vertex and the B decay vertex is needed, in order to suppress background. This requirement may be approximated by a cut in the proper decay time $t > t_0$. The integrated asymmetry is written in this case as

$$A_{int} = \frac{\int_{t_0}^{\infty} n(t)dt - \int_{t_0}^{\infty} \overline{n}(t)dt}{\int_{t_0}^{\infty} n(t)dt + \int_{t_0}^{\infty} \overline{n}(t)dt} = M_{int}(t_0)\sin(2\beta). \tag{2.1}$$

with the mixing factor M,

$$M_{int}(t_0) = \frac{\sin xt_0 + x\cos xt_0}{1+x^2} \ , \tag{2.2}$$

where x is the mixing parameter. The main factors affecting the achievable precision in $\sin(2\beta)$ are statistics and mistagging either because of the tagging B oscillating before detection or because of particle misidentification. Taking into account all these effects, the total error in $\sin 2\beta$ can be written as [14]

$$\Delta \sin 2\beta = \frac{1}{M_{int}(t_0)} \frac{1}{P} \frac{1}{\sqrt{N_B(t_0)}} \ , \tag{2.3}$$

where $N_B(t_0)$ is the total number of reconstructed B decays and

$$P = D_M D_T \sqrt{\varepsilon_{tag}} \tag{2.4}$$

is the tagging power, with D_M and D_T the mixing and wrong tag dilution factors, and ε_{tag} the total tagging efficiency. In the case of HERA-B for $N_B = 1500$ decays and $t_0 = 0.7\tau_B$ the following values are expected: $M = 0.7$, $D_M = 0.7$, for the lepton tag $D_T = 0.7$ and $\varepsilon_{tag} = 0.95$. This leads to an error $\Delta \sin 2\beta$, sufficient for 3 sigma effect detection for $\sin 2\beta \approx 0.5$, which is of the order 0.13. From Eq. 2.3 and Eq. 2.4 it is clear that excellent particle identification is necessary, with a good efficiency (ε_{tag}) and low misidentification probability.

In what follows, each HERA-B detector subsystem design shall be briefly described and its main tasks presented.

2.1 The internal target

An intrinsic part of the experiment, which is integrated into the detector and positioned in the halo of the HERA proton beam is **an internal target**. The basic idea of the target is to bring protons, which leave the beam core, drift outwards and would be lost anyhow, to interact in the target before they hit any aperture limitation in the beam tube. An efficient competition of the target with collimators, which define the aperture of the beam is thus needed.

As already mentioned, four proton interactions with the target are required per bunch crossing which should be compared with the natural loss rate of the proton beam. With a typical proton bunch current of 100 mA (i.e. 1.4×10^{13} protons in 220 bunches circulating with the frequency of 45 kHz) and a lifetime of 100 hours, the HERA proton beam looses 40×10^6 protons per second.

This demonstrates that the target has to collect the protons before they get lost with high efficiency in order to arrive at an interaction rate of 40 MHz. We note that at the present mode of operation the target does not severely interfere with the efficiency of the other experiments, because the HERA luminosity lifetime is usually less than 10 hours, mainly determined by the lifetime of the electron beam.

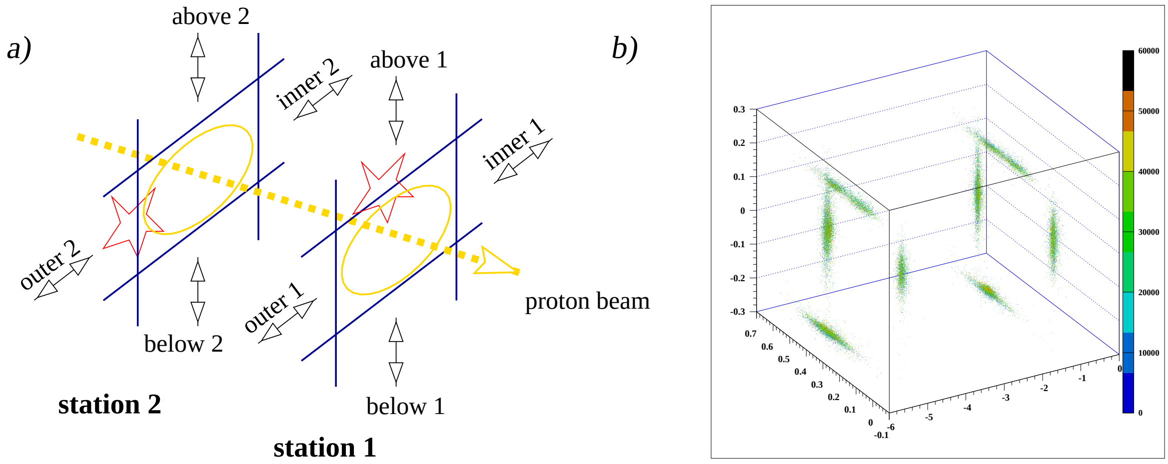

Figure 2.5: a) Schematic drawing of the eight target wires surrounding the HERA proton beam with the names of the wires. b) Reconstructed vertices with all eight target wires operating simultaneously in the beam [18].

The target mechanics is mounted inside a conical extension of the beam pipe, which houses the movable parts of the vertex detector. The target consists of a set of eight movable ribbons with 50 μm width perpendicular to the beam, 500μm thickness along the beam and 30 mm length (Fig. 2.5). The ribbons are positioned at a distance of $4\,\sigma$ to $6\,\sigma$ from the beam with R.M.S. width σ. The ribbons are grouped in two stations separated by 4 cm along the beam. Within one station four ribbons approach the beam from four different sides (see Fig. 2.6). Each ribbon is mounted on a ceramic fork, which can be independently moved with a nominal step size of 50 nm. A constant target interaction rate with equal sharing among ribbons can be achieved by an automatic feedback system which continuously adjusts the wire positions via stepping motors [17].

The described target system provides a well localized source of B hadrons. It also allows multiple interactions in a single bunch crossing in up to eight ribbons, which result in an unambiguous assignment of particles to vertices and last but not least it is robust and simple to operate.

2.2 The dipole magnet

To determine the momentum of particles which are produced in the collisions of protons with the internal target, the spectrometer uses **a dipole magnet** of 2.2 Tm field integral. It consists of two iron poles, an iron flux return yoke and two cylindrical copper coils. The momentum is calculated from the curvature of the particle trajectories in the magnetic field. The magnet position presents a compromise between the acceptance for late decaying $\mathrm{K_s}$ and magnet aperture for fixed solid angle coverage. The location of the magnet center is fixed at 4.5 m downstream of the target, which determines the vertical magnet aperture to 160 mrad and the horizontal

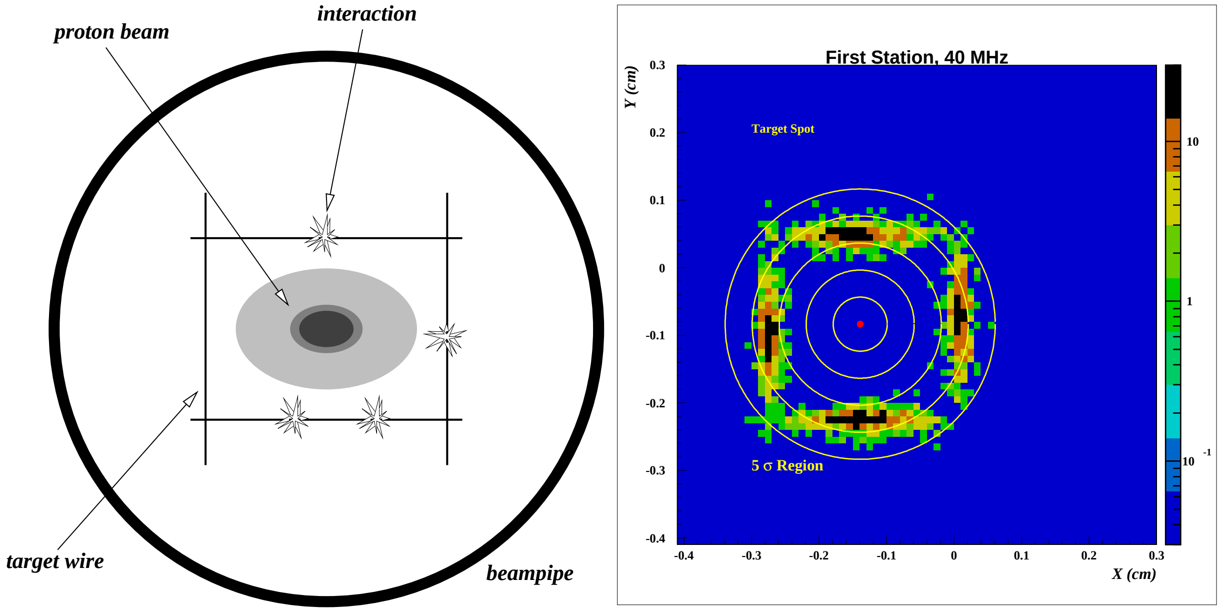

Figure 2.6: Sketch showing the basic idea of a halo target. Protons leaving the beam core interact in the target (typical interaction points are indicated by stars) before getting lost on aperture limitations (left). Reconstructed vertices with four target wires operating simultaneously [18].

aperture to about 250 mrad.

2.3 The tracker system

The tracking of charged particles is performed by a vertex detector, followed by an inner tracking system closer to the proton beam and an outer tracking system at distances larger than 20 cm from the beam.

2.3.1 The vertex detector system

The vertex detector system provides the track coordinates information for reconstruction of the $\mathrm{J}/\psi \to \mathrm{e}^+\,\mathrm{e}^-$, $\mu^+\,\mu^-$ decay vertices and the impact parameters of all tagging particles. From the reconstructed tracks, the primary interaction is reconstructed in the primary vertex. The secondary reactions in the chain result in secondary vertices. In Fig. 2.7 a longitudinal distribution of $J/\psi \to \mu^+\mu^-$ reconstructed vertices is shown. The information of the vertex detector is also used at the trigger level in order to reject events, where the two leptons do not form a common vertex which is displaced from the target wire.

The vertex detector system has eight layers with four modules in each layer (Fig. 2.8). The eight layer is contrary to the others situated outside the beam vacuum vessel just in front of the magnet and functionally belongs to the magnet tracker. Each module carries two double sided silicon detectors and the front end electronics. The first three modules in a quadrant are

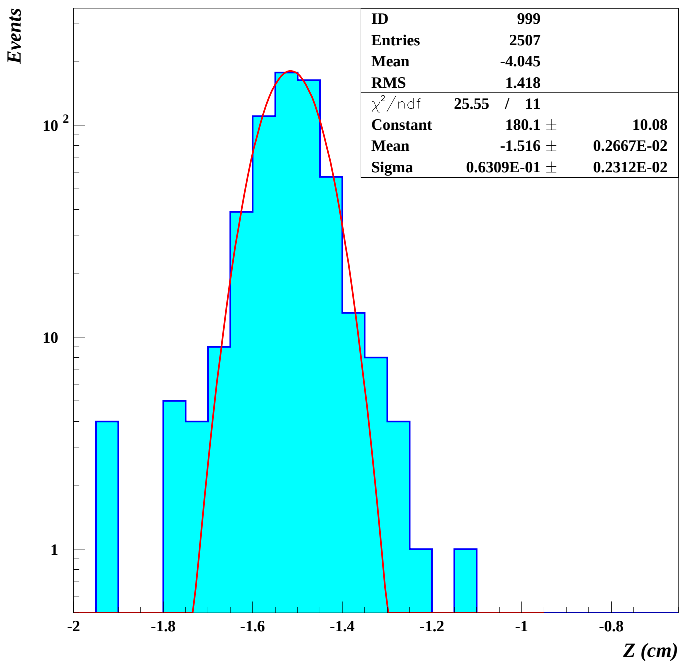

Figure 2.7: Longitudinal distribution of vertices of $J/\psi \to \mu^+\mu^-$ candidates from the "below-1" titanium wire as reconstructed in the vertex detector system [18].

integrated in one pot. Layers four to seven have each module mounted in a separate roman pot. All detectors are mounted perpendicular to the beam. The vertex detector system uses $300\ \mu\mathrm{m}$ thick double sided n type bulk silicon strip detectors. Each detector has an overall size of $53 \times 73\ \mathrm{mm}^2$, while the active area is $50 \times 70\ \mathrm{mm}^2$. On the two detector sides the strips are orthogonal and are tilted by 2.5^0 with respect to the detector edge. The two detectors in a module are mounted back to back (Fig. 2.9). That results in four views per module with a stereo angle of 5^0. Electronics and detectors are mounted on separate plates to establish different cooling paths. The vertex detectors have to be replaced once per year due to the radiation damage.

The vertex detector system acceptance is from 10 mrad up to 250 mrad vertically and horizontally. The minimum distance between the active area of the silicon detectors and the beam is 1 cm. The overall detector system length is 2.5 m. The resolution of the vertex detector is limited by multiple scattering in the material between track vertex and the point of the first track measurement [19]. Thus the detector layout is based on a roman pot system, which allows the minimization of the in-between material. The roman pots are mounted inside a cone shaped vacuum vessel (Fig. 2.2). Each roman pot provides a secondary vacuum of $10^{-6}\ \mathrm{mbar}$, because it would be impractical to operate in the primary HERA vacuum of $10^{-8}\ \mathrm{mbar}$. Individual modules have a $150\ \mu\mathrm{m}$ thin aluminum cap separating the primary from the secondary vacuum. The detectors can be retracted during the beam injection or adjustment.

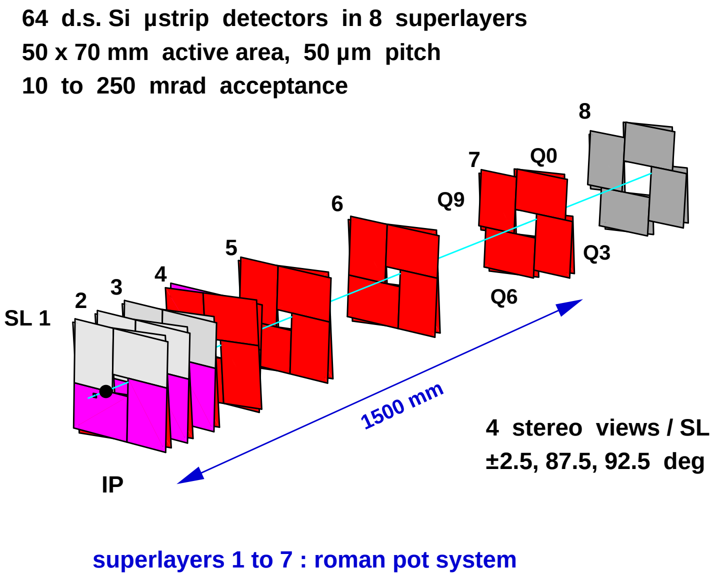

Figure 2.8: Isometric view of the arrangement of detector wafers in the VDS. The first seven superlayers are mounted inside the beam shroud, while the structurally same superlayer 8 is positioned outside the beam shroud and functionally belongs to the magnet tracker.

2.3.2 The inner tracking system

The main tracking system is segmented into parts of different granularity, in order to keep occupancies below a level of 20%. In accordance with the increasing particle densities towards small polar angles the system is divided into an inner and an outer section. Besides track information it also provides momentum measurements.

The inner tracking system is covering the angular range larger than 10 mrad and extends up to a radial distance of 20 cm from the proton beam. This region comprises about half of all the tracks of a typical event, thus the detectors have to cope with particle rates of up to $10^4 \mathrm{mm}^{-2}\mathrm{s}^{-1}$. The inner tracker detector consists of low gain micro strip gas chambers (MSGC) operated with $Ar - CO_2$ gas mixture and combined with a gas electron multiplier (GEM) [20].

The micro strip gas chamber cover consists of a G10 plate to ensure mechanical stability and a kapton foil covered with copper, which serves as the drift cathode (Fig. 2.10). Below the drift gap the gas electron multiplier foil is mounted. It consists of a $50\ \mu\mathrm{m}$ thick kapton foil, which is covered with $7\ \mu\mathrm{m}$ copper on each side. The holes in the kapton are staggered with a pitch of $140\ \mu\mathrm{m}$ and have a diameter of about $55\ \mu\mathrm{m}$. The charge produced in the GEM foil is transfered by an electrical field through the transfer gap of 2.8 mm to the standard MSGC substrate. A gold layer is deposited onto a glass wafer and the electrode structure which consists

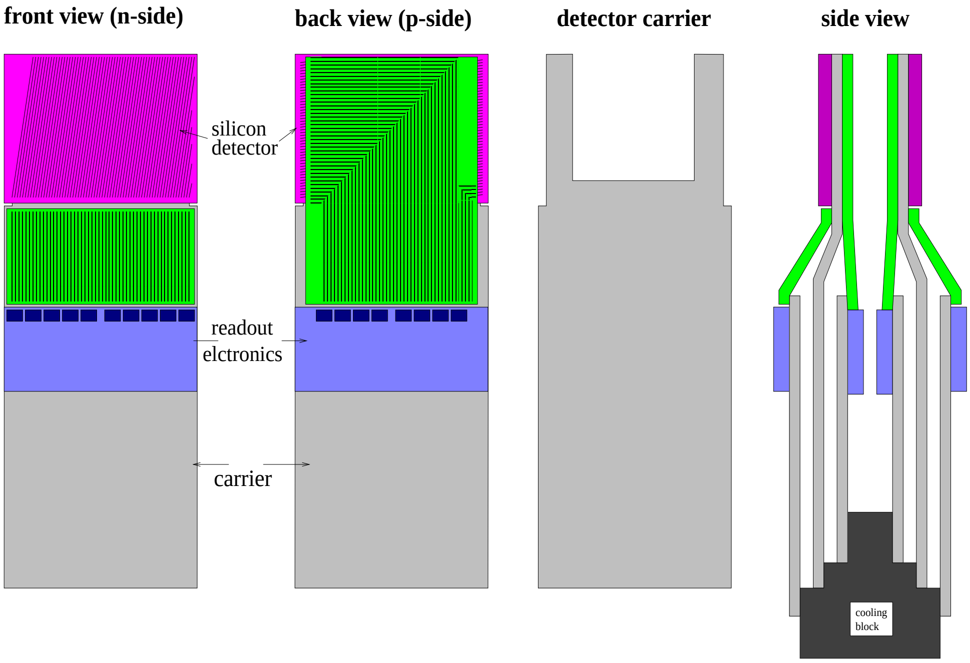

Figure 2.9: Schematic view of the vertex detector module.

of 10 $\mu\mathrm{m}$ wide anodes and 170 $\mu\mathrm{m}$ wide cathodes strips, with a gap of 60 $\mu\mathrm{m}$ in between (see Fig. 2.10). The micro strip gas chambers pitch of $300\mu\mathrm{m}$ provides maximum occupancies of about 5% and the spatial resolution better than $80\mu\mathrm{m}$. The momentum resolution is limited by multiple scattering, while photon conversions represent a significant background source. Single detector layer thickness is thus minimized and presents less than 0.35 % of a radiation length.

The inner tracking system has 48 detector layers, each being composed of four independent L shaped detector planes (see Fig. 2.10). Tracking is performed by using three stereo strip orientations i.e. vertical strips (0^o) and strips with $(\pm 5^o)$ orientation. Several layers with different strip orientation, mounted together in a common support structure form eleven supermodules. Two super modules in front of the calorimeter are used for triggering. Four supermodules between the magnet and the RICH are used to start track finding and pattern recognition. They provide three dimensional hit information. Six layers of these supermodules are also used for triggering. The remaining supermodules near the vertex detector and in the magnet are used to extrapolate the tracks to the vertex detector (see Fig. 2.2).

2.3.3 The outer tracking system

The purpose of **the outer tracking system** is to measure charged particle tracks in almost the whole geometrical acceptance of the experiment, down to a distance of 20 cm from the proton

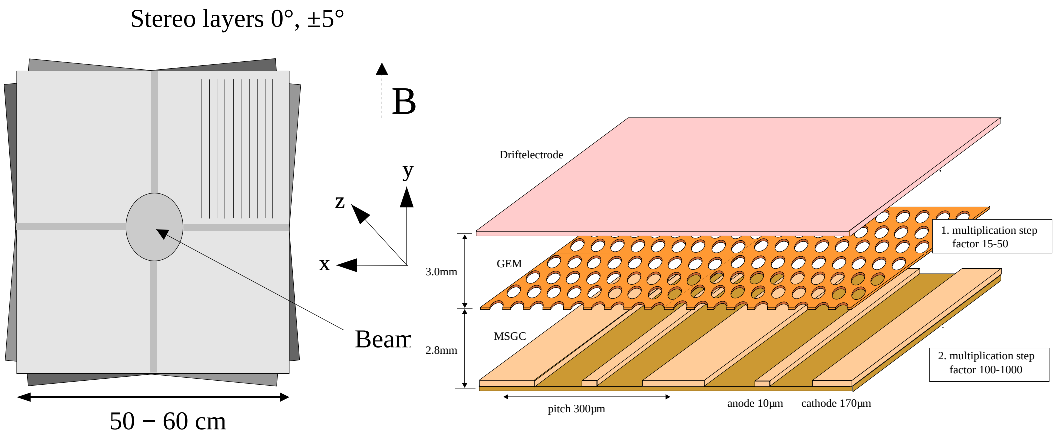

Figure 2.10: Geometry of the inner tracker detector in front of the RICH detector and a schematic view of a low gain micro strip gas chamber combined with a gas electron multiplier foil.

beam. The outer limit of the spectrometer acceptance is at 250 mrad in the horizontal plane and at 220 mrad in the vertical plane. This translates to lateral dimensions of about $6\ \mathrm{m}$ by $4.5\ \mathrm{m}$ for the sensitive area of the largest subdetectors.

A modular design has been adopted in the construction of the stations, building blocks of the outer tracker system. Each detector plane consists of an array of independent honeycomb modules which are fixed to a common support. These modules have a standard width of 32 cm, whereas their length differs from station to station, such that one module covers the full height of the sensitive area. The basic drift cell in an honeycomb drift chamber is a tube of hexagonal cross section with a signal wire strung along its center (Fig. 2.11, right). The tube is formed from a conductive foil which acts as the cathode. In order to minimize the number of readout channels while keeping the cell occupancy at an acceptable level, two different cell sizes are used. Modules with a cell size of 5 mm are placed in the regions nearer to the beam pipe, the outer regions are covered by modules with 10 mm cell size (see Fig. 2.11, left).

The basic station design consists of detector planes with wires strung at 0 mrad, +80 mrad and -80 mrad with respect to the vertical direction. The coincidence of hits in the three layers should thus assure spatial resolution of the order of $150\mu m$ per station in the horizontal direction and about $150\mu m/80mrad = 1.9mm$ in the vertical direction.

The outer tracking system consists of fifteen planar drift tube stations oriented perpendicularly to the beam direction and at distances from about 2 m up to 13 m downstream from the target (see Fig. 2.2). In the region from the end of the target vessel to the end of the magnet nine chambers are positioned. They are used for finding and fitting the curved continuations of already found straight track sections. Four layers in the region from the end of the magnet up to the front side of the RICH vessel are used for pattern recognition of straight tracks and for trigger decisions. The remaining two stations in the region between the RICH and the electromagnetic calorimeter are used by the trigger and to extrapolate tracks to the calorimeter and the muon system.

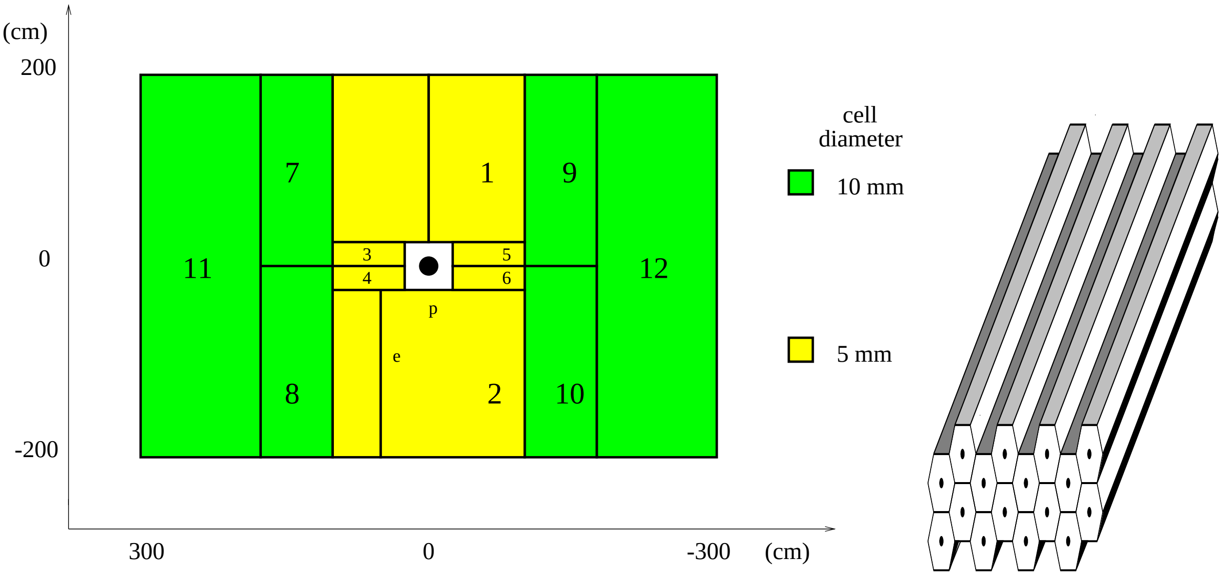

Figure 2.11: A lateral segmentation of a superlayer station into twelve sections (left). Each section consists of modules of honeycomb drift chambers, shown in the right plot.

2.4 The ring imaging Cherenkov counter

Identification of hadrons (pions, kaons and protons) is performed by a **ring imaging Cherenkov counter** (RICH) which uses perfluorobutane gas (C_4F_{10}) as the radiator, and a photon detector consisting of multi-anode photomultiplier tubes. The structure and operation of the ring imaging detector system will be described in detail in the following chapter.

2.5 The transition radiation detector

The transition radiation detector (TRD) is a part of the electron identification system. It efficiently separates electrons from hadrons in the region where the angular density of secondary particles and occupancy are highest. The transition radiation detector is positioned between the last two outer tracker super layers and covers the region around the proton beam pipe in transverse dimensions of $(134 \times 89\ \mathrm{cm}^2)$.

The detector is designed of the transition radiator interleaved with planes of straw proportional drift chambers as detecting elements (Fig. 2.12). The radiator consists of polypropylene fibers with a diameter of 20 μm resulting in a total radiator thickness of 1.6 cm per layer. The active detector elements of the TRD are straws made of thin multilayer (Kapton, carbon load Kapton, aluminum) cylindrical drift tubes. The straws of two different lengths (65 and 135 cm) and a diameter of 6 mm are used. The detector is operating with a gas mixture of Xe:CF_4:CO_2 70:20:10 at a gas gain of $2.5{\times}10^4$. This mixture combines the advantages of efficient transition radiation -absorption, short total drift time and stability with respect to discharge. The total drift time for 6 mm straws is 64 ns.

The transition radiation tracker consists of 2 superlayers with straw planes tilted by ± 30 degrees relative to the horizontal axes. Each superlayer contain 16 planes of straws interlayered by a radiator.

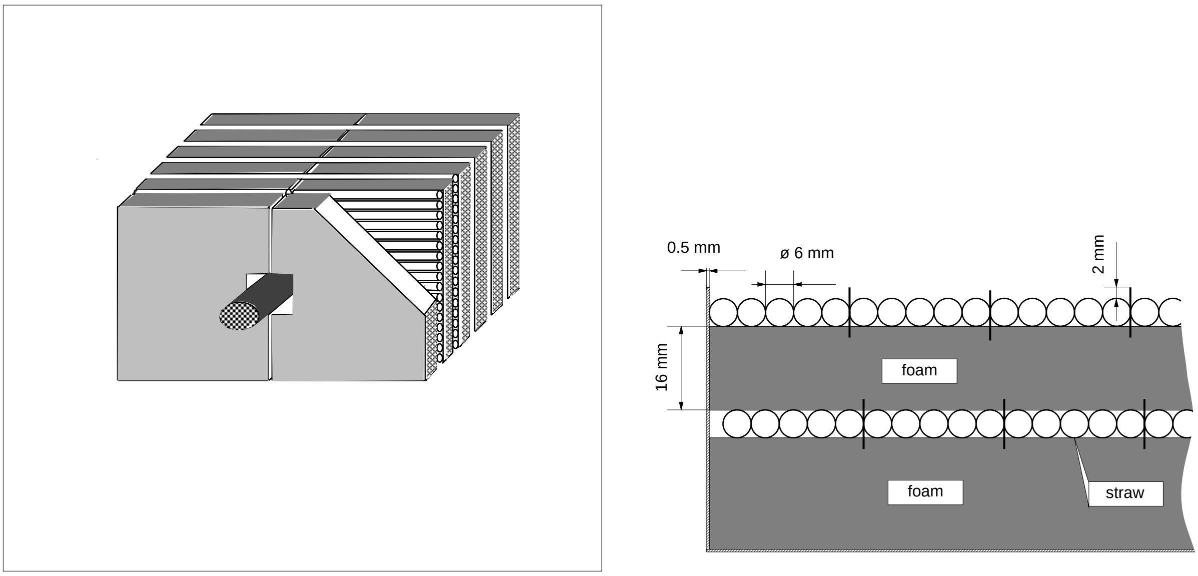

Figure 2.12: The isometric view of the transition radiation tracker (left) and the cross section of a block of the transition radiation detector (right).

2.6 The electromagnetic calorimeter

The electromagnetic calorimeter (ECAL) provides pretrigger signals on lepton candidates of $\mathrm{J}/\psi \rightarrow \mathrm{e}^{+}\mathrm{e}^{-}$ decays, a good hadron electron separation as well as energy and position measurements, mainly used at the trigger level. The calorimeter is positioned at 13.25 m from the target (Fig. 2.2 and Fig. 2.13). In order to have high detection efficiency both for the electrons produced in J/ψ decays and for tagging electrons, the calorimeter covers the range of 310 cm horizontally and 235 cm vertically. The geometrical acceptance to detect both the electron and the positron from J/ψ is 70% [14]. The corresponding acceptance loss is caused mainly by the inner hole of the calorimeter, where the proton beam pipe goes through.

The calorimeter has modular structure with a basic unit of $11 \times 11 \mathrm{cm}^2$ transverse dimensions (as shown in Fig. 2.14). The modules were built using shashlik technology with a sampling plastic scintillator and absorber sandwich. The scintillator and absorber plates are perforated to let plastic wavelength shifting fibers penetrate perpendicular through the plates. The light is collected by these wavelength shifter fibers which are joined in bundles arriving at a photomultiplier face.

The granularity of the detector is increasing with decreasing distance from the beam axis (see Fig. 2.13). Thus the inner, middle and outer modules comprise twenty five, four and one calorimeter basic cell respectively. The schematic view of the inner calorimeter module is

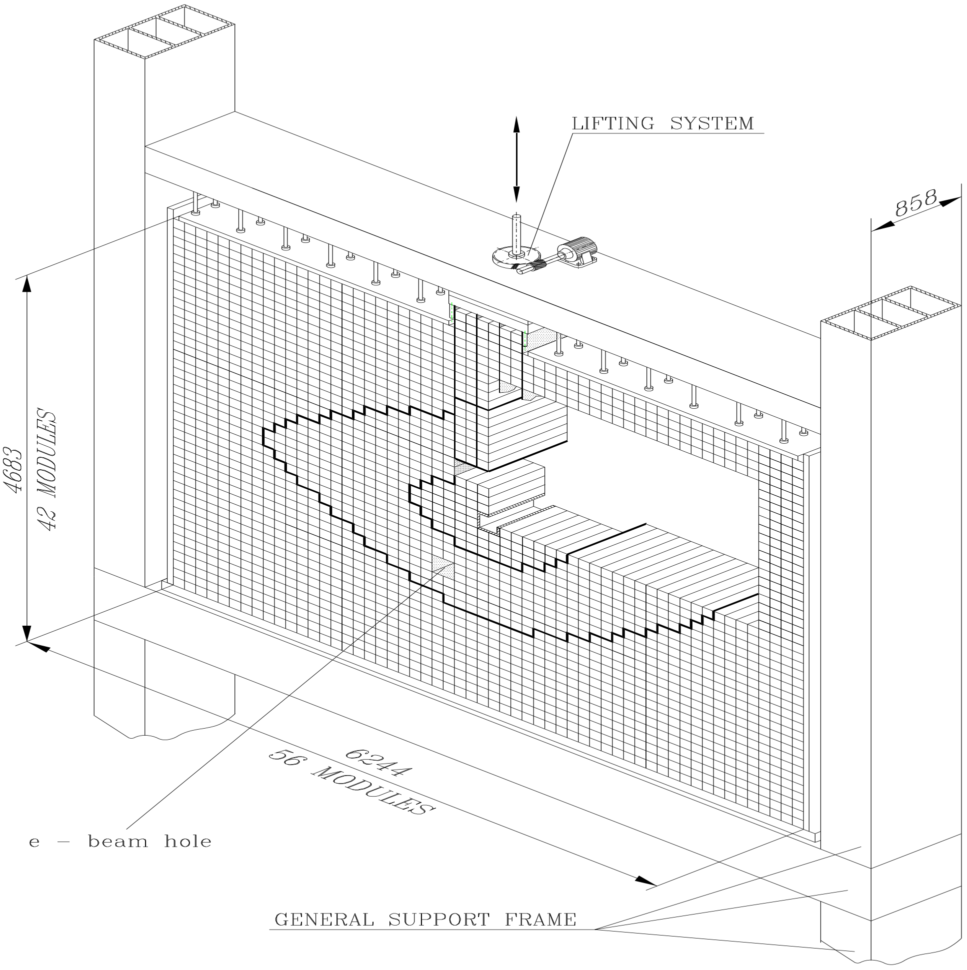

Figure 2.13: The electromagnetic calorimeter geometry. The 84 modules of the inner section are composed of 25 channels, the 532 ones of the middle section of 4 channels, while each of 1728 outer modules represent one channel.

shown in Fig. 2.14. Each module is made of alternating perforated tungsten and scintillator plates being $2\ \mathrm{mm}$ and $1\ \mathrm{mm}$ thick respectively. Altogether there are 40 tungsten and scintillator layers resulting in a total thickness of 23 radiation lengths. Each module has a transverse segmentation of 5×5 basic cells. Each basic cell employs its own photomultiplier tube. The middle and outer calorimeter modules consist of 37 layers of 3 mm thick lead and 6 mm thick scintillator plates resulting in a 20 radiation length depth. The outer calorimeter module consists of one individual basic cell, while the middle module is subdivided into 2×2 basic cells.

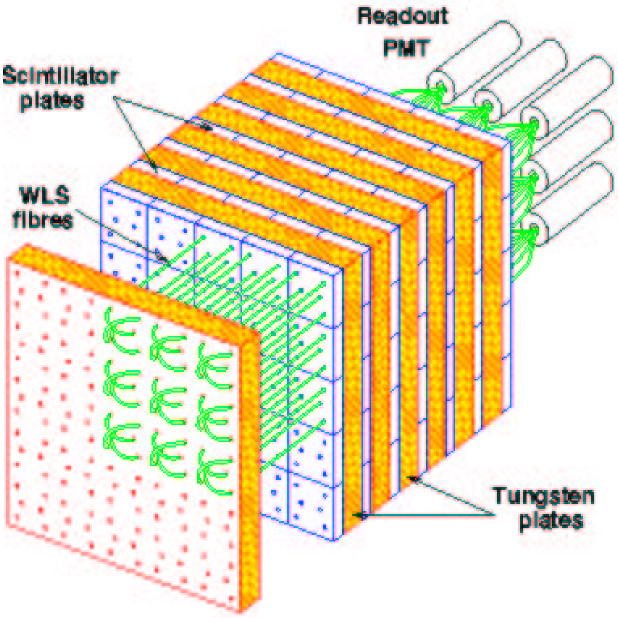

Figure 2.14: Schematic view of the inner module. The scintillator and absorber plates are perforated to let plastic wavelength shifting fibers penetrate perpendicular through the plates. The light is collected by the photomultipliers at the back.

In total there are 84 modules for the inner, 532 for the middle and 1728 modules for the outer calorimeter sections.

Using only position information of the clusters, one can already use the detector for the physics analysis. In the early stages of operation, when the main tracking system was still in the commissioning phase, the ECAL detector was used to extract the J/ψ signal from the decay $J/\psi \rightarrow e^+e^-$ (Fig. 2.15). The tracks have only been registered in the silicon vertex tracker and in the ECAL. From the hits in the vertex detector straight segments were reconstructed. They were propagated to the ECAL in the non-bending y direction, and if a cluster was found, the momentum was calculated from the bending in x direction. The invariant mass (i.e. the mass of the particle that decayed into a pair [†]) was than calculated for pairs of such track segments resulting in the clean J/ψ signal.

The performance of the electromagnetic calorimeter is illustrated also in Fig. 2.16. In the analysis it was assumed that π^0 decayed in the target wire to two γ photons. The two-cluster invariant mass distribution is shown in the Fig. 2.16. In the histogram only pairs, where each of the clusters had transverse energy [‡] E_T above $0.3\ GeV$ are registered. A clear π^0 peak with the width of $\sigma(m)/m \sim 7\%$ is seen. When events with two clusters with $E_T \geq 0.6\ GeV$ are selected with additional cuts on distance between clusters (more than 4 ECAL cells), E_T of

---

[†] $m = (\sqrt{m_1^2 + \vec{p_1}^2} + \sqrt{m_2^2 + \vec{p_2}^2})^2 - |\vec{p_1} + \vec{p_2}|^2$

[‡] $E_T = E\frac{p_T}{p}$

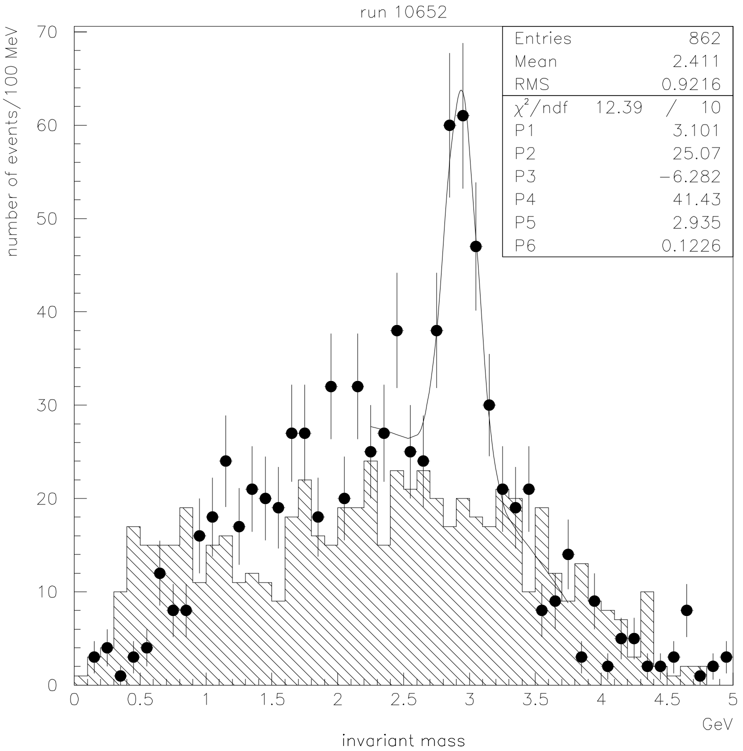

Figure 2.15: Invariant mass distribution for the e^+e^- pairs. The J/ψ resonance can be clearly seen [18]. Wrong sign combinations are hatched.

cluster pair above $2\ GeV$, a very clear η peak can be seen. In this case the mass resolution is about $\sigma(m)/m \sim 5\%$ which is better than for π^0, as expected.

Fitting the π^0 mass peak allowed to extract information on energy and position resolutions. As shown in [21] energy resolution was estimated to be $\sigma(E)/E = (22.5\pm0.5)\%/\sqrt{E} \bigoplus (1.7\pm 0.3)\%$ in the region $12-60\ GeV$, comparable to design values $17\%/\sqrt{E} \bigoplus \pm1\%$ [14]. Spatial resolution was estimated to be $\sigma_{x,y} = 0.2\ cm$ and linearity better than 0.5% in the $12-80\ GeV$ range.

2.7 The muon system

The muon system detects muons in the momentum range between a few GeV up to about 200 GeV/c. Identified muon pairs with an invariant mass in the region of the J/ψ meson provide the trigger signal for $\mathrm{B}^0 \rightarrow \mathrm{J}/\psi\mathrm{K_s}$ decays. The muon system also serves to select additional single muons from semileptonic decays, which provide a tag of the B meson flavor. Angular detector acceptance is 250 mrad horizontally and 160 mrad vertically. The geometrical acceptance for detection of the $\mu^+\mu^-$ pairs with momenta above $5\ \mathrm{GeV/c}$ from J/ψ decays is 71%, while the acceptance for the tagging muon is 81% [14].

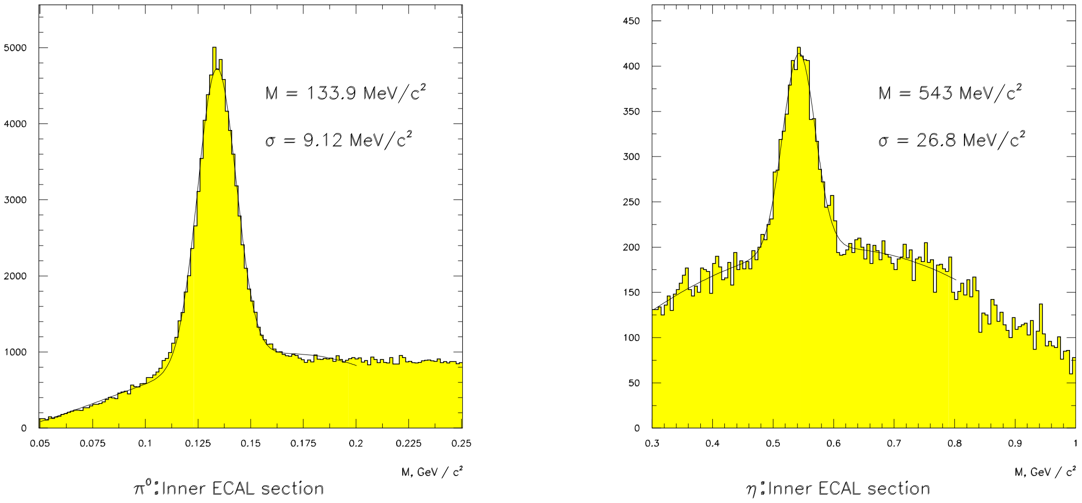

Figure 2.16: Two-cluster invariant mass spectrum [18]: π^0 (left) and η signal (right) in two-cluster invariant mass spectrum, Inner ECAL.

The separation of muons from hadrons in the muon system is achieved by exploiting the higher penetration capability of muons. The muon system consists of the muon filter and four superlayers of muon chambers as shown in Fig. 2.2. Three hadron absorber segments, built of iron and armored concrete blocks, alternate with three detector superlayers. A fourth superlayer is added to provide together with the third superlayer a clean multiple scattering free measurement of track directions.

The muon detection superlayers are composed of three different chamber types: tube chambers, pad chambers and gas pixel chambers. In the outer regions of the first two superlayers of the muon system the tube chambers are used, while the last two employ pad chambers. In the region around the beam pipe gas pixel chambers in all four layers are used.

The tube chamber is a closed-cell proportional wire chamber made of an aluminum profile with a 14×12 mm^2 large drift cell in cross section. A gold plated tungsten anode wire of a diameter of $40\mu m$ and of a length of nearly 3 m is stretched in the center. To ensure a high efficiency, each chamber consists of two layers of 2×16 cells shifted one against the other by half a cell (Fig. 2.17).

The pad chamber is a proportional wire chamber assembled from an open aluminum profile and closed with the copper phenolic board. This board is divided into 60 pads with an anode wire of length 3 m stretched inside each cell. Again, the pad chambers consist of two monolayers shifted by half a cell width with respect to each other.

Gas pixel chambers, single-layer multiwire proportional chambers, are composed of square cells formed by one sense wire and four potential wires with the length of about 3 cm, oriented

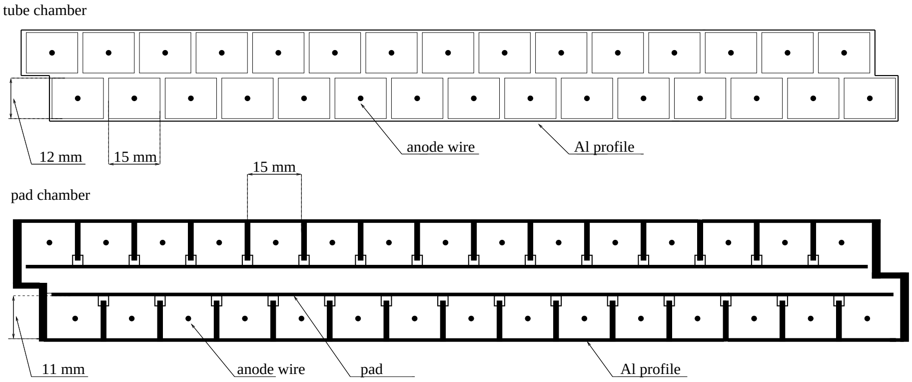

Figure 2.17: Schematic drawing of the tube chamber and pad chamber construction.

along the beam direction. Cells of a size of $9 \times 9\ \mathrm{mm}^2$ are used in the first three superlayers, while cell size of $9.4 \times 9.4\ \mathrm{mm}^2$ is chosen for the last superlayer in order to follow the projective geometry. The cell sizes of the muon chambers are determined exclusively by the maximum allowed drift time as the accuracy for the measurement of the track position is limited by multiple scattering in the calorimeter and in the absorber.

The first and the second superlayers consist of three layers of muon tube chambers, with anode wires perpendicular to the horizontal plane in one layer and wires oriented by $\pm 20^0$ with respect to the vertical line in the other two (Fig. 2.18). The information is used in the trigger decision and in the analysis. The third and fourth superlayer consist of one layer with pad and wire readout. Information from the superlayers is used to determine particle directions and for the trigger decision.

2.8 The data acquisition system and the triggering system

The triggering system controls the data acquisition (DAQ) at the HERA-B experiment. The DAQ must cope with more than half a million of detector channels, a 10 MHz bunch crossing rate and a signal to background ratio of 10^{-10}. The physics program of the experiment determines the trigger algorithms. Since the signal to background ratio is very small, the event selection scheme is divided into four sequential triggering levels. There are two requirements to the DAQ of the HERA-B system, the logging rate and the processing power. A typical HERA-B event has a size of 100 kbyte, which corresponds to a data flow rate of 1 Tbyte/s at an event rate of 10 MHz. Such a high data flow rate cannot be accommodated by the available storage logging systems. In addition, the complete event reconstruction takes a few seconds on the state of the art processors. As the required processing power cannot be implemented, events must be selected before they are saved on tape or disk.

The DAQ and the triggering system architecture is presented in Fig. 2.19 and will be briefly described in the following. Each of the trigger levels has a characteristic data flow and rate requirement. At the first level the detector channels are fed into the different front end elec-

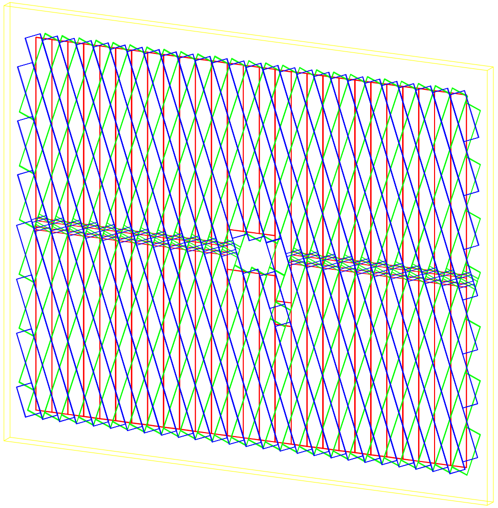

Figure 2.18: View of the superlayer with three layers of muon tube chambers.

tronics. If needed, the signals are amplified, shaped and digitized already at the detector. The signal wires are connected to a Front End Driver (FED) system. There are four different types of front end drivers for different types of the measurements needed: analog type FED for the inner tracker and the silicon vertex detector, hit type FED for the muon system, the RICH, the High-Pt system and the TRD, timing type FED for the outer tracker, and a pulse height type FED for the electromagnetic calorimeter.

The Fast Control System is designed to synchronize the detector, assign the detector signals to events and identify events. Therefore it distributes signals to the FED's. Among these signals are the bunch clock, the FED specific delay between bunch clock and detector signals, the current event number and event numbers of First Level Trigger (FLT) accepted events. The Fast Control System consists of one central “mother” unit, a signal distribution system and a “daughter” board in each Front End Driver crate. There are all together 210 daughters in the HERA-B detector.

The first level trigger processes only part of the event information with data stream of 150 Gbyte/s and delivers its result after a delay not longer than 12 μs. It searches for e^+e^- and $\mu^+\mu^-$ track pairs with a J/ψ signature. The high rejection rate of the first level trigger is expected to reduce the input event rate by a factor of 200. After an event is accepted by the first level, all data belonging to this event are read out of the pipelines and pushed into a second level buffer, which is implemented with the SHARC cluster VME boards [22]. The same SHARC cluster board is used to implement a switch which carries the event control traffic, the dialog between second level trigger and second level buffer and runs the event controller. The second level trigger operates only on selected data information at 50 kHz to 100 kHz input rate and

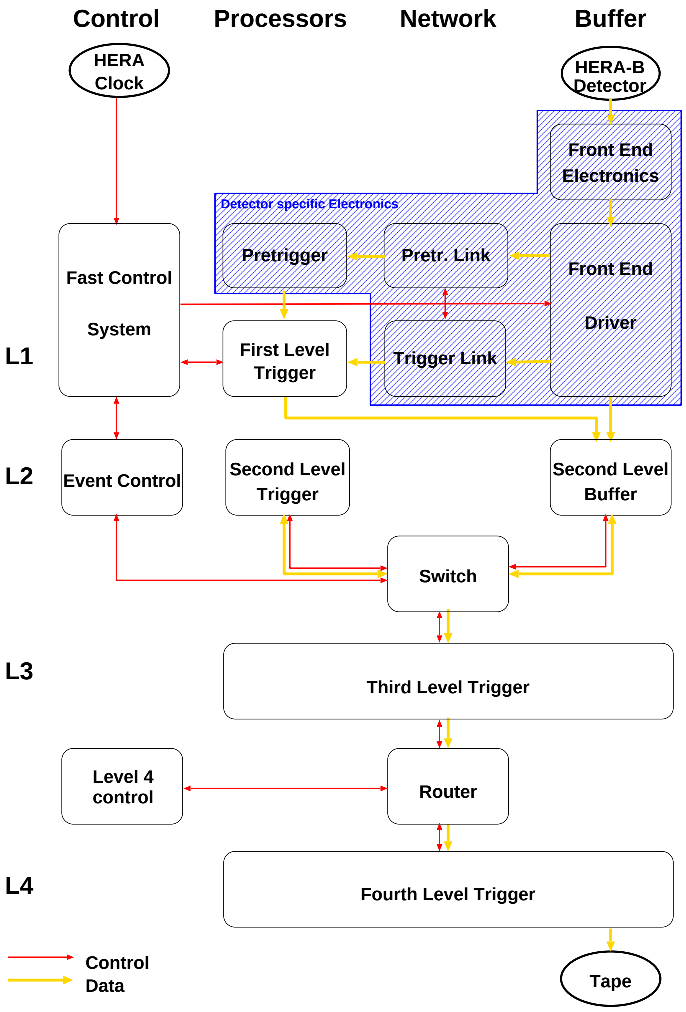

Figure 2.19: Data acquisition and triggering system architecture used in the HERA-B experiment.

therefore digests 50 Mbyte/s.

More than hundred dedicated second level trigger PC processors repeats the first level trigger algorithm with a higher precision. It adds more hits with the full chamber resolution in the tracking layers behind the magnet and projects tracks through the magnet and vertex detector. The silicon tracker data is used to reject dileptons generated in different interactions during the same bunch crossing and to enhance J/ψ candidates from secondary vertices downstream of the target. A rejection factor of 10 should be obtained by eliminating events which do not contain reconstructed tracks of acceptable quality and an additional rejection of factor 10 is expected after the vertex cuts are applied. Events surviving the second level trigger cuts are passed to the third level trigger. It is the first trigger level which does not use only selected information, but requires a complete event data assembled and available in processor memory. The third step operates at a rate below 1 kHz which amounts to a data rate of 100 Mbyte/s. The third level trigger does the full track and vertex fitting with high precision. More stringent cuts on particle mass and vertex positions for all the tracks in the event should reduce the data stream by a factor of 10. Accepted events are routed to the fourth level trigger. It actually does not act as a real trigger because it performs the full event reconstruction which calls for the entire detector alignment and calibration data. The fourth step works at the event input rates smaller than 50 Hz which presents a data stream of moderate 5 Mbyte/s. A few seconds of computing time per event is needed on one of more than one hundred dedicated processors, where pattern recognition and event reconstruction procedures are running. A reduction of a factor 2.5 is expected such that the event data would be routed to the storage media at a moderate event rate of 20 Hz as a final step of the DAQ and triggering system procedure.

The major part of the DAQ and the trigger system has already been commissioned and works as expected. The first level trigger is not ready and is still being commissioned.

3

Particle identification in the HERA-B experiment

Particle identification is equivalent to a determination of particle mass. As mass cannot be measured directly, this has to be done in several steps. Usually momentum is measured for each particle by the tracking system from the curvature of the particle path in the magnetic field. To uniquely determine the mass another measurement is performed. In the HERA-B detector there are several subsystems that provide independent measurements to identify particles.

Muons, electrons and photons are adequately identified within the electromagnetic calorimeter, the muon detector and the transition radiation detector. The electromagnetic calorimeter identifies particles on the basis of energy loss and cluster shape. Also, electrons are separated from hadrons in the transition radiation detector. The separation of muons from hadrons in the muon system is based on the higher penetration capability of muons. As already mentioned, the muon system consists of three hadron absorber segments, built of iron and armored concrete blocks, and three detector superlayers in between. Thus, reconstructing a track in the muon detector identifies it as a muon.

Hadrons have to be identified by other means. At high momenta ($pc >> mc^2$) the difference in velocity of two particles falls with the square of the momentum, and the separation becomes increasingly more difficult:

$$\Delta\beta = \frac{m_K^2 c^2 - m_\pi^2 c^2}{2p^2} \ . \tag{3.1}$$

The difference in time of flight of a kaon and a pion of 30 GeV/c momentum, which is a typical momentum, is only 4 ps over a flight path of 10 m. Since this cannot be measured with adequate precision, the use of the time of flight technique for hadron separation is not feasible. While the measurement of the specific energy loss in the tracking chambers could in principle exploit the relativistic rise to separate pions from kaons, the rather small total gas thickness, around 70 thin samples of either 5 mm or 10 mm length, would only allow for a very modest and therefore insufficient resolution [24]. The problem of hadron identification can only be solved by measuring the photon yield and Cherenkov angle in the ring imaging Cherenkov counter (RICH).

3.1 Cherenkov counters

When a charged particle moves through a dielectric medium, it causes local, non-isotropic polarization in the atoms of the dielectric (Fig. 3.1). These atoms return to normal states by emitting light. If the velocity of the particle is less than the velocity of light in the medium, the light is destroyed by destructive interference. If however, the velocity of the particle is greater than the velocity of light in the medium, light is emitted due to constructive interference as shown in Fig. 3.2. The equivalent phenomenon in acoustics is the formation of the acoustical shock wave generated by a body moving with supersonic velocity. The emitted radiation is called Cherenkov radiation after P. Čerenkov who received the 1958 Nobel Prize for Physics with Igor Y. Tamm and Ilya M. Frank for their investigation of the phenomenon [25].

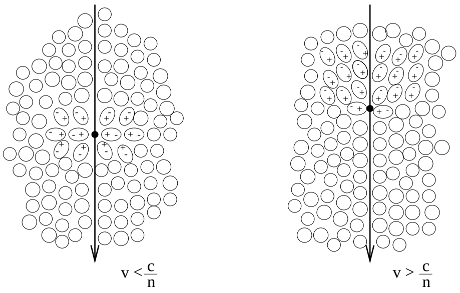

Figure 3.1: The distribution of dipoles in a dielectric as caused by the passage of a charged particle at a low (left) and at a high (right) velocity.

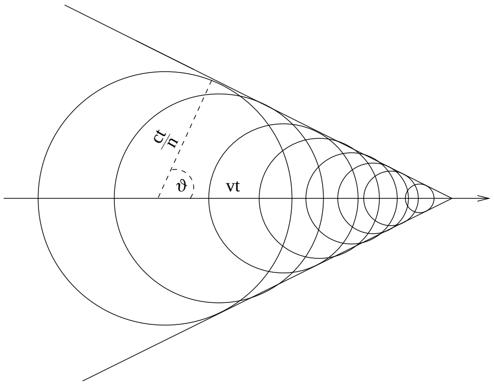

Figure 3.2: The Cherenkov wave front construction by the superposition of elementary spherical waves produced by the particle along its trajectory.

The characteristic Cherenkov angle θ_c, at which photons are emitted, is given by the equation:

$$\cos\theta_c = \frac{1}{n(E)\beta}. \tag{3.2}$$

where $n(E)$ is the refractive index of the medium for photons of a given energy $E = \hbar\omega$. The radiated photons are equally distributed with respect to the azimuthal angle of emission. The minimal velocity, at which a charged particle radiates, is derived from Eq. 3.2

$$\beta < \beta_t = \frac{1}{n} \,. \tag{3.3}$$

At threshold, the light is emitted in the forward direction. The maximal Cherenkov angle in a medium is reached when the particle velocity approaches the speed of light.

The number of Cherenkov photons emitted per unit photon energy in a radiator of length L can be obtained by solving Maxwell's equations for a moving point charge [26]:

$$\frac{\mathrm{dN}}{\mathrm{dE}} = \left(\frac{\mathrm{e}_0^2}{4\pi\varepsilon_0\hbar^2\mathrm{c}^2}\right)\mathrm{Z}^2\mathrm{L}\sin^2\theta_\mathrm{c}, \tag{3.4}$$

where Ze_0 is the charge of the particle. Combining both equations (Eq. 3.4 and Eq. 3.2) one obtains the spectral dependence

$$\frac{\mathrm{dN}}{\mathrm{dE}} = \left(\frac{\mathrm{e}_0^2}{4\pi\varepsilon_0\hbar^2\mathrm{c}^2}\right)\mathrm{Z}^2\mathrm{L}\left[1 - \left(\frac{1}{\mathrm{n(E)}\beta}\right)^2\right]. \tag{3.5}$$

The Cherenkov radiation phenomenon is exploited in, Cherenkov detectors used for the velocity measurements. Two groups of counters have been developed. Threshold counters exploit the existence of threshold velocity at which particles start to radiate. Differential Cherenkov counters, Proximity Focusing Ring Imaging Cherenkov counters and Ring Imaging Cherenkov counters utilize the measurement of the angle at which photons are radiated.

Threshold Cherenkov counters exploit the fact that threshold momentum for the heavier of two particles is higher. In the region between the two thresholds, a particle of a certain species is uniquely identified. Using serial combinations of different radiators threshold Cherenkov counters allow e.g. pion kaon separation in the momentum range up to 30 GeV/c.

Differential Cherenkov counters take into account the emission angle in order to identify particles. The cone of Cherenkov light emitted in a radiator of a finite length expands to a ring on the plane some distance away from the radiator. Using a diaphragm of appropriate diameter, one can detect particles of certain velocity. The problem of this type of counters is a small acceptance in $\Delta\theta_c$ and in $\Delta\beta$ and in incident angle of the particle.

The principle of **Proximity Focusing Ring Imaging Cherenkov counters** is based on a simple geometrical configuration, involving no focusing device. The counter consists of a simple thin solid or liquid radiator, separated from the photon detector plane by a drift space allowing the Cherenkov cone to develop. This type of configuration is suitable for a large detection area and a large angular acceptance, for which classical focusing devices cannot be used. The resolution is usually limited by the chromatic dispersion of the radiator medium or radiator thickness.

Ring Imaging Cherenkov detectors [27] determine the Cherenkov angle θ_c of the particle by measuring the radius of the ring on the detector surface (Fig. 3.3). They are based on the principle of ray optics. The parallel light rays are focused into one point on the focal surface after the reflection on the spherical mirror. Thus, all Cherenkov photons emitted under the same azimuthal angle are parallel and are focused into one point after the reflection on the spherical mirror with a radius of curvature R. Since the Cherenkov light is emitted in a cone around the direction of the charged particle, it is focused onto a ring in the focal plane of the mirror. In this way spherical mirrors transform angular into positional information.

By measuring the diameter $2r$ of the ring one can determine the angle of emission of the Cherenkov light θ_c via the relation $\tan\theta_c = \frac{2r}{R}$. Using Eq. 3.2, the velocity of the particle can be calculated. If in addition the momentum of the particle is measured from the curvature of its trajectory in a magnetic field, the mass and thus its identity are determined from the relation between the momentum and velocity of the particle:

$$\mathrm{p} = \frac{\mathrm{mc}\beta}{\sqrt{1-\beta^2}}. \tag{3.6}$$

To measure the Cherenkov angle accurately, not only precision in the position of the photon detection point but also the number of detected photons is important. It is therefore crucial to have a large detector area with good position resolution and a good detection efficiency. These properties can be obtained with detectors utilizing the photo-ionisation process in gases in combination with charge multiplication due to electron avalanche generation in strong electric fields (wire chambers), or by using position sensitive photomultiplier tubes. A schematic view of a ring imaging Cherenkov counter is illustrated in Fig. 3.3. In this optimal configuration the volume between the spherical surfaces is filled with a gas radiator.

Using equation 3.5, the average number of detected photoelectrons N_{det} can be written as

$$\mathrm{N_{det}} = \int \mathrm{T_r(E)} \cdot \mathrm{R_m(E)} \cdot \epsilon_{\mathrm{d}}(\mathrm{E}) \cdot \frac{\mathrm{dN(E)}}{\mathrm{dE}}\,\mathrm{dE}, \tag{3.7}$$

where $\mathrm{T_r(E)}$ is the transmission of the radiator and the windows , $\mathrm{R_m(E)}$ is the mirror reflectivity and $\epsilon_{\mathrm{d}}(\mathrm{E})$ is the detection efficiency of the photon detector. In Fig. 3.4 the typical values for these terms are shown as a function of Cherenkov photon energy. Neglecting the dispersion in the radiator, the integral of Eq.3.7 can be rewritten in the following form

$$\mathrm{N_{det}} = \mathrm{N_0 Z^2 L sin^2}\theta_{\mathrm{c}}, \tag{3.8}$$

where N_0 is the detector response parameter or the so called merit factor of the photon detector

$$\mathrm{N_0} = \left(\frac{\mathrm{e_0^2}}{4\pi\varepsilon_0\hbar^2\mathrm{c}^2}\right)\int \mathrm{T_r(E)R_m(E)}\epsilon_{\mathrm{d}}(\mathrm{E})\,\mathrm{dE}. \tag{3.9}$$

The constant factor in front of the integral can be evaluated as

$$\left(\frac{\mathrm{e_0^2}}{4\pi\varepsilon_0\hbar^2\mathrm{c}^2}\right) = 370\mathrm{cm^{-1}eV^{-1}}. \tag{3.10}$$

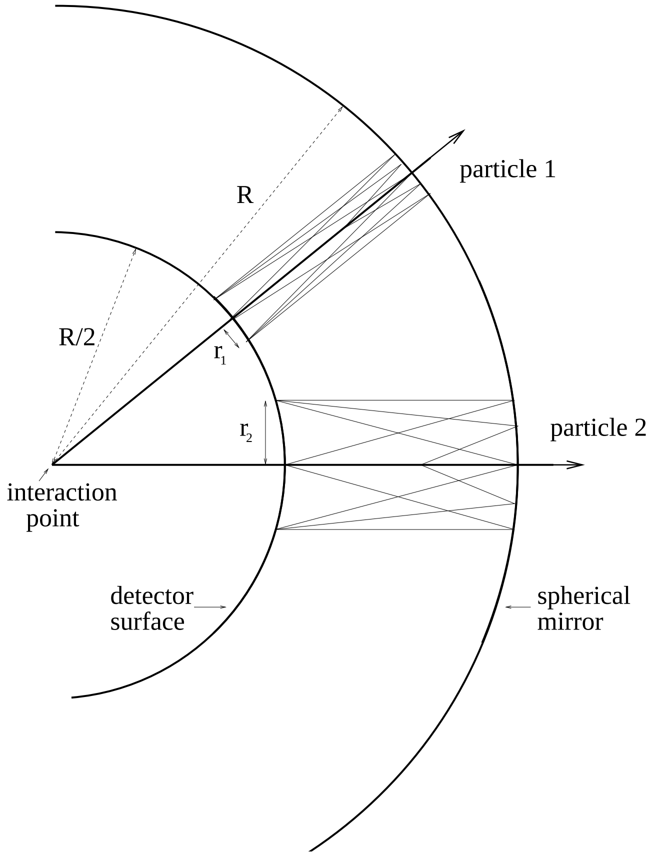

Figure 3.3: Principle of the ring imaging Cherenkov counters. The Cherenkov cone is focused onto a ring with radius r on the detector sphere.

The velocity measurement error of a RICH counter is derived from Eq. 3.2:

$$\frac{\sigma_\beta}{\beta} = \sigma_{\theta_c}^{ring} \tan\theta_c, \tag{3.11}$$

where $\sigma_{\theta_c}^{ring}$ is the Cherenkov angle measurement error of the ring. This error originates from the experimental uncertainties in the determination of the Cherenkov angle and from the variation of the radiator refractive index with the photon energy. The error on the measurement of the Cherenkov angle $\sigma_{\theta_c}^{ring}$ decreases with the number of photons N that contribute to the measurement, each with the single photon error σ_{θ_c}. In the case of isolated rings with little background,

$$\sigma_{\theta_c}^{ring} = \frac{\sigma_{\theta_c}}{\sqrt{N}}\,. \tag{3.12}$$

The single photon error σ_{θ_c} is determined by the following dominant sources:

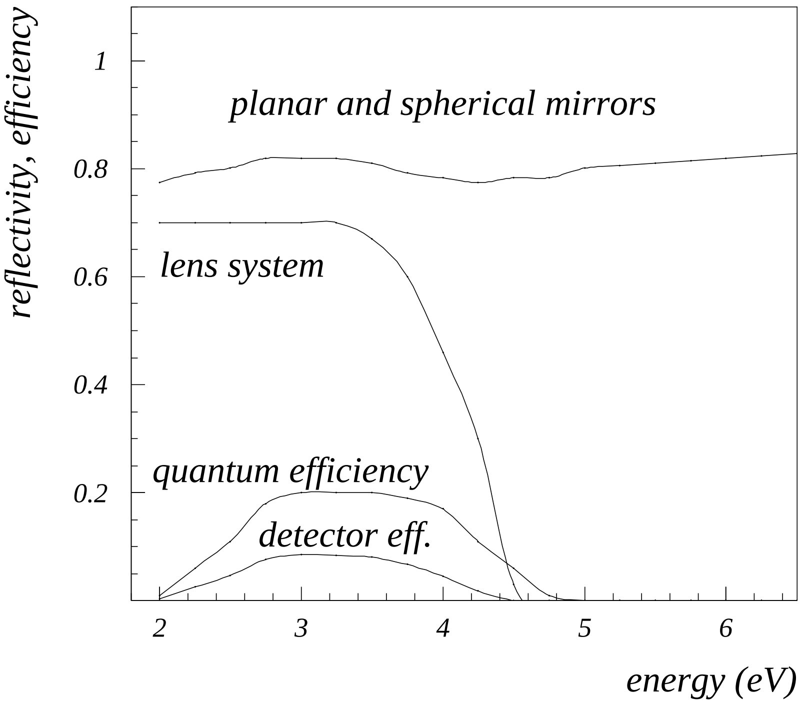

Figure 3.4: Reflectivity of planar and spherical mirrors and the detection efficiency of the photon detector as a function of photon energy, all in the case of the HERA-B RICH. Note that the photon detector efficiency includes the efficiency of the light collection system, photomultiplier tube quantum efficiency and photoelectron detection efficiency [28].

- the chromatic aberration, a consequence of the variation of the refractive index over the sensitive energy range of the photon detector, which results in

$$\sigma_{\theta_c}{}^{\mathrm{dis}} = \frac{1}{\mathrm{n}\sqrt{\mathrm{n}^2\beta^2-1}}\frac{\mathrm{dn}}{\mathrm{dE}}\sigma_{\mathrm{E}} \approx \frac{1}{\sqrt{2\mathrm{n}-1}}\frac{\mathrm{dn}}{\mathrm{dE}}\sigma_{\mathrm{E}}, \tag{3.13}$$

  where σ_{E} is the standard deviation of the energy distribution of detected photons. Approximations $(\mathrm{mc/p}) \ll 1$ and $(\mathrm{n}-1) \ll 1$ have been used.

- The finite coordinate resolution of the photon detector (if hits within the square pad are uniformly distributed) amounts to

$$\sigma_{\theta_c}{}^{\mathrm{det}} = \frac{\mathrm{a}}{\mathrm{f}\sqrt{12}}, \tag{3.14}$$

  where f is the focal length of the spherical mirror and a is the photon detector pad size.

- In cases when the ring center is not determined from the RICH detector, an external track direction information from the tracking system should be used for the Cherenkov angle calculation. Thus, imperfections in the determination of the track direction ${\sigma_{\theta_c}}^{track}$ also enter the achievable Cherenkov angle single photon resolution. Note that for large errors on the track direction ($\sigma_{tx} \gg 2\ mrad$) the measured Cherenkov angle distribution is not Gaussian.

In addition, a multiple Coulomb scattering in the radiator from a straight line and optical system imperfections contribute to the error on the measurement of the Cherenkov angle.

3.2 The HERA-B Ring Imaging Cherenkov detector

The Ring Imaging Cherenkov detector (RICH) of the HERA-B experiment was designed mainly to separate kaons, that tag the flavor of B decays, from pions in the momentum interval between 3 to about 50 GeV/c (Fig. 3.5). It consists of a gas radiator, spherical and planar mirrors, exit windows and photon detectors (Fig. 2.2). To meet the requirements of wide momentum interval, the radiator had to be carefully chosen.

The difference in the velocity of two particles of the same momentum decreases with square of momentum (Eq. 3.2), and the difference in the Cherenkov angle for $\beta \approx 1$ particles is

$$\Delta\theta \approx \frac{1}{n^2\theta}\Delta\beta\ . \tag{3.15}$$

Thus, the difference in the Cherenkov angle between two species is larger, if a radiator with a lower refractive index is used. Since the expected ring radius resolution is around 0.2 mrad at momenta around 50 GeV/c [14], the difference in Cherenkov angle of pions and kaons should be around 1 mrad assuming 35 detected photons per $\beta \approx 1$ track. This limits the choice to gas radiators with as small refractive index as possible ($n - 1 \leqslant 10^{-3}$). On the other hand, the threshold momentum for pions and kaons should be as low as possible in order to use the identification capabilities of the detector already in the momentum range around a few GeV/c. Thus, one should use the radiator with high refractive index $n - 1 \geqslant 10^{-3}$. These two features limit the choice of the radiator to gases with $n - 1 \approx 10^{-3}$.

Among comercially available gases, freons have the highest refractive index. For the HERA-B RICH gaseous perfluorobutane C_4F_{10} was chosen, since it combines a relatively high refractive index

$$n(3.3eV) - 1 = 1.330 \cdot 10^{-3} \tag{3.16}$$

and a low dispersion

$$\frac{\Delta n}{\Delta E}(3.3eV) = 3 \cdot 10^{-5}\frac{1}{eV}\ . \tag{3.17}$$

The Cherenkov threshold momentum for pions is at 2.7 GeV/c, for kaons at 9.6 GeV/c, while the threshold for other charged particles can be seen in Table 3.2. In Fig.3.6 the variation

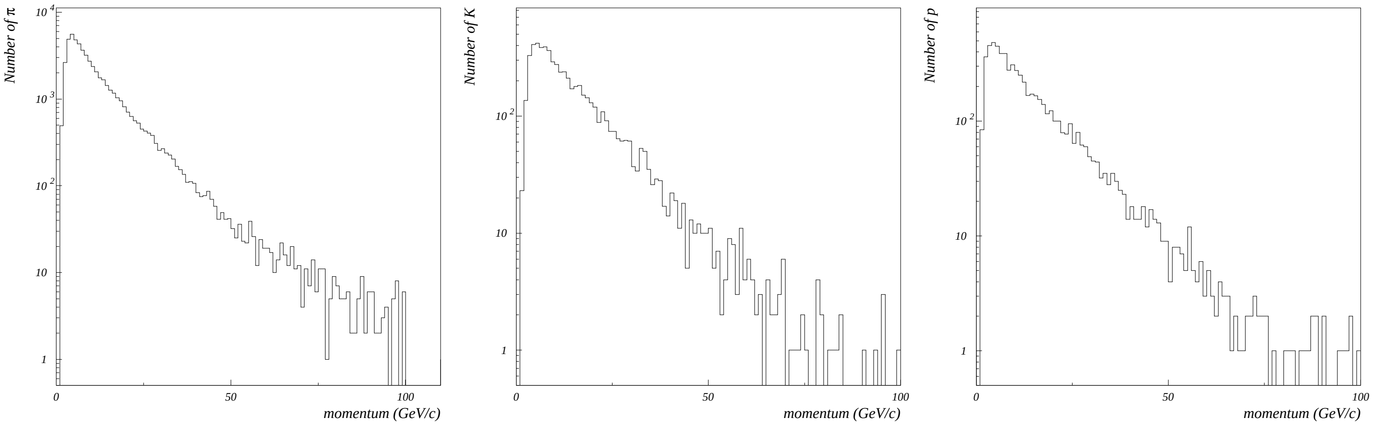

Figure 3.5: Monte Carlo prediction of the momentum spectrum of pions(left), kaons(middle) and electron(right) produced in the reaction $B \to J/\psi\, K_S$ in the HERA-B experiment. Only particles within the RICH acceptance window (approximately. 200 mrad×250 mrad) are taken into account.

of the expected Cherenkov angle for different particles as a function of momentum is shown. For $\beta = 1$ particles, the Cherenkov angle is 51.5 mrad, while the pion - kaon difference in Cherenkov angle is 34 mrad at 10 GeV/c and falls to 0.9 mrad at 50 GeV/c.

Particle type	Threshold momentum
electron	9.8 MeV/c
muon	2.03 GeV/c
pion	2.7 GeV/c
kaon	9.6 GeV/c
proton	18 GeV/c

Table 3.1: The Cherenkov threshold momentum for different charged particles traversing the RICH detector.

When designing the HERA-B ring imaging Cherenkov counter the following criteria were used:

1. the length of the radiator should be fixed to a few meters in order to detect enough photons on each ring image,
2. the photon detector must be kept outside the solid angle of the charged particle flux,
3. the photon detector surface has to be divided into pads to accomplish position detection and to cope with a high rate environment and

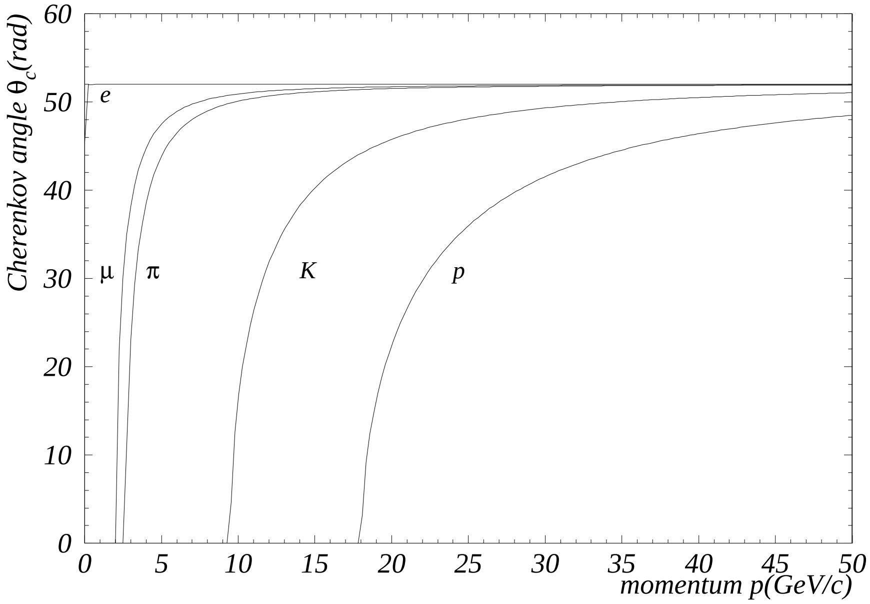

Figure 3.6: Cherenkov angle as a function of momenta for different particles (electrons, muons, pions, kaons and protons) in a C_4F_{10} radiator.

4. the spherical mirror focal length is should be several meters to achieve the required high resolution in the Cherenkov angle, assuming a pad size of the order of less than a cm (Eq.3.14).

According to the above requirements the RICH detector consists of (see Fig. 3.7):

- the C_4F_{10} gas radiator where Cherenkov photons are produced by charged particles,
- the two segmented spherical mirrors which reflect Cherenkov photons onto the corresponding planar mirror,
- two segmented planar mirrors which reflect Cherenkov photons to the focal surface above and below the beam pipe outside of the charged particle fluxes,
- the photon detector, in the focal surface which is capable of detecting photons with high efficiency and with good position resolution in two dimensions and
- the read-out system with low noise electronic components.

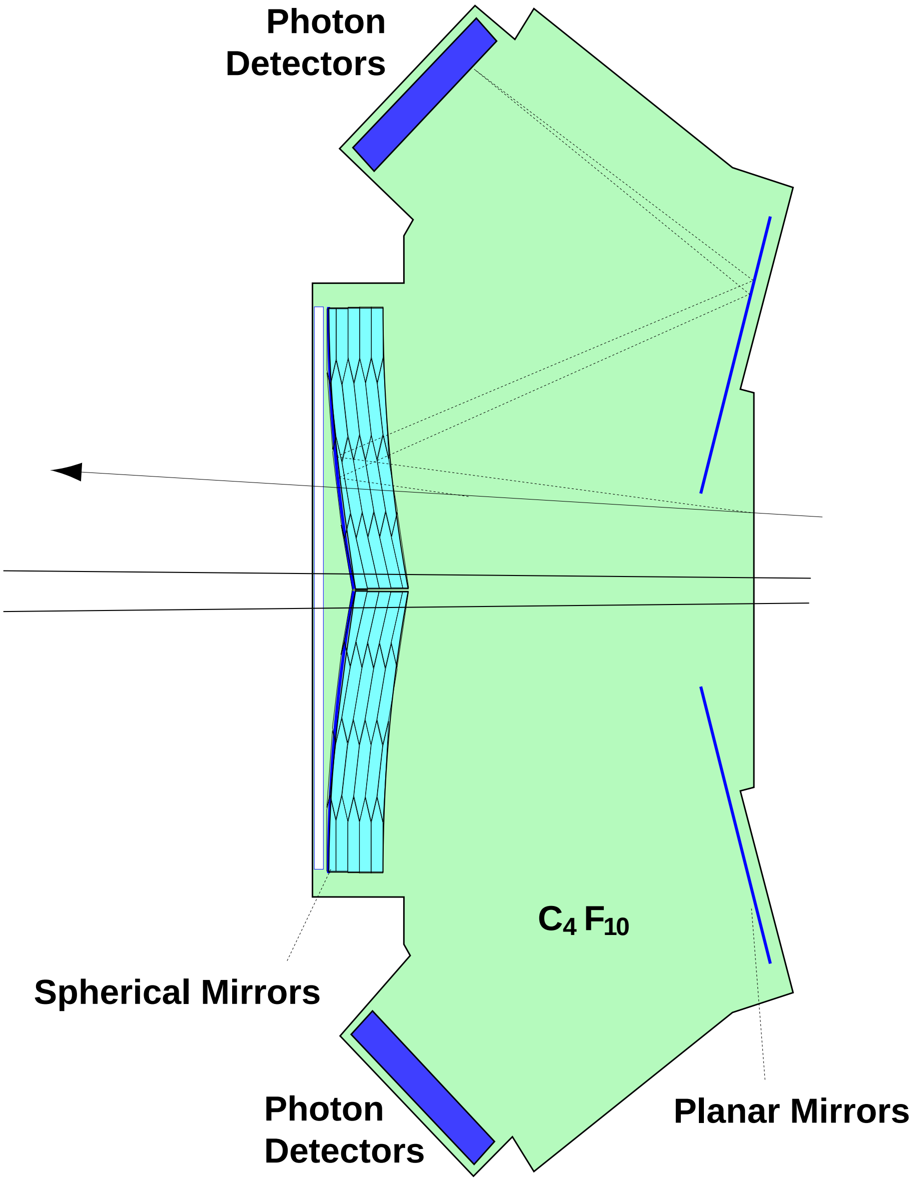

Figure 3.7: Side view of the RICH counter with the overall dimensions 2.7 $m \times 9$ $m \times 7$ m.

3.2.1 Radiator

The $\mathrm{C_4F_{10}}$ gas radiator [29] is supplied to the radiator vessel by a dedicated system [30]. The system has to maintain the gas purity (O_2 and H_2O concentrations below 100 ppm) to reduce the production of hydrofluoric acid, one of the strongest and most corrosive acids, which forms when the gas mixture of $\mathrm{C_4F_{10}}$, water and oxygen is exposed to high fluxes of charged particles. The vessel has a volume of 106 m^3 and has been constructed from stainless steel, except for the particle entry and exit windows (1 mm Al) and the photon exit windows (UVT perspex). Also, two beam shrouds close the gas volume around the two beam pipes for protons and electrons.

3.2.2 Mirrors

Two mirror systems, a spherical and a planar one, are made of hexagonal and rectangular units, respectively. The hexagonal mirror segments with 11.4 m radius of curvature have been produced from 7 mm thick grinded glass.

By making use of the optical quality data gathered on all the mirror segments, it was possible to group them in a tiling scheme according to the resolution requirements [31]. Each spherical mirror segment is supported at three points, two of which can be moved, and are motor driven via a transmission mechanism with a feed-troughs to the exterior of the vessel.

The planar mirrors are made of float glass, thus being significantly cheaper at the required optical quality.

3.2.3 Photon detector

The initially foreseen detectors based on wire chambers [14] had to be abandoned; the TMAE detector showed a prohibitive decrease of avalanche gain due to aging effects [32], while the CsI photocathode could not be routinely produced and maintained with sufficiently high quantum efficiency in addition to problems with rates in excess of a few kHz per pixel [33]. The final photon detector thus consists of Hamamatsu multianode R5900 M16 and M4 photomultiplier tubes. The photomultipliers have high gain at reasonably low voltage of below 1 kV. They offer a high quantum efficiency of the order of 20% in the range from 250 nm to 650 nm [34]. In the preliminary tests they showed a good single photoelectron pulse height distribution [35, 36] (Fig. 3.8). The M16 photomultiplier consists of 16 anode pads with dimensions $4\ mm \times 4\ mm$ in 4 rows and 4 columns. The M4 photomultipliers have only 4 anode pads which are four times bigger ($8\ mm \times 8\ mm$), so that the total sensitive area ($16\ mm \times 16\ mm$) is the same for both types. In the preliminary test it was showed that the surface sensitivity of the photomultiplier is very uniform (Fig. 3.8). Due to the smaller photocathode surface compared to the photomultiplier cross section, a demagnification system was designed in order to adjust the required pixel size to the PMT pad size (Fig. 3.9). The granularity of the photon detector has been chosen on the basis of expected occupancy and the required position resolution to be either 9 x 9 mm^2 for the inner part or 18 x 18 mm^2 for the outer part of the detector. Still, a typical event recorded in the HERA-B RICH detector (Fig. 4.2) consists of a huge number of hits (around 10% of the channels are hit). The tests have also shown a satisfactory performance under an elevated counting rate of 3 MHz per channel during a period of 30 days [35, 36].

The required demagnification of a factor of 2 is achieved with a two lens system consisting of a field lens and a condenser [38](Fig. 3.9). The lenses are made of UVT perspex with high transparency over most of the wavelength region where the photocathode is sensitive [34]. The angular acceptance of the optical system is also satisfactory and is uniform for incident angles below about 110 mrad.

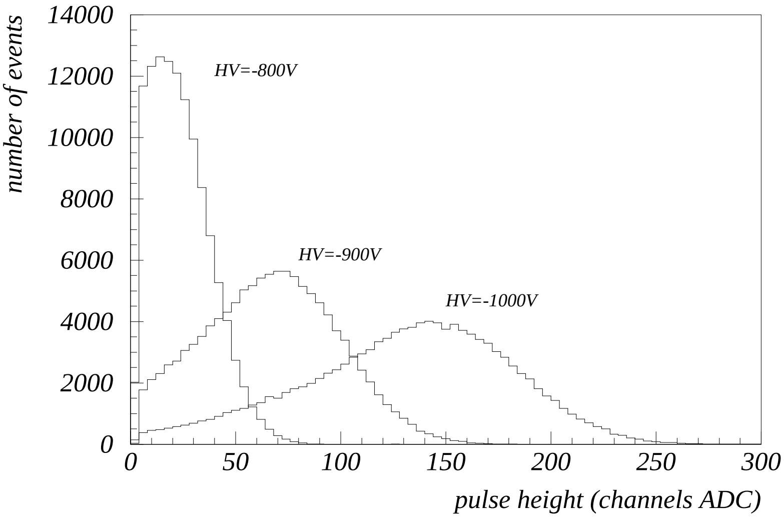

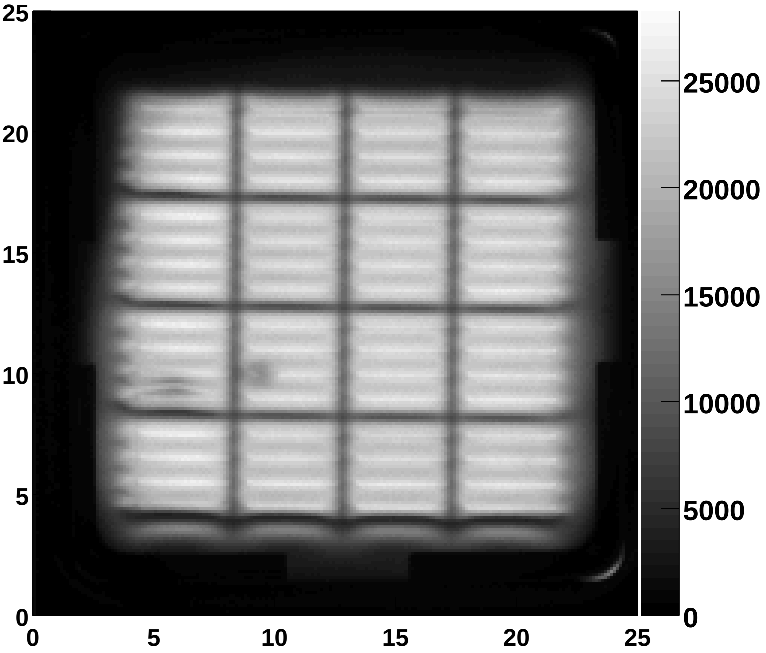

Figure 3.8: Pulse height distributions due to single photoelectrons for three different anode voltages (top). Sensitivity of a M16 PMT surface when scanned by a light beam spot of about 20 μm diameter. The scale is in mm (bottom) [37].

In order to reduce the contribution of spherical aberration to the overall resolution of the Cherenkov angle, an optimal surface of the Cherenkov photon detector has been calculated [39]. Each half-detector (upper and lower) consists of 5 flat supermodules placed in order to approximate the optimal surface, which is close to the shape of a flattened (ellipsoidal) cylinder. Such an arrangement also ensures better acceptance for the Cherenkov photons, which should be incident onto the flat supermodules at angles below 110 mrad.

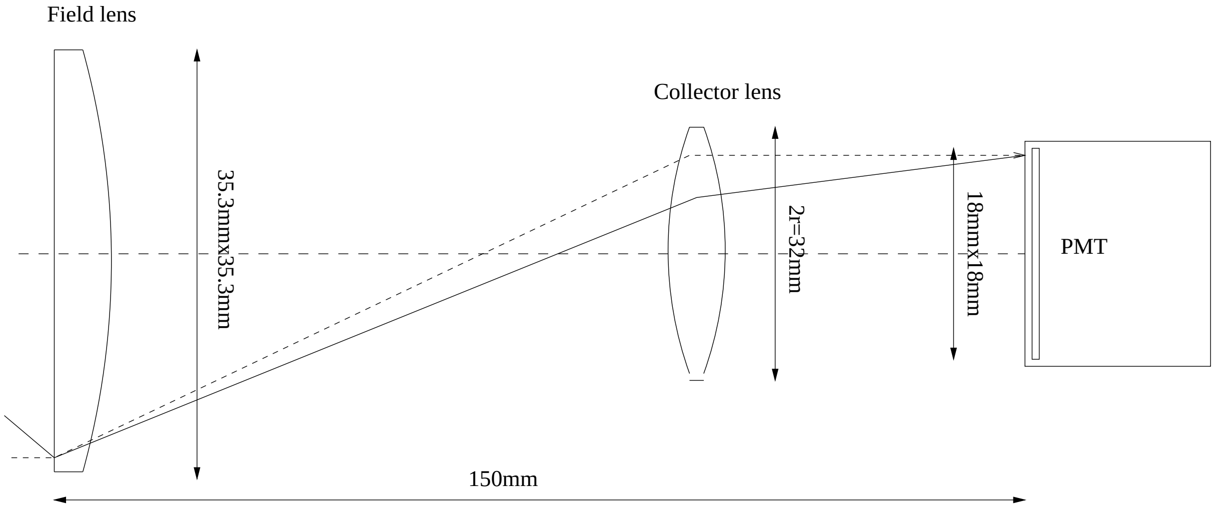

Figure 3.9: The light collection system consists of a square field lens and a round collector lens.

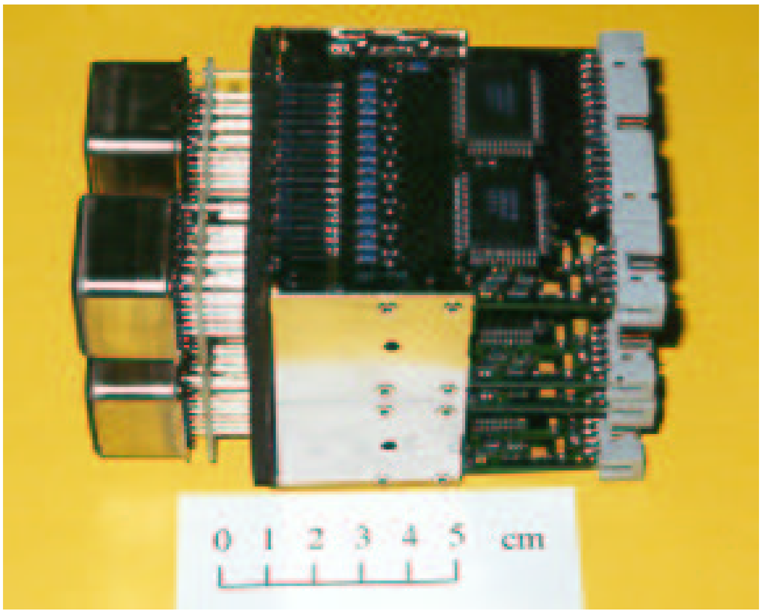

Figure 3.10: Fully equipped photomultiplier basic module equipped with Hamamatsu R5900 photomultiplier tubes type M16.

The supermodule consists of a support for 6×16 base boards. The base board with four sockets for the multianode photomultipliers and with front end electronics is shown in Fig. 3.10. It accepts four photomultipliers and provides positioning. In addition it houses the voltage divider, signal lines and the front-end electronics consisting of a 16-channel board based on the ASD8 (amplifier-shaper-discriminator) chip [40].

3.2.4 Detector parameters

On the basis of properties of the elements constituting the RICH (Fig. 3.4 and Eq. 3.9) we expected to detect 32±2 photons per ring of a β=1 particle, for the case when the radiator vessel is filled with C_4F_{10} gas. This corresponds to a figure of merit N_0=42 cm^{-1} and should allow identification of kaons up to momenta of at least 50 GeV/c. From the tests performed in the research and commissioning phase of the RICH detector [28], by analyzing the background events with well separated Cherenkov rings (Fig. 3.2.4) the above prediction was confirmed (Figs. 3.12 and 3.13).

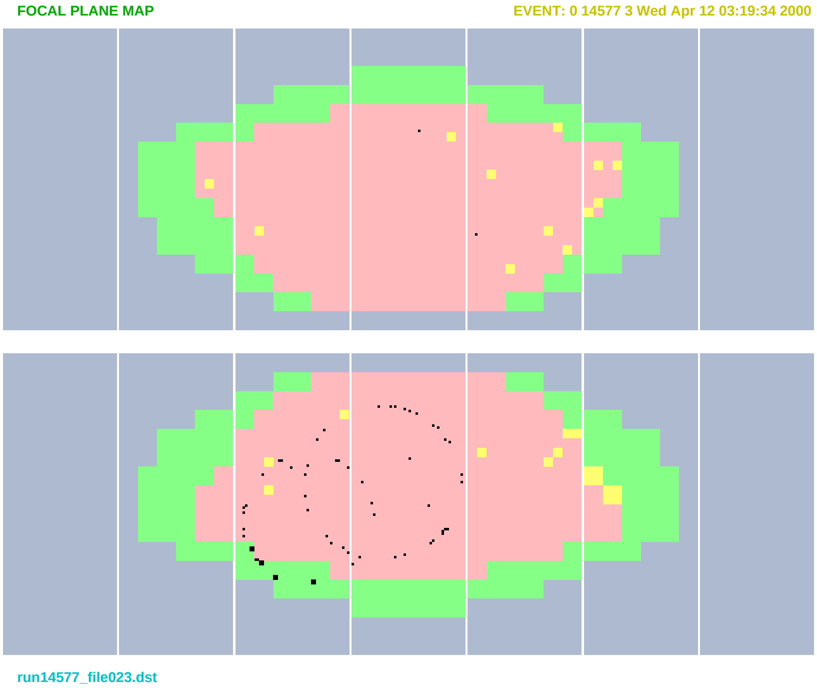

Figure 3.11: A HERA-B background event with two rings clearly visible.

If one takes into account only events with rings radiated by particles approaching the velocity of light, the average number of detected photons per ring would be 30.2 ± 3.6. In Fig. 3.13 the photon detector response parameter distribution for analyzed events is presented. It's average value is $43.8 \pm 3.5\ \mathrm{cm}^{-1}$.

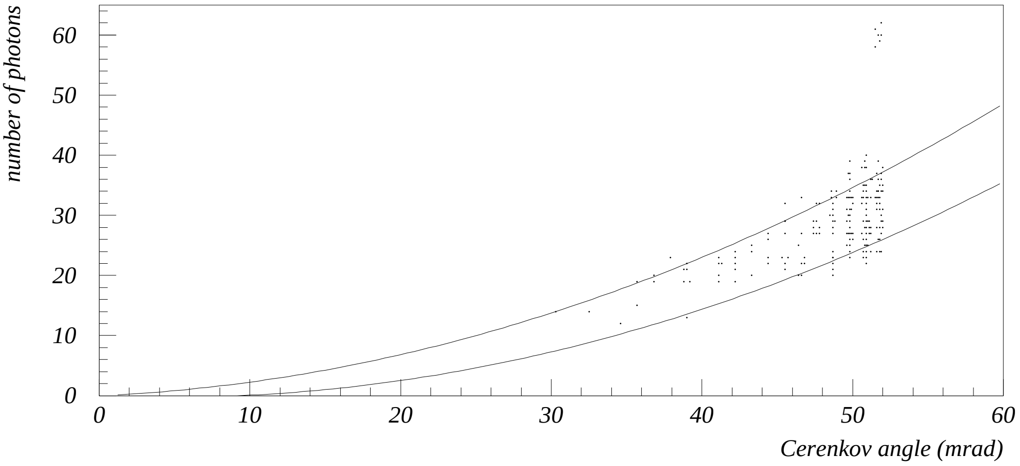

Figure 3.12: Number of detected photons versus Cherenkov angle for nearly 200 rings which could be well separated. Some events with two times more detected photons per ring, than would be expected are seen. They are due to Cherenkov radiation of an overlapping e^+e^- pair.

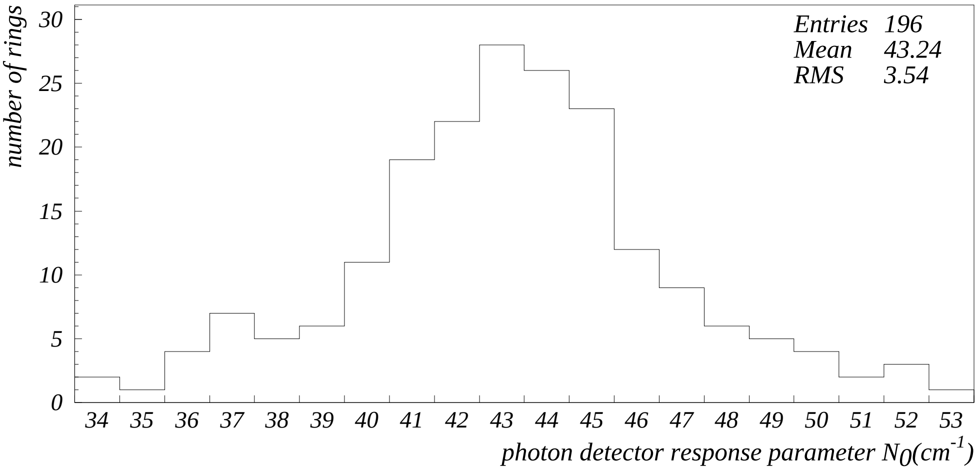

Figure 3.13: The distribution of the photon detector response parameter N_0.

The Cherenkov angle is obtained from the photon hit position as measured by the photon detector and from the particle trajectory measured from the tracking devices. The sources of errors which were listed in the Section 3.1 amount to the values for the HERA-B RICH detector given in Table 3.2.4. The chromatic aberration error is approximately 0.2 mrad, granularity resolution 0.46 mrad for the inner part and 0.92 mrad for the outer part of the detector. The multiple Coulomb scattering error [10] amounts to 0.1 mrad for the tracks with momentum of 50 GeV/c and the spherical aberration due to the non zero angle of incidence of photons upon

Error type	Error value -inner(outer) part
chromatic abberation	0.2 mrad
granularity resolution	0.46 mrad (0.92 mrad)
multiple scattering	0.1 mrad @ p=50 GeV/c
spherical abberation	0.16 mrad @ $\theta_{incident} = 9^o$
optical mirror imperfection	0.15 mrad
optical mirror misalignment	0.18 mrad
SUBTOTAL	0.7 mrad (1 mrad)
track slope design	0.2 mrad
track slope measured	1.5 mrad
TOTAL measured	1.65 mrad (1.9 mrad)

Table 3.2: The error contributions to the Cherenkov angle determined from single photon for tracks of momentum of 50 GeV/c.

the spherical mirror is 0.l6 mrad for tracks with the angle of incidence upon the spherical mirror of 9 degrees [41]. The optical errors due to mirror imperfections are estimated to 0.15 mrad [14], and the error due to the mirror misalignment to 0.18 mrad. The above errors are uncorrelated, and the combined error amounts to 0.7 mrad for the inner, and 1 mrad for the outer detector region.

The uncertainties of the particle trajectory due to the error in the track parameters as determined by the tracking system were expected to amount to 0.06 mrad, thus not contributing significantly to the Cherenkov angle error. During the year 2000 data taking period, the tracking devices were not capable of measuring tracks with such a high resolution due to a different gas used in the gaseous detectors (problems with the discharging when using a proposed gas) and due to the problems with the internal alignment. The error on the track parameters amounts to values around 1.5 mrad. With such an error, a reduced particle identification efficiency if compared to the MC estimation was expected. The determination of both single photon error and the errors in the track parameters is discussed in Section 5.

4

Particle Identification Algorithm for the RICH subsystem

In the analysis of the data recorded by the ring imaging Cherenkov detector, all the hits on the photon detector have to be considered (Fig. 4.1). The first task in the analysis is the determination of the Cherenkov angle for each hit on the photon detector and for each track.

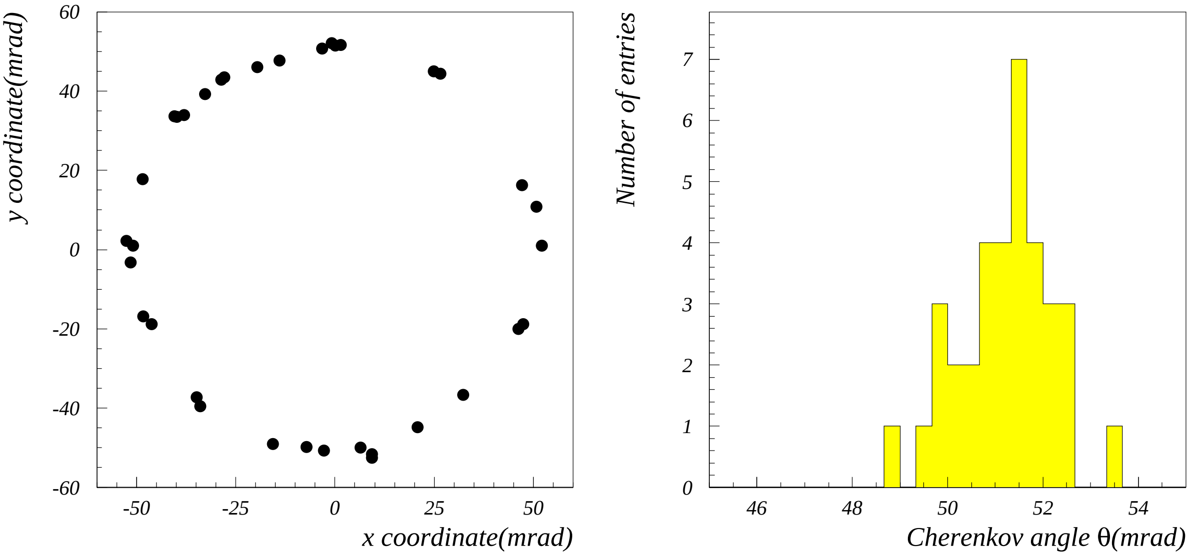

Figure 4.1: Example of a distribution of hits on the photon detector (left). Cherenkov angle distribution of the same hits (right).

If there would be no overlap between the rings, the Cherenkov angle distribution would show a clear Gaussian peak of the signal photons at the expected angle (Fig. 4.1). In cases where ring radii are large and track density is high, the overlap between rings becomes possible. This is the case in the HERA-B RICH. In Fig. 4.2 a typical event recorded is shown. In such a case the photons that are not radiated by the observed track represent a background contribution in the Cherenkov angle distribution histogram. If the track density is higher, the background contribution is also higher at the same signal level (Fig. 4.3). It may even happen that the signal sinks in the huge background of photons not belonging to the observed track. An efficient algorithm is therefore needed to identify particles crossing the RICH system. One of the possible algorithms used in HERA-B searches for rings and fits the ring radius and the ring center. From the ring radius, the identity of the track is determined [43].

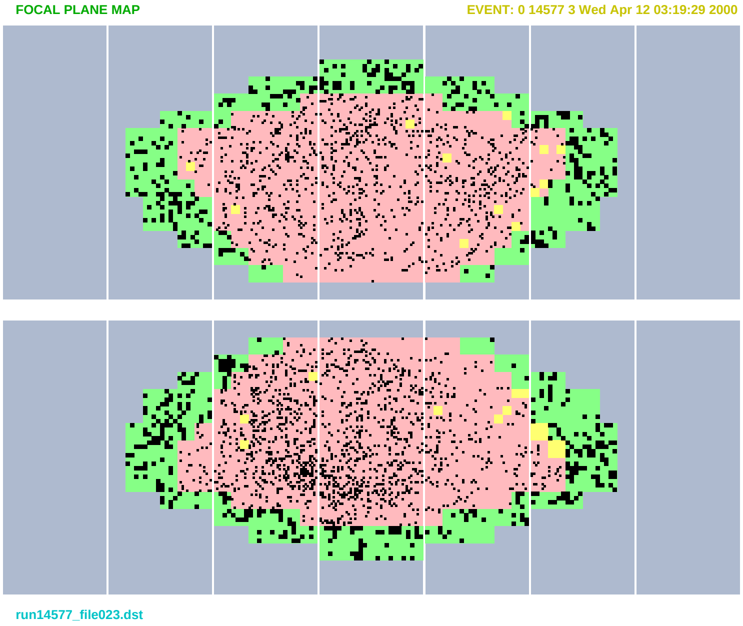

Figure 4.2: A typical event recorded in the HERA-B RICH counter.

Another approach, which is presented in this thesis, uses the information from the tracking system, that is the track momentum, the track slopes and the point on the track in front of the RICH. Within these track based methods the probabilities are constructed for different particle hypotheses. An elegant way to calculate such probabilities is the maximum likelihood technique.

4.1 Measurement of the Cherenkov angle

One of the first things in the analysis of the data recorded in the RICH is a determination of the Cherenkov angle for each trach-photon hit pair. The algotithm should be fast, since it the number of possible pairs is huge, e.g. 100 tracks with 35 detected photons per track result in

350000 combinations. To be able to process such amount of combinations, first a fast and rough calculation is performed. An analysis does not take into account the pairs with the Cherenkov angle much larger than it is the Cherenkov angle for $\beta = 1$ particles.

This simple approximate formula, which is only used for a rough estimation of the Cherenkov angle θ, assumes that the image of the radiation process in the RICH detector is a ring on the detector surface. It is then enough to propagate the track to the detector plane to obtain the ring center. The Cherenkov angle is then calculated for each photon using the following formula

$$\theta = \frac{|\vec{r}_D - \vec{r}_{RC}|}{R/2} \, . \tag{4.1}$$

Here $\vec{r}_D$ is the position of the hit on the photon detector, $\vec{r}_{RC}$ is the virtual intersection of the track with the detector plane and R is the radius of curvature of the spherical mirror.

A more accurate determination of the Cherenkov angle is based on the examination of the detection process. Since between the emission (E in Fig. 4.4) and the detection point (D in Fig. 4.4) there is only one light ray joining them, the direction of the photon can be reconstructed. For any measured photon and track it is possible to calculate the Cherenkov angle. The procedure is illustrated in Fig. 4.4. A photon is emitted under the angle θ in the point E on the track. The emission point is not exactly known, it lies somewhere on the track path inside the radiator. Since the spherical abberation is relatively small (see Table 3.2.4) and the incident track angles small in the case of the HERA-B RICH, it is sufficient to take it on the track path in the middle of the radiator. The photon is then propagated to the spherical mirror where it is reflected under the angle γ with respect to the normal of the mirror. Point C represents the

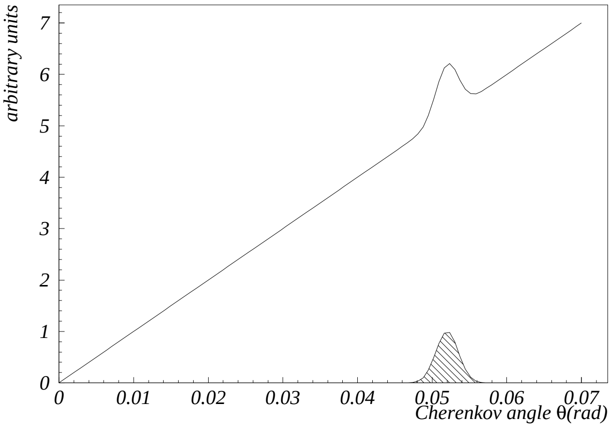

Figure 4.3: Cherenkov angle distribution histograms: the isolated Cherenkov rings would give the hatched histogram, while overlapping rings result in a distribution schematically shown in the open histogram.

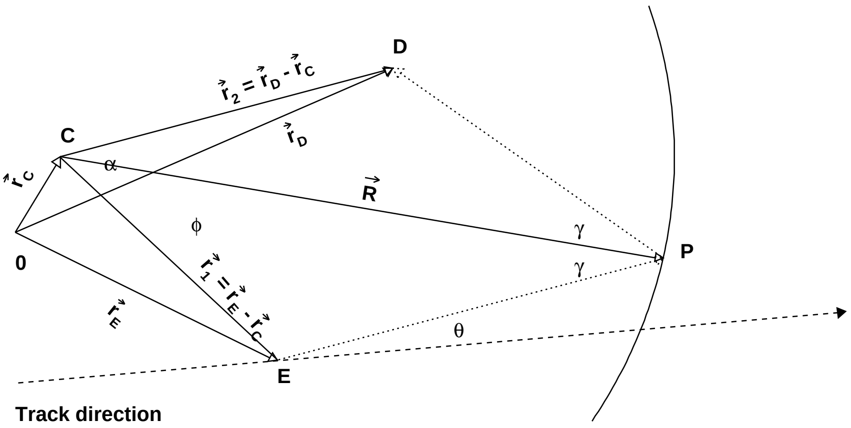

Figure 4.4: Reconstruction of the photon emission angle θ. The photon is emitted at point E on the track. It is then reflected on the spherical mirror and detected at point P on the detector.

center of curvature of the mirror. After reflection, the photon is detected at point D in the focal plane of the mirror.

To calculate the Cherenkov angle θ one has to solve a set of trigonometric equations emerging from similar triangles. The first equation comes from a triangle $\triangle PEC$,

$$\frac{\sin \sphericalangle PEC}{\overline{CP}} = \frac{\sin \sphericalangle CPE}{\overline{CE}} \tag{4.2}$$

$$\text{or} \quad \frac{\sin(\phi+\gamma)}{R} = \frac{\sin\gamma}{r_1}\,. \tag{4.3}$$

To arrive at the second equation, the triangle $\triangle CPD$ is used:

$$\frac{\sin \sphericalangle CDP}{\overline{CP}} = \frac{\sin \sphericalangle DPC}{\overline{CD}} \tag{4.4}$$

$$\text{or} \quad \frac{\sin(\alpha-\phi+\gamma)}{R} = \frac{\sin\gamma}{r_2}\,. \tag{4.5}$$

To calculate the angles ϕ and γ one solves the above equations using an iterative procedure. First the system is rewritten in the explicit form:

$$\begin{aligned} \gamma^{(i+1)} &= \arcsin\left(\frac{r_1}{R}\sin(\phi^{(i)}+\gamma^{(i)})\right) \\ \phi^{(i+1)} &= \alpha+\gamma^{(i)} - \arcsin\left(\frac{R}{r_2}\sin\gamma^{(i)})\right) \end{aligned} \tag{4.6}$$

The initial values are $\gamma^{(0)} = 0$ and $\phi^{(0)} = \alpha$. To obtain the single float precision 8 to 10 iterations are enough. Different approximative solutions can be obtained. If the angles α, γ and

$\phi \ll 1$ one can linearize the equations. For the initial values one expands the upper system of equations 4.6 to the first order:

$$\begin{aligned} \gamma^{(0)} &= \frac{r_1}{R}(\phi^{(0)} + \gamma^{(0)})) \\ \gamma^{(0)} &= \frac{r_2}{R}(\alpha + \gamma^{(0)} - \phi^{(0)}) \end{aligned} \tag{4.7}$$

The initial values are used to calculate the next order values $\phi = \phi^0 + \Delta\phi$ and $\gamma = \gamma^0 + \Delta\gamma$. The corrections $\Delta\gamma$ and $\Delta\phi$ are calculated solving the following system of equations

$$\sin\gamma^0 + \cos\gamma^0\,\Delta\gamma = \frac{r_1}{R}\sin(\gamma^0 + \phi^0) + \frac{r_1}{R}cos(\gamma^0 + \phi^0)\ (\Delta\gamma + \Delta\phi) \tag{4.8}$$

$$\sin\gamma^0 + \cos\gamma^0\,\Delta\gamma = \frac{r_2}{R}\sin(\gamma^0 - \alpha + \phi^0) + \frac{r_2}{R}cos(\gamma^0 - \alpha + \phi^0)\ (\Delta\gamma + \Delta\phi)\ . \tag{4.9}$$

When the second order expansion is used, one gains about a factor of two in the computing time while loosing around 1% in the resolution on the angle determination in comparison to the none-linearized form. From the angle γ reconstructed in the previous step, and from the track direction, it is then easy to calculate the Cherenkov angle θ.

The measurements of the Cherenkov angle for each track- photon hit pair should be combined into an interpretable value, which should express identity of the tracks. One way how to do it is based on the maximum likelihood method.

4.2 Maximum Likelihood method

If a probability density function of a data sample is known, the maximum likelihood method can be applied. It is from a theoretical point of view the most general method of estimation known so far.

For illustration, suppose we have a sample of n independent observations $x_1, x_2, ..., x_n$, from a probability density function $f(x|s)$ where s is the parameter to be estimated. The maximum likelihood method consists of calculating the likelihood function

$$L(s|x) = f(x_1|s).f(x_2|s)...f(x_n|s)\ , \tag{4.10}$$

which can be recognized as the probability for observing the sequence of measured values x_1, x_2, ..., x_n. The maximum likelihood principle states that this probability should be a maximum for the observed values. Thus, the parameter s must be such that the likelihood function L is a maximum. If L is a regular function, the unknown variable s can be found by solving the equation

$$\frac{dL}{ds} = 0 \tag{4.11}$$

If there is more than one parameter, then the partial derivatives of L with respect to each parameter must be taken to obtain a system of equations. Depending on the form of L, it may also be easier to maximize the logarithm of L rather than L itself. Solving the equation

$$\frac{d(\ln L)}{ds} = 0 \tag{4.12}$$

then yields results equivalent to 4.11. The solution, $\hat{s}$, is known as the maximum likelihood estimator for the parameter s.

In case of few available discrete values of the parameter s, e.g. five particle masses, it is sufficient to calculate the likelihood function L for those discrete values. The solution $\hat{s}$ is then the discrete value of s with maximal value of its likelihood function L. This approach will be used in the analysis of the RICH data.

4.3 Construction of the extended likelihood function in the RICH

The analysis of the data recorded in the RICH is based on the above described maximum likelihood technique [44]. In constructing the likelihood function we first assume that the momentum of the particle and its direction in the RICH counter can be measured in the tracking system. For each hypothesis hyp the corresponding Cherenkov angle θ_c^{hyp} can thus be calculated.

From the measurements, the Cherenkov angle distribution for a given hypothesis can be obtained. In the search for the signal photons, any photon hit inside a range of three standard deviations around expected Cherenkov angles for particle hypotheses p, K, π, μ and e is retained. Note that for each track also the background hypothesis is tested, i.e. the hypothesis that the photon yield around the track is consistent with the background. The expected Cherenkov angle θ_c^{hyp} and the average number of detected photons is therefore known. The probability density function $p_i^{hyp}(\theta)$ for a particular hit i at the angle θ, calculated relative to the specific track, is for a given mass hypothesis *hyp* equal to

$$p_i^{hyp}(\theta) = n_e^{s,hyp} S(\theta, \theta^{hyp}) + n_e^b \, B(\theta, \theta^{hyp}). \tag{4.13}$$

Here S and B are the probability density functions corresponding to the signal and background, respectively, and $n_e^{s,hyp}$ is the expected number of signal and n_e^b the expected number of background hits. For the background hypothesis, the expected number of signal hits is zero. The signal probability density function S is a Gaussian with a mean θ_c^{hyp}

$$S^{hyp}(\theta) = \frac{1}{\sqrt{2\pi}\sigma_i} \exp((\theta - \theta_c^{hyp})^2/(2\sigma_i^2)) \; , \tag{4.14}$$

where the R.M.S. width of the Gaussian σ_i could vary from hit to hit (e.g. in case of different granularities). The background probability density function B is the unknown quantity in the analysis. In the first approximation it can be assumed that the hit density function dN/dS is constant on the detector surface. It is then easy to see that the distribution over Cherenkov angle is a linear function [§], which we normalize in a window between θ_{min} and θ_{max},

$$B(\theta, \theta^{hyp}) = \frac{\theta}{\int\limits_{\theta_{min}}^{\theta_{max}} \theta d\theta} \tag{4.15}$$

This assumption is not completely true since the background is not only a function of a detector occupancy but also a function of the event type. It depends on the position of the track in the detector. For large Cherenkov angles the background distribution is limited also by the geometrical acceptance of the photon detector.
The normalization of the probability density function $p^{hyp}(\theta)$ is such that

$$\int\limits_{\theta_{min}}^{\theta_{max}} p^{hyp}(\theta) d\theta = n_e^{s,hyp} + n_e^b \tag{4.16}$$

The probability for one hypothesis L^{hyp} to produce the set of angles θ_1,..,θ_n, can be factorized in two terms

$$L^{hyp} = L_a^{hyp} \cdot L_b^{hyp} \ . \tag{4.17}$$

The first term describes the probability to see a photon in each of the locations θ_i,..,θ_n surrounded by a small interval $\Delta\theta_i$:

$$L_a^{hyp} = \prod_i^n p_i^{hyp}(\theta_i)\Delta\theta_i. \tag{4.18}$$

Here the product runs over all detected photons. The second term L_b^{hyp} in the probability density function describes the probability of not seeing any photon elsewhere. This probability is independent of the location and the number of photons seen since we can make the surrounding $\Delta\theta_i$ as small as required:

$$\begin{aligned} L_b^{hyp} &= \prod(1 - p^{hyp}(\theta)\Delta\theta) \qquad (4.19) \\ \log(L_b^{hyp}) &= \sum \log(1 - p^{hyp}(\theta)\Delta\theta) \\ &= -\sum p^{hyp}(\theta)\Delta\theta \\ &= -\int\limits_{\theta_{min}}^{\theta_{max}} p^{hyp}(\theta) d\theta = -n_e^{s,hyp} - n_e^b \end{aligned}$$

[§] If $\frac{dN}{dS} = const.$, then $\frac{dN}{d\theta} \propto \frac{dN}{dS}\frac{dS}{dr} \propto r \propto \theta$.

and

$$L_b^{hyp} = e^{-n_e^{s,hyp} - n_e^b}. \tag{4.20}$$

Eq. 4.18 can be transformed into a probability density by transforming the term $d\theta_1 ... d\theta_n$ to an element of integration. Since the labeling $1...n$ does not imply any ordering, the same term will occur $n!$ times, so that the probability density should be rewritten as

$$L_a^{hyp} = \frac{1}{n!} \prod_i^n p_i^{hyp}(\theta_i) \tag{4.21}$$

By multiplying the probability density Eq. 4.21 by the probability Eq. 4.20, we obtain the extended probability density for each hypothesis

$$L^{hyp} = \frac{1}{n!} (\prod_i^n p_i^{hyp}(\theta_i)) e^{-(n_e^{s,hyp} + n_e^b)}. \tag{4.22}$$

By integrating Eq. 4.22 using Eq. 4.16, we get the Poisson distribution for n photons when $n_e^{s,hyp} + n_e^b$ is the expected number of photons in the interval $(\theta_{min}, \theta_{max})$

$$\int\limits_{\theta_{min}}^{\theta_{max}} L^{hyp} d\theta_1 ... d\theta_n = \frac{1}{n!} (n_e^{s,hyp} + n_e^b) e^{-n_e^{s,hyp} - n_e^b}. \tag{4.23}$$

The method of maximum likelihood can be used to maximize L^{hyp} for each mass hypothesis when n_e^b is left free (fit of n_e^b) or to give the relative probability between two possible hypotheses hyp_1, hyp_2:

$$L_{12} = \frac{L^{hyp_1}}{L^{hyp_2}}, \tag{4.24}$$

or if the likelihoods are renormalized on the sum of likelihoods for all possible hypotheses hyp,

$$\lambda^{hyp} = \frac{L^{hyp}}{\sum\limits_k L^k}, \tag{4.25}$$

This second approach is applied in the track based versions of the RICH identification algorithms implemented in the HERA-B experiment. The version with working name RIRE is described in [45] and the other is discussed in this thesis.

The HERA-B subsystem specific likelihood function does not include any information about a priori known particle fractions x^{hyp}. To take this into account, new normalized likelihood functions λ_x^{hyp} can be constructed in the following way

$$\lambda_x^{hyp} = \frac{x^{hyp} L^{hyp}}{\sum\limits_k x^k L^k} \ . \tag{4.26}$$

The summation runs over all particle hypotheses hyp that are tested in the subsystem. In principle, the output of single subsystem det identification algorithms are likelihood functions L_{det}^{hyp} which are calculated for each particle hypothesis hyp. They can be combined in a single likelihood function λ_{HERA-B}^{hyp},

$$\lambda_{HERA-B}^{hyp} = \frac{x^{hyp} \prod\limits_{det=RICH,ECAL,TRD,MUON} L_{det}^{hyp}}{\sum\limits_{k=e,\mu,\pi,K,p} x^k \prod\limits_{det=RICH,ECAL,TRD,MUON} L_{det}^{k}} \ , \tag{4.27}$$

without having to know the subsystem specific information. The hypothesis is accepted if the likelihood λ^{hyp} exceeds some specific value. The single cut in this multidimensional space is expected to achieve high selection efficiencies [12].

For example, in the transition radiation detector the likelihood function for the electron and the hadron hypothesis is assigned. From the amount and shape of energy deposition, the electromagnetic calorimeter is able to separate electrons from other minimum ionizing particles and hadrons, and the likelihood functions for the electron, minimum ionizing particle and hadron hypotheses are assigned. The output of the muon identification system are two likelihood functions for the muon and the hadron hypotheses.

4.4 The iterative method

We first recall Fig. 4.2 where a typical measured event is shown. To be able to cope with such high occupancies, an algorithm is needed to efficiently separate particles. When the track density is high and rings overlap, the peak in the Cherenkov angle distribution sinks in a huge background. One method how to clear such histograms is an iterative method [46]. The aim of the method is to ascribe each hit on the detector to a track, from which the photon was most probably emitted.

Let us illustrate the method on a simple example of three overlapping rings, displayed in Fig. 4.5. For each of the tracks and for each of the photons we first calculate the corresponding ring radius, and fill a histogram shown in Fig. 4.6. Here the usual likelihood method [44] would first estimate background and would then calculate the likelihood for each particle hypothesis. In the iterative approach we continue, however, to clear up the histograms. We proceed in the following way: instead of putting a given photon in all the three histograms with weight one, as we did in the first step, we ascribe weights to each photon so that the sum of weights is equal to

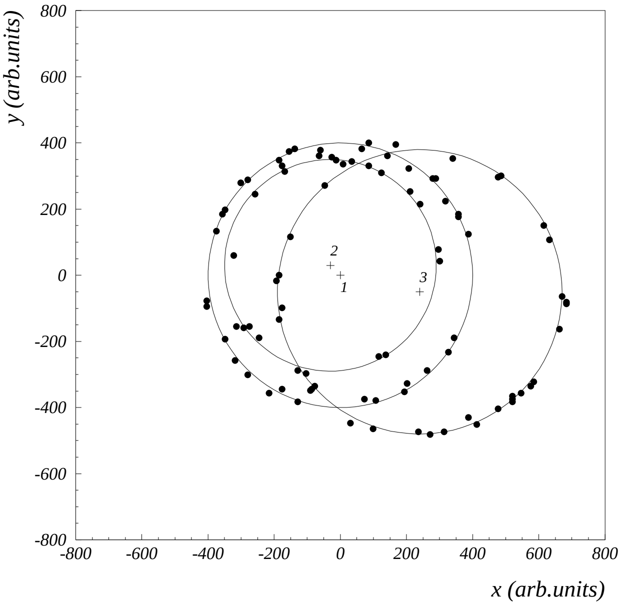

Figure 4.5: The test example: three overlapping Cherenkov rings.

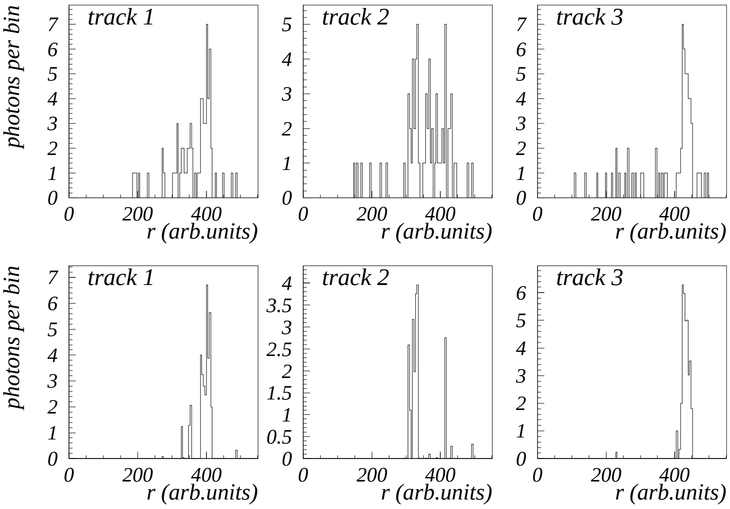

Figure 4.6: Photon hit histogram for tracks 1, 2 and 3, from left to right, at the beginning of the iteration procedure (top row) and after 16 iterations (bottom).

one for each photon. The weight for a specific photon i in the histogram corresponding to the track j is calculated for the next iteration according to the formula

$$w_j^i = \frac{y_j^i}{y_1^i + y_2^i + y_3^i}, \tag{4.28}$$

where y_1^i, y_2^i and y_3^i is the number of entries in the bin, into which the given photon fits, in histograms 1, 2 and 3, respectively. As a result, a given photon is given the highest weight in the histogram, where it fits into a peak, and lowest, where it is part of a scarcely populated background.

In the next iteration the procedure is repeated, and the resulting histograms after sixteen iterations are shown in the lower row of Fig. 4.6. Note that the method is convergent, i.e. the difference between weights of adjacent iterations decreasis fast (Fig. 4.8). The number of photons in the beginning of the iterative procedure is obtained by a sum of all photons in the peak. After the iterative procedure, we define the number of photons in the peak n_r as a weighted sum:

$$n_r = \sum_i w_j^i \ . \tag{4.29}$$

In the expression index i runs over all photons within $\pm 3\sigma$ from the expected Cherenkov angle for a given hypothesis. A closer inspection shows that the distribution of photons remains

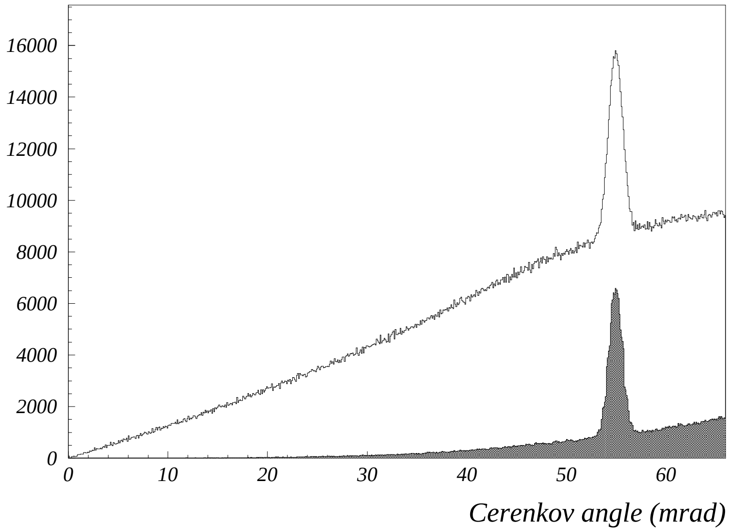

Figure 4.7: Cumulative Cherenkov angle distribution for pions above 15 GeV/c in simulated events as expected in the HERA-B RICH (open histogram). After the iterative procedure the histogram is filled with the resulting weights (hatched histogram). The signal to background ratio is considerably improved.

Gaussian with the same r.m.s width. Also, the number of photons in the peak, n_r, remains the same (or is only slightly reduced) if compared with the input (Fig. 4.7). The variation in the number of photons is, however, larger than the Poissonian value because of correlations between weights w_j^i (Fig. 4.9).

This last point needs a further study, since it could influence the proper evaluation of the likelihood function. From Fig. 4.9 we conclude that the width of the distribution only slightly exceeds the expected value for small numbers of expected photons (and thus rings with a small radius), while the difference becomes significant in the case more photons are expected and the rings get larger. For the specific example displayed in Fig. 4.9 one expects an r.m.s. of 5 photons if 25 photons are detected on average, and the observed value is 8.1. To model the distribution, we replaced the Poisson distribution $P(\bar{n}_e, n_r)$ of the number of reconstructed photons n_r with mean $\bar{n}_e$,by a Poisson like function $P'(\bar{n}_e, n_r)$,

$$P'(\bar{n}_e, n_r) = P(\frac{\bar{n}_r}{f}, \frac{n_r}{f}), \tag{4.30}$$

where the factor f is determined from the r.m.s width and mean of the distribution,

$$f = \sigma_{n_r}^2 / \bar{n}_r. \tag{4.31}$$

As can be seen from Fig. 4.9, the function defined in such a way describes the observed distributions reasonably well. The value of f was calculated for several intervals of $\bar{n}_r$.

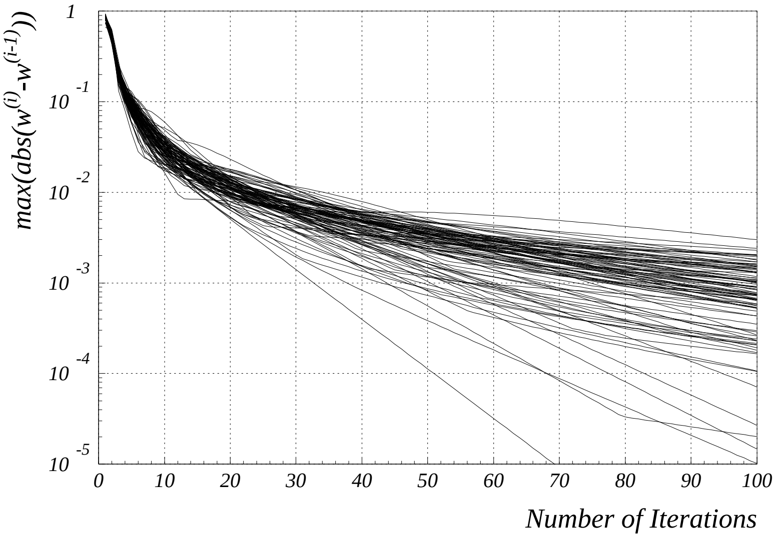

Figure 4.8: The convergence of the iterative procedure: maximal difference between weights of adjacent iterations versus the number of iterations for 100 HERA-B Monte Carlo simulated events.

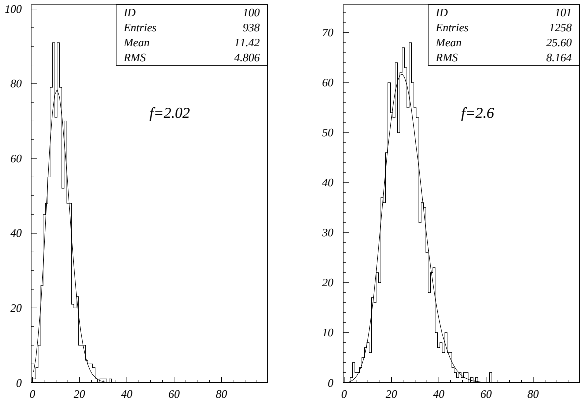

Figure 4.9: Number of reconstructed photons in the proper hypothesis window after 16 iterations, for 10 expected photons (left) and 25 expected photons (right). The curves correspond to a Poissonian-like distribution Eq. 4.30, with the value of factor f (Eq. 4.31) indicated for each case.

4.4.1 Likelihood function

The extended likelihood function calculated for a specific track under the assumption of the track mass hypothesis hyp constructed above reads

$$\log L^{hyp} = \sum_i \log p^{hyp}(\theta_i) + \log P(n_e, n_r), \tag{4.32}$$

where the number of signal photons is assumed to be distributed according to the Poisson distribution $P(n_e, n_r)$ with mean n_e. This likelihood function does not include weights w_j^i of each photon i in a given histogram j. Instead of the above expression we therefore use the function

$$\log L^{hyp} = \sum_i w_j^i \log p^{hyp}(\theta_i) + \log P(n_e, n_r), \tag{4.33}$$

where the index i runs over all photons in the $background/e'\mu/\pi/K/p$ hypotheses windows. It should be noted that the proper likelihood function would include the factor f from Eq. 4.31. Since for separation we are only interested in ratios between likelihood functions, the changes due to an additional factor in the Poissonian part turn out to cancel approximately.

In the calculation of the likelihood, the background represents an important term. In order to minimize the influence of the background shape on the identification, only photons within $\pm 3\sigma_\theta$ around each of the possible particle hypotheses (signal windows $S.W.$) are taken into account when calculating the log-likelihood function. Underestimation or overestimation of the background hits in these regions where the signal is expected. i.e. signal windows, results in wrong likelihood estimation and correspondingly in the wrong identification. The background hits are estimated from the background level in the side bands of signal windows, i.e. in the background windows. The term background windows ($B.W.$) describes the range of $\pm 9\sigma_\theta$ from any of the expected Cherenkov angles, θ^{hyp}, excluding the signal windows (see Fig. 4.10).

Background is in the first approximation uniformly distributed over the detector surface, i.e. in the one dimensional Cherenkov angle distribution it is a linear function of the Cherenkov angle (Eq. 4.15). After the iterative analysis, the shape of the background turns out to change to a cubic form (Fig. 4.7)

$$B(\theta) = A\,\theta^3 \tag{4.34}$$

with the normalization requirement

$$\int_{B.W.} B(\theta) d\theta \quad = \quad \int_{B.W.} A\,\theta^3\, d\theta = 1 \tag{4.35}$$

where the integral in the equation runs over all background windows $B.W.$. The parameter A then reads

$$A = \frac{4}{\sum\limits_{k \in B.W.} b_k^4 - a_k^4}\,, \tag{4.36}$$

where b_k and a_k are upper and lower limits of the background windows.

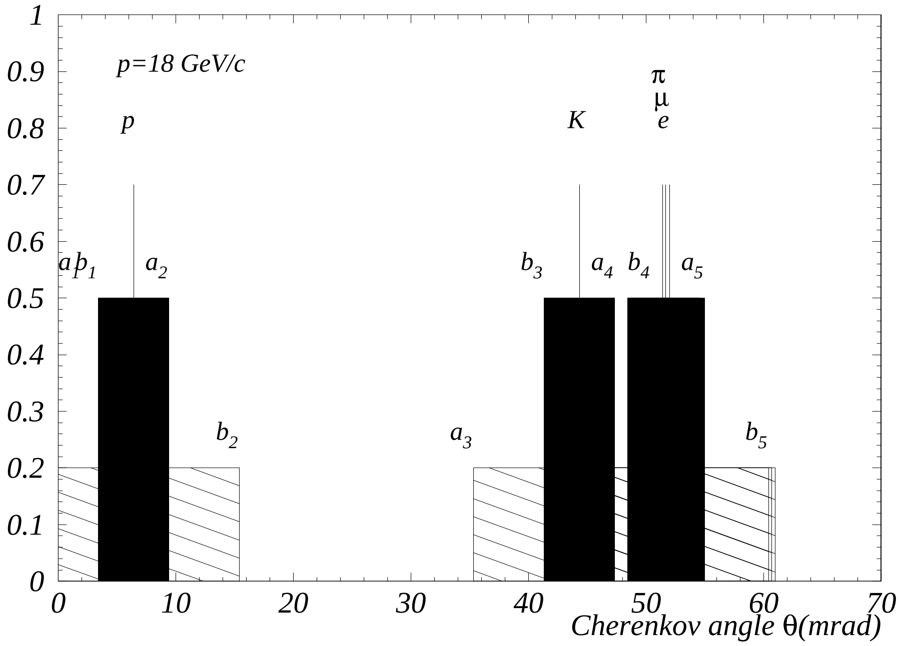

Figure 4.10: The signal windows (filled) are used for the counting of the signal photons while the background windows (hatched) are used for the estimation of the background level in the signal windows. The background windows have lower and upper limits a_i and b_i respectively, while the signal windows are limited by b_i and a_{i+1}.

4.5 Implementation

The method is implemented inside ARTE, the event reconstruction and analysis tool for HERA-B [49]. The ARTE code is organized in function modules, each module being called at a certain step of the reconstruction. The identification in the RICH with the iterative method is performed in the module RITER.

At the start of the event reconstruction procedure, first the initialization of each of the modules is performed. For the RITER, the detector geometry and the index of refraction of the radiator are read from a database. The internal module structures are then initialized.

The input for the RITER module are the parameters (momenta, slopes) of the reconstructed tracks in the tracking system, and the hits in the RICH system. The output of the module are likelihoods for electron, muon, pion, kaon, proton and background hypotheses.

In the module, first the intersections with the RICH counter elements are calculated for each track. This includes the calculation of the intersection of the particle trajectory with the spherical mirror and intersections of the virtually reflected ray with the upper and the lower photon detector plane. The geometrical acceptance for each hypothesis ε_{geo}^{hyp} is determined using an approximative technique. One hundred photons are generated under the expected Cherenkov angle for a particular hypothesis. The photons are then traced to the spherical mirrors, reflected there and traced to the detector plane. Intersections with proton and electron beam shrouds are taken into account as well. An example how the position and inclination of the track affects the geometrical acceptance, is shown in Fig. 4.11.

If the particle has full geometrical acceptance for the electron hypothesis, it is set to one for all heavier hypotheses as well. Photons which are emitted under smaller angles have higher probability to reach the detector. If the acceptance for the electron hypothesis is zero, the analysis is not performed on that track, and the flag is set to zero. If the Cherenkov angle for a given hypothesis does not differ by more than 2 mrad from the previous one, the geometrical acceptance is set to the value of that hypothesis.

The number of expected signal photons $n_e^{s,hyp}$ for different hypotheses is determined after the track path length $L_{radiator}$ is calculated

$$n_e^{s,hyp} = N_0 \sin^2 \theta^{hyp} L_{radiator} \, \varepsilon_{geo}^{hyp}. \tag{4.37}$$

where ε_{geo}^{hyp} is the geometrical acceptance for a given hypothesis, θ^{hyp} is corresponding expected Cherenkov angle and N_0 is the figure of merit.

In the next step for each track and for each hit, the Cherenkov angle θ is determined by a rough estimation (Eq. 4.1). The Cherenkov angle is recalculated with a higher accuracy using Eq. 4.9 and a new table is filled with those pairs which have Cherenkov angle in the background or in the signal window. These photons are later used for the signal and background estimation. For each track, the Cherenkov angle distribution histogram is filled with initial weight w of one for each photon.

We now start with the iterative procedure to clear the Cherenkov angle histograms. First,

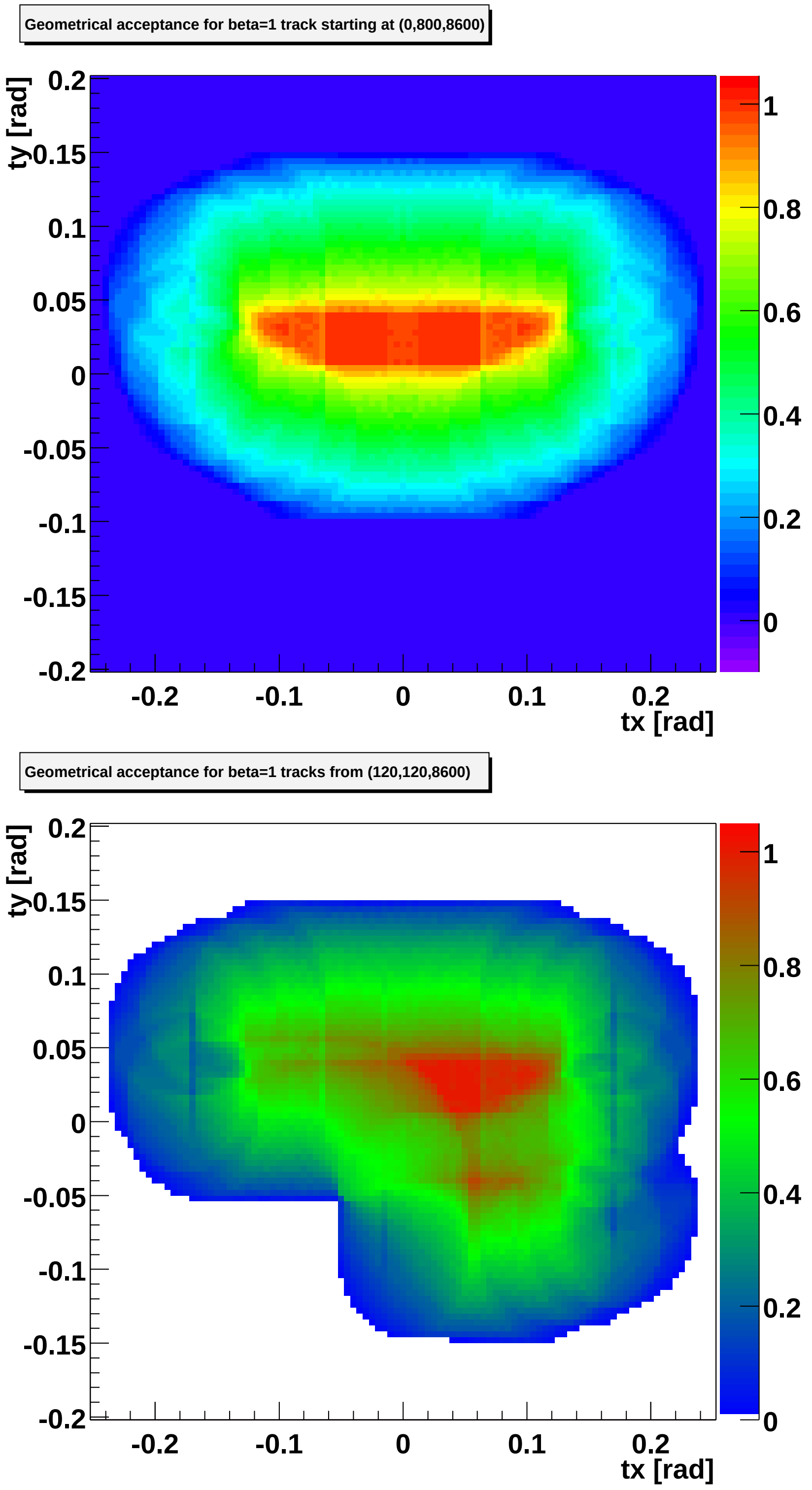

Figure 4.11: Expected geometrical acceptance for hypothetical tracks with different inclinations. In the upper plot it was assumed that all tracks enter the RICH detector at the point (0,0.8m,8.6m). Clearly, the acceptance is not symmetric as more photons are lost on the way to the lower detector plane. We also see the limits of the RICH geometrical acceptance. In the lower plot the hypothetical tracks entered the RICH detector area close to the beam pipe at the point (0.12 m, 0.12 m, 8.6 m). It can be seen how the beam pipe shadows the detector plane resulting in a low geometrical efficiency for some tracks.

for each photon i, the sum of weights y^i_{sum} is calculated:

$$y^i_{sum} = \sum_j y^i_j. \tag{4.38}$$

Here summation runs over the tracks j and y^i_j is the number of of entries in the bin into which the given photon falls in the track histogram j. New weights are calculated for each photon and track as the normalized values of entries

$$w^i_j = \frac{y^i_j}{y_{sum}}. \tag{4.39}$$

In the next step the Cherenkov angle histograms are filled with the new weights. Weights are then recalculated.

After 10 iterations we determine the signal and the background level. The number of measured photons n_r is determined by taking into account different weights of photons for a given track j. To suppress background influence, only the photons within the signal windows are taken into account,

$$n_r = \sum_{i;\theta_i \in S.W.} w^i_j\,. \tag{4.40}$$

In the similar way the number of background hits in the background windows $B.W.$ is calculated

$$N_{B.W.} = \sum_{i;\theta_i \in B.W.} w^i_j\,. \tag{4.41}$$

The expected number of background photons n^b_e in the signal windows is estimated using the estimated background level parameter A (Eq. 4.36) and the counted number of photons $N_{B.W.}$ in the background windows $B.W.$ for a given track,

$$n^b_e = N_{B.W.} \int_{S.W.} B(\theta) d\theta\,. \tag{4.42}$$

The likelihood function is then constructed for each of the particle hypotheses hyp (Eq. 4.33). The extended likelihoods L^{hyp} are then normalized to the sum of likelihoods over all the hypotheses (Eq. 4.25). Finally, they are written to the corresponding field in the track table from where they are available for further analysis.

4.6 Monte Carlo study

To check the efficiency of the method, simulated tracks with known identity have been used. Events have been generated by the ARTE program [47]. The ARTE simulation module is based on GEANT [48]. It consists of a general framework for handling geometry and tracking.

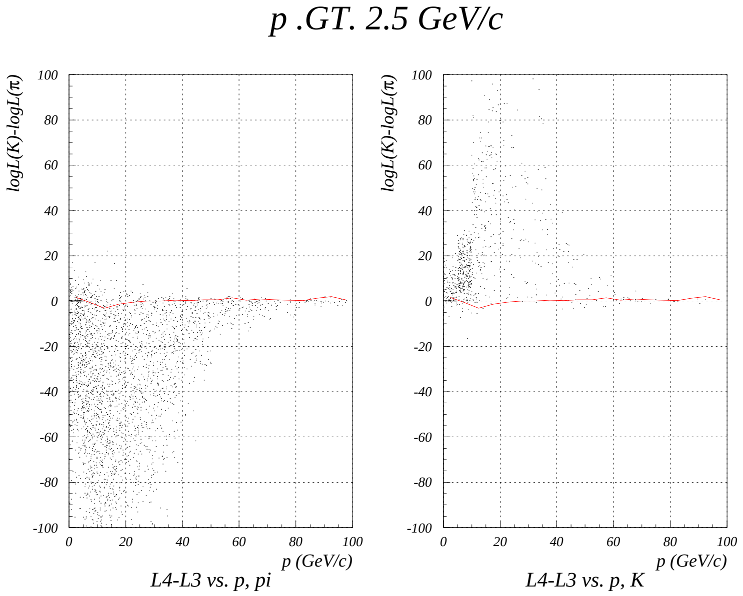

Figure 4.12: The log-likelihood difference of the kaon and pion hypotheses for pions (left) and kaons (right), as a function of momentum. In the simulation, it was assumed that on average 32 photons are detected per β = 1 charged particle, and that a single photon determines the Cherenkov angle with $\sigma_\theta = 0.7\ 10^{-3}$.

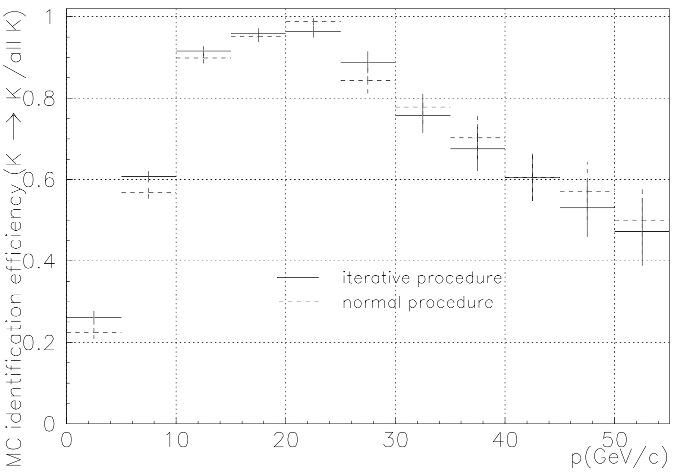

Figure 4.13: The momentum dependent efficiency for resolving a kaon from a pion, extracted from Fig. 4.12 under the requirement that the probability for a pion to be identified as a kaon amounts to 5%. The corresponding cut in the log-likelihood difference is shown in Fig. 4.12. For comparison, we show as a dashed histogram the efficiency of the pion-kaon separation without performing the iterative procedure. Note that the ideal information for the track parameters was used in the efficiency evaluation..

In the simulation a required reaction is generated. The generated particles are stored in the memory. Each particle is tracked through the detector where its response is simulated. In the Cherenkov detector, photons are generated and propagated to the photon detector. The event is then packed in an event record and stored on the disk. To check the performance of the particle identification method, the simulated event from the file is read into the memory of the computer and subsequently analysed in the same way as real data. The efficiency is determined on the set of the charged tracks traversing the RICH counter. The real identity of a reconstructed track is determined by matching its hits to the hits of a generated track. If the two have more than 70% of hits in common, the reconstructed track is declared to be equal to the simulated one. If a reconstructed track cannot be matched to any of the generated tracks, it is declared to be a ghost.

As an example, the pion-kaon separation is shown in Fig. 4.12, where the logarithm of the ratio of likelihoods $\log\left(L^{\pi}/L^{K}\right)$ is plotted against the particle momentum. Of course, the efficiency and fake probability depend on the cuts in the likelihood ratio applied to separate pions from kaons. By fixing the pion fake probability to a certain value, a momentum dependent cut on the likelihood ratio is defined. In Fig. 4.13 the efficiency of the method is shown for a fixed pion fake probability of 5%. It is interesting to compare the result with the performance of the usual method, in which the likelihood functions are calculated without the iteration procedure. As can be seen from Fig. 4.13, the performance of the iterative method is similar to the performance of the identification based on likelihood function as determined on original histograms. The iterative method seems to be somewhat better in the low momentum region. Note that in this performance evaluation an ideal track finding was assumed, and track directions were smeared according to Gaussian distribution with expected widths.

The final results, which summarize the performance of the employed particle identification algorithm in combination with the present version of the track finding and fitting procedure, are shown in Fig. 4.14 and in Fig. 4.15. Fig. 4.14 shows how particles of a given identity id_1 are identified as a particle of type id_2. The identity of the particle in the RICH was determined on the basis of the maximal likelihood functions for all hypotheses. If, however, the likelihood is required to exceed 0.35 to identify a particle, the transition matrix changes to Fig. 4.15. Note that the background hypothesis in the simulated data correspond to a reconstructed ghost track.

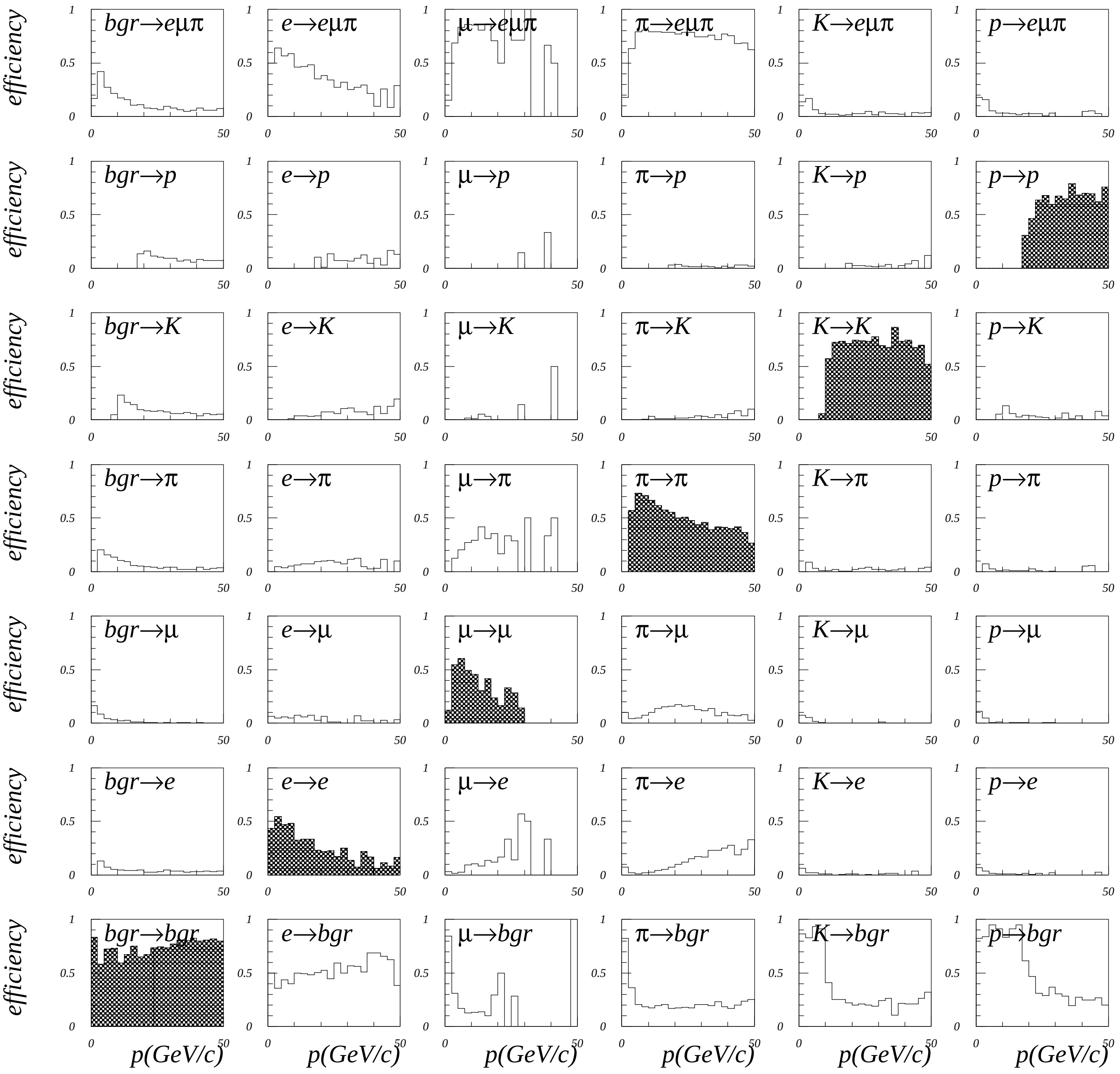

Figure 4.14: Transition matrix $id_1 \to id_2$; Probability to identify a particle with the Monte Carlo identity id_1 as p, K, π, μ, e or background identity id_2 as a function of momentum. Particle was identified as hyp if the likelihood for that hypothesis was maximal of all the likelihoods for different hypotheses.

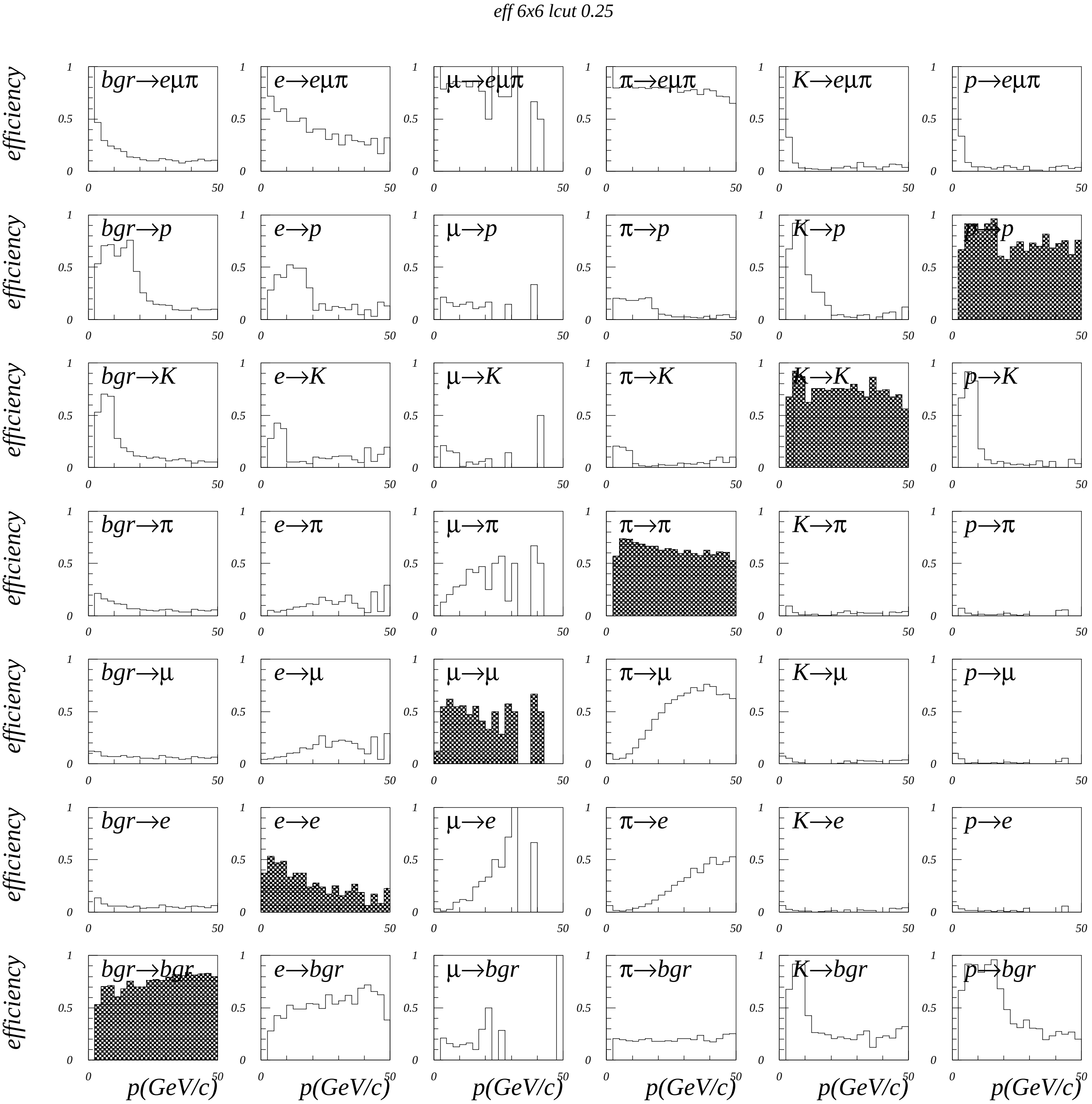

Figure 4.15: Transition matrix $id_1 \to id_2$; Probability to identify a particle with the Monte Carlo identity id_1 as p, K, π, μ or background identity id_2, as a function of momentum. Particle was identified as hyp if the likelihood for that hypothesis exceeded a value of 0.25.

5

Reconstruction of tracks in the HERA-B experiment

Track reconstruction in HERA-B is performed within a reconstruction program ARTE [49]. For each event the data is read into a computer's memory and the reconstruction chain is called. Bitmaps are decoded into space points with a defined position on the detector. Track reconstruction is functionally implemented in several steps. First functions are called which perform a reconstruction within each of the subsystems separately. From the hardware point of view the main tracking system consists of the inner and the outher tracking systems. Since the input for the track reconstruction procedure are already reconstructed space points, the data from both main tracking subsystems are treated equally. For the procedure, it is much more important the functional divison of the main tracking system (Fig. 2.2), namely the tracking in the pattern chambers (PC), the tracking in the trigger chambers (TC) and the tracking in the magnet chambers (MC) [50]. For the track finding the most important part is the tracking in the pattern chambers, the chambers between the magnet and the RICH. The trigger chambers (TC) consist of the chambers after the RICH and before the electromagnetic calorimeter, while the magnet chambers (MC) occupy the area inside the magnet and include the eighth superlayer of the vertex detector system. Part of the reconstructed track which is found in the one of the HERA-B subsystems is called a segment. The segment may be a straight line, but may also be an arc in the magnetic field. From the found segments in different subtracking modules the whole track is later built in a matching procedure.

The reconstruction of the tracks is implemented in the following way. First segments from the vertex detector system and from the pattern and trigger chambers are reconstructed from the space points. The track segments in the vertex detector system are reconstructed using a cellular automata algorithm known as CATS [52]. The cellular automata are dynamical systems that evolve in discrete usually two dimensional spaces consisting of cells. They can be regarded as discrete neural networks. The tracking algorithm based on them leads to a good recognition of events with a small number of tracks. In comparison to the method of Kalman filtering, the use of the cellular automata for track searching is faster.

Each superlayer in the vertex detector provides a position measurement in four different projections. This is more than enough because the algorithm creates track candidates using two different projections only. The redundant information is used to compensate detector inefficiencies. The performance studies on the Monte Carlo simulation showed an efficiency for track finding in the veretex detector of 95% for an average of four interactions per event.

In the main tracking system, reconstructed segment of the tracks are formed using a Kalman filter algorithm. The track finding in the main tracker is divided into four steps. The first step finds straight track candidates in the horizontal projection using only the hit information from the vertical wire layers of the pattern chambers. The second pass finds the corresponding vertical track projection candidates in the vertical projection using simultaneously the hit information from the tilted stereo layers. Hits assigned to the vertical and horizontal track candidates are then combined and a three dimensional track candidate is created. In the next two steps this three dimensional candidate is propagated through the magnet chambers and through the trigger chambers behind the RICH.

A recursive growth procedure is then applied. This procedure consists of passing step by step through planes of the tracking system and trying to include new hits in the candidates. During track following a weighted number of hits for the each candidate is calculated. The track segments with enough hits are later used for the track construction.

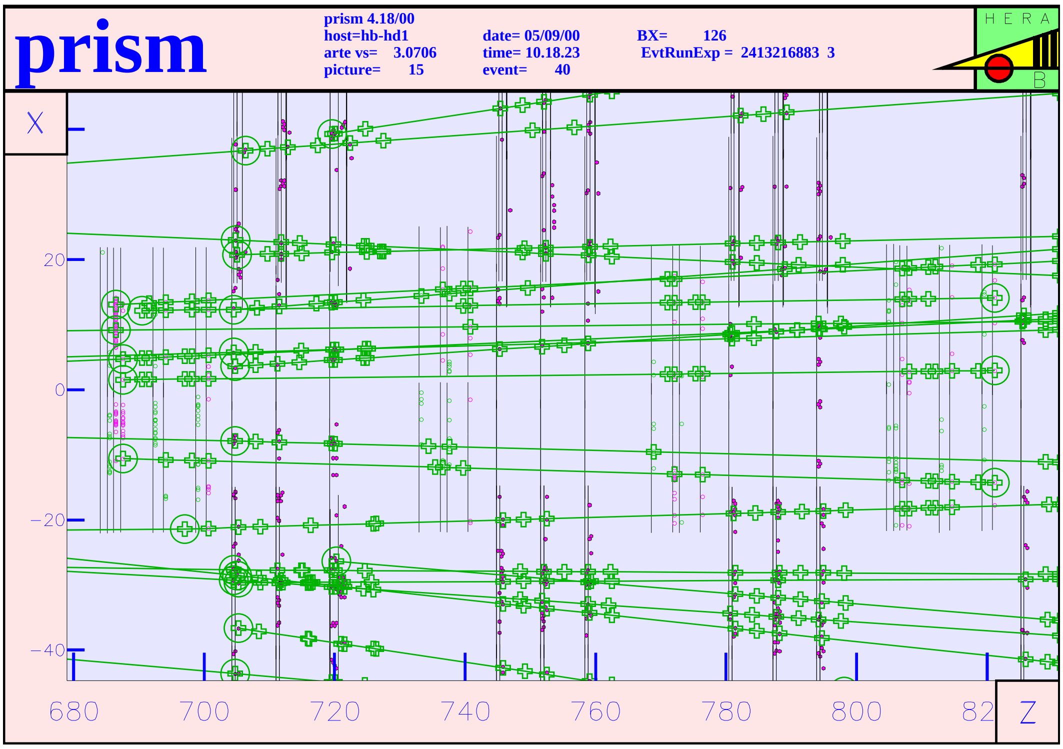

Figure 5.1: Event data display showing the tracking area of the inner tracker stations MS10 to MS 13 with hits and reconstructed track segments in the inner and in a part of the outer tracking system.

5.1 Matching of the track segments

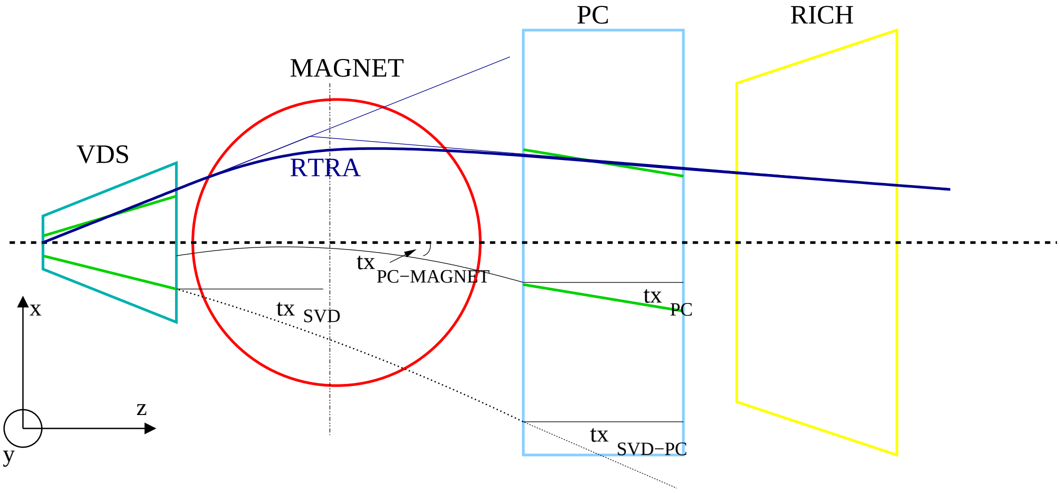

Figure 5.2: The HERA-B track reconstruction. The segments of the tracks are found first in the silicon vertex tracker (VDS) and in the pattern tracker of the main tracker (PC). A reconstructed track (RTRA) is constructed from a pair of matched segments in the vertex detector system and in the pattern tracker.

The inner tracking system was not yet commisioned and the magnet chambers of the outer tracking system were not aligned during the reconstruction of the data in August 2000. Therefore the track finding procedure had to be modified to reconstruct tracks from the available segments in the vertex detector system, the pattern and the trigger chambers. The implemented track reconstruction procedure is as follows (Fig. 5.2). The segments from the pattern chambers, which are constructed using a minimum of twenty hits per segment, are matched with the segments from vertex detector system with a minimum of six hits per segment. The input to the matching procedure are the parameters at the end of the silicon vertex segment and at the beginning of the pattern tracker segment. First the vertical position y of the segments was compared at the beginning of the pattern tracker segment z_{pc} (Fig. 5.3), and it was required that

$$|y_{svd} + (z_{pc} - z_{svd}) * ty_{svd} - y_{pc}| < \Delta y_0 \,. \tag{5.1}$$

The svd indices correspond to endpoint of the vertex detector segment and pc to indices at the start-point of the pattern tracker segment, x, y, z to the coordinates of the space points on the segment and ty to the slope of the segment in y direction (Fig. 5.2).

For a matched combination of segments from vertex detector system and from the patteren chambers, momentum is estimated. Both segments are propagated through the magnetic field. For the tracking in the magnetic field area, the numerical integration is used with the parametrized magnetic field. The momentum is calculated by requiring that both segments have equal inclination tx in a horizontal plane in the middle of the magnet. This difference must be smaller than 0.01 mrad. Both segments are then propagated into the middle of the magnet where a more stringent cut is applied on the horizontal position x

$$|x_{svd-magnet} - x_{pc-magnet}| < \Delta x \ , \qquad (5.2)$$

where $svd - magnet($ $pc - magnet$) index corresponds to the vertex (pattern) segment propagated to the middle of the magnet. The last cut is then applied on the vertical position y of the vertex segment propagated to the beginning of the pattern tracker segment $svd - pc$

$$|y_{svd-pc} - y_{pc}| < \delta y_1 \ . \qquad (5.3)$$

For each pair of a vertex segment and a pattern tracker segment, which survived all the above cuts, a new track (RTRA) is formed. The construction of the track using a vertex detector segment and pattern tracker segment is illustrated in Fig. 5.2. The values Δy_0, Δx and Δy_1 are extracted by checking the correlations as shown in Fig. 5.3. In the standard reconstruction from August 2000 the value for Δy_0 was 35.7 cm, Δx was 2.6 cm and Δy_1 5.6 cm. For such Δx and Δy_1 there are also wrong combinations of segments possible, i.e. combinations where an unphysical ghost track was formed from segments from two different particles (Fig. 5.4. There was a non-negligible number of tracks, which were formed from a segment from vertex detector system or pattern tracker and was already used in the construction of another track. Such tracks are called clone tracks. The efficiency of finding a track with such a procedure is 92% and was obtained from Monte Carlo studies. With the same values of δx and δy the ghost rate was 11% [53]. After the track is reconstructed, a refit is performed on it to improve the track parameters and to recalculate the momentum of the track.

5.2 Errors in track parameters

Normally, a track is constructed from the segments from the vertex detector system and the main tracking system. During the commissioning phase, the magnet tracking was not working properly, and as a result, tracks were formed using the segments from the pattern chambers. The pattern tracker chambers consist of wire chambers which are organized in three types of layers: vertical and tilted from the vertical for ± 80 mrad. The resolution in the vertical slope measurement is thus ten times worse than the horizontal direction measurements. When combined with the silicon vertex segment, the resolution in the vertical slope improves because of the much better measurements of angle in the vertex detector system. On the other hand particles from the vertex detector system to the pattern tracker undergo multiple scattering in the magnet tracker chambers resulting in the limited improvement of the vertical slope resolution.

A misalignment of the detector parts also worsens the resolution. The procedure to align the detector includes first an alignment of components within subsystems (internal alignment) and an alignment of different subsystems between themselves (global alignment). The internal misalignment comes from misalignments of different subsystem components, i.e. in the case of the outer tracker the misalignment of detectors within one layer, between layers and between

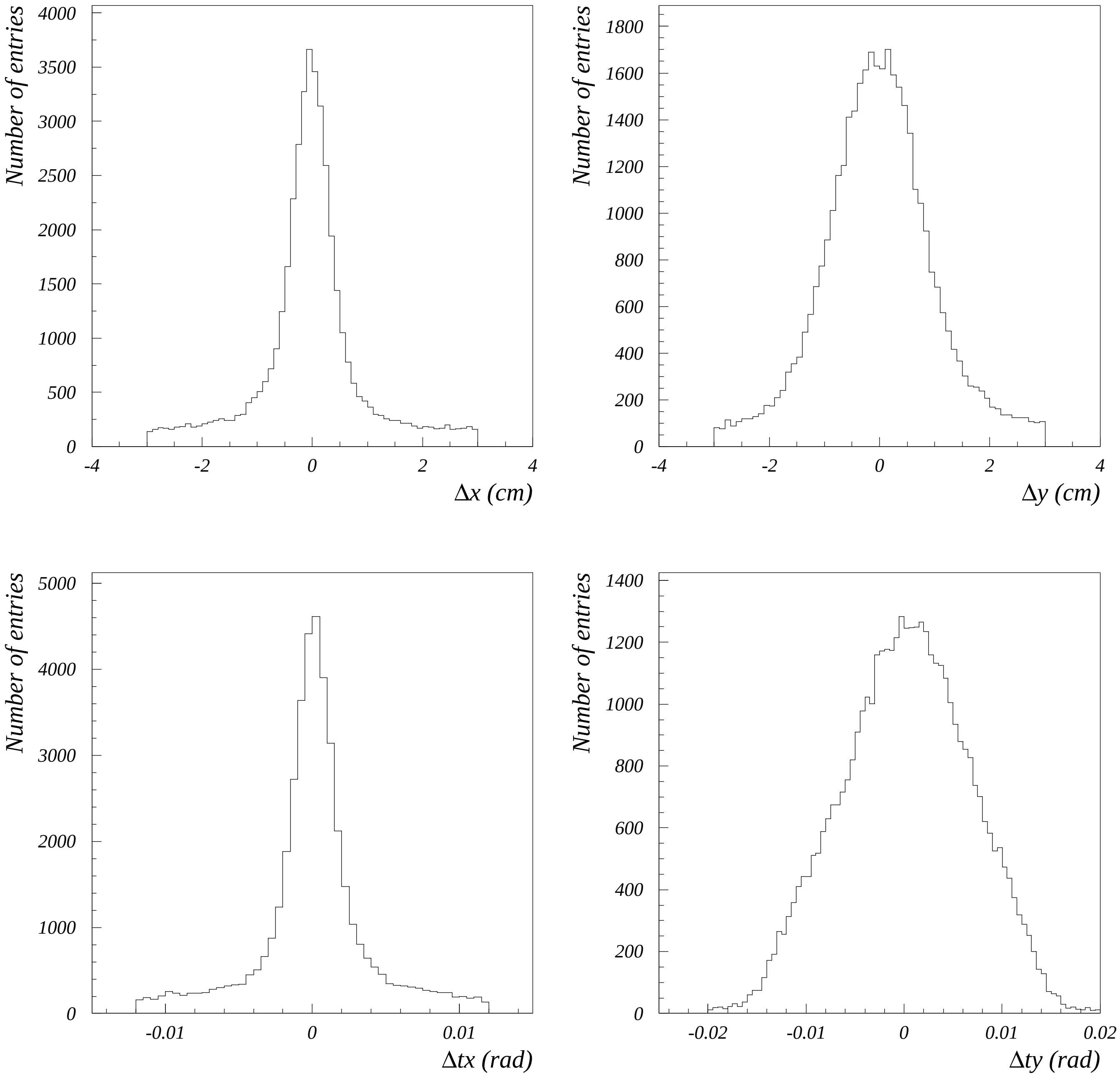

Figure 5.3: Difference between the silicon vertex tracker segments and the pattern tracker segments. The segment from the vertex detector system is propagated to the first point of the segment from pattern chambers. In the upper plots propagation is done in such a way that the horizontal direction tx is matched and the resulting difference in the horizontal coordinate x (upper left) and vertical coordinate y (upper right) is shown. In the lower plots the horizontal position x is matched, and difference in the horizontal direction (lower left) and vertical direction (lower right) is shown. Note that in the standard matching the matching of the segments in the horizontal direction is used.

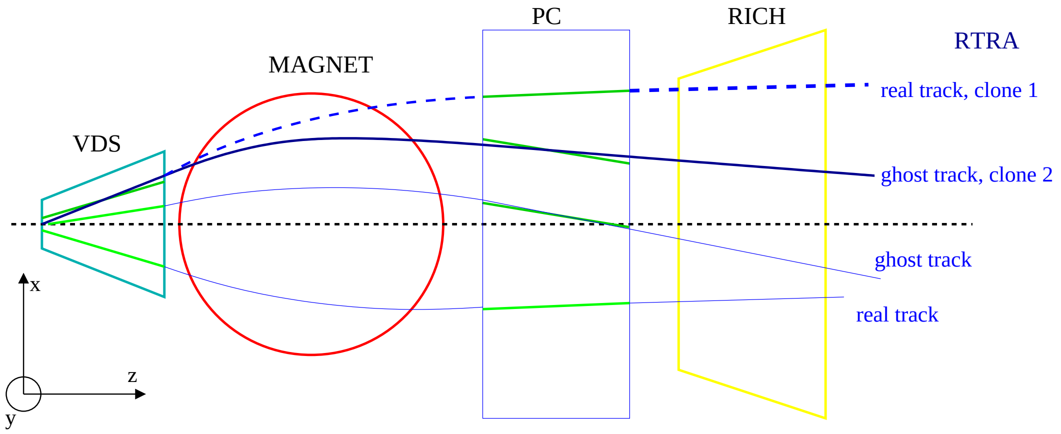

Figure 5.4: The clone and the ghost tracks, reconstructed from a pair of a vertex segment and a pattern tracker segment. A real track is a track resulting from the passage of the particle through detector. A ghost track is a track formed from two segments belonging to different particles. A clone track is a track which shares one of the segments with one or more reconstructed segments.

superlayers. As a result of misalignment, the efficiency for reconstruction of a track segment drops and at the same time the resolution of the found segments is poor. After subsystems are aligned internally, one can align them globally, i.e. with respect to the HERA-B coordinate system. One would need good tracks built from already aligned subsystems for such a procedure. Unfortunately such tracks are not available until at least two subsystems are aligned with respect to each other. An alignment of the detector thus leads to a complex iterative procedure which gradually produces an aligned detector.

Another factor that worsens the resolution is the miscalibration of space time relations of the outer tracker drift chambers All the above mentioned effects had impact on the resolution of reconstructed tracks from data taken in the year 2000. The angular resolution of tracks was not better than the internal RICH resolution, contrary to what was expected. It was therefore anticipated that the RICH particle identification efficiency would be somewhat worse than the design value.

5.2.1 Track errors in the RICH detector

The quality of reconstructed tracks influences the particle identification in the RICH. The input parameters for the analysis are track momentum, track direction and errors on these parameters. In addition, the algorithm uses the space point on the track, closest to the entrance wall of the RICH, to estimate a track geometrical acceptance. If the track direction is not measured with high enough precision, the track will not be identified correctly. This is due to the non Gaussian distribution of hits in the Cherenkov angle histogram. In Fig. 5.5 the distributions are shown for different direction displacements of the hypotetical track. Note that in case of large errors in the direction determination, the signal hits in the Cherenkov angle distribution will sink in the background. An estimated error in the vertical and horizontal track direction, calculated by the

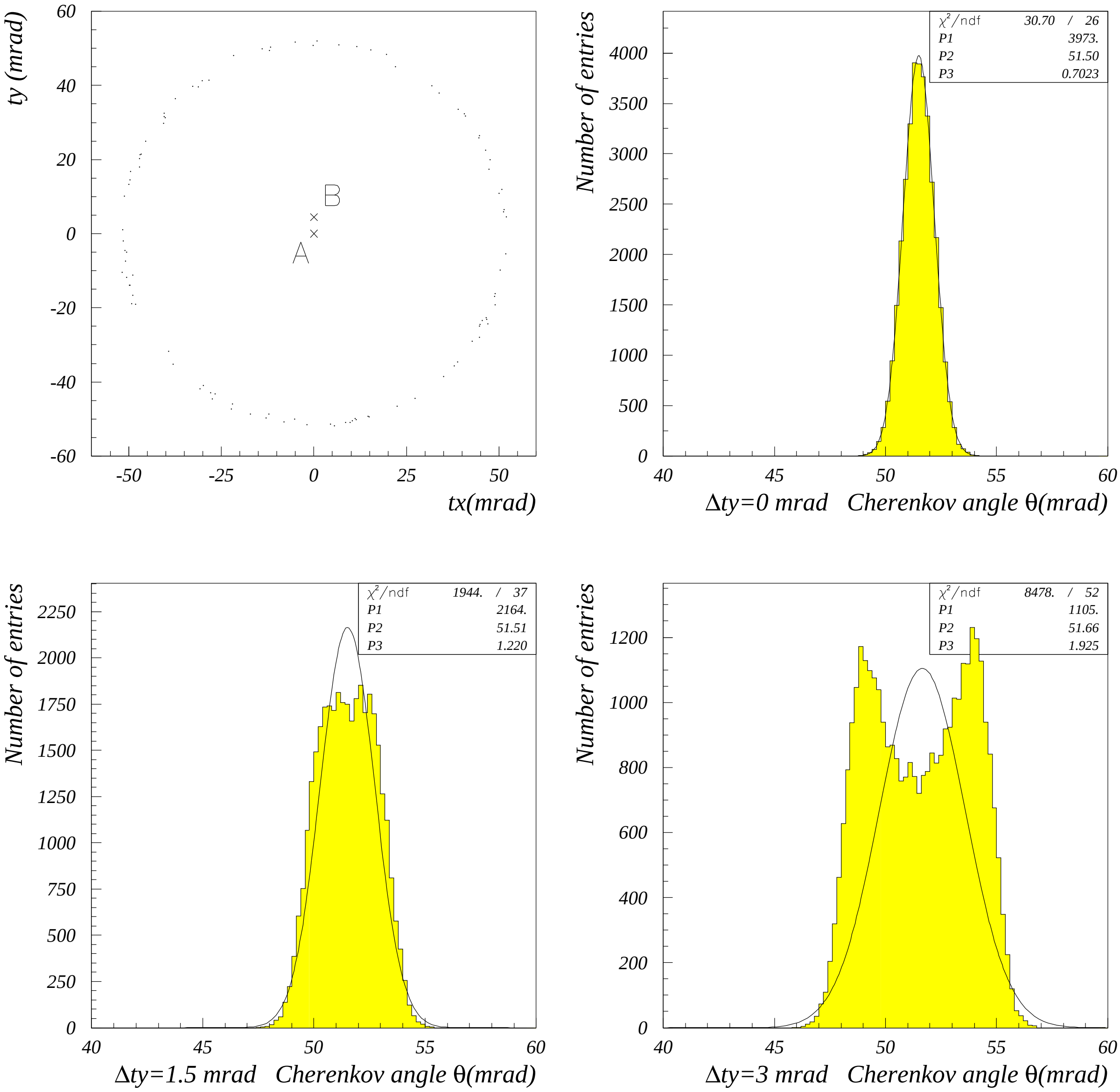

Figure 5.5: Influence of track direction on the Cherenkov angle distribution. Distribution of photon hits on the detector surface with the center of the ring (A) and displaced virtual track intersection (B) (top left). Cherenkov angle distributions for different track displacements in vertical direction: 0 mrad (top right), 1.5 mrad (bottom left) and 3 mrad (bottom right).

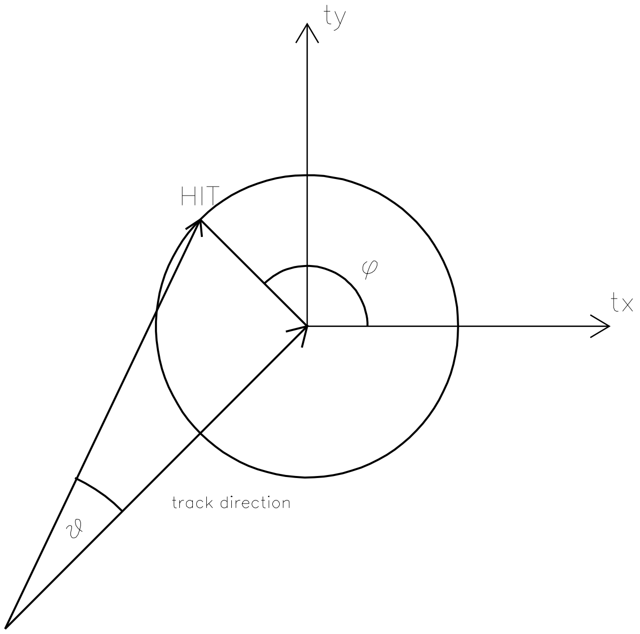

Figure 5.6: Image of the Cherenkov light emitted in the cone is the Cherenkov ring on the detector surface. The azimuthal angle φ is obtained relative to the horizontal tx axis.

track reconstruction program, is used in the particle identification algorithm for determination of the signal and the background. Since the influence of the estimation of the error in the track direction may worsen the particle identification in the RICH, this estimate was cross-checked using the RICH hit information as will be shown below. A relatively low photon hit yield (max. 35 photons per track) does not enable to study the error estimates on the track by track basis, but forces to use the cumulative distributions to estimate average values.

If the track directions are measured without errors, the Cherenkov angle distribution should be a sum of a uniform background and a Gaussian signal with a mean at the expected Cherenkov angle and spread only due to the RICH internal errors. For the measured data, the errors introduced by alignment, calibration and reconstruction can be obtained by analyzing the Cherenkov angle distribution histogram.

To calculate the overall track errors and the alignment of the ring imaging Cherenkov detector with respect to the tracks, we first calculate for each track-photon hit pair the Cherenkov angle θ and the azimuthal angle φ (Fig. 5.6). The azimuthal angle φ is calculated as the angle between the line on the photon detector, which connects the track intersection and a given photon hit, and the horizontal direction. A two dimensional histogram Cherenkov angle versus azimuthal angle is filled for all these pairs (Fig. 5.10). Slices in the azimuthal angle (Fig. 5.9) are then fitted with a sum of a polynomial and a Gaussian function. From the resulting Gaussian mean and width, the value of $\theta(\varphi)$ and $\sigma(\varphi)$ are determined.

If the RICH detector would be perfectly aligned with respect to the tracks, the centers of peaks for different azimuthal angles would lie in one line. Due to misalignment, the line trans-

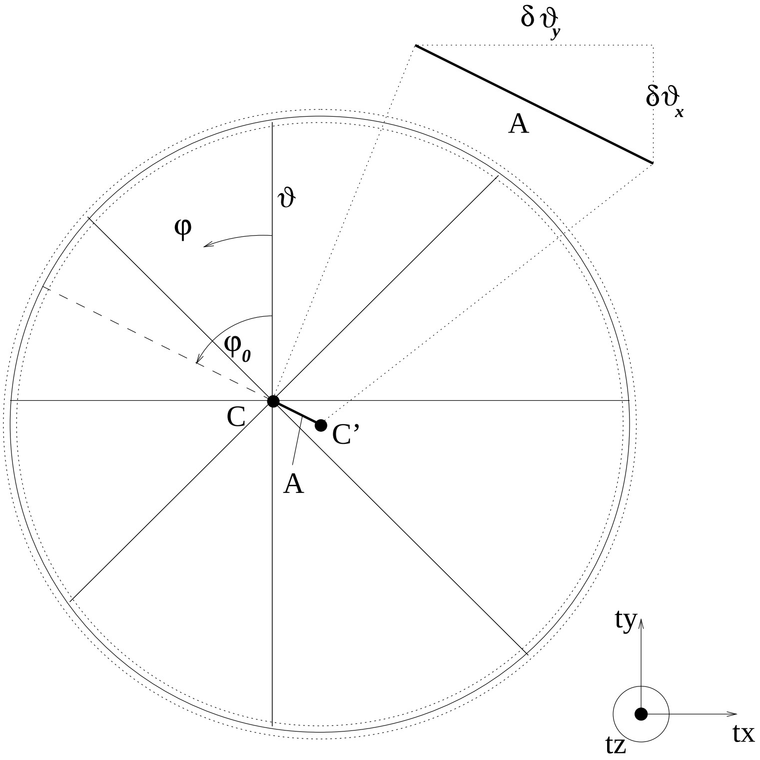

Figure 5.7: Cherenkov ring: Photons that were radiated by a track are statistically smeared on a ring. Point C is the point, where the track virtually intersects the detector plane, and point C' is the center of the ring. If the detector would be perfectly aligned the points C and C' would be the same. Due to misalignment, the point C is displaced in the horizontal and in the vertical direction.

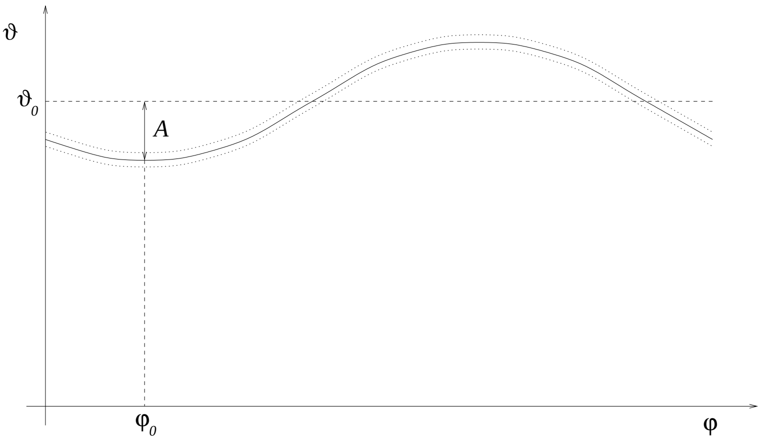

Figure 5.8: The displacement in Fig. 5.7 can be represented as a function $\theta(\varphi)$. The displacement of the center results in a sine modulation over the constant mean value.

forms into a sine function (Fig. 5.8). The peak in the Cherenkov angle distribution θ is the

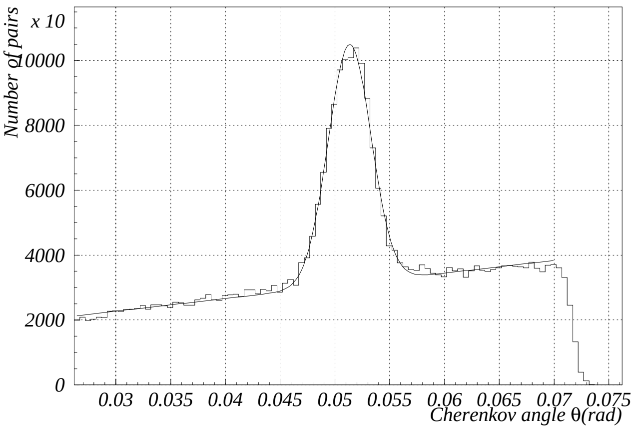

Figure 5.9: Cherenkov angle distribution histograms are filled and the peak position θ and width σ are fitted for a given momentum interval and a given bin in the azimuthal angle φ.

following function of the azimuthal angle φ

$$\theta(\varphi) = \theta_{+}\delta\theta_x \cos\varphi + \delta\theta_y \sin\varphi \ , \tag{5.4}$$

where θ_π corresponds to the expected Cherenkov angle for the most frequent pion hypothesis for a given momentum, and $\delta\theta_x$ and $\delta\theta_y$ are the detector displacements in the horizontal and in the vertical direction. The resulting displacements turn out to be negligible (of the order of 0.1 mrad) and show no momentum dependence (Fig. 5.11).

The spread depends on the angle φ in the following way

$$\sigma^2(\varphi) = (\sigma_{tx} \cos\varphi)^2 + (\sigma_{ty} \sin\varphi)^2 + \sigma^2_{RICH} \tag{5.5}$$

where σ is the total spread of the distribution at the azimuthal angle φ, σ_{RICH} is the RICH internal error, σ_{tx} and σ_{ty} are the horizontal and vertical track direction errors. For different momenta of the tracks the width of the Cherenkov peak was fitted to extract σ_{tx} and σ_{ty} (Fig. 5.12). In Fig. 5.13 track errors σ_{tx} and σ_{ty} are plotted as a function of momentum of the particle. In addition, track errors as calculated by the track reconstruction program for each of the tracks, are displayed in the same plot. The delivered track error is one of the most important external data for the particle identification algorithm in the RICH. In the data reconstructed in the year 2000, the track error was under-estimated due to misalignment effects, which were not taken into account properly in the track reconstruction. Since the origin of the wrong error estimate is the misalignment of the detector, not properly taken into account, the ad hoc solution was to rescale the track direction errors to fit the measured average track direction errors in the RICH. The scaling factors, which have been used in the particle identification algorithm in the reconstruction in the year 2000 are listed in Table 5.1.

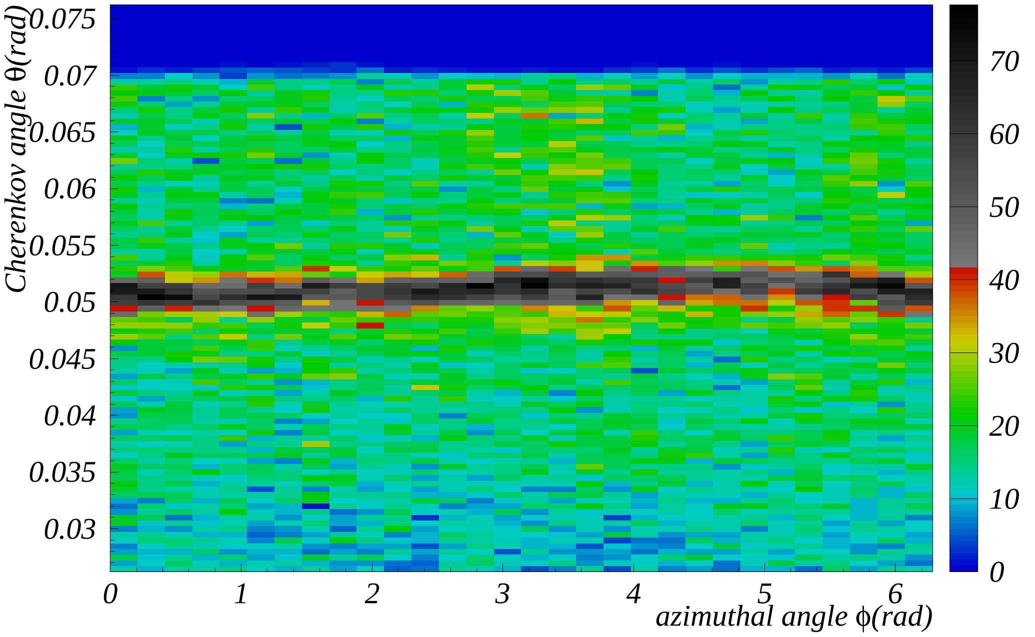

Figure 5.10: The Cherenkov angle versus azimuthal angle distribution for tracks of momentum between 40 GeV/c and 50 GeV/c. The alignment shifts of the RICH counter with respect to the track coordinate system $\delta\theta_x$ and $\delta\theta_y$ is extracted from the position of the Cherenkov peak in different azimuthal bins, while the track direction errors σ_{tx} and σ_{ty} are obtained from the width of the Cherenkov peak in different azimuthal bins.

Data type	σ_{tx} scaling factor	σ_{ty} scaling factor
measured	4	1.7

Table 5.1: The rescaling factors for the track direction errors as used for the year 2000 reconstruction. The scaling factors correspond to the ratio between the resolution of the tracks measured in the RICH and the resolution of the tracks as delivered by the track reconstruction program.

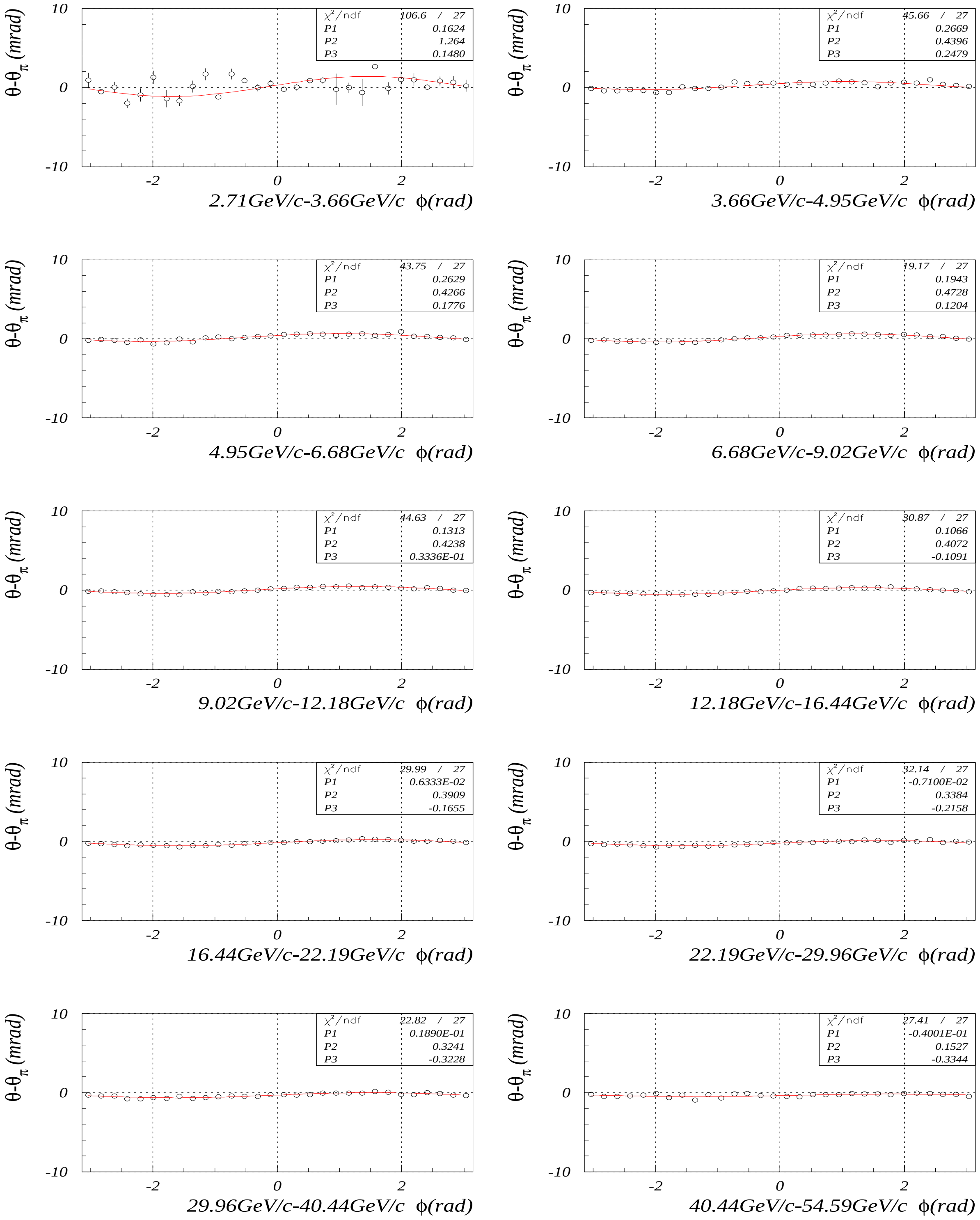

Figure 5.11: Alignment of the RICH counter ant the reconstructed tracks for different momenta. The Cherenkov angle histograms are fitted with a sum of a Gaussian and a linear function for different φ slices. The horizontal $P1$ and vertical $P2$ angle shifts are extracted for different momentum bands by fitting Eq. 5.4 to the Cherenkov peak values for different φ bins.

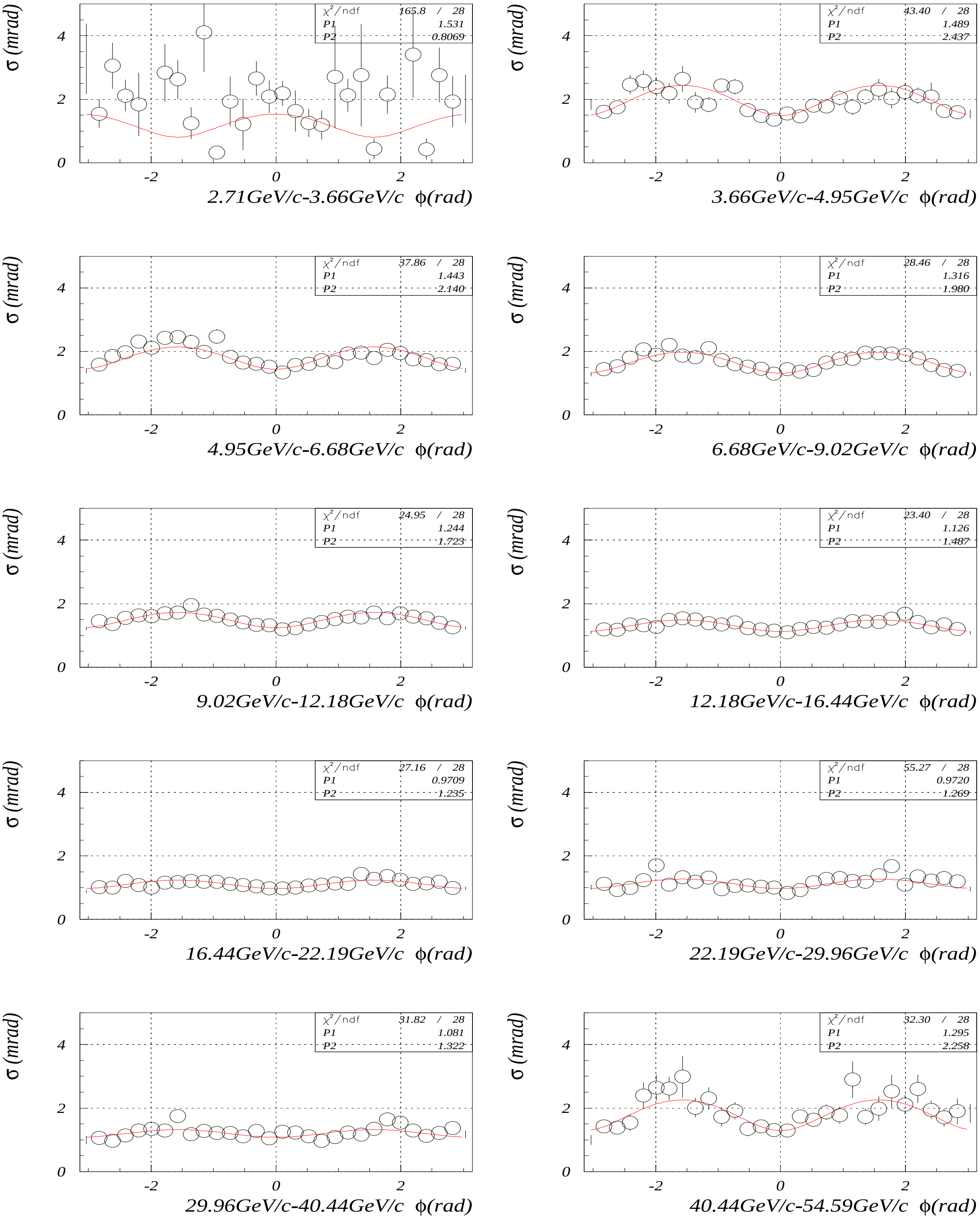

Figure 5.12: Track direction error for different momenta. The Cherenkov angle histograms are fitted with a sum of a Gaussian and a linear function for different φ slices. The horizontal direction $P1$ and vertical direction track errors ($P2$) are extracted for different momentum bands by fitting Eq. 5.5 to the width of the Cherenkov peak for different φ bins.

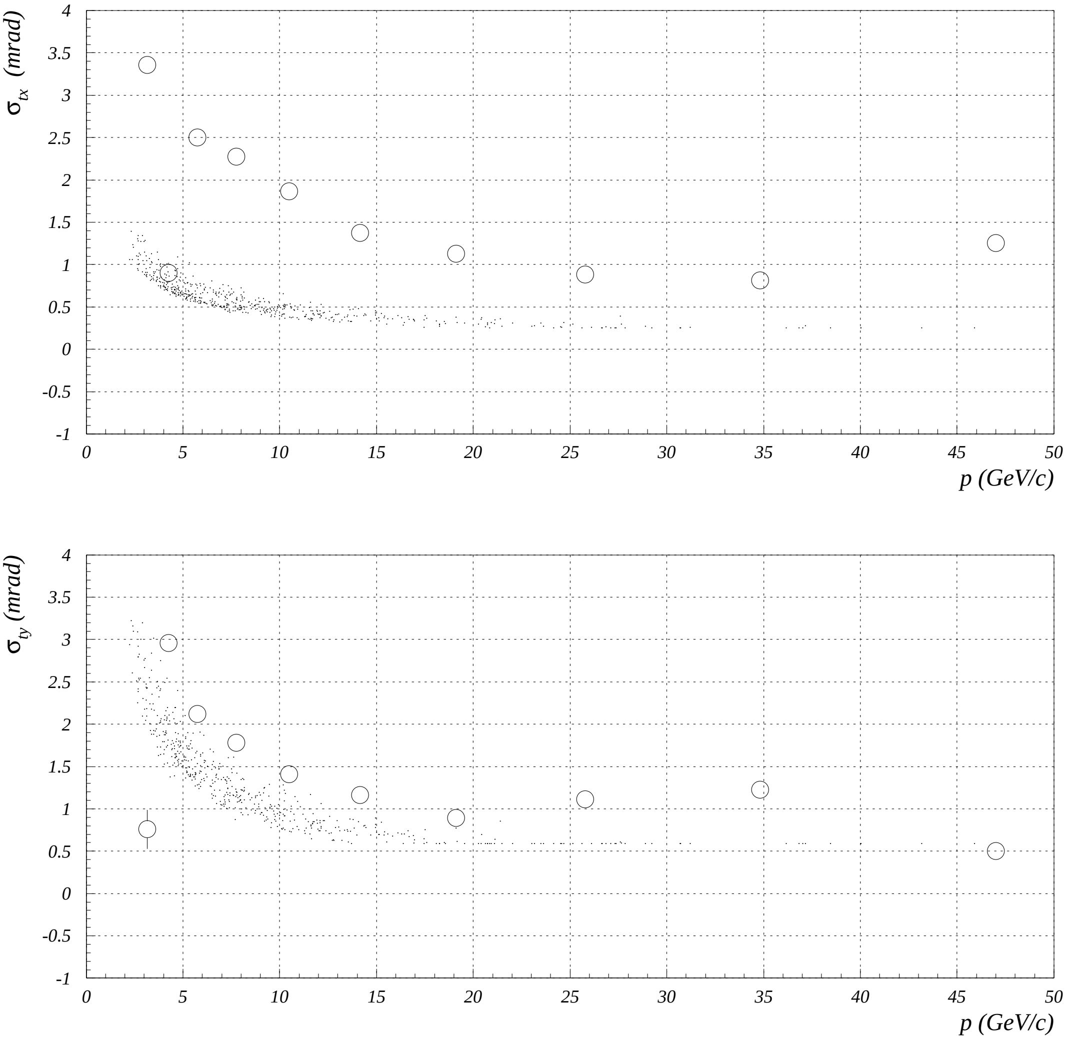

Figure 5.13: Track errors in the RICH σ_{tx}, σ_{ty} (see Eq. 5.5) (circles) compared with track direction errors of individual tracks calculated in the tracking program (dots), as a function of momenta for the horizontal (upper plot) and vertical direction (lower plot).

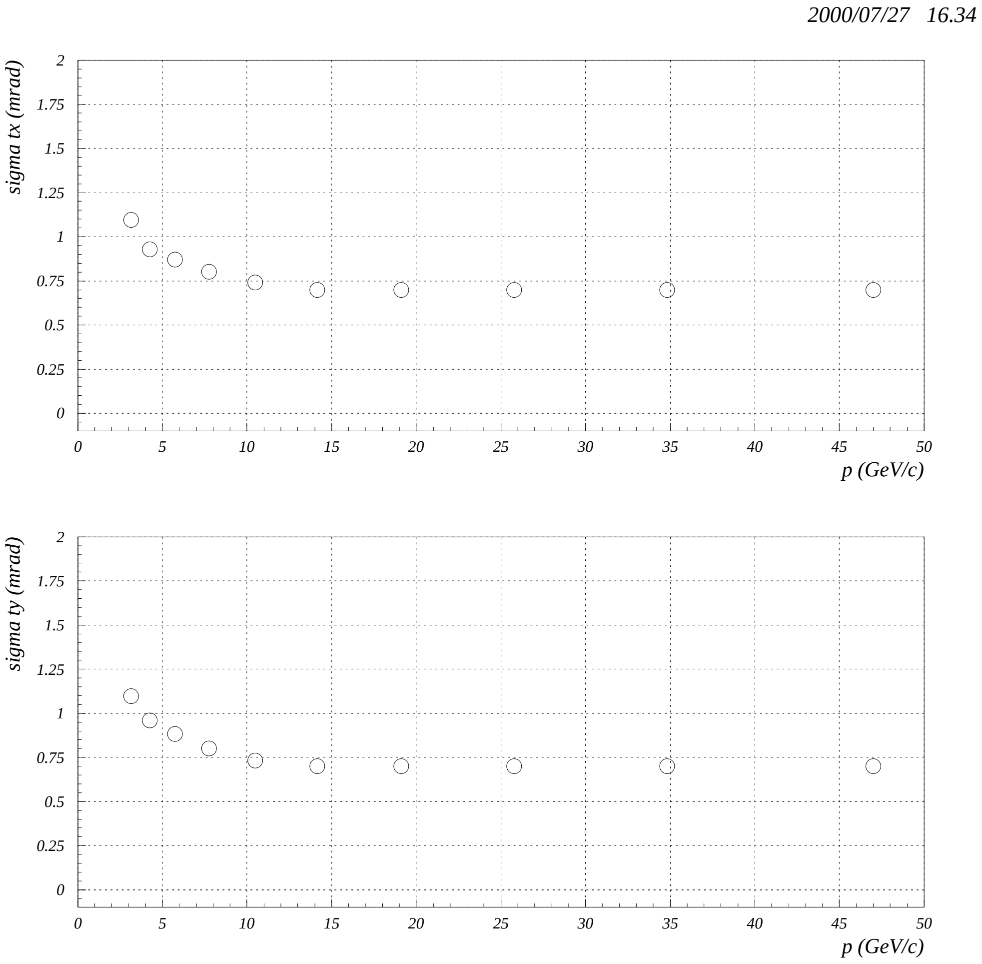

Figure 5.14: Momentum dependence of the RICH internal errors (σ) in the horizontal direction (upper plot) and in the vertical direction (lower plot).

The internal RICH resolution σ_{RICH} was calculated from the same measurements. It was found that it is consistent with the proposed value of 0.7 mrad [28]. The internal RICH resolution was also checked on the simulated data. For the Cherenkov angle distribution histograms the tracks with the ideal parameters were used. The resulting resolution (Fig. 5.14) is consistent with the expected value as well. The measurements of σ_{RICH} is in agreement with the results obtained in the study of the alignment of the RICH with the electromagnetic calorimeter [54], and by analyzing rings on the photon detector as found by the stand alone ring search package RISE [55].

6

Particle identification efficiency of the RICH

The iterative method for particle identification of hadrons which was described in Section 4 should be applied to the measured data. One of the important tasks is to determine the separation efficiency as it was done for the Monte Carlo generated events.

The separation efficiency of the RICH can be determined on the samples of clean particles already identified by other methods. The cleanest determination, not biased by any of the other identification algorithms, is to identify particles exclusively by the kinematical and geometrical cuts. The identity of such particles can then be compared to the identity as found in the RICH. The identity is deduced from the values of the likelihoods for different hypotheses. As already mentioned, a certain hypothesis hyp is accepted (identity proved), if the likelihood for that hypothesis exceeds a certain value or is maximal of all likelihood values. In the analysis, the first method was used.

The simplest check can be performed on the particles decaying to two final state particles traversing the RICH. Such selection might be problematic due to huge combinatorial background of tracks coming from the target. For K_S particles with an average decay length of about a meter in HERA-B, additional cuts can be made on the vertex position to suppress the background. This results in a very clean signal seen in Fig. 6.1.

In parallel to the efficiency also the misidentification probabilities, identification of a particle as a particle of wrong identity, can be determined.

The following simple two body decays were investigated for different trigger conditions and different running periods : $K_S \to \pi^+\pi^-$, $\Lambda \to p^+\pi^-$, $J/\psi \to \mu^+\mu^-$ and $\phi \to K^+K^-$. The decay of ϕ to K^+K^- is very important for performance evaluation of the RICH counter, but unfortunately, we have only a small ϕ sample available for the analysis. The ϕ particles are rather rare and are decaying in the primary vertex, and the background from other particles is huge there.

In what follows the particle identification efficiency obtained on the samples of the above listed particles will be presented. The efficiency was calculated for specific data sets, which will be discussed first. In the next subsection it will be explained how the tracks were selected. The

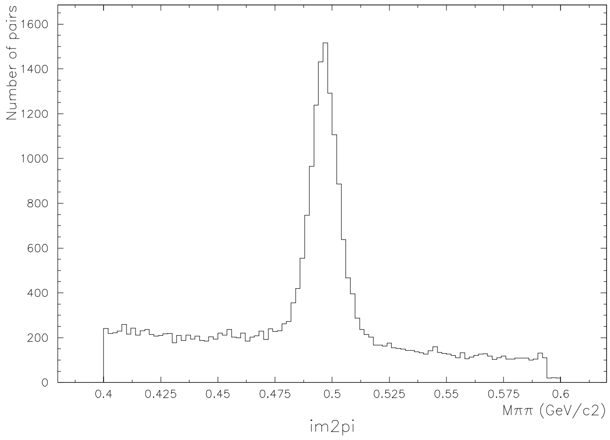

Figure 6.1: K_S signal as detected in the HERA-B experiment in single lepton triggered data taking mode.

identification efficiency as a function of different likelihood cuts and as a function of momentum will then be presented.

6.1 Event selection and reconstruction

Except for the J/ψ analysis the data were not preselected. All the analyzed runs have been recorded at the interaction rate of 5 MHz. At the present knowledge of the detector performance, it was not feasible to take physics data at higher interaction rates. Correspondingly, mainly the events with one interaction per bunch crossing were recorded and used later in the analysis. Several types of trigger condition were used in the data taking.

- Minimum Bias Trigger: Events are selected by the second level processor farm by requiring minimal signals above noise threshold in the detector. The trigger is implemented as a logical OR of the requirement for the minimal energy of the clusters in the electromagnetic-calorimeter and the minimum number of hits in the RICH counter. It was shown that this type of trigger selects practically all inelastic events with particles inside the HERA-B geometrical acceptance.

- Single Lepton Trigger: Events were preselected by the muon and electron pretrigger and then selected by the second level processor farm by requiring at least one lepton has p_T above a given threshold.

- Double Lepton Trigger: Events were preselected by the muon and electron pretrigger and then selected by the second level processor farm by requiring at least two leptons with the invariant mass in the J/ψ range.

The particle identification efficiency of the RICH was estimated using random minimum bias triggered data (run 14577) and single lepton triggered data (physics runs from 17127 to 17266). These events were searched for K_S, Λ and for ϕ particles, while for efficiency determination from J/ψ, a hard selection of the double lepton triggered data was used. The data used are summarized in Table 6.1.

run no	Trigger conditions	number of events
14577	random minimum bias	0.5 $\times 10^6$
17242-17266	single lepton +FLT+SLT (p_t >1.5GeV)	1.876.933
17137	single lepton +SLT (p_t >1GeV)	412.451
17127-17134	single lepton +FLT+SLT (p_t >1GeV)	912.437
hard jpsi selection	Double lepton SLT	3200

Table 6.1: The data samples, trigger conditions and number of the events taken. FLT (SLT) stands for first (second) level trigger included during the data taking. Transverse momentum p_t cut corresponds to minimal transverse momentum of the triggered lepton.

After the reconstruction of track segments in the vertex detector system, the found segments were used to find a vertex close to the wire, where the interaction has happened. Those vertices are called primary vertices. Their presence proves that the event is a result of an interaction of a proton with the nucleus in the target wire. To select events with a proton-nucleus interaction and significant detector response it was required that the event should have at least three reconstructed segments in the pattern tracker and that the primary vertex was reconstructed.

All the data were taken from April to August 2000. During the data taking, information from almost all the subdetectors was recorded but only certain reconstruction packages were switched on. Therefore the measured data were reconstructed again later in August 2000 (from now on referred as reprocessing). The silicon vertex detector hits were used for reconstruction of the track segments in front of the magnet. The reconstructed hits of the pattern and trigger chambers of the outer tracker were used in the track reconstruction program. Due to problems with the operation and reconstruction of the inner tracker, this subsystem was not used in the reconstruction of the tracks. The tracks were refit and the particle identification algorithms were called. For separation of hadrons, the RICH detector hits were used and likelihoods were calculated with the iterative ring particle identification method.

The reconstructed events with the track and electromagnetic cluster tables and with other relevant event information were then stored on the disk and were available for the analysis.

6.2 Track selection

During the reconstruction a track is created from the matched segment in the vertex detector system and the pattern tracker segment. A minimum of 6 associated hits is required for the silicon detector segment and a minimum of 20 associated hits for the pattern tracker segment. Such a procedure requires widely open matching windows due to misalignments of the tracking chambers in order not to loose too many real tracks [51]. During the reconstruction a lot of clone tracks are created, i.e. tracks which share one of the segments with one or more other tracks. It can happen, however, that clone tracks share the same signal hits in the RICH counter. During the iterative procedure, a certain fraction of the hits is assigned to one of the clone tracks and a certain fraction to another. In this way the hits which are not assigned to a physical track are lost, and identity of that track as found in the RICH may not be correct. Since the particle identification analysis is performed on all tracks and not only on the selected ones, this leads to decreased efficiency of the identification with respect to a tracks which were not clones.

On the other hand we did not want to limit ourselves to the non clone tracks in order not too overestimate the efficiency. Therefore the procedure to accept only one of the clone tracks [56] was used for the analysis. In this procedure only one of the clone tracks is selected for further analysis. The selection is based on the quality value Q calculated for each of the tracks

$$Q = N_{vertex} + N_{main} + \frac{1}{1+\chi^2}\,. \tag{6.1}$$

Here N_{vertex} and N_{main} are number of track hits found in the vertex detector system and in the main tracking system and χ^2 contains the information how well the tracks were matched. Only the clone track with the highest Q was selected.

The invariant mass was then calculated for all track pairs with the opposite charge. Depending on the particle under study, the invariant mass was calculated assuming that both tracks are pions for K_S, that the negative track is a pion and the positive is a proton for Λ (there were very few $\bar{\Lambda}$), that both tracks are muons for J/ψ and that are kaons from ϕ.

The coordinates of minimal distance were calculated for all track pairs from the parameters at the beginning of the track. As most of the particles traversing the RICH are pions and they represent a huge background, initially no K_S mesons and Λ particles have been observed in the invariant mass plot. A K_S meson with momentum 20 GeV/c has a decay length of 1.1 m , while Λ's with a typical momentum 10 GeV/c decay 0.8 m from the origin. Therefore an additional cut on the z vertex position of 4 cm downstream from the target was made for these two particle species resulting in a clear visible signal.

To further clear the signal, an additional cut was made on the minimal distance of both tracks in the pair. The distributions of minimal distance for all pairs and pairs with invariant mass in the K_S range from 0.48 GeV/c to 0.51 GeV/c have been plotted (Fig. 6.2). From them a cut on the minimal distance was chosen to be 200 μm. With this cut, almost all K_S particles are selected for further analysis while background is substantially reduced.

The resulting invariant mass distributions of the selected samples of K_S, Λ, J/ψ and ϕ which were used for further analysis are shown in Fig. 6.3. The numbers of particles used are gathered in Table 6.2. The average momentum of the pions from K_S is 9 GeV/c, of the pions from Λ is 5 GeV/c, of the protons from Λ is 20 GeV/c, of the muons from J/ψ it is 20 GeV/c and of the kaons from ϕ 16 GeV/c. The momentum distributions of the studied particles are shown in Fig. 6.4. The J/ψ signal was checked also by identifying a track in the muon system. The resulting peak in the invariant mass of two muons is shown in Fig. 6.5. Note that in the

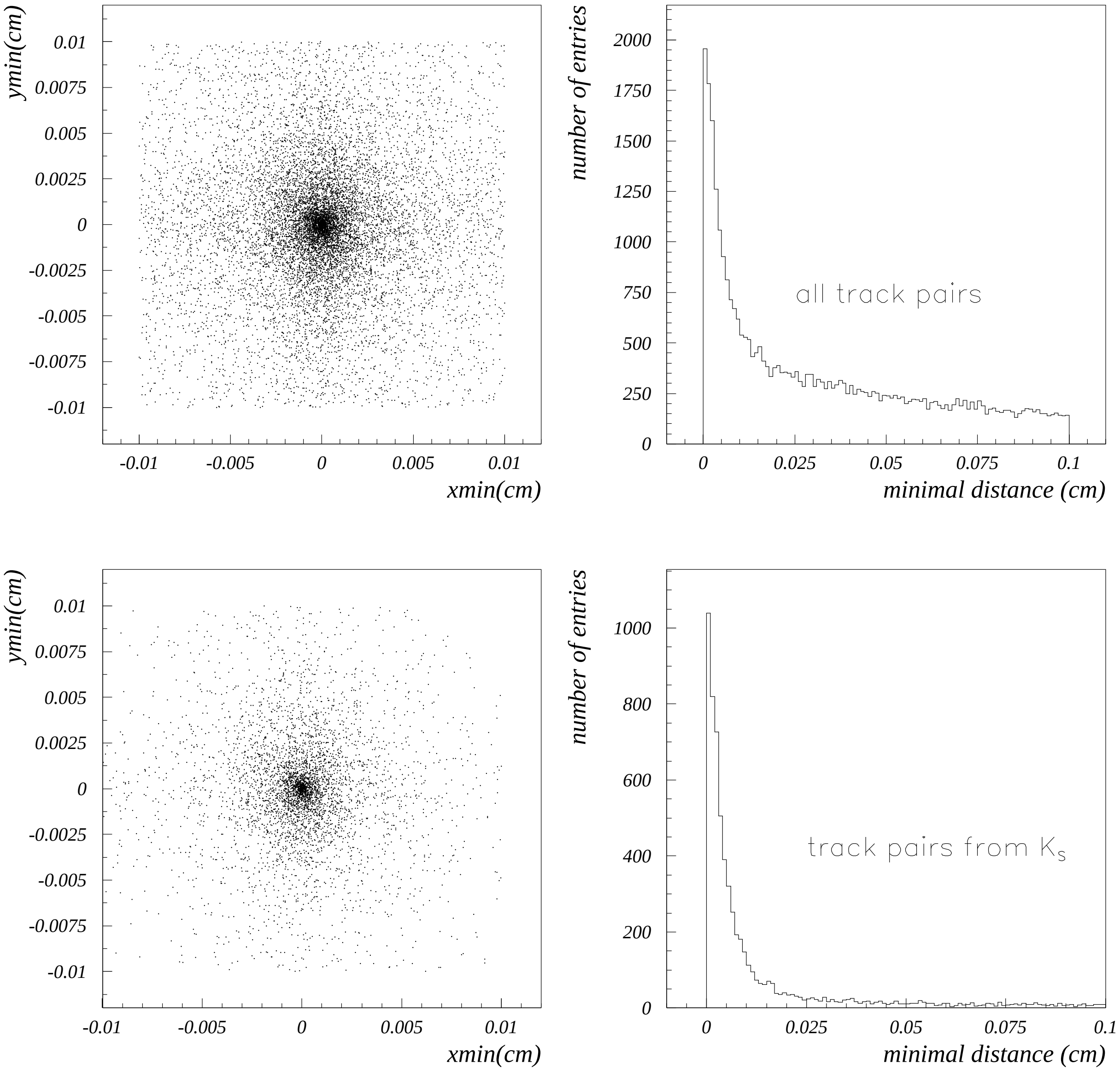

Figure 6.2: Minimal distance of two tracks: Vertical versus horizontal distance (left above) and number of track pairs as a function of distance (right above) for all track pairs and vertical versus horizontal minimal distance (left below) and number of track pairs as a function of minimal distance (right below) for track pairs within K_S mass region. The vertex was required to be well separated from the target (minimal distance from the target wire 4 cm).

Particle type	Number of particles
π from K_S	4270
π from Λ	972
p from Λ	972
μ from J/ψ	1970
K from ϕ	43

Table 6.2: Number of particles used in the analysis.

efficiency estimation no identification was required from the muon system.

To illustrate the performance of the RICH counter, the invariant mass distributions of the particles with the cut on the corresponding RICH likelihood are shown in Fig. 6.6.

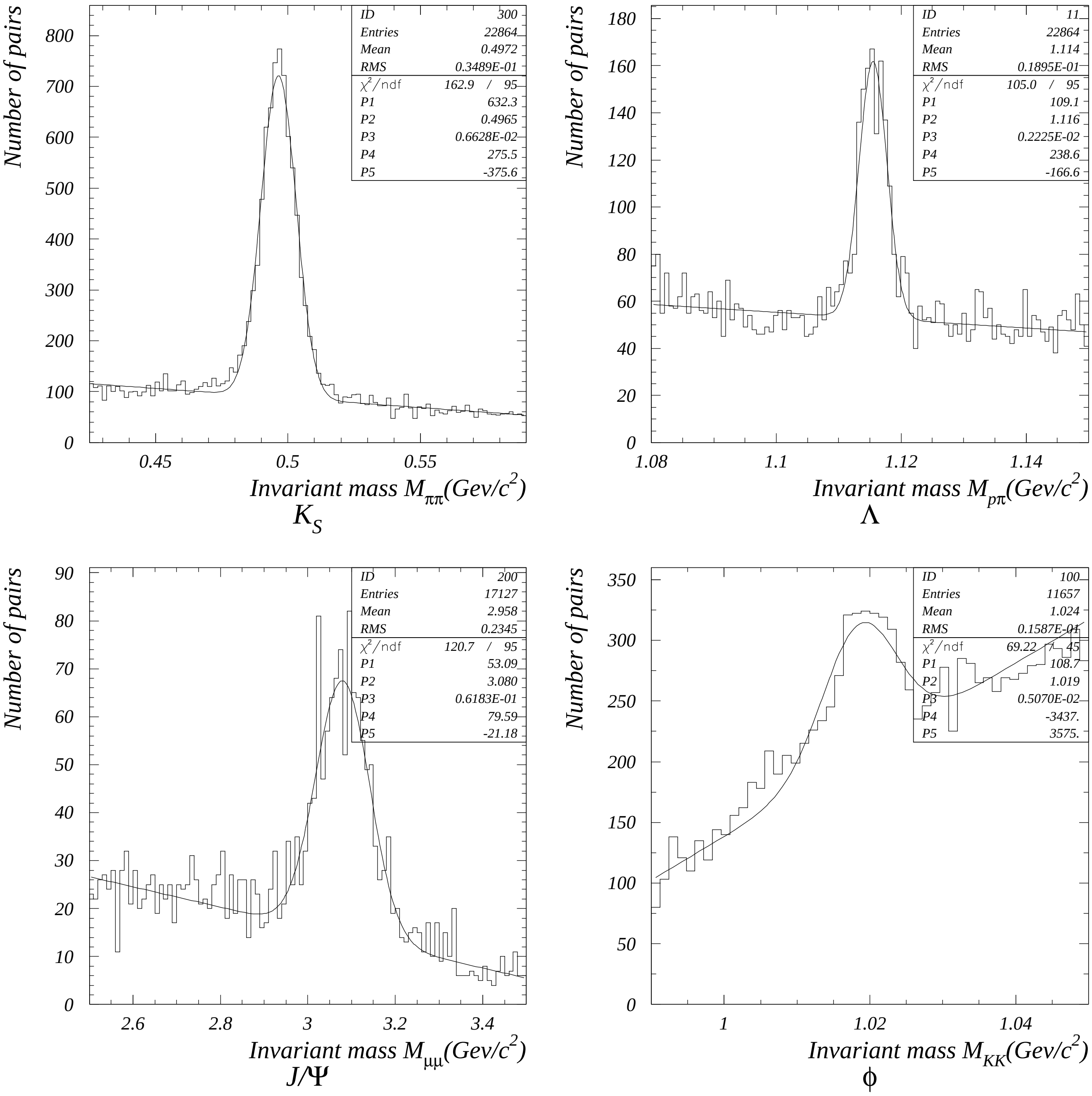

Figure 6.3: Invariant mass distribution of different particles. In all except the ϕ sample, where one of the particles was identified in the RICH by requiring its kaon likelihood to exceed 0.5 only, only cuts on the minimal distance and on the distance from the vertex for K_S and Λ were applied in the selection. Samples correspond to K_S (upper left), Λ (upper right), J/ψ (lower left) and ϕ particles (lower right).

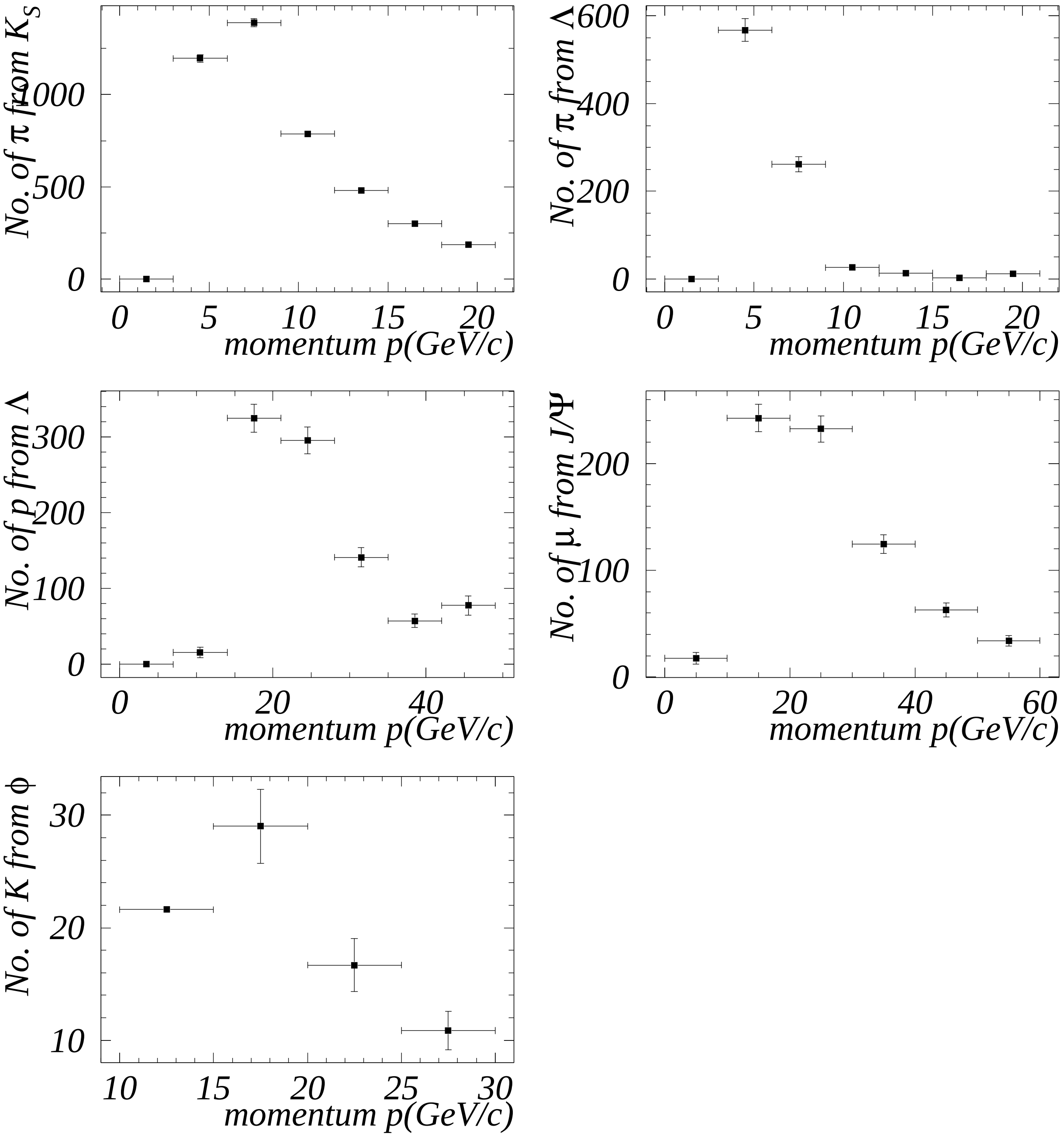

Figure 6.4: Momentum spectrum of the particles: pions from K_S (upper left), pions from Λ (upper right), protons from Λ (middle left), muons from J/ψ (middle right), and kaons from ϕ (lower left).

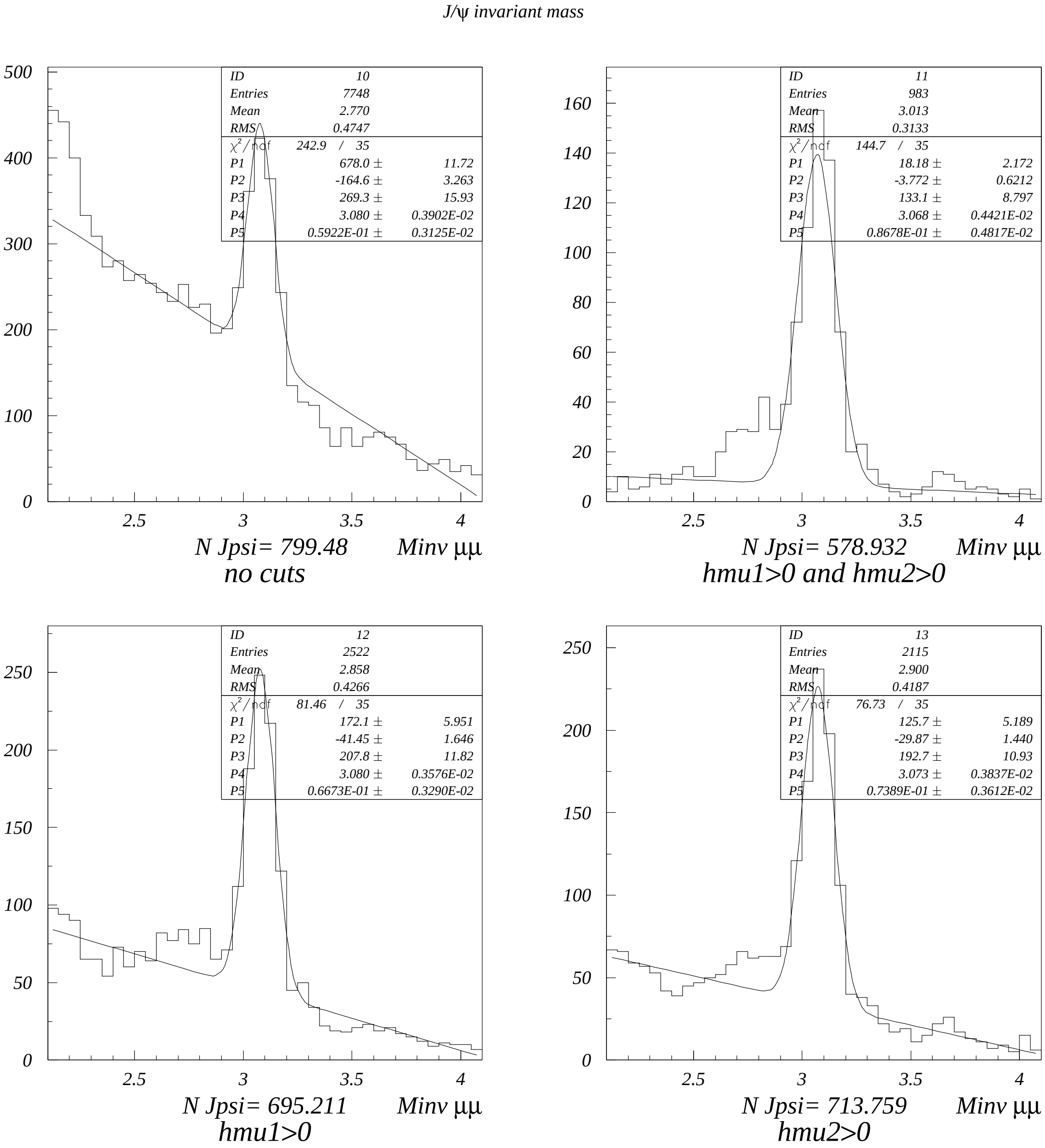

Figure 6.5: J/ψ signal after additional cuts were applied on the associated segment in the muon system: pure geometrical cuts (upper left), first track (lower left) or second track (lower right) has an associated segment found in the muon system, both tracks have an associated muon segment (upper right).

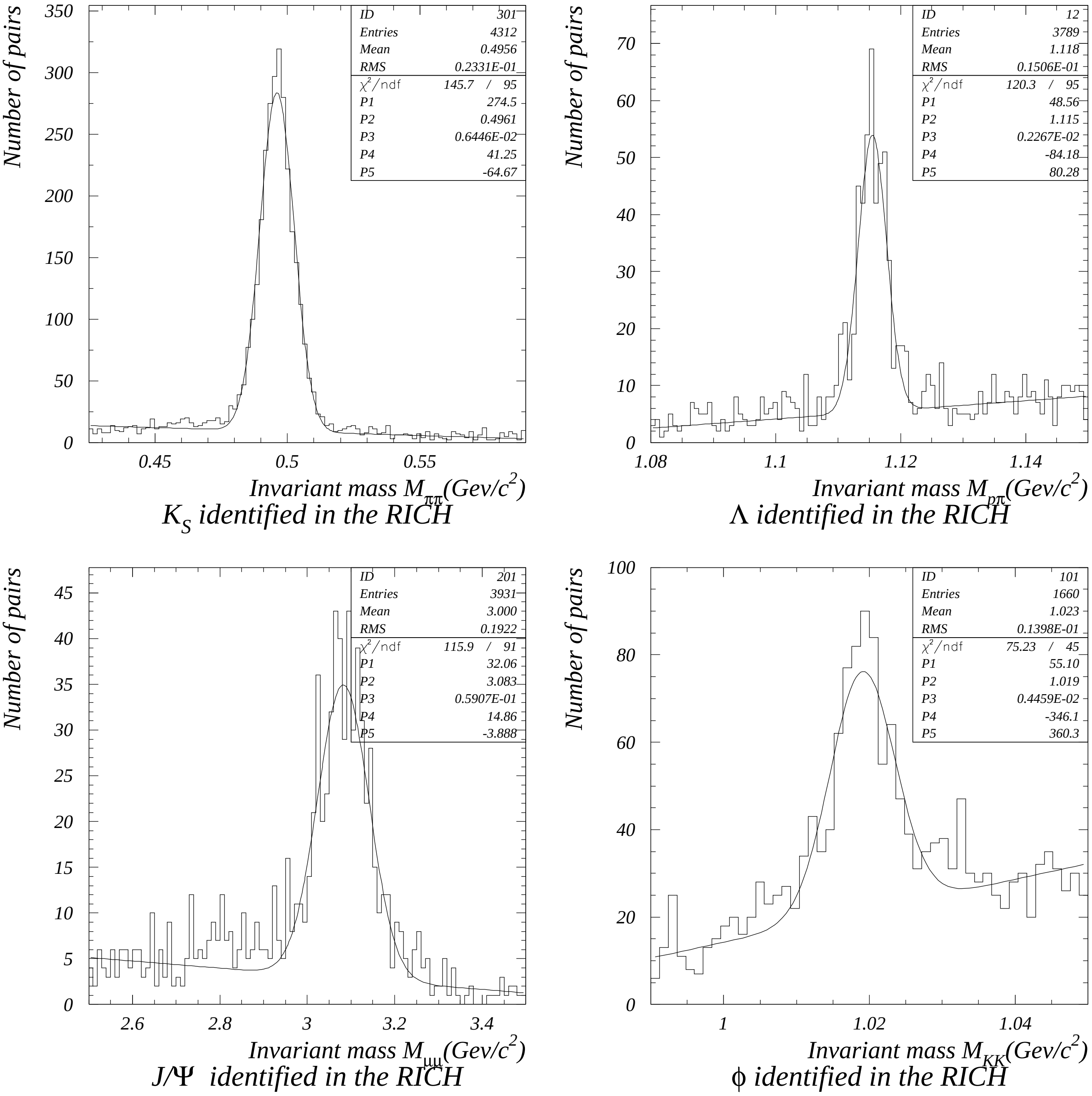

Figure 6.6: Invariant mass distribution of different particles after the RICH identification cuts are applied to the data in Fig. 6.3. Samples correspond to K_S (upper left), Λ (upper right), J/ψ (lower left) and ϕ particles (lower right).

6.3 Efficiency determination

6.3.1 Efficiency as a function of a cut on the likelihood value

To determine the efficiency of identifying a pion from the K_S decay as a pion, the following method was used. First a histogram was filled with invariant mass tracks with a cut on the pion likelihood of the first particle. To increase the statistics and to determine the mean efficiency the same histogram was filled with the same likelihood cut on the second particle. The reference histogram was filled in parallel without any likelihood cuts. For both cases the track was required to be within the RICH geometrical acceptance.

Both histograms were then fitted with a sum of a Gaussian and a linear function, and the number of entries in the K_S peak was determined (Fig. 6.7, left). The efficiency for a given likelihood cut was then calculated as the ratio of entries in the peak,

$$\varepsilon = N_{cut}/N_{reference} \ . \tag{6.2}$$

In parallel, the fake efficiency, i.e. efficiency of identifying a pion from K_S decay as a kaon (proton) was calculated. A kaon (proton) hypothesis was accepted if the kaon (proton) likelihood exceeded the given likelihood cut (Fig. 6.7, right). A similar procedure was used for calculating likelihood cut dependence of the identification efficiency for pions and protons from Λ decays, for muons from J/ψ and for kaons from ϕ.

Note that the HERA-B RICH detector is not a device to distinguish well between electrons, muon and pions over large momentum regions, therefore it is meaningful to construct a combined likelihood λ^{sum} which is a sum of electron, muon and pion likelihoods

$$\lambda^{sum} = \lambda^{e} + \lambda^{\mu} + \lambda^{\pi} \ . \tag{6.3}$$

In this way electrons, muons and pions are identified as the same light particle. This can be accepted, since they are separated in other subsystems.

The resulting identification efficiency for pions from K_S decay is shown in Fig. 6.8. Note that there is a significant drop of misidentification probability at a kaon likelihood cut one third. Since in the kinematic region below kaon threshold, proton, kaon and background likelihoods have the same value (1/3), the above observation leads to the conclusion that K_S pions were misidentified as background. This implies that the track candidate points in the wrong direction by several mradians, and the Cherenkov peak in the Cherenkov angle distribution is smeared out (Fig. 5.7 and Fig. 5.8). This, in turn, could happen either because of errors in alignment or, if the wrong combination of hits in the tracking chambers is chosen in the track finding step. This problem will be further discussed in the next subsection. If ghost tracks are introduced during the reconstruction, their sub-threshold kaon likelihoods are around one third, resulting in a high misidentification efficiency. The misidentified tracks without real physical significance have no meaning. They just spoil the measurements which should consist of physical tracks. Correspondingly, a major part of high misidentification efficiency is a tracking inefficiency.

From Fig. 6.8 it can be seen that around 20% of pions have a kaon likelihood one third, i.e. the particle algorithm recognize them as background in the momentum region from 5 GeV/c to 10 GeV/c, where the likelihood probability is equaly shared between a kaon, a proton and a background hypotheses. This can be assigned to the imperfect pattern recognition and imperfect alignment. The question is further discussed in the next subsection, where some examples are shown.

The identification efficiency for pions from K_S as a function of likelihood cut is shown in Fig. 6.8, for pions from Λ in Fig. 6.3.1, for muons from J/ψ in Fig. 6.3.1, for kaons from ϕ and for protons from Λ in Fig. 6.3.1.

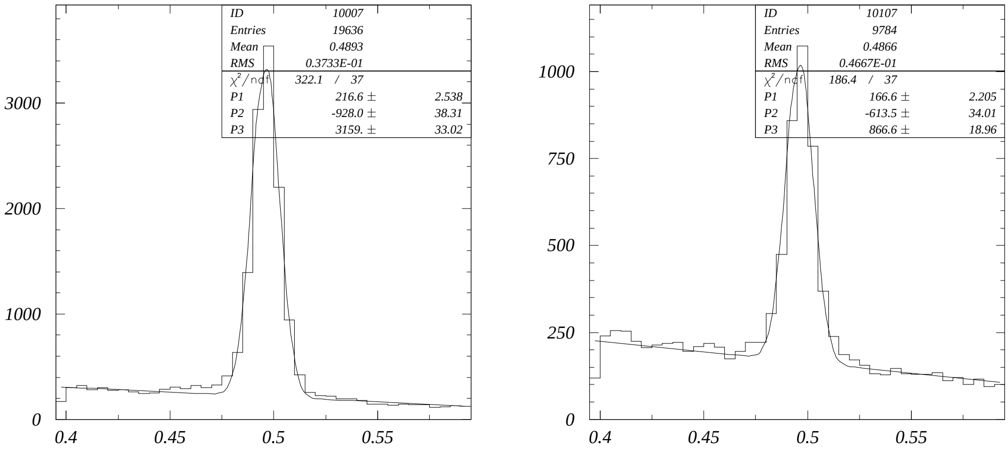

signal cut=0.3 *fake cut=0.3*

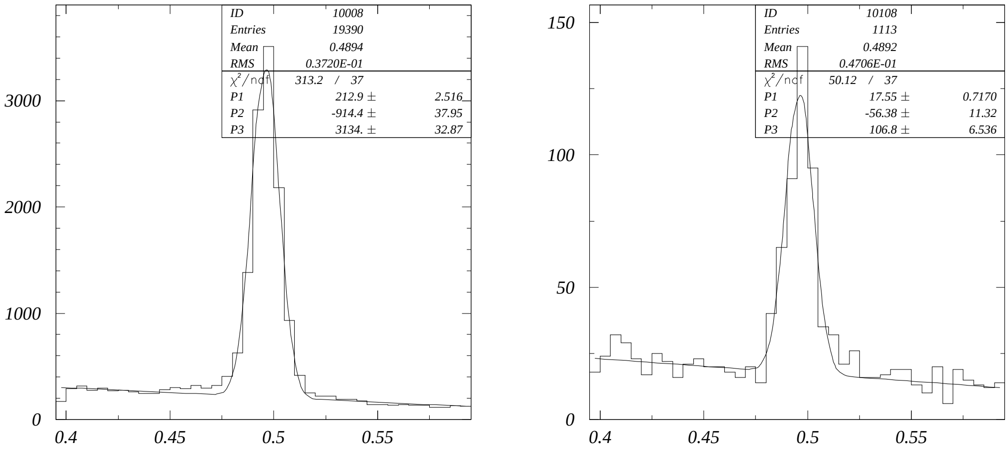

signal cut=0.35 *fake cut=0.35*

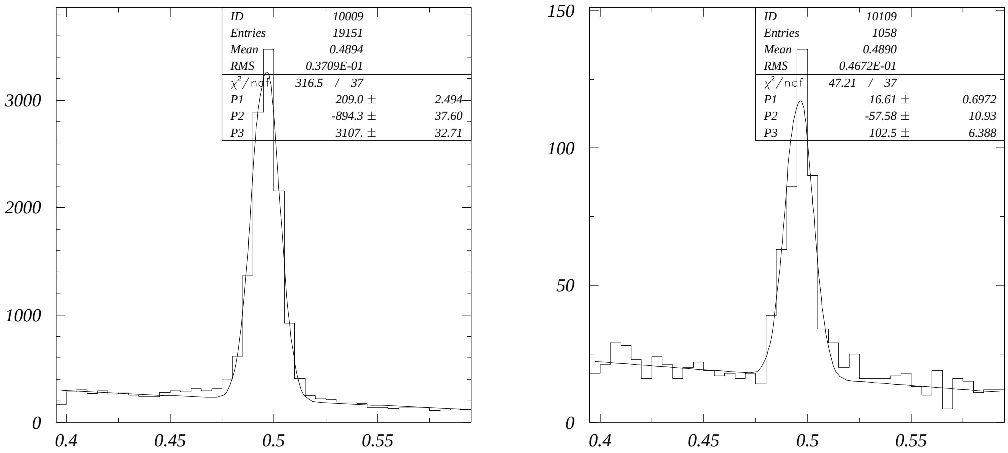

signal cut=0.4 *fake cut=0.4*

Figure 6.7: The method for efficiency calculation: Number of pairs in the invariant mass peak with likelihood pion cut imposed on one of the particles (left column) and number of pairs in the invariant mass peak with likelihood kaon cut imposed on one of the particles (right column) is compared to the number of pairs on the plot without any likelihood cut applied. Different rows correspond to different likelihood cuts.

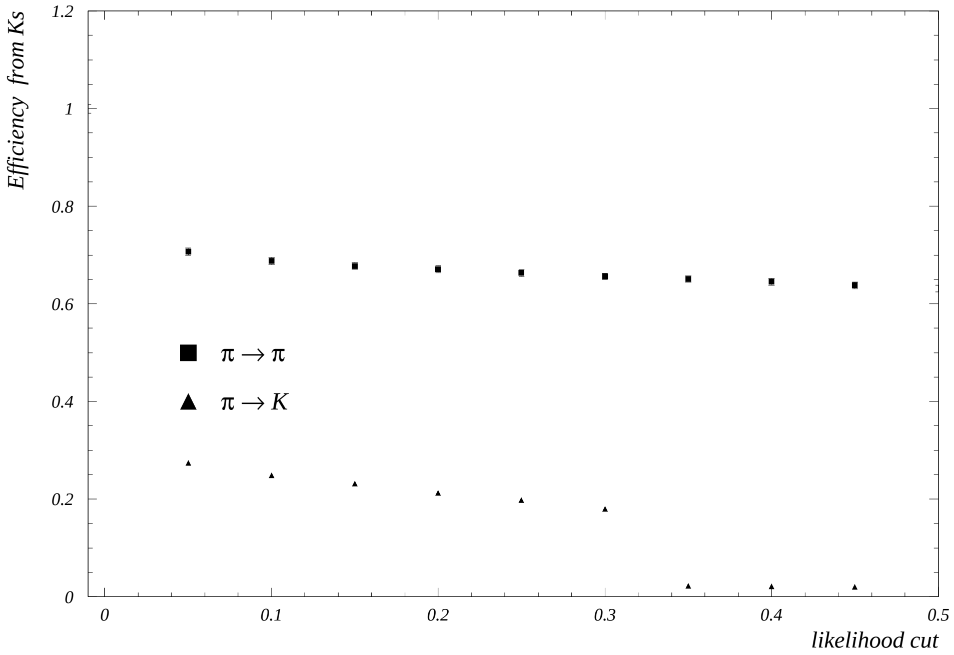

Figure 6.8: Pion identification efficiency from K_S: the efficiency of identifying a pion as a pion (squares) and misidentification probability of identifying a pion from K_S as a kaon (triangles).A pion is identified as a pion if the sum of the likelihoods λ^{sum} exceeds a given likelihood cut. A pion is identified as a kaon if the kaon likelihood exceeds a given likelihood cut. Data sample: single lepton triggered runs.

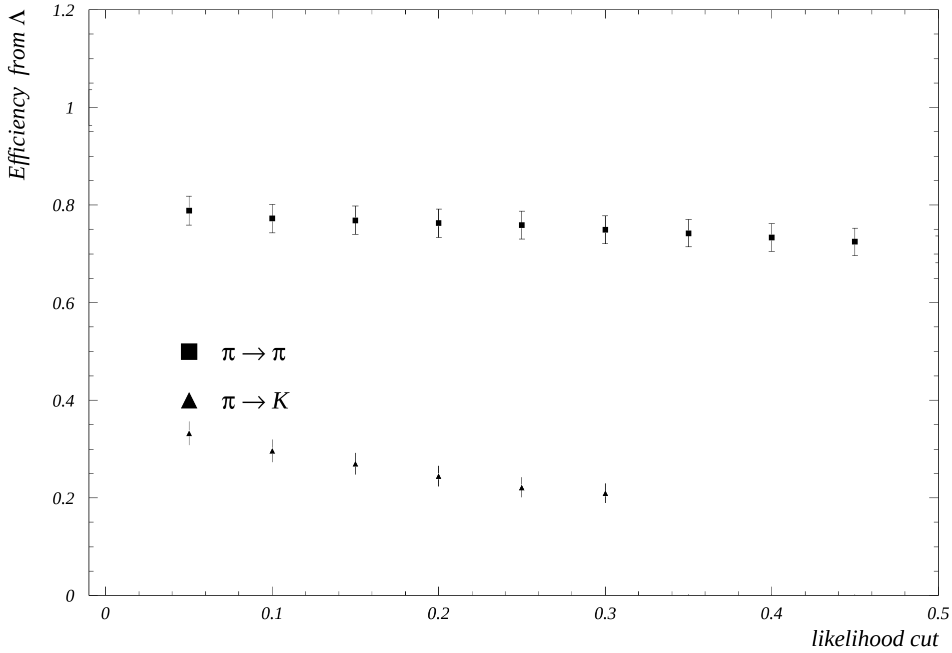

Figure 6.9: Pion identification efficiency from Λ: the efficiency of identifying a pion as a pion (squares) and misidentification probability of identifying a pion from Λ as a kaon (triangles). A pion is identified as a pion if the sum of the likelihoods λ^{sum} exceeds a given likelihood cut. A pion is identified as a kaon if the kaon likelihood exceeds a given likelihood cut. Data sample: single lepton triggered runs.

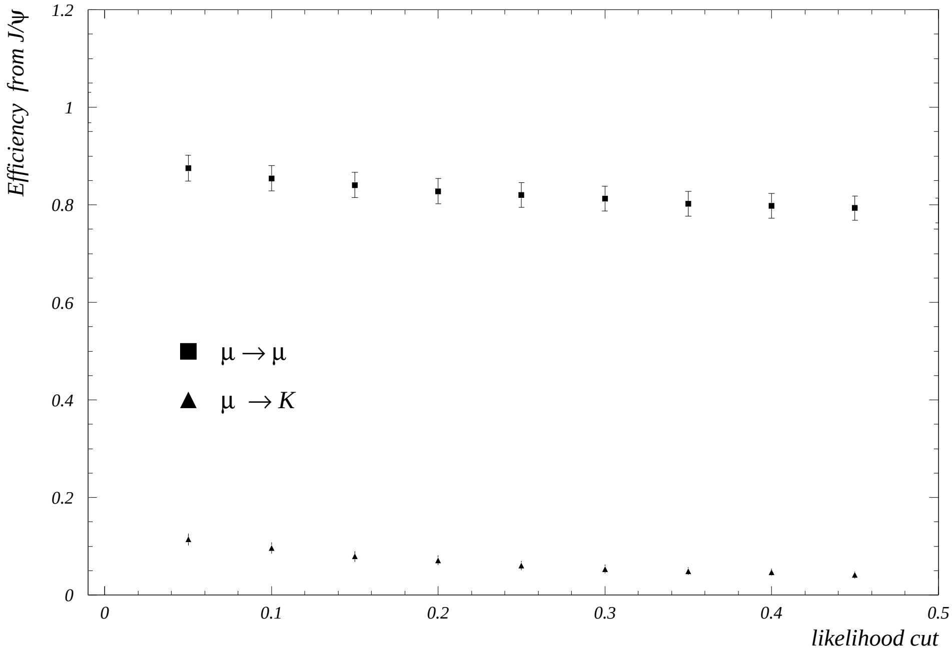

Figure 6.10: Muon identification efficiency from J/ψ: the efficiency of identifying a muon as a muon (squares) and misidentification probability of identifying a muon as a kaon (triangles). A muon is identified as a muon if the sum of the likelihoods λ^{sum} exceeds a given likelihood cut. A muon is identified as a kaon if its likelihood for a kaon exceeds a given likelihood cut. Data sample: muon hard selection from dilepton triggered runs.

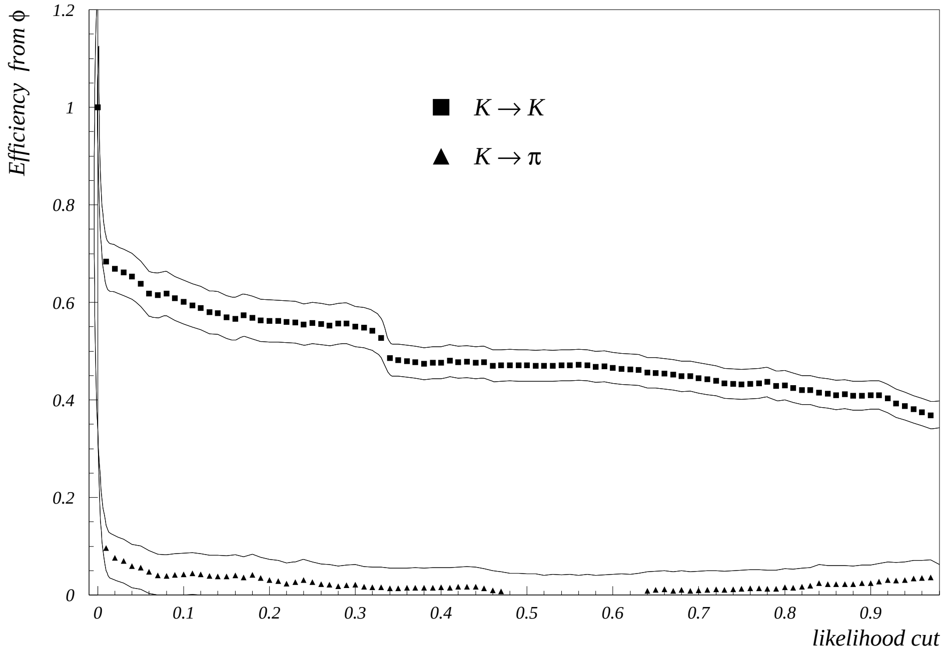

Figure 6.11: Kaon identification efficiency from ϕ: the efficiency of identifying a pion as a pion (squares) and misidentification probability of identifying a kaon from ϕ as a pion (triangles). A kaon is identified as a kaon if the likelihood for kaon exceeds a given likelihood cut. A kaon is identified as a pion if the sum of the likelihoods for λ^{sum} exceeds a given likelihood cut. Data sample: single lepton triggered runs.

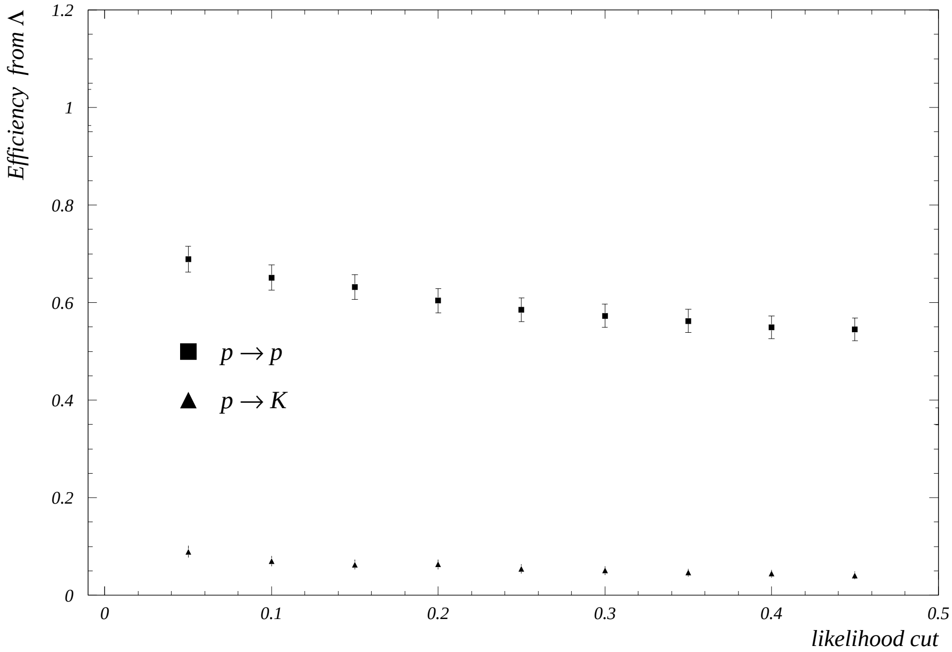

Figure 6.12: Proton identification efficiency from Λ: the efficiency of identifying a proton as proton (squares) and misidentification probability of identifying a proton from Λ as a kaon (triangles). A proton is identified as a proton if its likelihood for a proton exceeds a given likelihood cut. A proton is identified as a kaon if its likelihood for kaon exceeds a given likelihood cut. Data sample: single lepton triggered runs.

6.3.2 Efficiency as a function of momentum

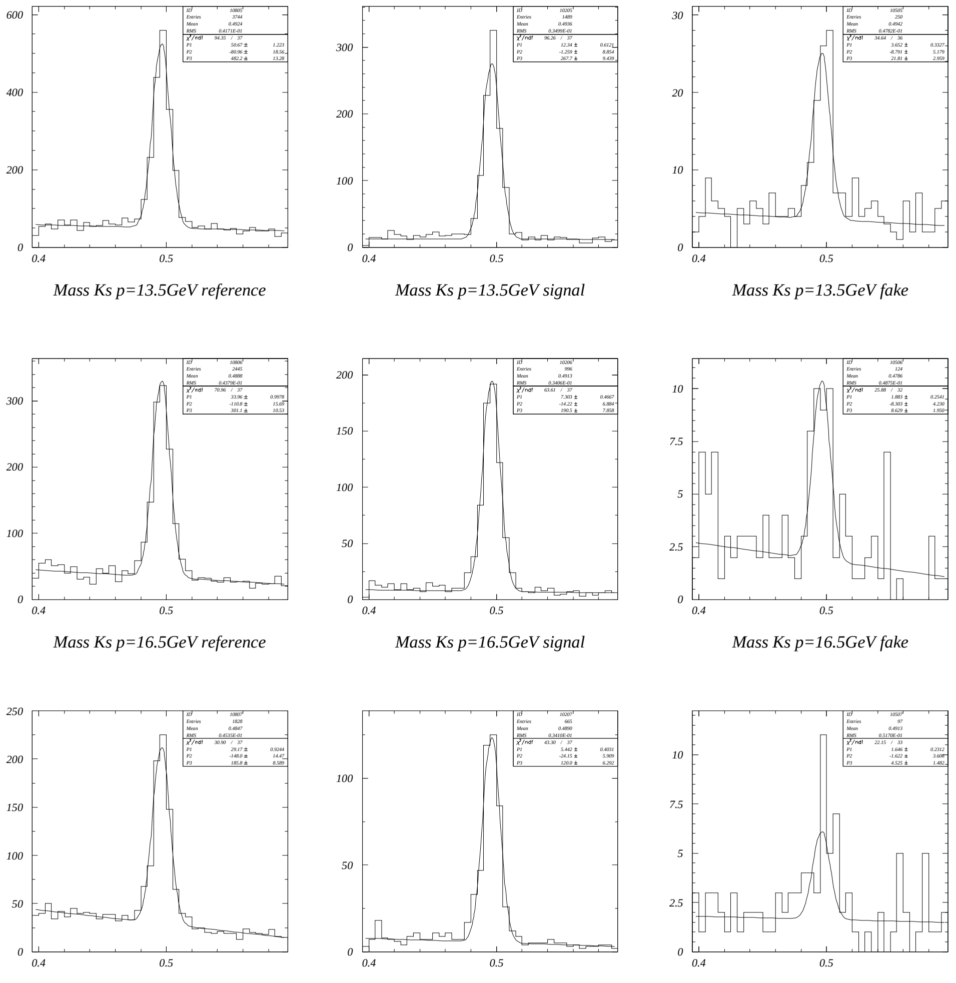

Mass Ks p=13.5GeV reference
Mass Ks p=13.5GeV signal
Mass Ks p=13.5GeV fake
Mass Ks p=16.5GeV reference
Mass Ks p=16.5GeV signal
Mass Ks p=16.5GeV fake
Mass Ks p=19.5GeV reference
Mass Ks p=19.5GeV signal
Mass Ks p=19.5GeV fake

Figure 6.13: Method for efficiency calculation: Number of pairs in the invariant mass peak of the reference set (left column) was compared to the number of pairs in the invariant mass plot with likelihood cut imposed on one of the particles (middle column - identified as pion, right column - identified as kaon).Different rows correspond to different momentum intervals.

To determine the momentum dependence of the identification and misidentification efficiency, the following method, analog to the method to calculate efficiency as a function of likelihood cut, was used. First a histogram was filled with invariant mass of both tracks if the momentum of the first particle was within certain momentum region (Fig. 6.3.2). The pion hypothesis was accepted if the combined likelihood λ^{sum} for the first particle exceeded a fixed

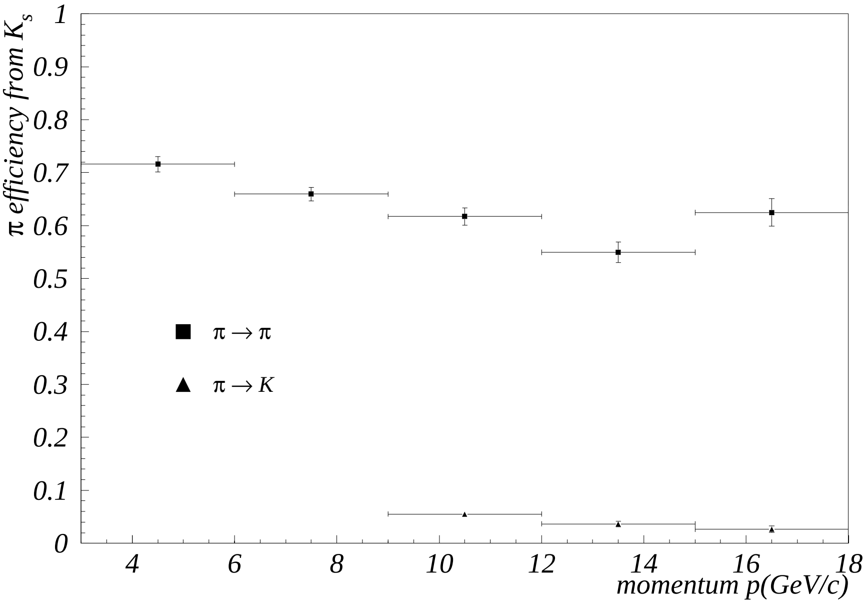

Figure 6.14: Efficiency as a function of momentum at a given likelihood cut 0.35 for π from K_S.

likelihood cut. Then the same histogram was filled with the analog requirements for the second particle. The reference histogram was filled in parallel in both cases without any likelihood cuts.

The resulting efficiency for identifying a pion from K_S at a given likelihood cut ($\lambda^{sum} = \lambda^{\pi} + \lambda^{\mu} + \lambda^{e} \geqslant 0.35$) is shown in Fig. 6.14. The efficiency was checked on several runs and within errors the values are consistent (Fig. 6.15). To increase the statistics we have therefore combined the samples for all efficiency calculations. The results for pions from K_S are shown in Fig. 6.16, for pions from Λ in Fig. 6.17, for muons from J/ψ in the Fig. 6.18, for kaons from ϕ in Fig. 6.19 and for protons from Λ in Fig. 6.20.

For comparison the Monte Carlo generated events were reconstructed with the same reconstruction chain as it was used for the reconstruction of measured events. The geometry assuming the year 2000 status was used for the reconstruction of tracks and particle identification algorithm in the RICH detector was applied. The resulting efficiencies are shown in the same set of histograms as for measured data.

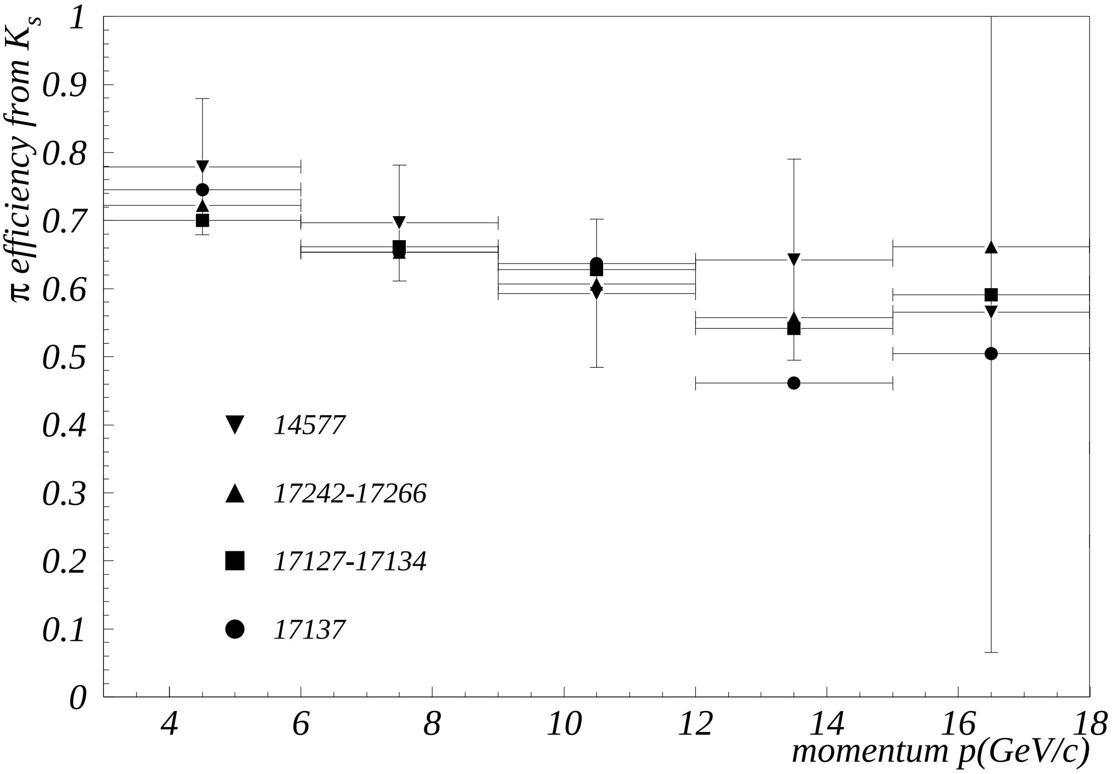

Figure 6.15: Efficiency as a function of momentum at a given likelihood cut 0.35 for π from K_S for different runs.

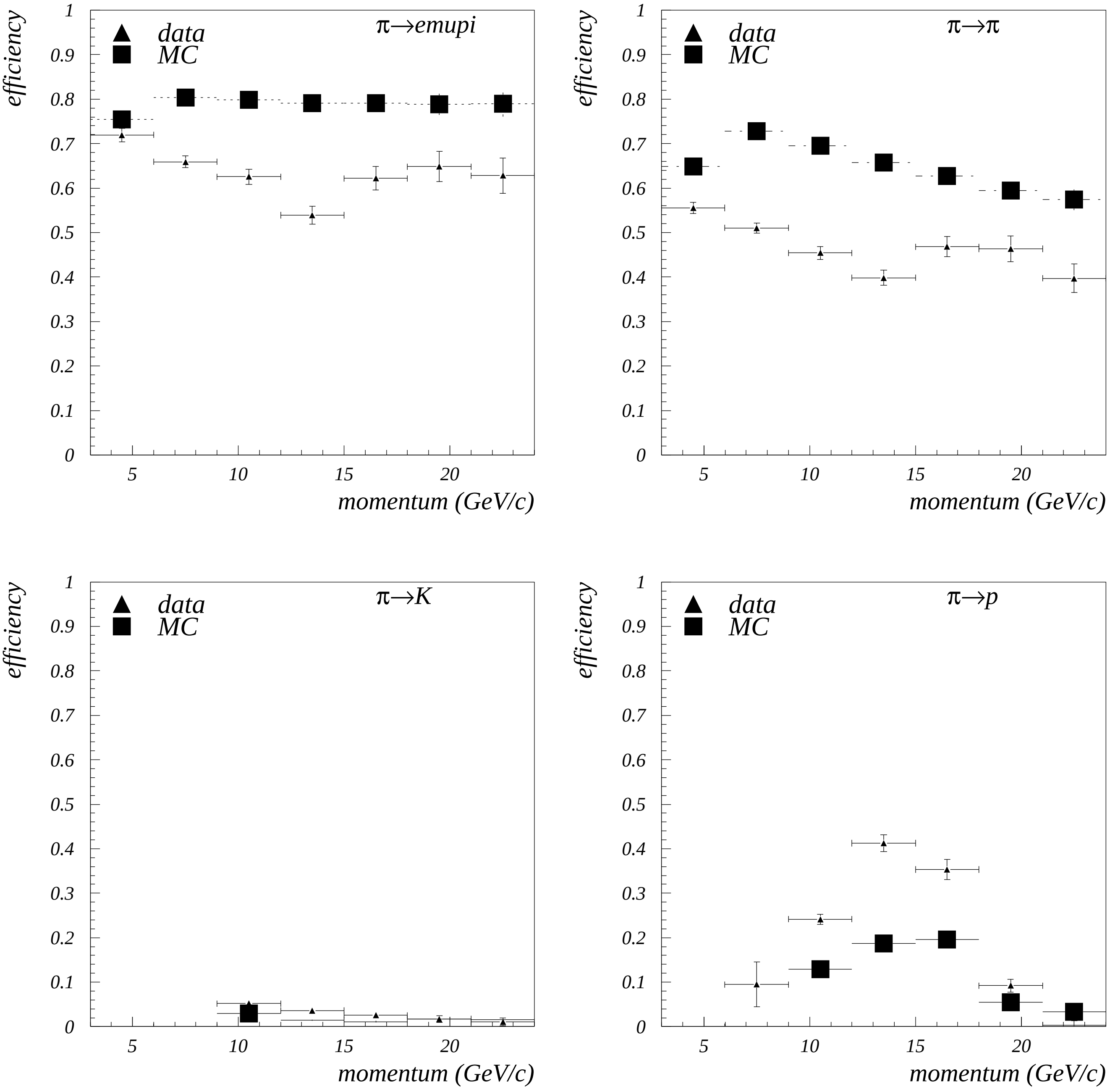

Figure 6.16: Identification efficiency of the RICH for pions from K_S as a function of pion momentum at a given likelihood cut 0.35 .

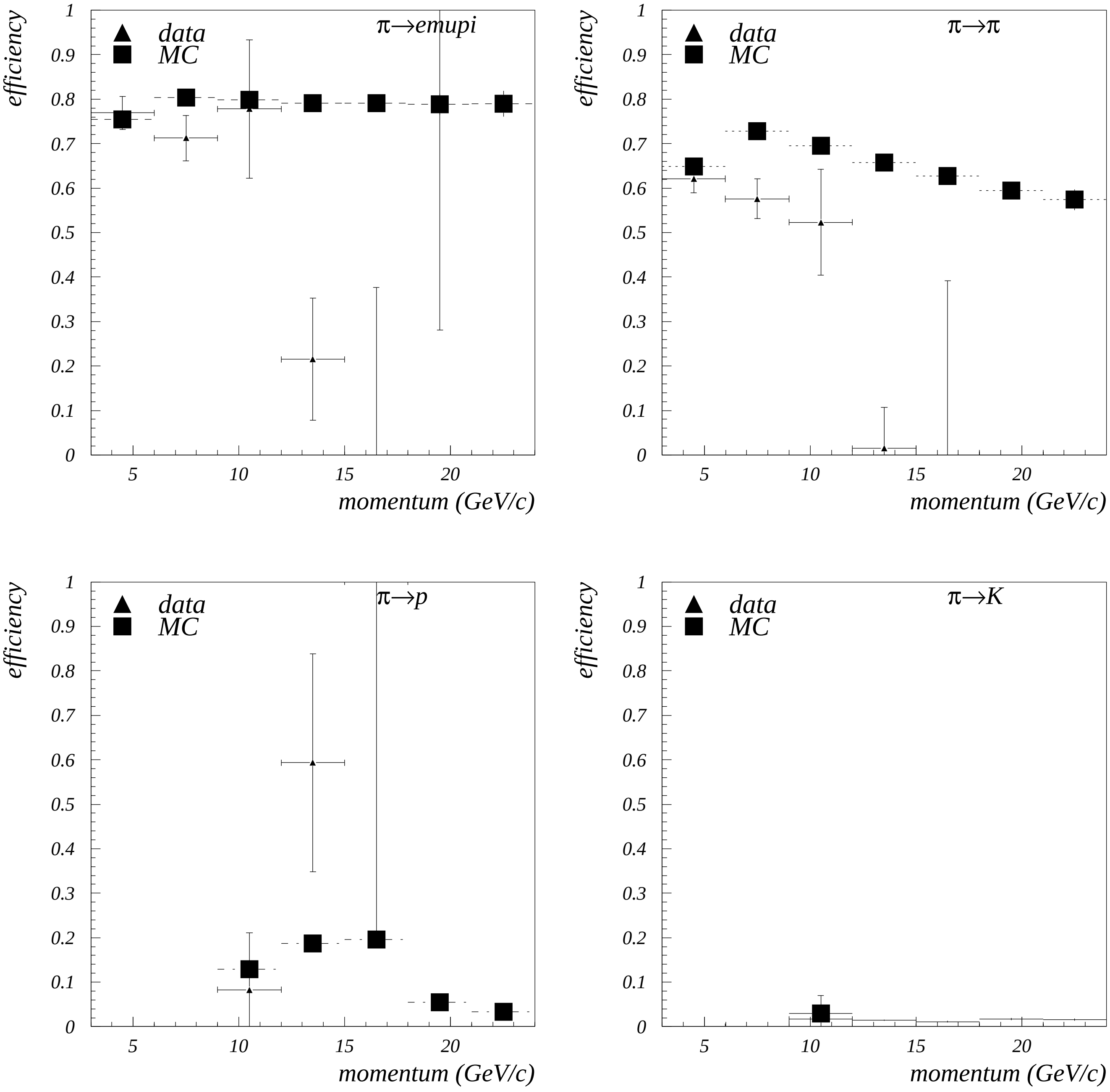

Figure 6.17: Identification efficiency of the RICH for pions from Λ as a function of pion momentum at a given likelihood cut 0.35.

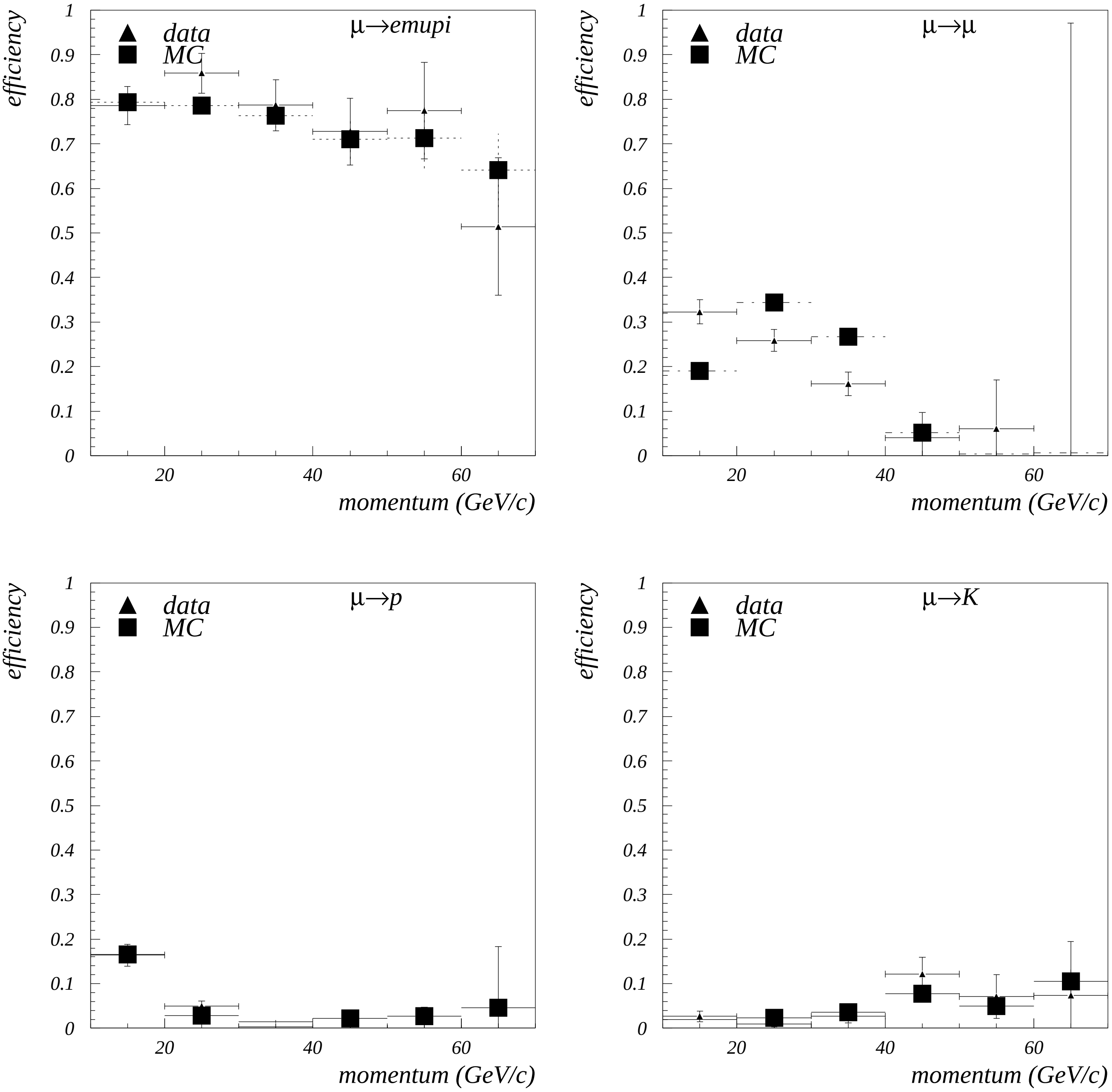

Figure 6.18: Identification efficiency of the RICH for muons from J/ψ as a function of muon momentum at a given likelihood cut 0.35.

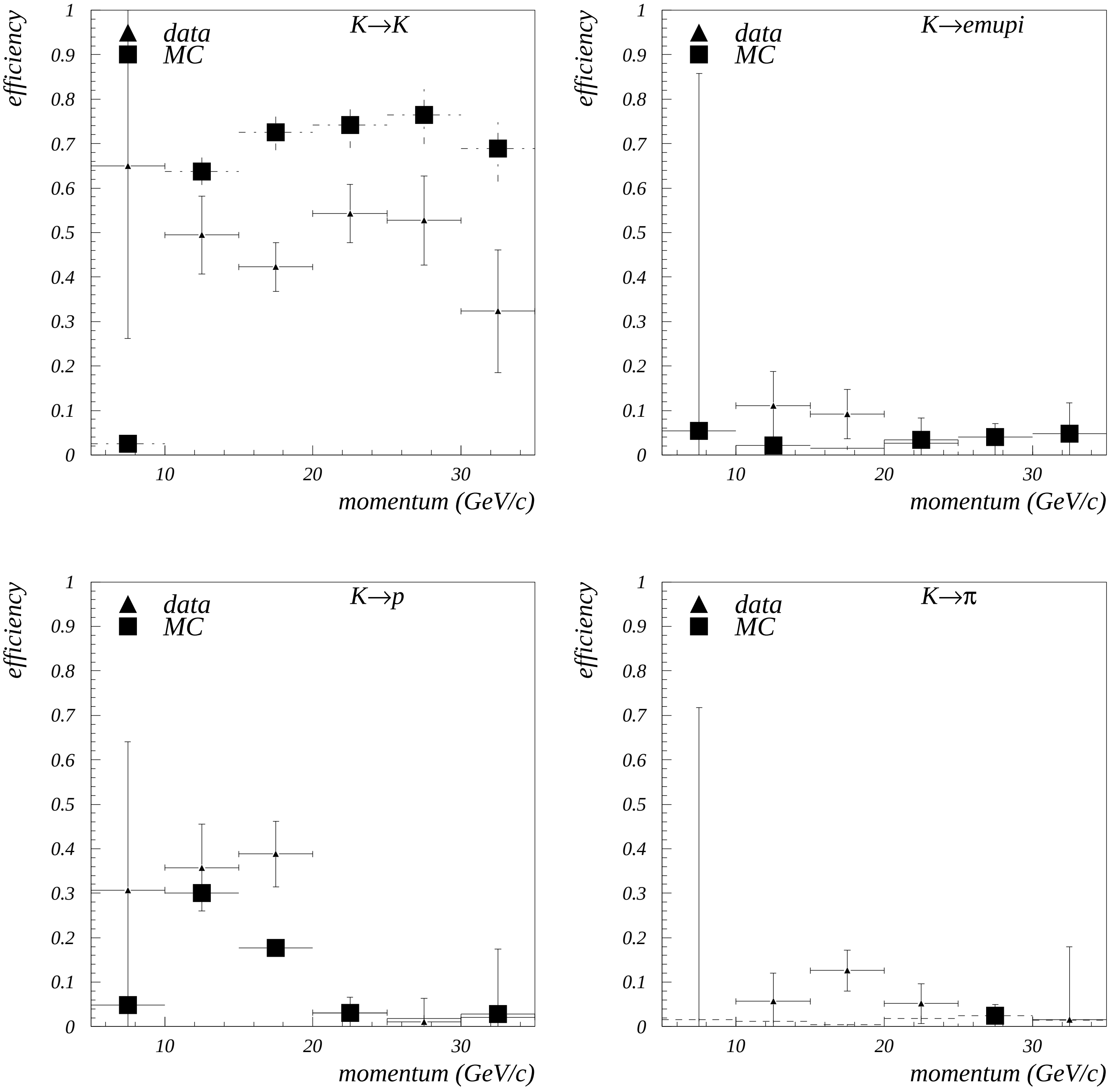

Figure 6.19: Identification efficiency of the RICH for kaons from ϕ as a function of kaon momentum at a given likelihood cut 0.35.

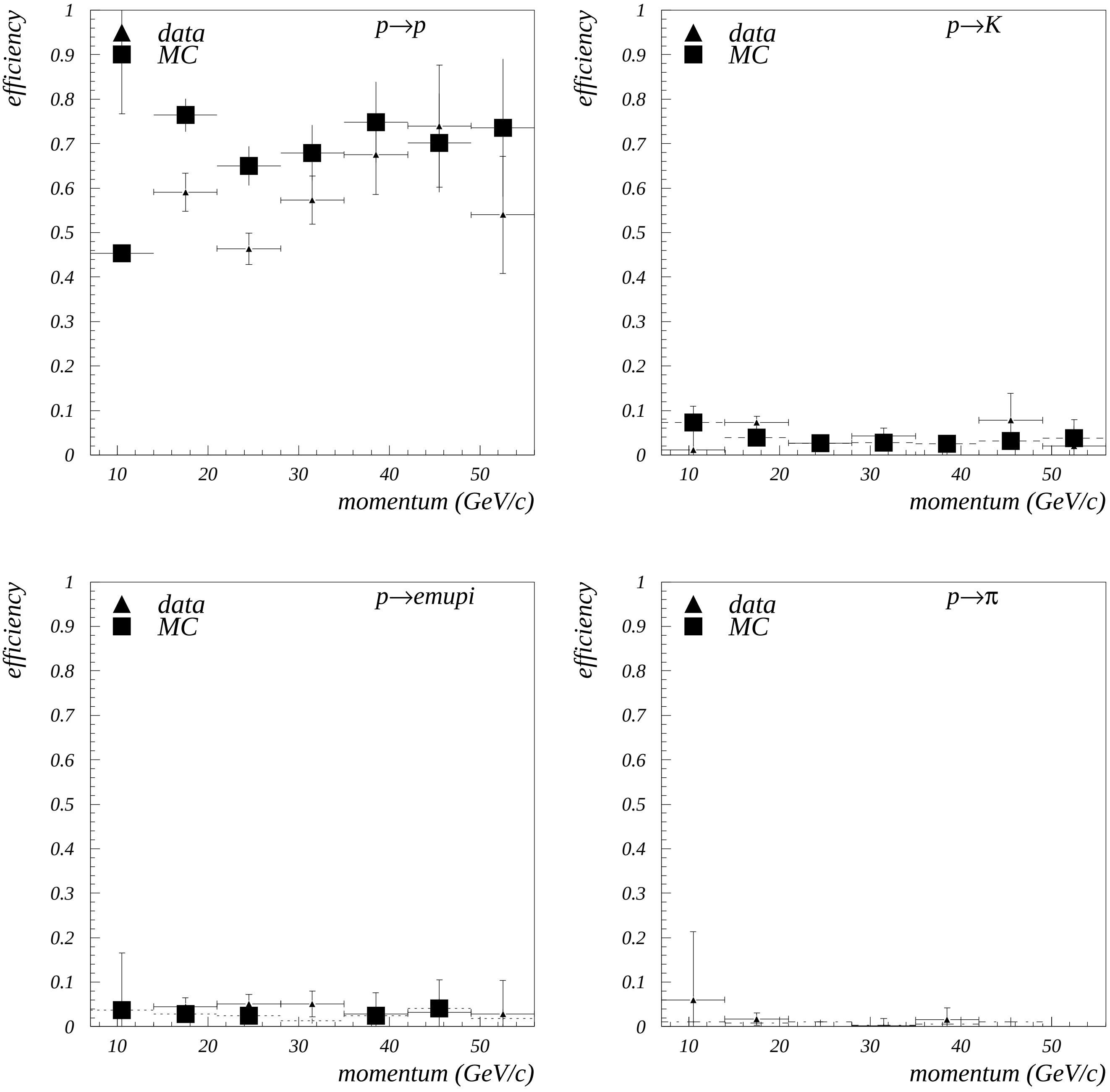

Figure 6.20: Identification efficiency of the RICH for protons from Λ as a function of proton momentum at a given likelihood cut 0.35.

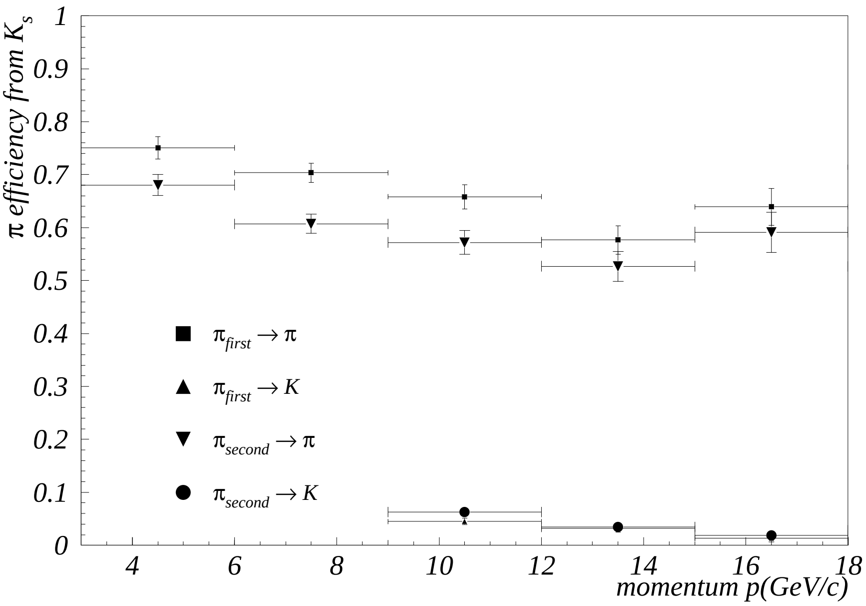

Figure 6.21: Influence of track quality on identification efficiency: efficiency as a function of momentum at a given likelihood cut 0.35 for π from K_S for first (better quality) particle and the second particle in the pair respectively.

As already discussed in the previous subsection, we atributed the lower identification efficiency with respect to the Monte Carlo to the imperfect track recognition and the imperfect alignment. This will be shown in the following examples. We first note that in the analysis the tracks are ordered within the event according to the quality factor Q (Eq. 6.1). This means that when choosing a pair of particles, one first loops over the list for the first particle, and then loops over the remaining list for the second particle. In this way the first particle in the pair has a higher Q value, and thus better determined track parameters. In Fig. 6.21 the effect of the quality of the tracks on the identification in the RICH is shown. Another example of the influence of the track quality on the efficiency could be the difference between pion efficiency as determined from K_S decays and muon efficiency from J/ψ decays (Fig. 6.22). In the later case, however, the influence of different occupancy for the high p_T muons cannot be excluded.

The influence of the track quality can be seen also in the Cherenkov angle distribution histogram (Fig. 6.23). Note that two Gaussian distributions with r.m.s widths of 1.1 mrad and 6.3 mrad, respectively, are needed to describe the peak. The wider of the two distributions can be attributed to the low quality tracks, with wrong direction information. The effect of wrong direction information can also be seen in Fig. 6.24, where the identity of the reconstructed tracks is shown separately for the tracks with well matched and poorly matched vertical (non-bending)

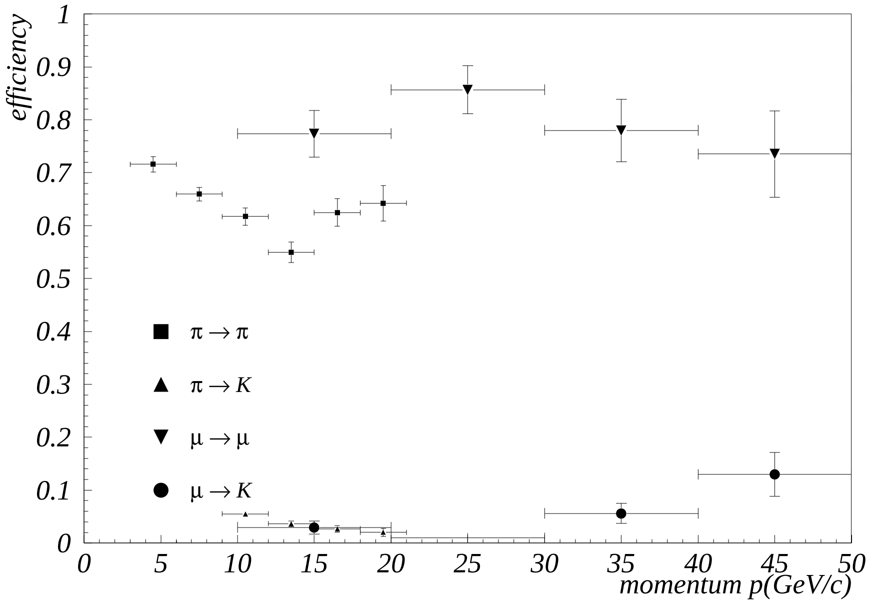

Figure 6.22: Influence of track quality on particle identification efficiency: comparison of well identified muons from the hard selected J/ψ sample and pions from K_S. A similar efficiency is expected in the overlap region.

direction in the vertex detector system and in front of the RICH counter. It is clearly seen, that the poorly constructed tracks are identified as background more often than the well matched ones.

Note also that the reduction of the signal can also be due to a partial misassignment of Cherenkov photon hits to the track candidates to which they do not belong. The detected photons are not fully assigned to one of the tracks but their weights are split between them. While this effect is properly handled in case of real tracks, it becomes significant in presence of clone tracks.

It is expected, the fraction of particles with no ring found will decrease with the improved alignment and with the better track recognition. We note that this improvement is extremly important for identification below threshold. Note that a large fraction of pions and kaons in the HERA-B RICH have momenta below threshold.

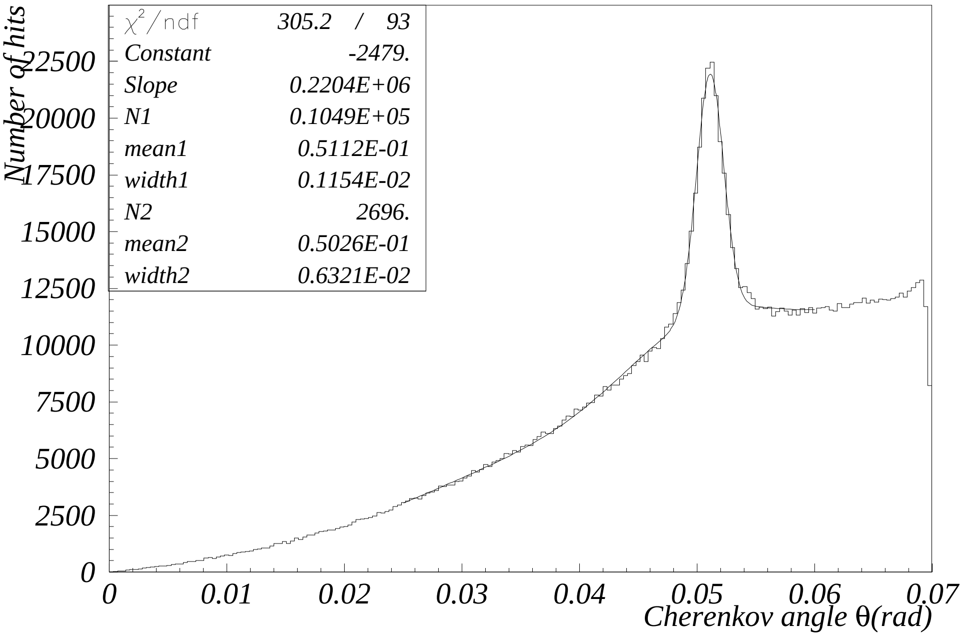

Figure 6.23: Cherenkov angle distribution for particles of momentum greater than 15 GeV/c. Note that two Gaussian distributions with parameters $N1, mean1, width1$ and $N2, mean2, width2$ are needed to describe the peak.

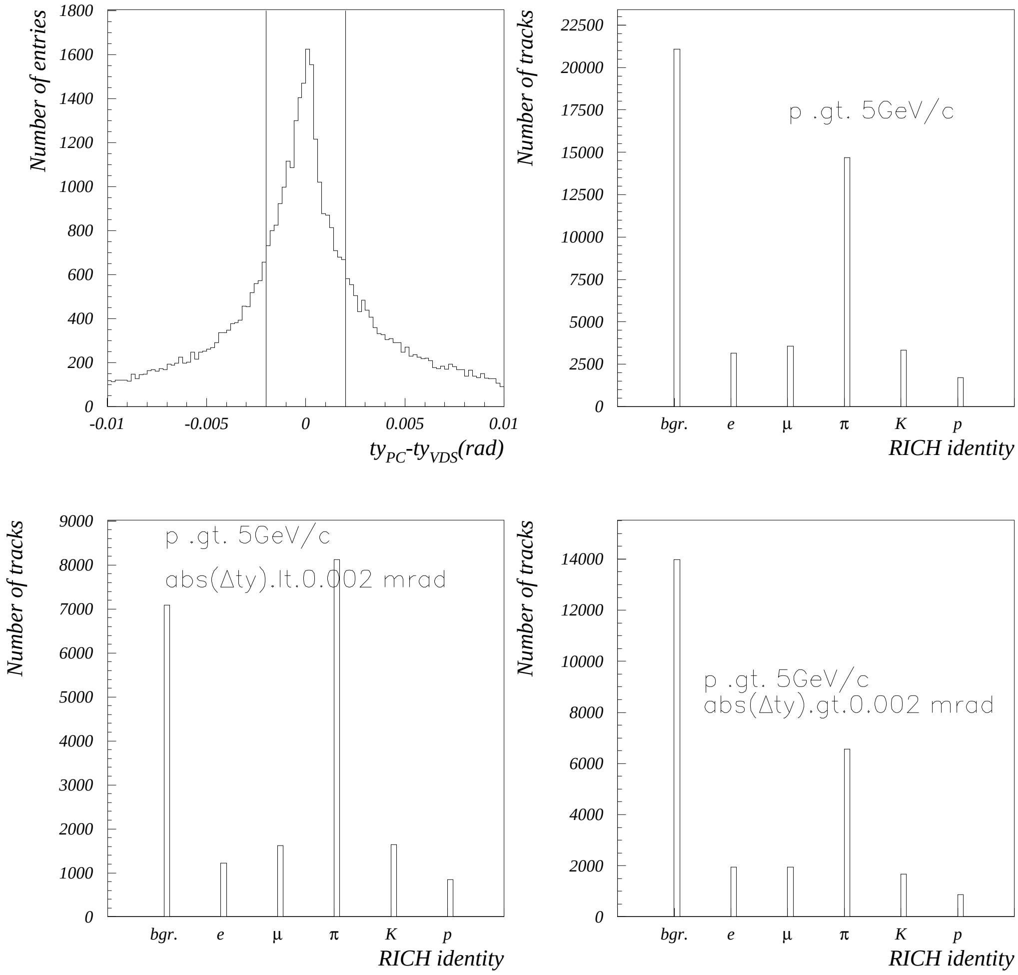

Figure 6.24: Influence of track quality on particle identification efficiency: Difference between the y directions of the reconstructed tracks in front of the RICH (ty_{PC}) and in the vertex detector system (ty_{VDS}) (top left). Distribution of particles of momentum greater than 5 GeV/c as identified in the RICH counter for all particles (top right), particles from the central part of the correlation ($|\delta ty| < 2$ mrad) (bottom left) and from the side bands (bottom right). Particles are identified according to the maximal value of the likelihood.

6.3.3 Efficiency as a function of misidentification probability

In the physics analysis of the data one needs to know what is relation between efficiency versus misidentification probability of the studied tracks. The higher the efficiency, the higher also the misidentification probability. This is represented in two sets of plots showing relations of efficiency versus misidentification probability for different momentum regions. The method for the efficiency determination is similar to the one where the momentum dependence was studied. Instead of keeping the likelihood cut fixed, it is varied from 0 to 1. For each momentum interval and likelihood cut the efficiency and different misidentification probabilities are calculated. The results of the scan are then plotted in different two dimensional plots.

In the first series of plots, the relation between misidentification probability versus efficiency is plotted for different momentum regions. In the each plot the efficiency of identifying a particle id_2, which is identified by other means, as a particle of the type id_2 versus the misidentification efficiency of identifying another particle id_1 as the particle of the type id_2. For the momentum region from 0 GeV/c to 5 GeV/c, where all the particles except electrons, are under threshold, the transition matrix is shown in Fig. 6.25. For the momentum region from 5 GeV/c to 10 GeV/c, where a kaon and a proton are under threshold the transition matrix is shown in Fig. 6.26, for the momentum from 10 GeV/c to 20 GeV/c, where only protons are under threshold, in Fig. 6.27 and above 20 GeV/c in Fig. 6.28.

In Fig. 6.29 the relation between identification efficiency versus misidentification efficiency for pions from K_S are plotted. The similar plots are presented for kaons from ϕ in Fig. 6.33 for pions from Λ in Fig. 6.30, protons from Λ in Fig. 6.31 and muons from J/ψ in Fig. 6.32.

In the next series of plots the same efficiencies are summarized in the plots where the misidentification efficiency of the particle id_1 to be identified as a particle of type id_2 is plotted versus the identification efficiency of that particle to be identified as a particle of type id_1. The results are for momentum ranges from 0 GeV/c to 5 GeV/c in Fig. 6.34, from 5 GeV/c to 10 GeV/c in Fig. 6.35, from 10 GeV/c to 20 GeV/c in Fig. 6.36, and from 20 GeV/c to 200 GeV/c in Fig. 6.37.

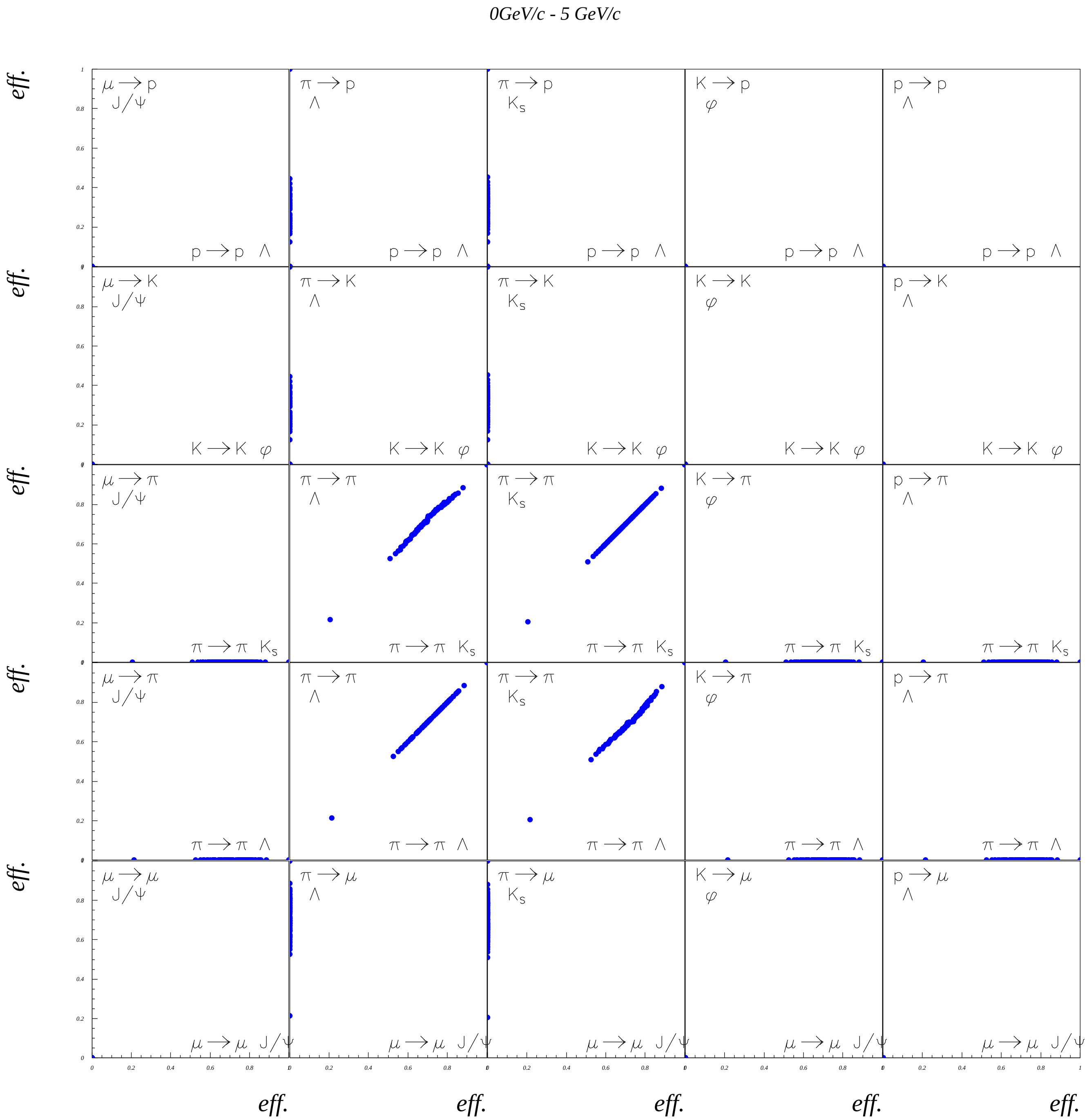

Figure 6.25: Transition matrix $id_1 \rightarrow id_2$ vs. $id_2 \rightarrow id_2$ for momentum range 0 GeV/c-5 GeV/c: Misidentification probability $id_1 \rightarrow id_2$ to identify a particle with the identity id_1 (μ from J/ψ, π from K_S, π from Λ, K from ϕ and p from Λ) as id_2 versus efficiency to identify a particle with the identity id_2 as the particle of identity id_2.

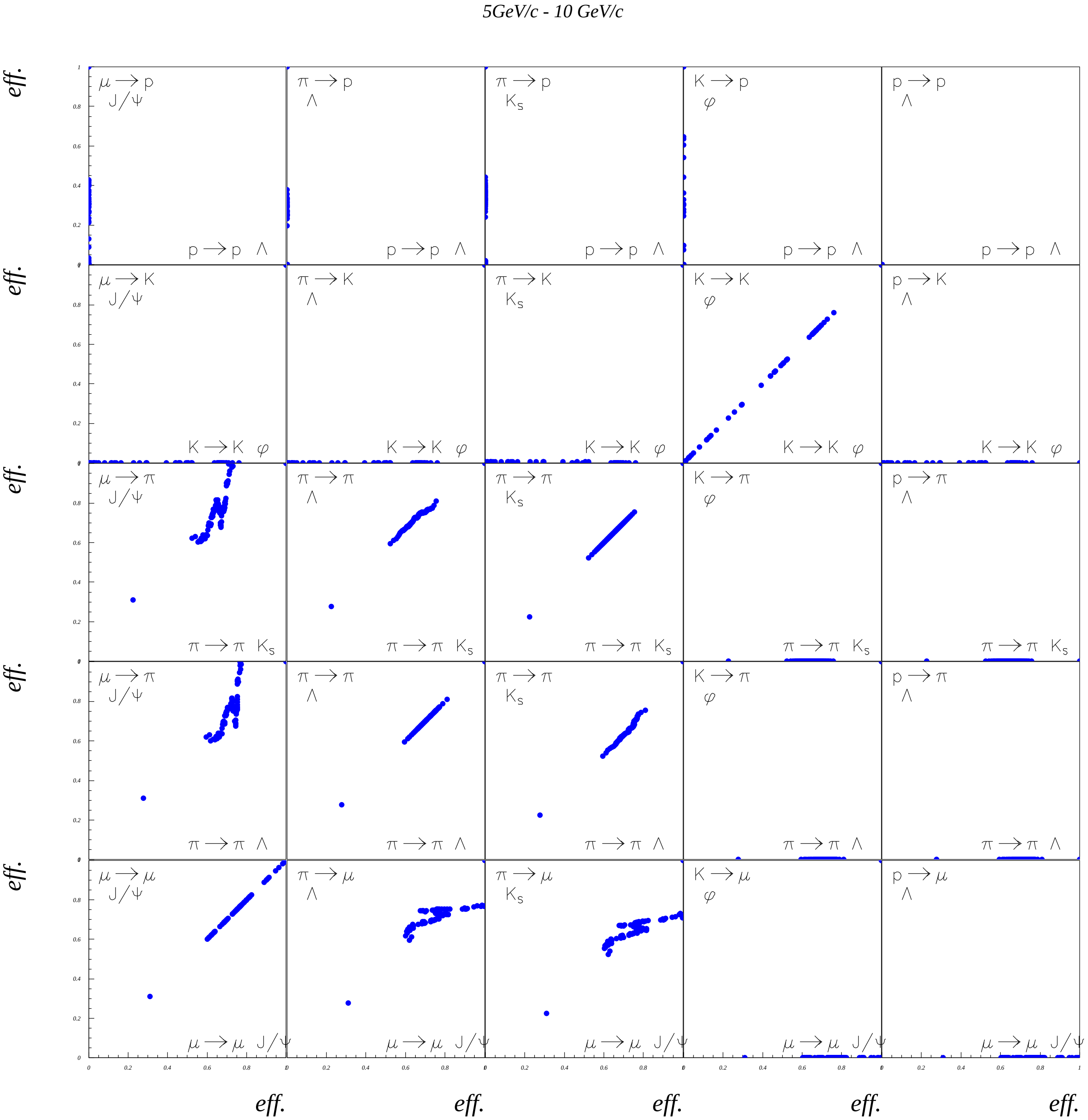

Figure 6.26: Transition matrix $id_1 \rightarrow id_2$ vs. $id_2 \rightarrow id_2$ for momentum range 5 GeV/c-10 GeV/c: Misidentification probability $id_1 \rightarrow id_2$ to identify a particle with the identity id_1 (μ from J/ψ, π from K_S, π from Λ, K from ϕ and p from Λ) as id_2 versus efficiency to identify a particle with the identity id_2 as the particle of identity id_2.

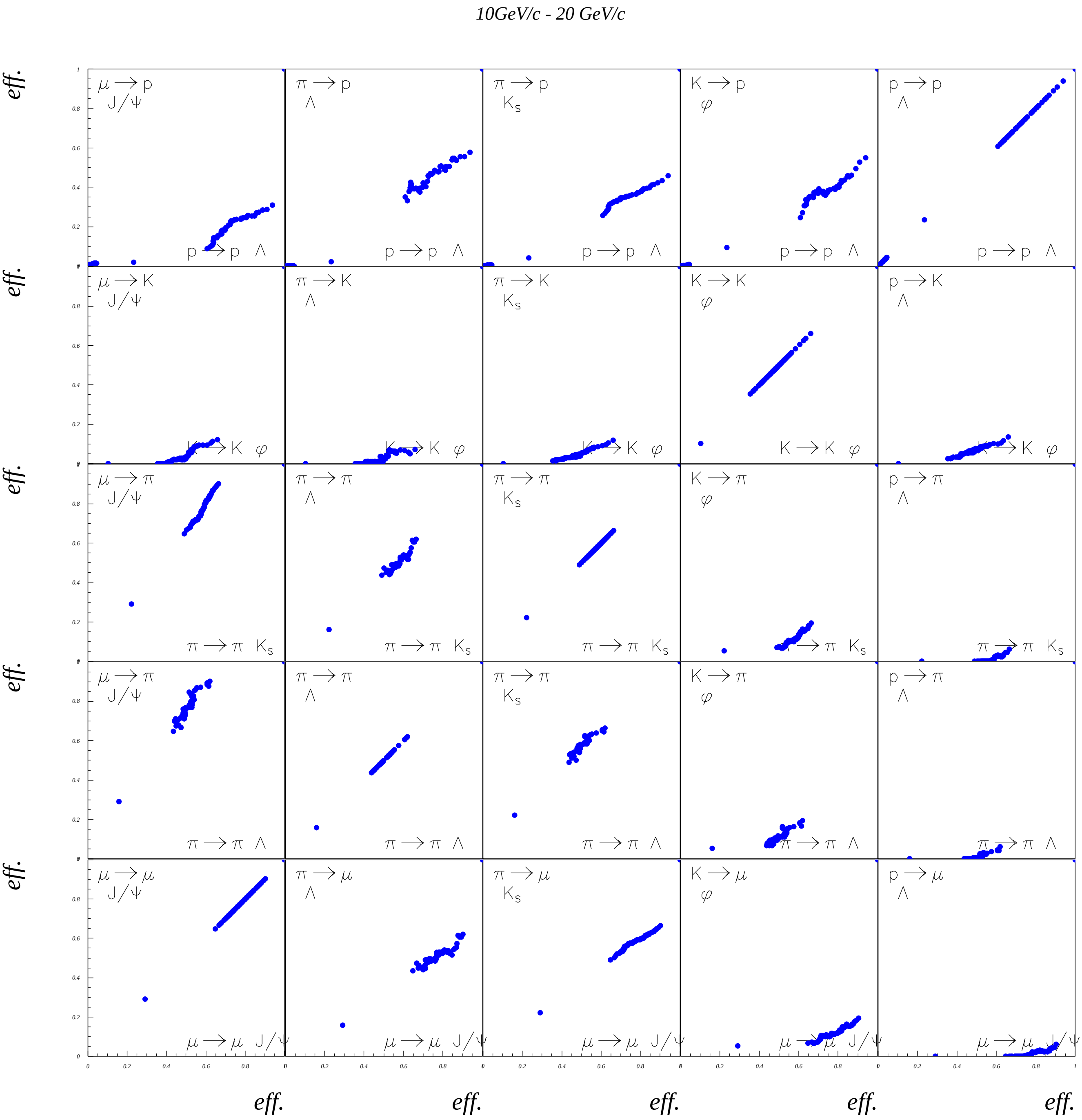

Figure 6.27: Transition matrix $id_1 \rightarrow id_2$ vs. $id_2 \rightarrow id_2$ for momentum range 10 GeV/c-20 GeV/c: Misidentification probability $id_1 \rightarrow id_2$ to identify a particle with the identity id_1 (μ from J/ψ, π from K_S, π from Λ, K from ϕ and p from Λ) as id_2 versus efficiency to identify a particle with the identity id_2 as the particle of identity id_2.

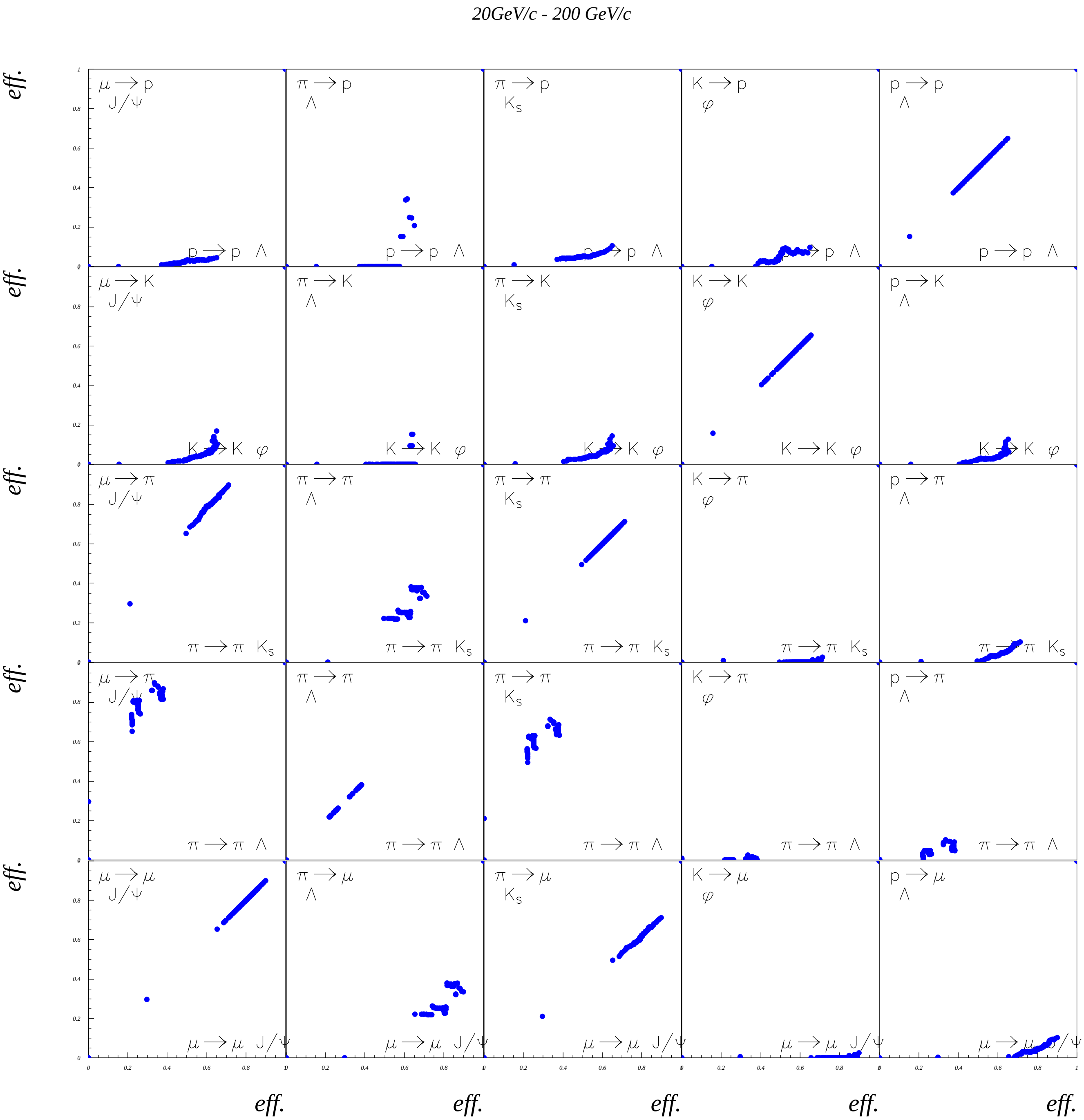

Figure 6.28: Transition matrix $id_1 \to id_2$ vs. $id_2 \to id_2$ for momentum range 20 GeV/c-200 GeV/c: Misidentification probability $id_1 \to id_2$ to identify a particle with the identity id_1 (μ from J/ψ, π from K_S, π from Λ, K from ϕ and p from Λ) as id_2 versus efficiency to identify a particle with the identity id_2 as the particle of identity id_2.

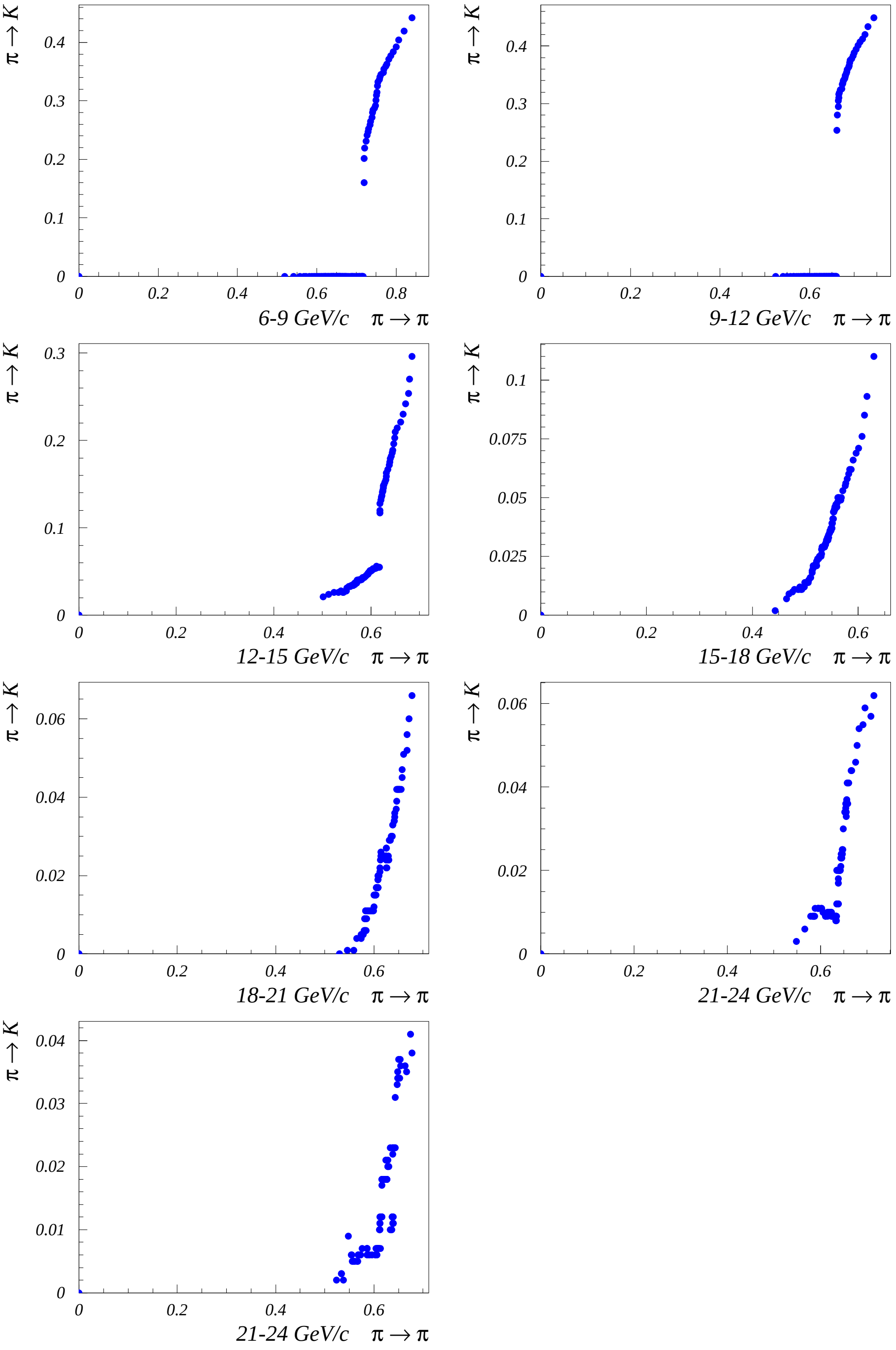

Figure 6.29: Misidentification efficiency vs. identification efficiency of the RICH detector of pions from K_S. Each plot corresponds to different momentum regions which are marked under plots.

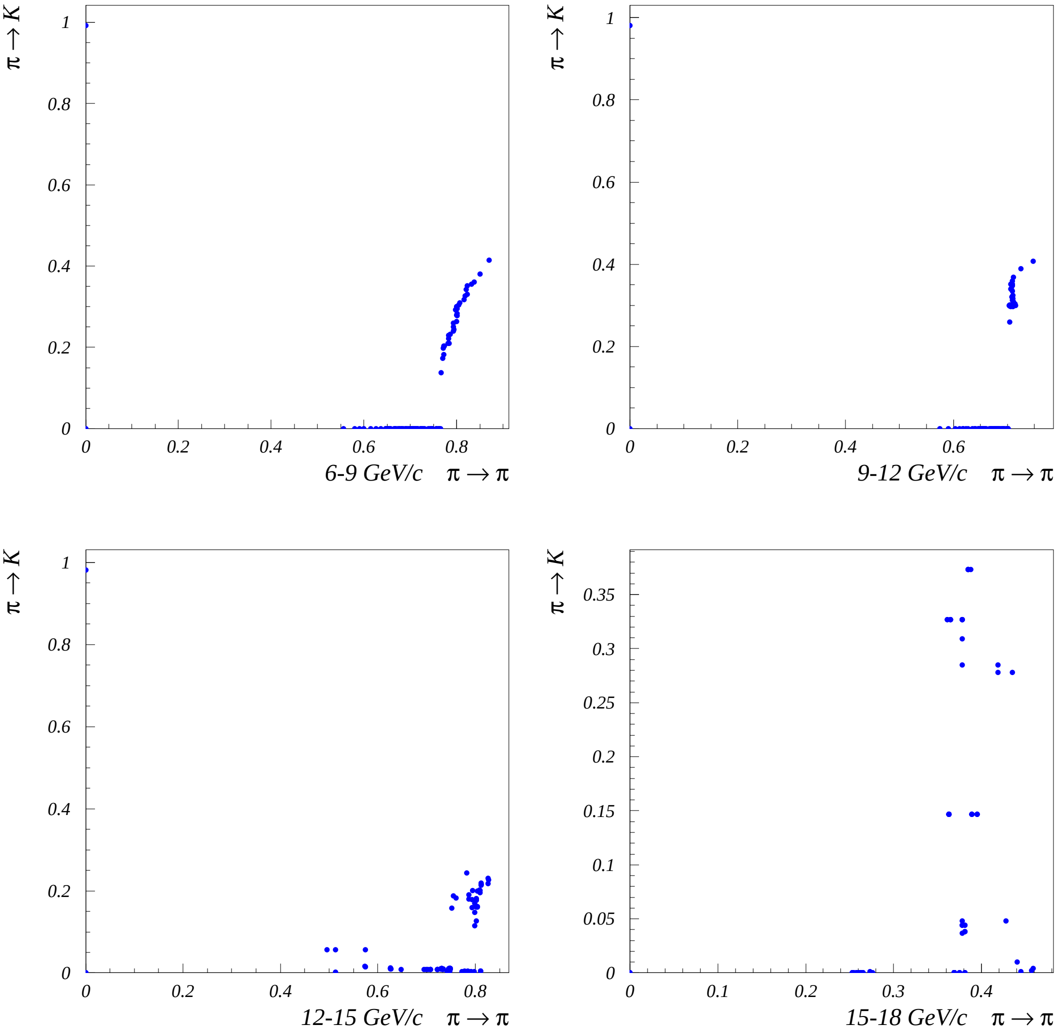

Figure 6.30: Misidentification efficiency vs. identification efficiency of the RICH detector of pions from Λ. Each plot corresponds to different momentum regions which are marked under plots.

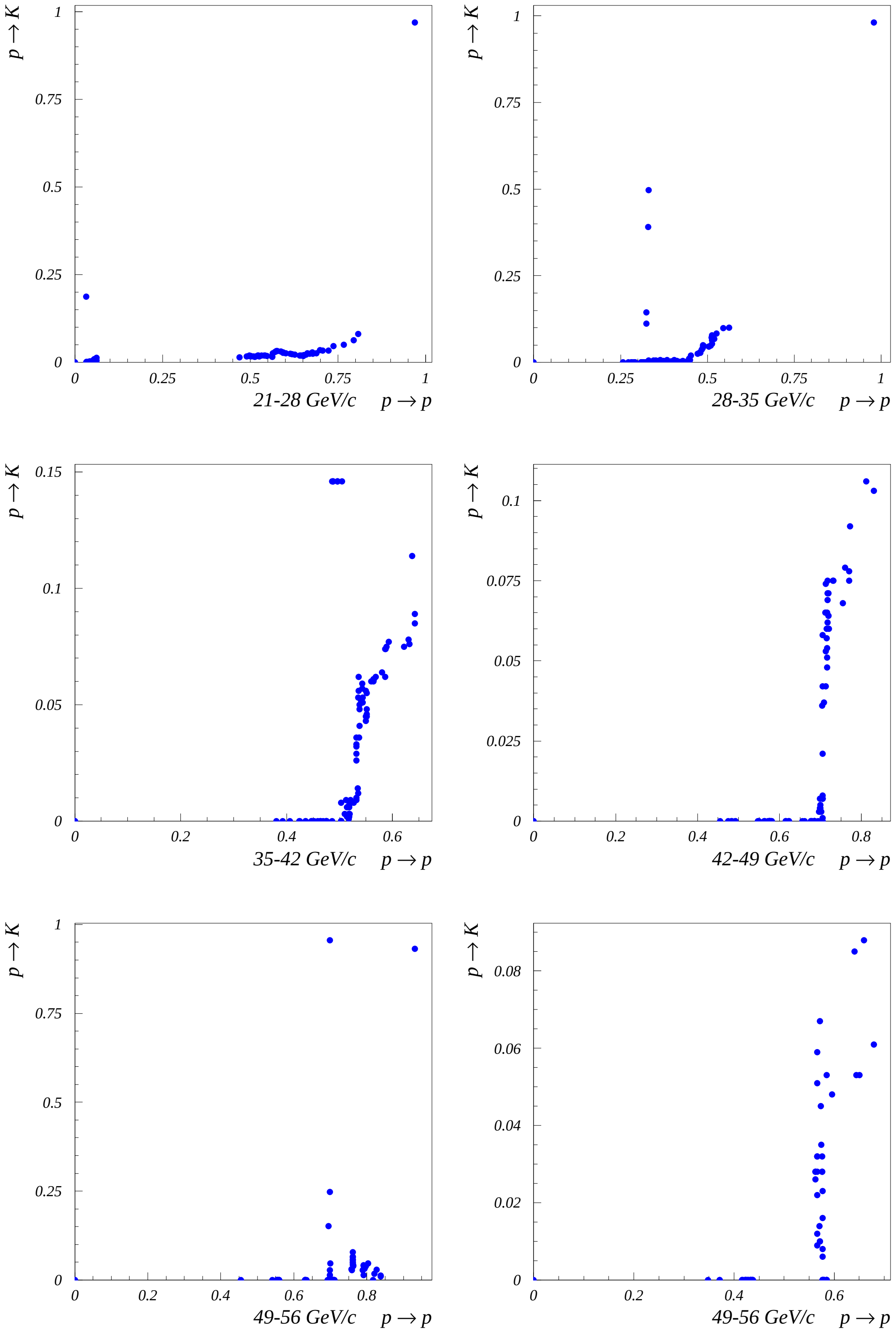

Figure 6.31: Misidentification efficiency vs. identification efficiency of the RICH detector of protons from Λ. Each plot corresponds to different momentum regions which are marked under plots.

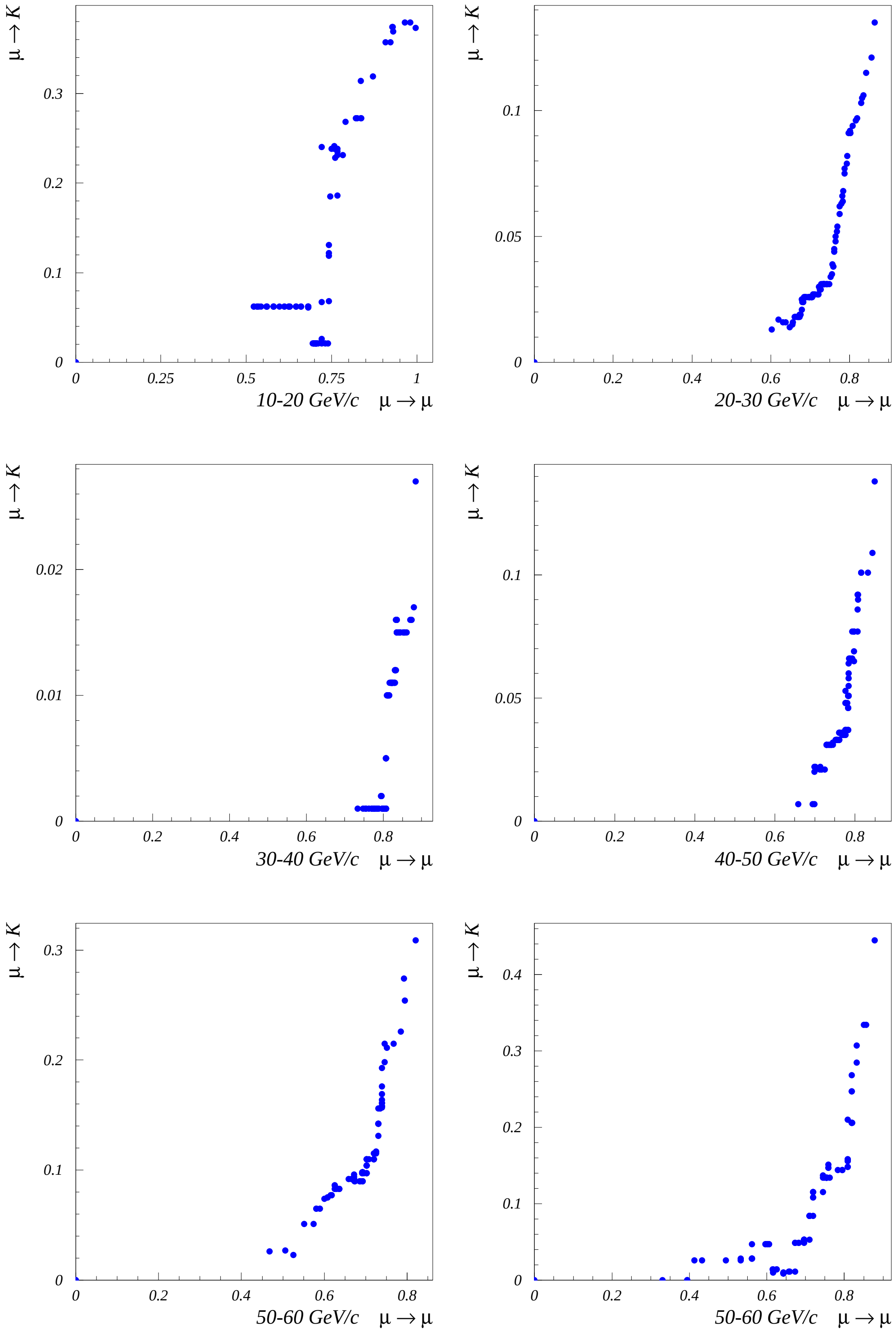

Figure 6.32: Misidentification efficiency vs. identification efficiency of the RICH detector of muons from J/ψ. Each plot corresponds to different momentum regions which are marked under plots.

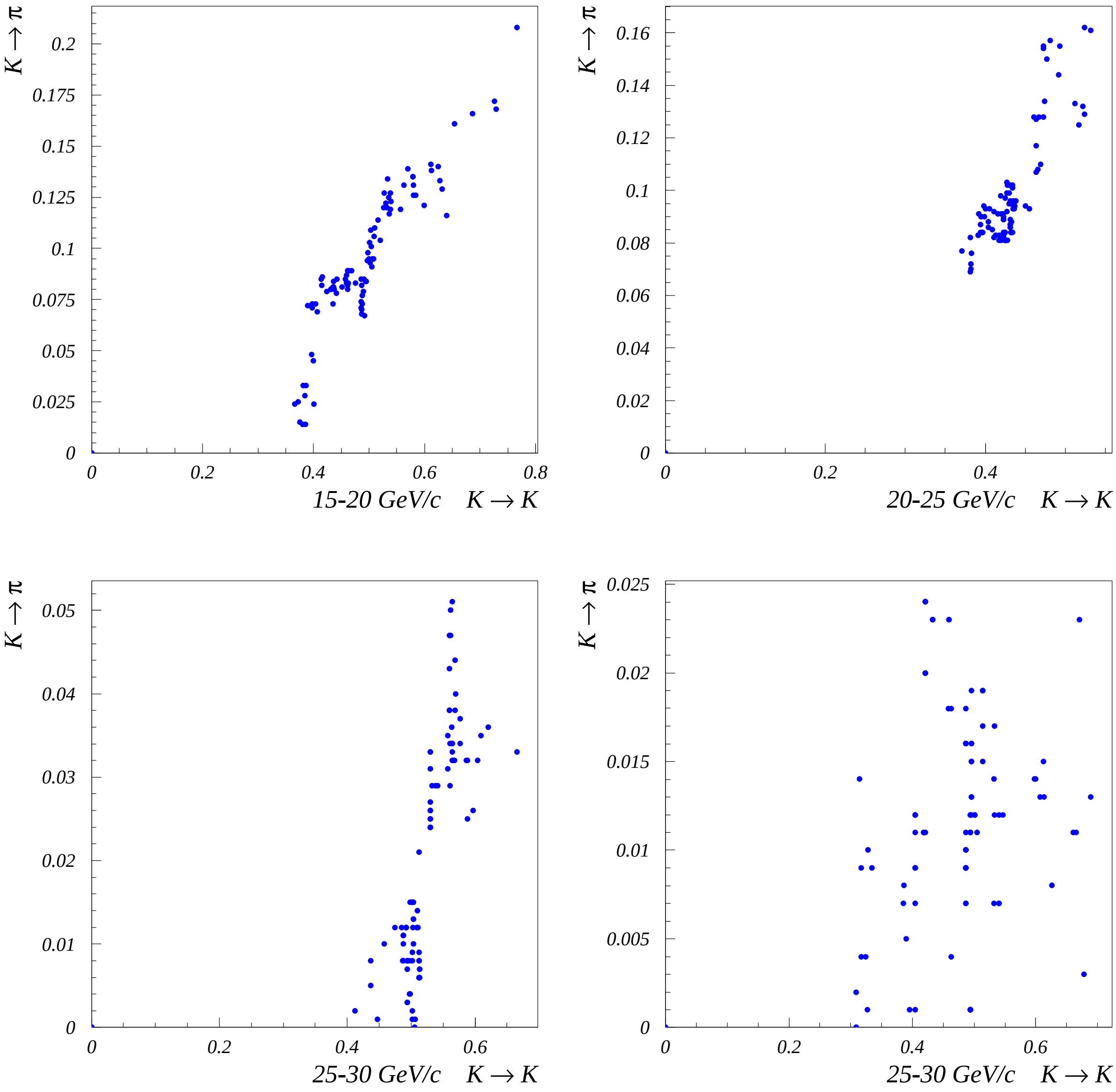

Figure 6.33: Misidentification efficiency vs. identification efficiency of the RICH detector of kaons from ϕ. Each plot corresponds to different momentum regions which are marked under plots.

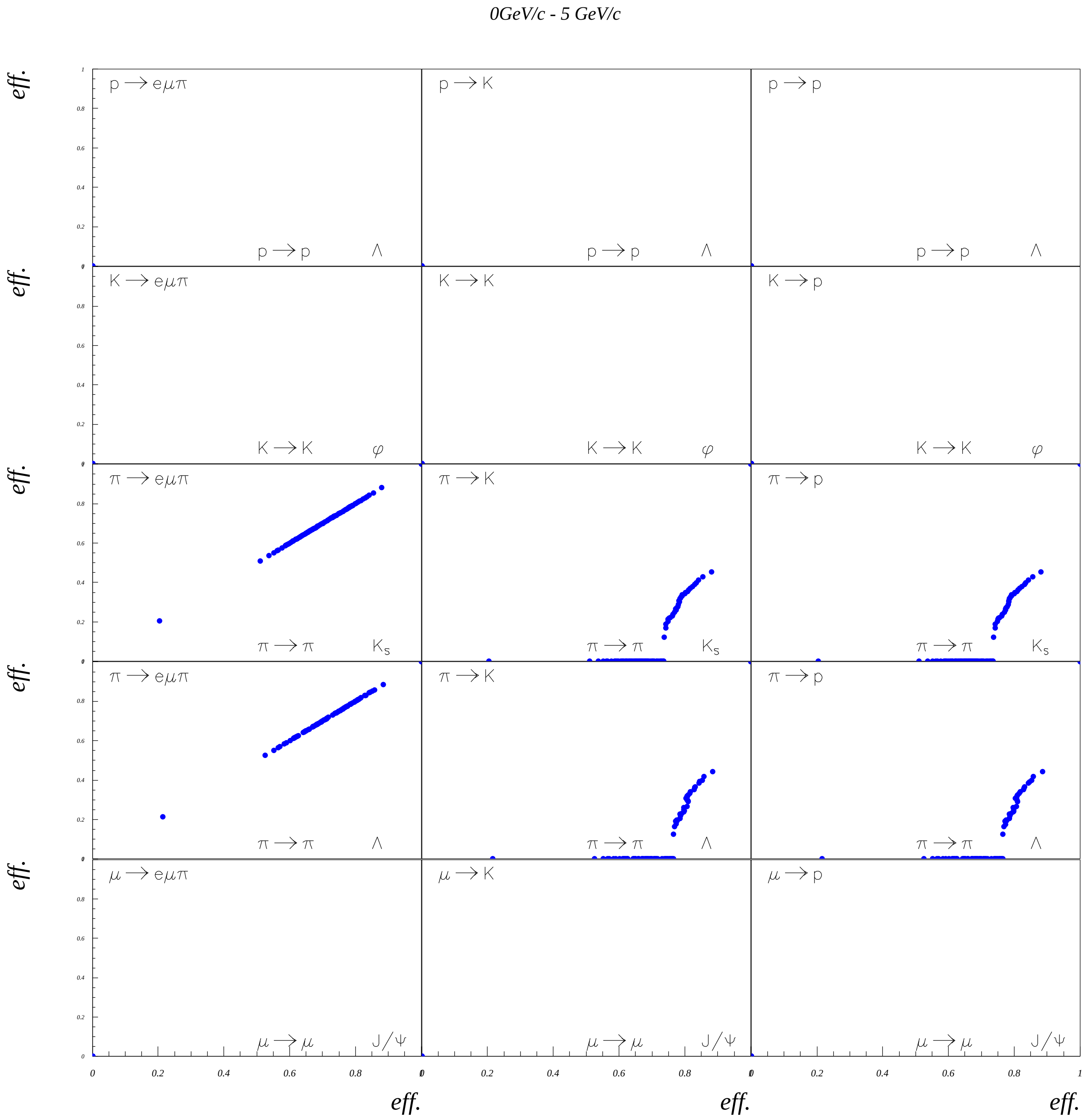

Figure 6.34: Transition matrix $id_1 \to id_2$ vs. $id_1 \to id_1$ for momentum range 0 GeV/c-5 GeV/c: Misidentification probability $id_1 \to id_2$ to identify a particle with the identity id_1 (μ from J/ψ, π from K_S, π from Λ, K from ϕ and p from Λ) as id_2 versus efficiency to identify a particle with the identity id_1 as the particle of identity id_1.

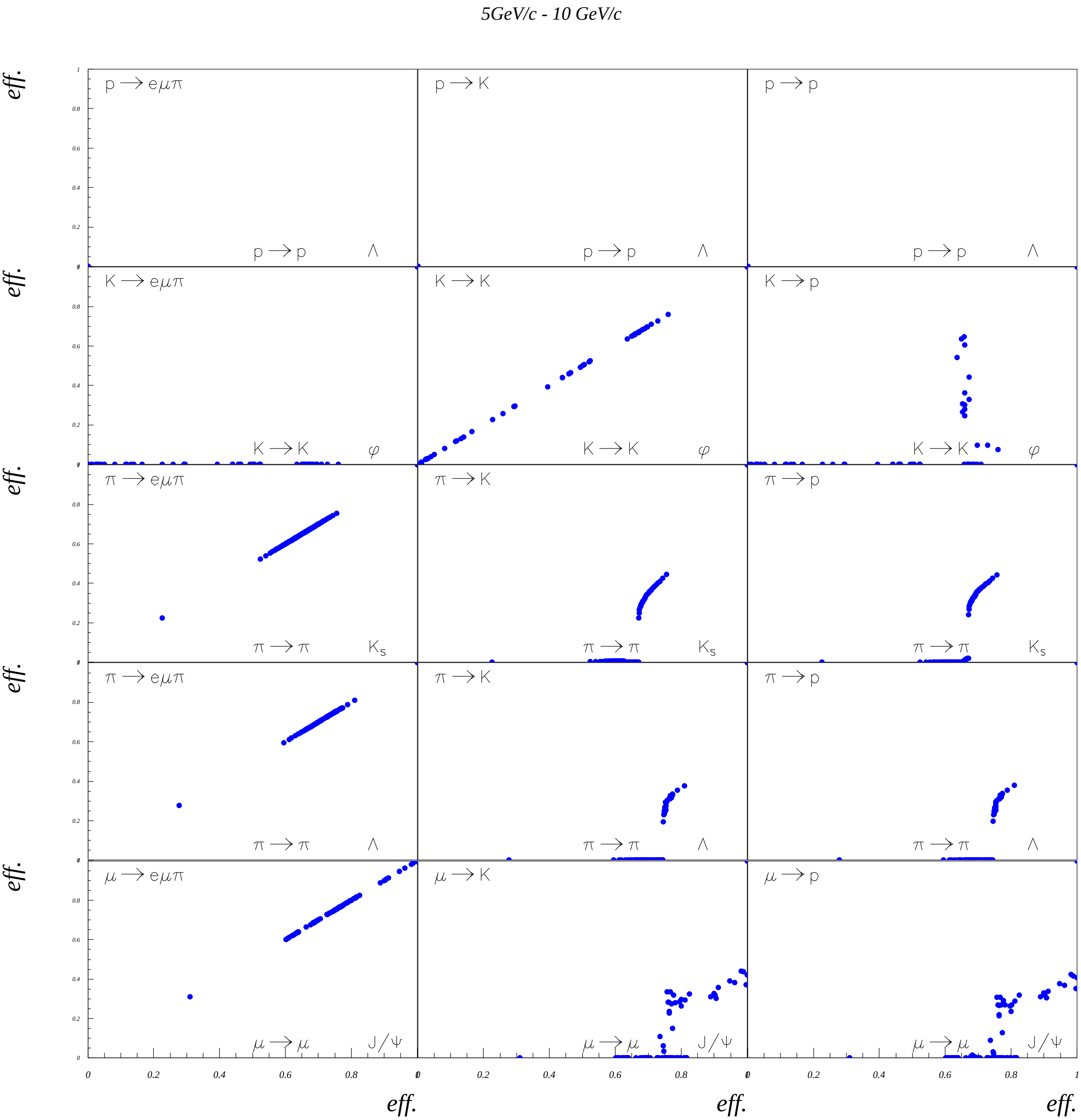

Figure 6.35: Transition matrix $id_1 \rightarrow id_2$ vs. $id_1 \rightarrow id_1$ for momentum range 5 GeV/c-10 GeV/c: Misidentification probability $id_1 \rightarrow id_2$ to identify a particle with the identity id_1 (μ from J/ψ, π from K_S, π from Λ, K from ϕ and p from Λ) as id_2 versus efficiency to identify a particle with the identity id_1 as the particle of identity id_1.

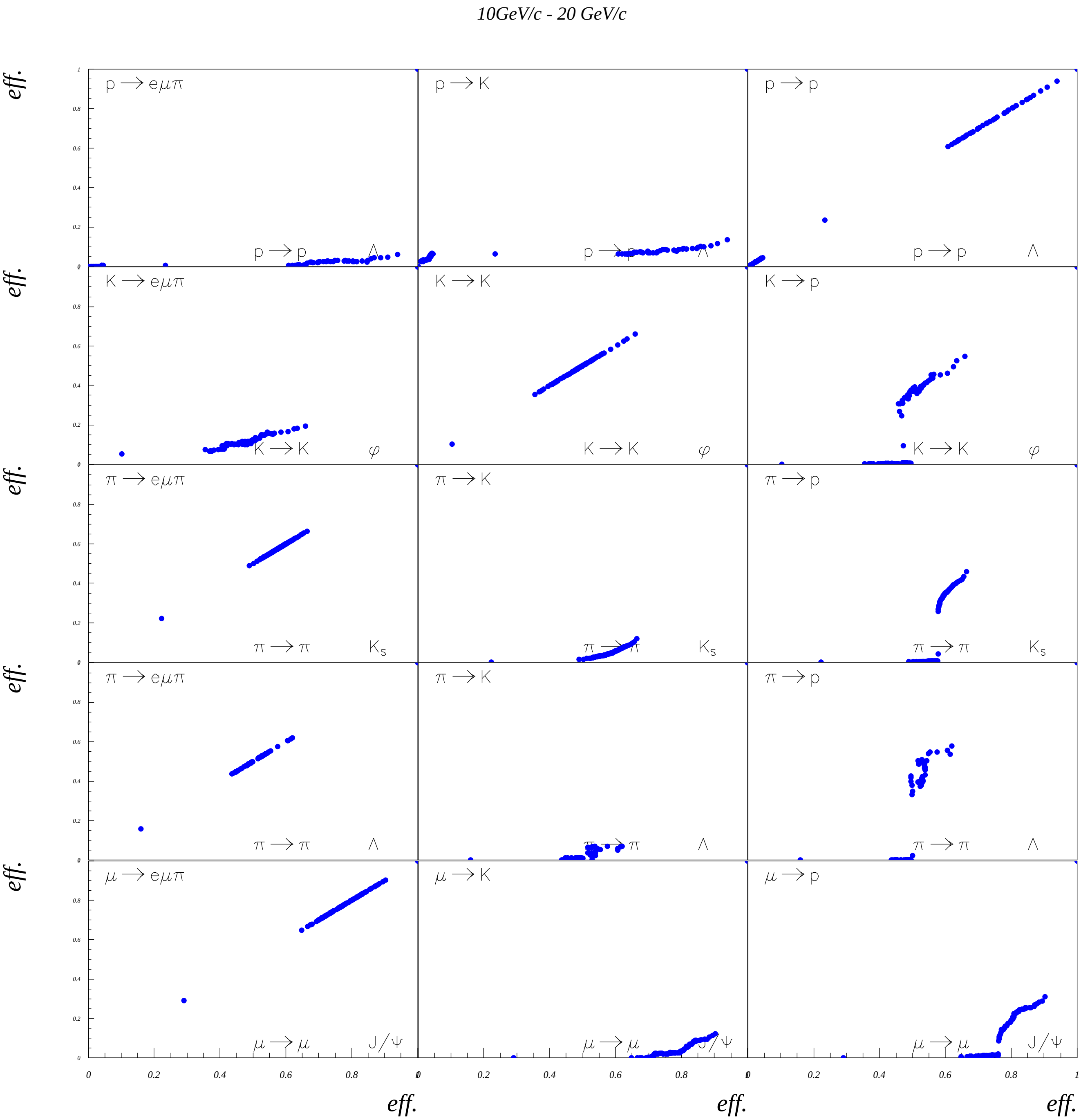

Figure 6.36: Transition matrix $id_1 \rightarrow id_2$ vs. $id_1 \rightarrow id_1$ for momentum range 10 GeV/c-20 GeV/c: Misidentification probability $id_1 \rightarrow id_2$ to identify a particle with the identity id_1 (μ from J/ψ, π from K_S, π from Λ, K from ϕ and p from Λ) as id_2 versus efficiency to identify a particle with the identity id_1 as the particle of identity id_1.

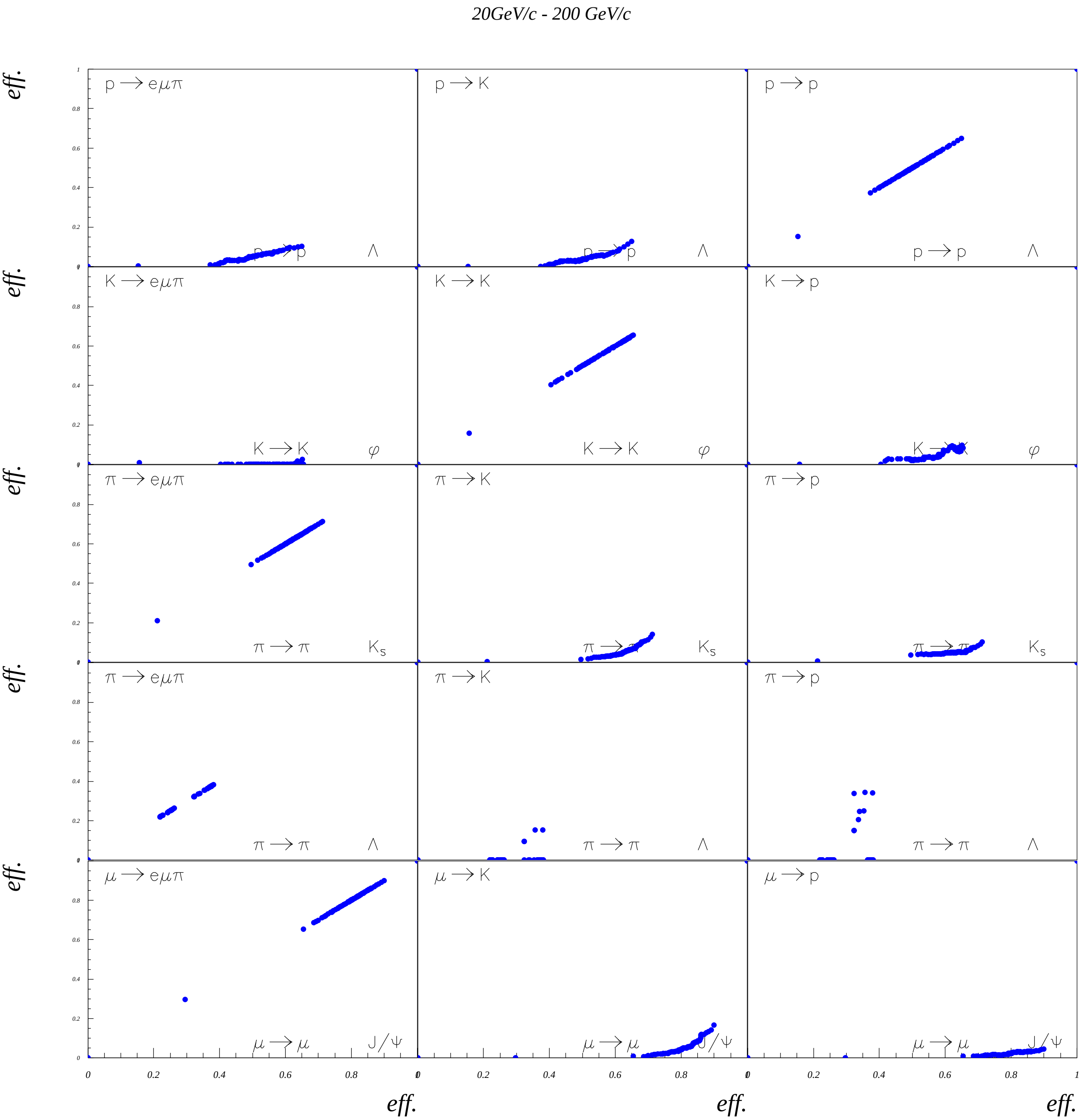

Figure 6.37: Transition matrix $id_1 \rightarrow id_2$ vs. $id_1 \rightarrow id_1$ for momentum range 20 GeV/c-20 GeV/c: Misidentification probability $id_1 \rightarrow id_2$ to identify a particle with the identity id_1 (μ from J/ψ, π from K_S, π from Λ, K from ϕ and p from Λ) as id_2 versus efficiency to identify a particle with the identity id_1 as the particle of identity id_1.

7

Summary

The subject of this thesis is a contribution to the complete particle identification in the HERA-B spectrometer. Electrons are well identified in the electromagnetic calorimeter and in the transition radiation detector, muons are identified in the muon system, while the hadrons, namely pions, kaons and protons, can only be identified in the ring imaging Cherenkov detector.

The primary function of the ring imaging Cherenkov detector is a separation of kaons from pions in the momentum range from 3 GeV/c up to 50 GeV/c.

At the nominal interaction rate 40 MHz, the track density is high and the average occupancy of the ring imaging Cherenkov detector is well above 10%. The detected rings overlap which complicates the identification of hadrons. The method for the particle identification in the ring imaging Cherenkov counter as presented in this thesis uses an iterative approach to gradually ascribe each hit on the photon detector to the individual reconstructed track, from which it was emitted. As a result, the background contribution in the Cherenkov angle distribution is substantially reduced and the identification of particles becomes easier.

The particle identification efficiency of the iterative method as first determined on Monte Carlo simulated events. For the measured data, the efficiencies were determined for the particles which have been well identified by imposing only kinematical and geometrical cuts (pions from K_S and Λ decays, muons from J/Ψ decays, kaons from ϕ decays and protons from Λ decays).

The errors on track parameters were investigated in some detail since they could lead to a substantial degradation of the performance of the RICH. It was found that the track direction error, estimated by the reconstruction program, differs from the average error determined from the RICH data. The rescaled errors were used then in the reconstruction of events.

The efficiencies were determined for the data taken between April 2000 and August 2000 and reconstructed in August 2000. No special event and track selection have been made on the data. The efficiency for identifying a muon from J/Ψ as a light particle (e,μ,π), is around 80% up to a momentum of 60 GeV/c. The pion efficiency from K_S and from Λ is slightly lower than expected, amounting to 70% at 5 GeV/c, and to 55% at the momentum above kaon threshold. The proton efficiency from Λ ranges from 50% to 70%. The kaon efficiency is also lower than expected and amounts to 40% to 60%. The reason that the efficiencies are lower than expected is attributed to the bad quality of the tracks. It was shown that the resulting efficiencies for the reconstructed tracks of higher quality are higher. The origin of the lower quality tracks are the worse reconstruction of the tracks and imperfect alignment of the tracking elements. In such a situation, the potential of the ring imaging Cherenkov counter is reduced especially in the sub-threshold region. It is expected that by a further development of the track finding algorithms and by a refined alignment, a substantial improvement of particle identification capabilities of the ring imaging Cherenkov counter is possible.

8

Povzetek doktorskega dela

Kršitev simetrije med materijo in antimaterijo, ki je ob Velikem poku pripeljala do današnjega vesolja, lahko poleg ostalih lastnosti osnovnih delvcev in interakcij med njimi učinkovito raziskujemo pri poskusih v visokoenergijski fiziki. Eden od njih, eksperiment HERA-B, je namenjen raziskavam redkih pojavov pri razpadih mezonov B in D, med katere sodita tudi meritev kršitve simetrije CP v sistemu nevtralnih mezonov B in meritev mešanja v sistemu nevtralnih mezonov D. Za enolično rekonstrukcijo takih redkih končnih stanj je bistvena identifikacija delcev v končnem stanju. Srce eksperimenta je spektrometer, ki je postavljen v protonski obroč trkalnika HERA v inštitutu DESY v Hamburgu.

8.1 Motivacija

Nastanek in obstoj današnjega vesolja je posledica dejstva, da nestabilni delci in antidelci različno razpadajo v druge bolj stabilne delce. Del te asimetrije uspešno pojasnjuje po letu 1970 formulirani Standardni model osnovnih delcev, vendar pa po njem pričakovana asimetrija ne zadošča, da bi z njo razložili obstoj našega vesolja. Odgovore na vprašanja, ki se pri tem pojavljajo, poskušajo danes odkriti v trkalnikih in so po pričakovanju skriti tudi v razumevanju razpadov nevtralnih mezonov B.

delci	naboj	barionski naboj	generacije		
			1	2	3
Quarks	$+2/3$	$1/3$	u	c	t
	$-1/3$	$1/3$	d	s	b
Leptons	0	0	ν_e	ν_μ	ν_τ
	-1	0	e	μ	τ

Tabela 8.1: Osnovni delci v standardnem modelu

Po Standardnem modelu sodi med osnovne gradnike snovi šest kvarkov in šest leptonov

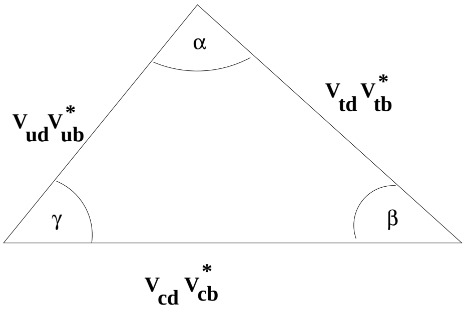

Slika 8.1: Unitarni trikotnik.

urejenih v tri generacije (tabela 8.1).

Masna lastna stanja kvarkov niso enaka šibkim lastnim stanjem, prehode med njimi pa opišemo z matriko Cabibbo-Kobayashi-Maskawa (CKM) matriko V_{CKM} [10],

$$V_{CKM} = \begin{pmatrix} V_{ud} & V_{us} & V_{ub} \\ V_{cd} & V_{cs} & V_{cb} \\ V_{td} & V_{ts} & V_{tb} \end{pmatrix} . \tag{8.1}$$

Na primer, verjetnost za prehod b kvarka v c kvark je sorazmerna absoulutni vrednosti matričnega elementa V_{cb}, prehod b kvarka v u kvark pa absolutni vrednosti elementa V_{ub}. Iz ohranitve verjetnosti sledi zahteva po unitarnosti matrike, zaradi česar so za opis matrike potrebni samo štirje neodvisni parametri. Ena od enačb, ki zagotavlja unitarnost,

$$V_{ud}V_{ub}^* + V_{cd}V_{cb}^* + V_{td}V_{tb}^* = 0 \ , \tag{8.2}$$

je še posebej zanimiva, saj so po do sedaj znanih vrednostih matričnih elementov V_{CKM} posamezni členi v vsoti istega velikostnega razreda.

Izraz lahko predstavimo kot trikotnik v kompleksni ravnini (slika 8.1), kjer so stranice enake absolutni vrednosti matričnih elementov matrike CKM, koti pa so določeni z razlikami v razpadih mezonov B^0, sestavljenih iz kvarkov ($\bar{b}d$) in mezonov $\bar{B}^0$. Tako na primer asimetrija med številom razpadov N mezonov B^0 in številom razpadov $\bar{N}$ mezonov $\bar{B}^0$ v J/ψ in K_S določa kot β:

$$A = \frac{N - \bar{N}}{N + \bar{N}} = \frac{x}{1 + x^2} \sin(2\beta). \tag{8.3}$$

V izrazu nastopa še mešalni parameter $x \sim 0.7$ [12], ki je povezan z verjetnostjo za mešanje v sistemu mezonov B.

8.2 Uvod

Na inštitutu DESY (Deutsches Elektronen Synchrotron) v Hamburgu deluje ob obroču trkalnika HERA eksperiment, kjer v nasprotnih smereh krožijo gruče elektronov in protonov. Eksperiment HERA-B izkorišča protone z energijo 920 GeV, ki se sipljejo na mirujoči tarči. Z analizo identitete in kinematičnih lastnosti delcev, ki nastanejo ob trku protonov v tarči, želi eksperiment raziskovati redke pojave v fiziki mezonov B [14].

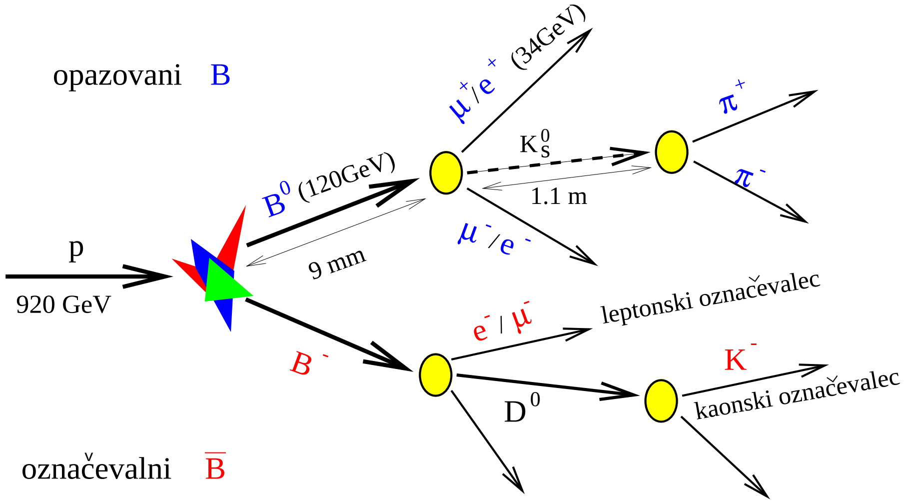

Slika 8.2: Razpad $\mathrm{B}^0 \to \mathrm{J}/\psi\ \mathrm{K_s}$ s tipičnimi vrednostmi za gibalne količine in razpadne razdalje.

Ena od nalog je meritev kršitve simetrije CP v razpadnem kanalu

$$B^0\ ali\ \bar{B}^0 \to J/\psi\ K_s{}^0 \to l^+l^-\pi^+\pi^-.$$

Razpad mezona B v J/ψ in K_S pusti v detektorju značilno sled, ki jo sestavljata par visokoenergijskih leptonov z invariantno maso J/ψ ter par visokoenergijskih pionov z invariantno maso K^0 in mestom nastanka, premaknjenim za tipično 1m glede na tarčo(slika 8.2). Omenjeni razpad je tako eksperimentalno in teoretično najprimernejši za opazovanje kršitve simetrije CP in je zato spektrometer HERA-B nanj optimiziran.

Za meritev so potrebni nevtralni mezoni B z znanim začetnim stanjem B^0 ali $\bar{B}^0$. Identifikacija nevtralnega mezona B sloni na meritvi para leptonov in pionov. Ker nastaneta kvarka b in $\bar{b}$ v paru, lahko določimo začetno stanje nevtralnega mezona B tako, da določimo okus kvarka b v mezonu, ki je nastal skupaj z njim. To dosežemo z merjenjem naboja kaona kot razpadnega produkta spremljajočega mezona B. Zato te kaone imenujemo označevalne, saj določajo začetno stanje nevtralnega mezona B. Iz ocenjenega preseka in razvejitvenega razmerja za te reakcije sledi, da željeni razpad mezonov B^0 nastopi na vsakih 10^{11} interakcij protona z jedri v tarči. Da bi lahko zaznali nekaj tisoč razpadov B^0 na leto, je potrebna interakcijska pogostost 40 MHz. Ker je časovni interval med zaporednimi prehodi gruč protonov v trkalniku HERA 96 ns, potrebujemo pri prehodu gruče v povprečju štiri interakcije. Tarčo sestavlja osem žičk v obrobju žarka, dovolj proč od njegove sredice, da s svojim delovanjem ne motijo ostalih eksperimentov v trkalniku HERA.

Zaradi velike energije protonov leti večina produktov interakcije pod majhnim kotom glede na smer protonskega žarka. Zato je spektrometer načrtovan tako, da pokriva 220 mrad ×

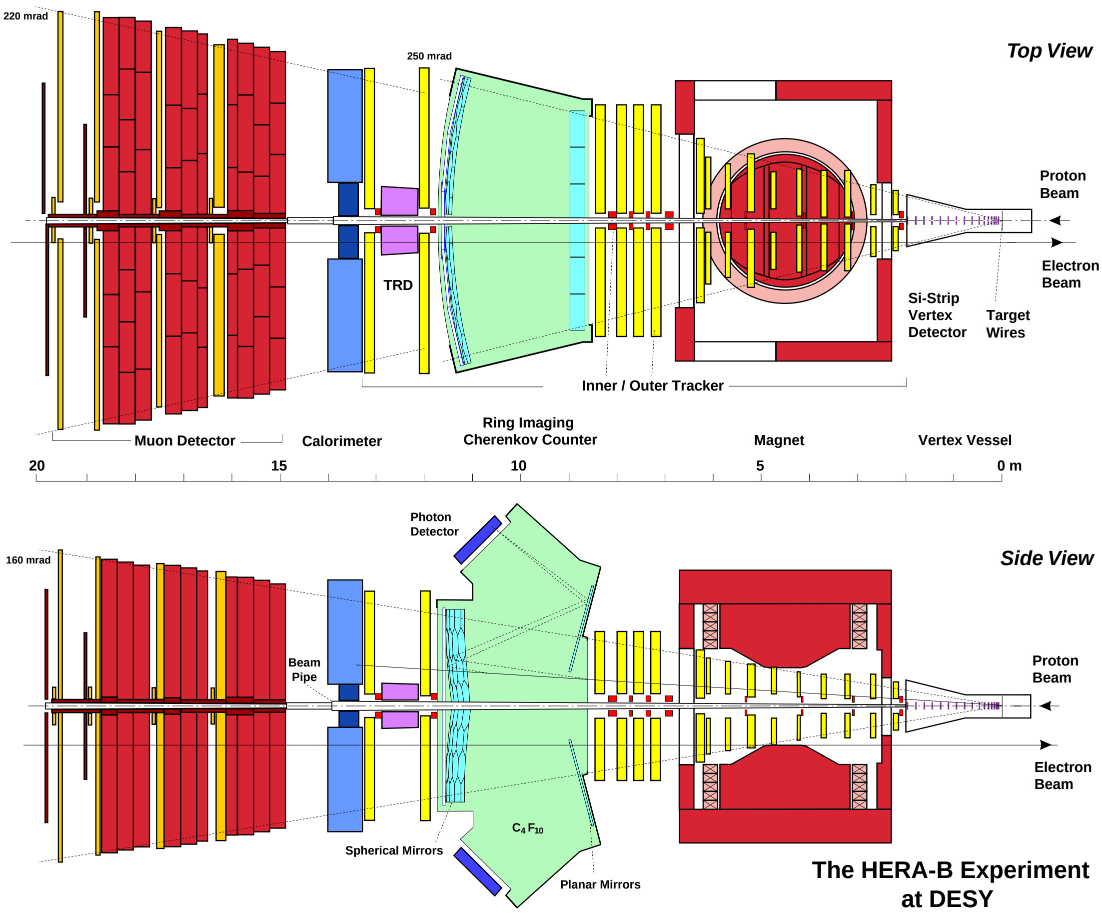

Slika 8.3: Prikaz vodoravnega in navpičnega vzdolžnega prereza detektorja HERA-B.

160 mrad prostorskega kota, kar zadošča za 90 odstotni geometrijski izkoristek pri detekciji razpadnih produktov. Spektrometer je sestavljen iz večih detektorjev, ki jih glede na njihove naloge delimo v dva sistema. S prvim sistemom detektorjev določimo sledi delcev, z drugim pa za njihovo identifikacijo. Sledilni sistem sestavljajo magnet, silicijevi pozicijsko občutljivi detektorji verteksov ter osrednji sledilni sistem. V sistem za identifikacijo delcev pa spadajo detektor prehodnega sevanja, detektor obročev Čerenkova (RICH), elektromagnetni kalorimeter in detektor mionov (slika 8.3).

8.3 Detektor Čerenkovih obročev

Glavni namen detektorja Čerenkovih obročev pri eksperimentu HERA-B je označevanje okusa mezona B. Najbolj učinkovito je označevanje okusa z nabitimi kaoni (slika 8.2), razpadnimi produkti pridruženega nastalega mezona B. Glavna težava pri identifikaciji je ločevanje kaona od piona na področju gibalnih količin od 3 GeV/c do 50 GeV/c pri pogostosti interakcij 40

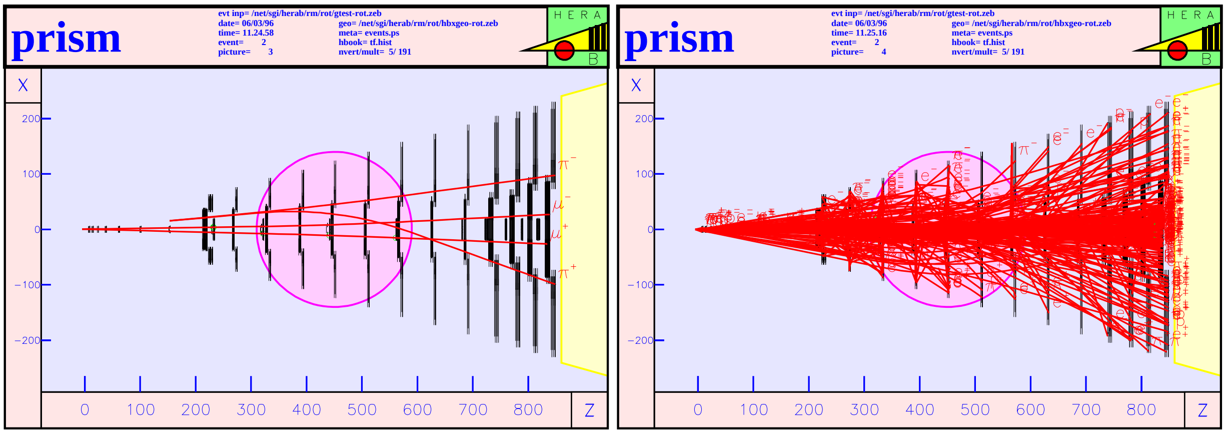

Slika 8.4: V eksperimentu HERA-B bomo iskali dogodke, ki bodo v detektorju pustili značilne sledi. Žal pa je en tak dogodek skrit v množici nezanimivih dogodkov, ki prispevajo k velikemu ozadju meritve. Na sliki je simuliran dogodek brez ozadja (levo) in z ozadjem vrste reakcij, ki jih povzročijo sekundarni delci (desno).

MHz.

Detektor Čerenkovih obročev [57, 58, 28] temelji na pojavu sevanja Čerenkova. Nabiti delci v snovi sevajo fotone, če je njihova hitrost večja od hitrosti svetlobe v tej snovi. Zvezo med Čerenkovim kotom θ in hitrostjo delca v v sredstvu z lomnim količnikom n podaja enačba

$$\cos\theta = \frac{1}{n(E)\beta} \tag{8.4}$$

kjer je β razmerje med hitrostjo delca v in hitrostjo svetlobe v vakumu c (slika 8.5).

Detektor Čerenkovih obročev pri eksperimentu HERA-B je sestavljen iz plinskega sevalca, krogelnih in ravnih ogledal in fotonskega detektorja (slika 8.7). Smer fotonov, ki so bili izsevani vzdolž poti nabitega delca z uporabo sferičnega ogledala pretvorimo v koordinato. Vzporedni žarki, ki padajo nanj, se sekajo v točki v gorišćni ravnini. Ker seva delec fotone enakomerno po azimutalnem kotu, preslikamo stožec izsevane svetlobe Čerenkova s sferičnimi ogledali na obroč na goriščni ravnini. Z meritvijo polmera obroča lahko tako za vsak delec določimo njegovo hitrost. Vsaka od dveh polovic sferičnih ogledal je nagnjena, kar omogoča, da sta fotonska detektorja izven toka nabitih delcev in tako zaščitena pred sevalnimi poškodbami. Za detekcijo svetlobe v fotonskem detektorju skrbi nad 2500 večanodnih fotopomnoževalk [36]. Ker aktivna površina vsake od fotopomnoževalk znaša 18 mm×18 mm, fotone s sistemom dveh leč usmerimo na njihova vstopna okna.

Zaradi majhne aktivne površine fotopomnoževalk, ki so uporabljene za detekcijo, fotone z optičnim sistemom dvojnih leč zberemo na aktivno površino.

Če ne upoštevamo disperzije sevalca z dolžino L, lahko število detektiranih fotonov, ki se izsevajo pri preletu nabitega delca, zapišemo kot

$$\mathrm{N_{det}} = \mathrm{N_0 Z^2 L sin^2}\theta_\mathrm{c}, \tag{8.5}$$

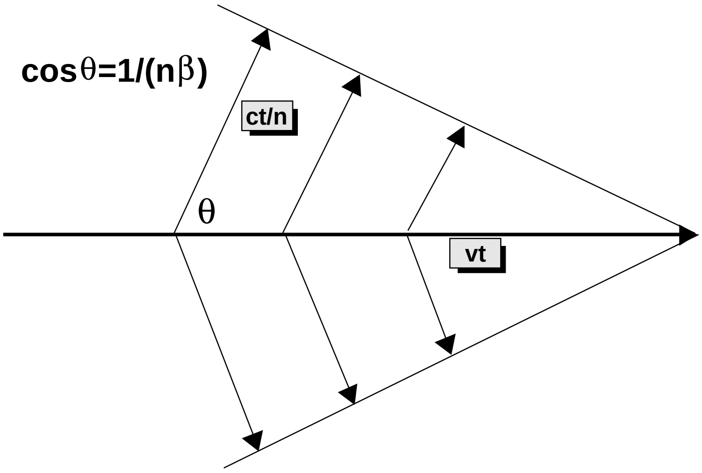

Slika 8.5: Nabiti delec v sredstvu z lomnim količnikom n seva fotone pod kotom θ, če je njegova hitrost večja od hitrosti svetlobe v dani snovi.

kjer je N_0 parameter odziva fotonskega detektorja. Zaradi šibke odvisnosti Čerenkovega kota θ_c od energije lahko na ta način lastnosti sevalca, dolžino in velikost Čerenkovega kota ločimo od značilnosti detekcijskega sistema, ki so zbrane v N_0,

$$\mathrm{N_0} = \left(\frac{\mathrm{e_0^2}}{4\pi\varepsilon_0\hbar^2\mathrm{c}^2}\right)\int \mathrm{T_r(E)R_m(E)}\varepsilon_\mathrm{d}\mathrm{(E)\ dE}. \tag{8.6}$$

V izrazu nastopajo prepustnost sevalca in izstopnih oken T_r, odbojnost ogledal R_m in izkoristek fotonskega detektorja za zaznavo fotonov ε_d, konstanta pred integralom v zgornji enačbi pa ima vrednost

$$\left(\frac{\mathrm{e_0^2}}{4\pi\varepsilon_0\hbar^2\mathrm{c}^2}\right) = 370\mathrm{cm^{-1}eV^{-1}}. \tag{8.7}$$

Na sliki 8.6 je kot funkcija energije Čerenkovih fotonov predstavljena odvisnost posameznih faktorjev v izrazu 8.6.

Zaradi ustreznega lomnega količnika in majhne disperzije je bil za sevalni plin izbran perfluorobutan $\mathrm{C_4F_{10}}$. V tem plinu je prag za sevanje Čerenkova za elektrone pri gibalnih količinah 9.8 MeV/c, mione pri 2.03 MeV/c, pione pri 2.7 GeV/c, kaone pri 9.6 GeV/c in za protone pri 18 GeV/c. Za delce, ki se približajo svetlobni hitrosti, je Čerenkov kot v tem sevalcu 51.5 mrad, medtem ko je razlika med Čerenkovima kotoma za pione in kaone pri gibalni količini 50 GeV/c zgolj 0.9 mrad.

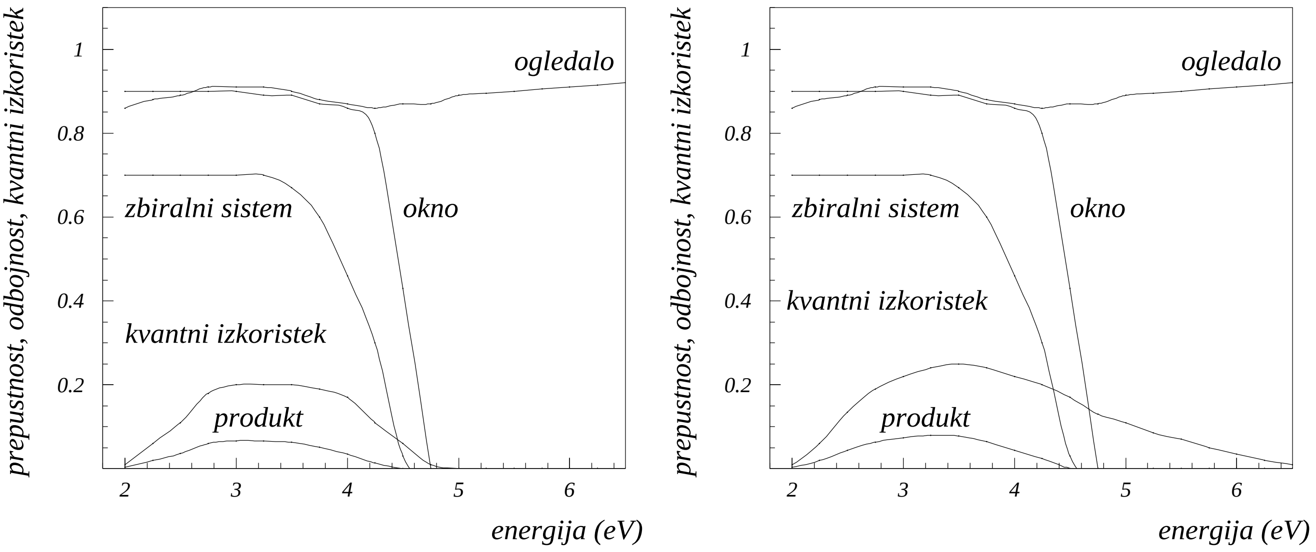

Slika 8.6: Odbojnost ravnih in krogelnih zrcal in izkoristek fotonskega detektorja za detekcijo kot funkcija energije fotona, vse za primer detektorja Čerenkovih obročev pri eksperimentu HERA-B, za fotopomnoževalke z navadnim (levo) in UV prepustnim vstopnim oknom (desno).

V detektorju Čerenkovih obročev pri eksperimentu HERA-B je s sevalcem $\mathrm{C_4F_{10}}$ pričakovano število zaznanih fotonov 30.2 ± 3.6, parameter odziva detektorja N_0 pa znaša $(43.8 \pm 3.5)\mathrm{cm}^{-1}$.

8.4 Identifikacija delcev

Pri poskusih v fiziki osnovnih delcev opazujemo reakcije, pri katerih končna stanja razpadajo na kombinacije pet različnih nabitih delcev: elektrona, miona, piona, kaona in protona.

Če hočemo poznati identiteto nastalih delcev, moramo izmeriti njihovo maso, ki jo lahko določimo iz zveze med gibalno količino in hitrostjo. Gibalno količino izmerimo iz ukrivljenosti sledi delca v magnetnem polju, v detektorju Čerenkovih obročev pa mu določimo še hitrost. V splošnem moramo za vsako sled določiti verjetnosti za možne delčne hipoteze, da je delec e, μ, π, K, p ali pa da sled pripada ozadju.

V primeru majhne gostote nabitih delcev so Čerenkovi obroči na fotonskem detektorju lepo vidni, analiza pa enostavna (slika 8.9). Za vsak na fotonskem detektorju zaznan foton in za vsak nabit delec moramo izračunati Čerenkov kot med njima. V porazdelitvi po Čerenkovem kotu dobimo izrazit vrh. Pri eksperimentu HERA-B pa imamo opraviti z visokimi gostotami delcev v dogodku. V tem primeru se Čerenkovi obroči med sabo prekrivajo (slika 8.8) in se vrh v porazdelitvi po Čerenkovem kotu izgubi v ozadju fotonov, ki jih izsevajo ostali delci.

Pri standardnem pristopu za rešitev problema ocenimo velikost ozadja na danem delu de-

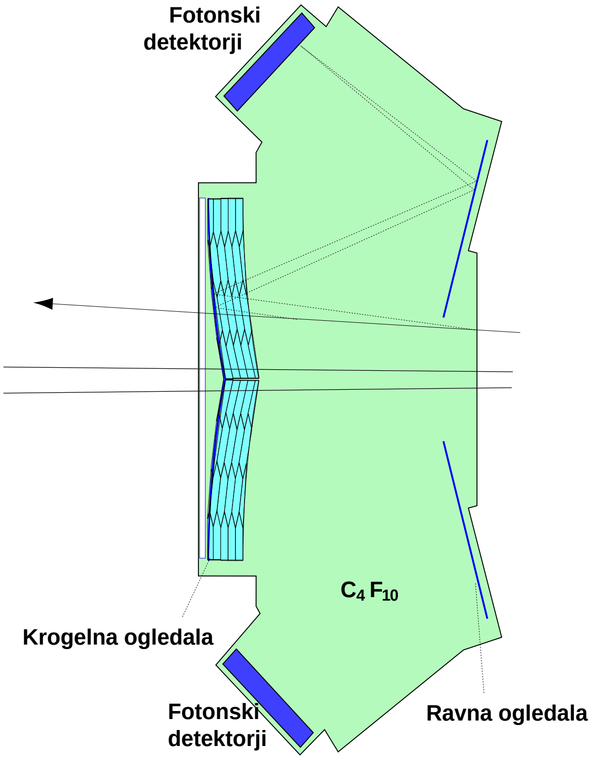

Slika 8.7: Shematičen prikaz detektorja Čerenkovih obročev v spektrometru HERA-B.

tektorja in za vsak delec izračunamo funkcijo največje zanesljivosti za različne delčne hipoteze, ki jih normirane uporabimo za oceno verjetnosti [44].

Pri iterativni metodi za identifikacijo hadronov v detektorju Čerenkovih obročev upoštevamo, da večina fotonov ozadja pripada drugim delcem znotraj istega dogodka. Fotonom za vsak nabit delec pripišemo utež, ki v iterativnem postopku postane največja za tisti delec, ki je najverjetneje izseval foton.

Ilustrirajmo metodo na primeru treh prekrivajočih se obročev, prikazanih na sliki 8.10. Za vsako sled in za vsak zadetek na fotonskem detektorju najprej izračunamo Čerenkov kot in napolnimo za vsako sled histogram na sliki 8.11. Z iterativnim postopkom želimo histograme očistiti prispevka ozadja. To storimo tako, da vsakemu fotonu pripišemo utež tako, da je vsota uteži za vsak foton v vseh treh histogramih ena. Utež za dan foton v histogramu, ki ustreza sledi i, izračunamo v naslednji iteraciji po obrazcu

$$w_i = \frac{y_i}{y_1 + y_2 + y_3}, \tag{8.8}$$

kjer je y_1, y_2 and y_3 število zadetkov v kanalu, v katerega dani foton spada, v histogramih 1, 2 in 3.

Foton ima največjo utež v histogramu, kjer je del vrha, in manjšo tam, kjer je del ozadja. V naslednji iteraciji postopek ponovimo, po 16 iteracijah so rezultat histogrami na sliki 8.11.

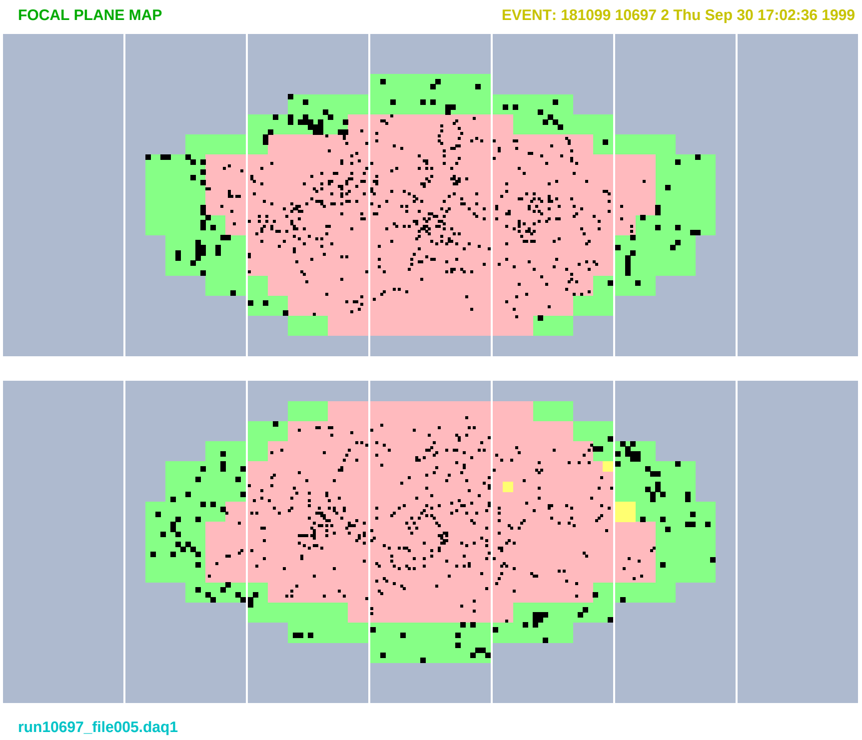

Slika 8.8: Digitalizirana slika, kot jo zabeležimo v detektorju Čerenkovih obročev pri trku protona z energijo 920 GeV z mirujočo tarčo.

Število fotonov v vrhu dobimo z uteženo vsoto

$$n_r = \sum_i w_i \ , \tag{8.9}$$

kjer i teče po vseh fotonih znotraj $\pm 3\sigma$ od pričakovanega Čerenkovega kota za dano hipotezo. Izkaže se, da je porazdelitev fotonov Gaussova z isto širino kot originalna, število fotonov v vrhu pa je enako, ali pa malo manjše. V kumulativni porazdelitvi na sliki 8.12 je večje stevilo sledi opazno znižanje ozadja. Določimo še število pričakovanih fotonov za vsako hipotezo n_e^{hyp},

$$n_e^{hyp} = N_{det}^{hyp} + n_b \ . \tag{8.10}$$

Iz znane gibalne količine očenimo stevilo signalnih fotonov N_{det}^{hyp} (enačba 8.5), iz fotonov, ki so oddaljeni več kot $\pm 3\sigma$ od pričakovanih kotov, pa ocenimo prispevek fotonov k ozadju n_b.

Po končanem iterativnem postopku za vsako sled za različne masne hipoteze hyp izračunamo funkcijo največje zanesljivosti z uteženimi fotoni [46],

$$\log L^{hyp} = \sum_i w_i \log F(\theta_i, \theta^{hyp}) + \log P(n_e, n_r), \tag{8.11}$$

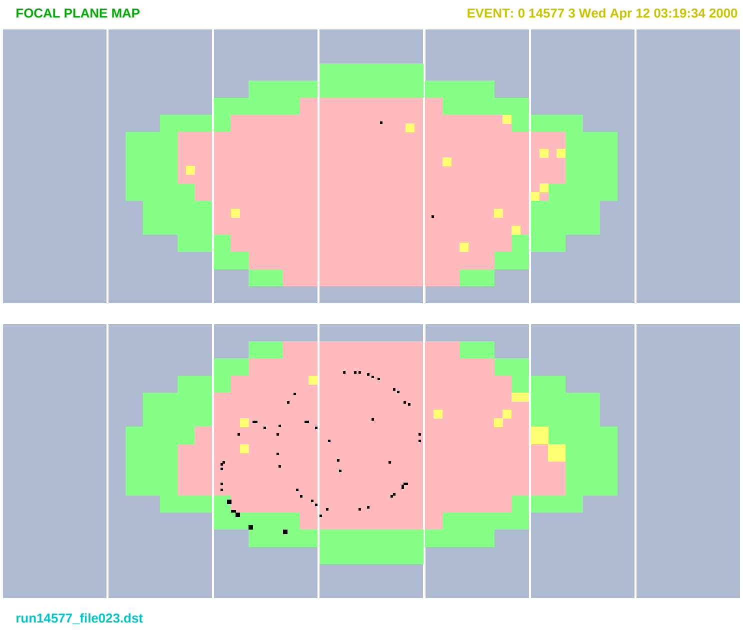

Slika 8.9: Dogodek iz ozadja, kot ga registriramo v detektorju Čerenkovih obročev, z jasno vidnima obročema.

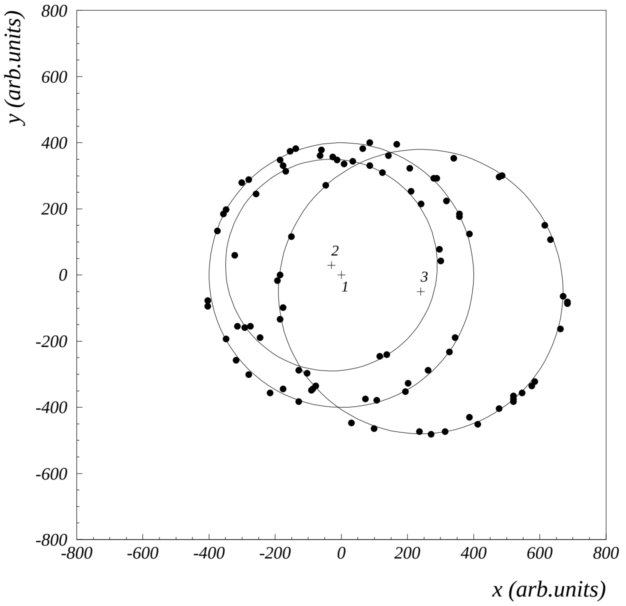

Slika 8.10: Primer: trije prekrivajoči se Čerenkovi obroči.

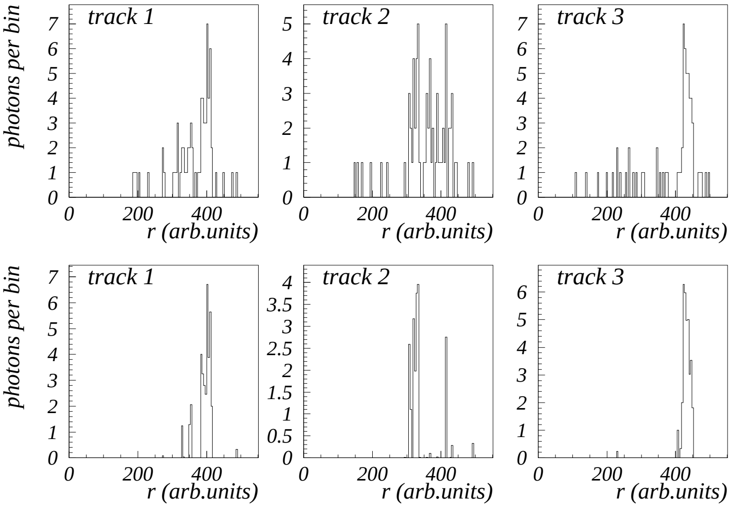

Slika 8.11: Porazdelitve po Čerenkovemu kotu za prvo, drugo in tretjo sled (od leve proti desni), na začetku iterativnega postopka (zgornja vrsta) in po 16 iteracijah (spodnja vrsta).

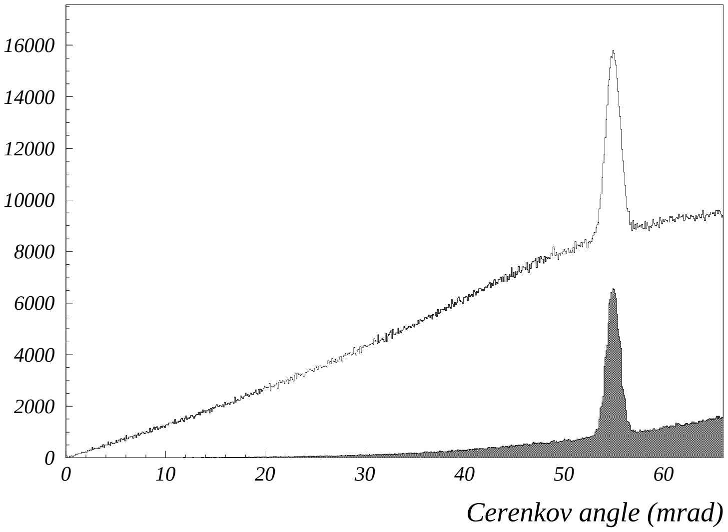

Slika 8.12: Kumulativna porazdelitev po Čerenkovemu kotu za pione z gibalno količino nad 15 GeV/c v simuliranih dogodkih, kot jih pričakujemo v detektorju Čerenkovih obročev eksperimenta HERA-B (odprt histogram). Po iterativnem postopku napolnimo histogram z izračunanimi utežmi (šrafiran histogram). Razmerje med signalom in ozadjem se občutno izboljša.

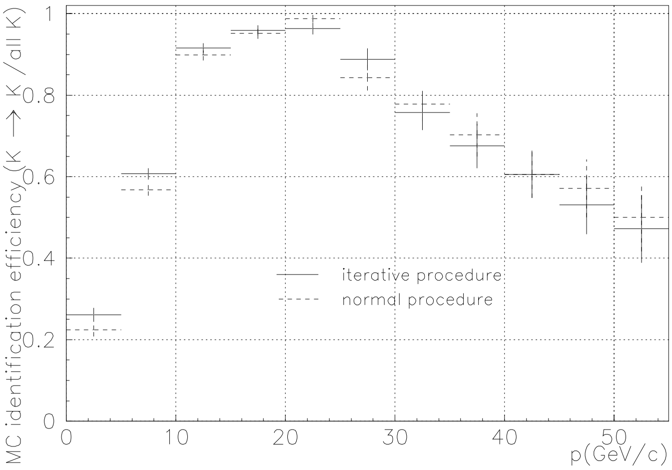

Slika 8.13: Izkoristek za ločevanje kaona od piona kot funkcija gibalne količine pod pogojem, da znaša verjetnost za identifikacijo piona kot kaona 5%. Za primerjavo je črtkano prikazan izkoristek za ločevanje kaona od piona za metodo, ki ne uporablja iterativnega postopka. Pri določitvi izkoristeka smo uporabili idealno informacijo o parametrih sledi.

kjer teče indeks i čez vse fotone v možnih hipoteznih oknih $ozadje, e, \mu, \pi, K, p$. Z n_r označimo izmerjeno, z n_e pa pričakovano število fotonov za izbrano hipotezo. Verjetnostna gostota F,

$$F^{hyp}(\theta) = n_e^{s,hyp} S^{hyp}(\theta) + n_e^b \, B(\theta). \tag{8.12}$$

je vsota Gaussove porazdelitve signala S,

$$S^{hyp}(\theta) = \frac{1}{\sqrt{2\pi}\sigma_i} \exp((\theta - \theta_c^{hyp})^2/(2\sigma_i^2)) \ , \tag{8.13}$$

in porazdelitve ozadja B, ki jo za primer iterativne metode dovolj dobro opišemo s kubično funkcijo,

$$B(\theta) = A \cdot \theta^3 \tag{8.14}$$

Poissonov del $P(n_e, n_r)$ v izrazu 8.11 opisuje statistično naravo procesa detekcije.

Rezultati identifikacije z iterativno metodo na simuliranih podatkih kažejo, da na kinematičnem področju, ki ga pokriva detektor HERA-B, iterativna metoda ločuje kaone od pionov nekoliko bolje od standardne (slika 4.13).

Funkcije največje zanesljivosti normiramo, tako da je njihova vsota ena,

$$\lambda^{hyp} = \frac{L^{hyp}}{L^e + L^\mu + L^\pi + L^K + L^p + L^{ozadje}}, \tag{8.15}$$

Detektor Čerenkovih obročev je namenjen ločevanju hadronov, ne ločuje pa dobro na širokem območju gibalnih količin med lahkimi delci, to je elektroni, mioni in pioni. Zaradi tega je smiselno uvesti kombinirano funkcijo največje zanesljivosti, ki je vsota funkcij za te tri hipoteze

$$\lambda^{sum} = \lambda^{e} + \lambda^{\mu} + \lambda^{\pi} \; . \tag{8.16}$$

Na ta način z rezom na λ^{sum} elektrone, mione in pione identificiramo kot iste lahke delce.

8.5 Rekonstrukcija sledi

Rekonstrukcija sledi v eksperimentu HERA-B poteka v okviru programa za rekonstrukcijo ARTE [49]. Program za vsak dogodek naloži podatke v spomin računalnika in pokliče rekonstrukcijsko verigo. Znotraj nje se binarne informacije iz vsakega od podsistemov dekodirajo v prostorske točke z dobro določenimi pozicijami na detektorju. Rekonstrukcija v osrednjem sledilnem sistemu poteka v več stopnjah. Najprej program rekonstruira segmente sledi znotraj sledilnega sistema med magnetom in detektorjem Čerenkovih obročev (PC). Najdene segmente sledi poskuša podaljšati v del sledilnega sistema v magnetu na eni strani in v prožilni del sledilnega sistema, ki se nahaja med detektorjem Čerenkovih obročev in elektromagnetnim kalorimetrom, na drugi strani. Umeritev komor sledilnega sistema znotraj magneta za rekonstrukcijo leta 2000 še ni omogočala izboljšanja kvalitete rekonstruiranih sledi, zato zadetkov v teh komorah pri rekonstrukciji sledi nismo upoštevali.

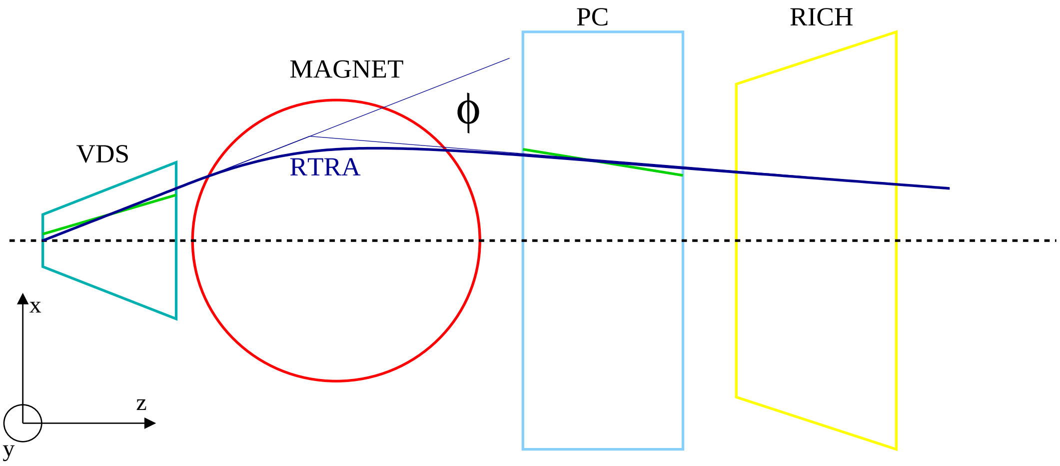

Slika 8.14: Rekonstrukcija sledi. Najprej rekonstruiramo segmente sledi v detektorju verteksov (VDS) in v “pattern” delu osrednjega sledilnega sistema (PC). Rekonstruirana sled je sestavljena iz usklajenih segmentov iz sitemov VDS in PC.

Segmente sledi iz osrednjega sledilnega sistema z vzporejanjem s segmenti sledi iz detektorja verteksov sestavimo v rekonstruirano sled. Za segmente iz osrednjega sledilnega sistema zahtevamo najmanj 20 pripisanih zadetkov v komorah, za segmente iz detektorja verteksov pa 6. Vstopni podatki za podprogram za vzporejanje so parametri na koncu segmenta iz detektroja verteksov in z začetka segmenta iz osrednjega sledilnega sistema. Na začetku vzporejanja primerjamo vertikalno koordinato y obeh segmentov na začetku segmenta iz osrednjega sledilnega sistema (PC) (slika 8.14. Za vsak par potem določimo gibalno količino z zahtevo, da imata segmenta enaki horizontalni (ukrivljajoči) smeri v sredini magneta. Za sledenje v magnetu uporablja program numerično integracijo s parametrizirano jakostjo magnetnega polja. Obema segmentoma sledi nato sledimo do sredine magneta, kjer se z dodatnim rezom na horizontalni koordinati x znebimo množice napačnih kombinacij. Še vedno seveda ostanejo, take sledi potem imenujemo duhove. Nekateri rekonstruirane sledi si delijo enega od segmentov z eno ali več sledmi. Take sledi imenujemo klonirane sledi. Izkoristek metode je bil preverjen na Monte Carlo simuliranih sledeh in znaša za standardne uporabljene reze v rekonstrukciji 92% ob verjetnosti za duhove 11% [53].

Po konstrukciji sledi parametre sledi izboljšamo tako, da sled še enkrat sestavimo z uporabo vseh pripisanih prostorskih točk. Za potrebe identifikacije, rekonstrukcijski program izračuna še parametre sledi na začetku vsakega od identifikacijskih sistemov.

8.6 Izkoristek identifikacije z detektorjem Čerenkovih obročev

Izkoristek iterativne metode za identifikacijo delcev določimo tudi na izmerjenih podatkih, na delcih, ki jih nedvoumno identificiramo z njihovimi kinematičnimi in geometrijskimi lastnostmi. To identiteto potem primerjamo z identiteto, kot jo določimo v detektorju Čerenkovih obročev. Identiteto v detektorju Čerenkovih obročev določimo na podlagi vrednosti funkcije največje zanesljivosti za različne delčne hipoteze. Določeno delčno hipotezo sprejmemo, če funkcija največje zanesljivosti za to hipotezo presega vnaprej določeno vrednost.

Izkoristek metode in verjetnost za napačno identifikacijo smo preverili na dvodelčnih razpadih $K_S \to \pi^+\pi^-$, $\Lambda \to p^+\pi^-$, $J/\psi \to \mu^+\mu^-$ in $\phi \to K^+K^-$. Razen za analizo razpadov J/ψ, dogodkov nismo predhodno izbirali. Analiziral sem podatke, ki so bili zajeti pri interakcijski pogostosti 5 MHz, ob različnih časih in različnih prožilnih pogojih. Izkoristek za identifikacijo sem določil za podatke prožene z minimalnim signalom v detektorju (run 14577) in za podatke prožene z enim leptonom (runi od 17127 do 17266). Iz teh podatkov smo izbrali delce K_S, Λ in ϕ. Za izbor delcev J/ψ smo uporabili predhodno prebrane podatke, ki so bili proženi z dvema leptonoma. Vsi podatki so bili zbrani v času od aprila do avgusta 2000.

Identifikacijski postopek poteka na vseh sledeh, zaradi iterativnega pristopa pa klonirane sledi lahko prispevaju k znižanju izkoristka. Lahko se namreč zgodi, da si klonirane sledi med iterativnim postopkom razdelijo signalne zadetke na detektorju Čerenkovih obročev.

Ker se nismo želeli omejiti na sledi brez klonov, da bi ne precenili izkoristka za identifikacijo, smo uporabili postopek, s katerim smo od vseh klonov izbrali tistega, za katerega je bila vrednost Q,

$$Q = N_{verteks} + N_{osrednji} + \frac{1}{1+\chi^2}\,, \tag{8.17}$$

največja. V izrazu nastopajo število zadetkov, ki jih pripišemo sledi v detektorju verteksov $N_{verteks}$ in v osrednjem sledilnem sistemu $N_{osrednji}$, in χ^2, ki vsebuje informacijo, kako dobro sta se segmenta sledi ujela.

Za par sledi z nasprotnim nabojem smo izračunali njuno invariantno maso, ob predpostavkah, da sta sledi piona iz K_S, miona iz J/ψ ali kaona iz ϕ ali po da je pozitivna sled proton in negativna pion iz Λ.

Za pare z invariantno maso v bližini mase K_S, Λ, ϕ ali J/ψ smo izračunali verteks kot koordinato, kjer je razdalja med sledema najmanjša. Zaradi dolge razpadne razdalje smo za delce K_S in Λ lahko zahtevali verteks ločen od tarče. S tem in pa z dodatnim rezom na razdalji med sledema 0.02 cm se je razmerje signala in ozadja močno izboljšalo, za nadaljno obdelavo pa smo dobili relativno čist izbor identificiranih sledi (slika 8.15), s spektrom gibalnih količin na sliki 8.16. Učinek identifikacije v detektorju Čerenkovih obročev na podlagi reza na funkciji največje zanesljivosti je predstavljen na sliki 8.17.

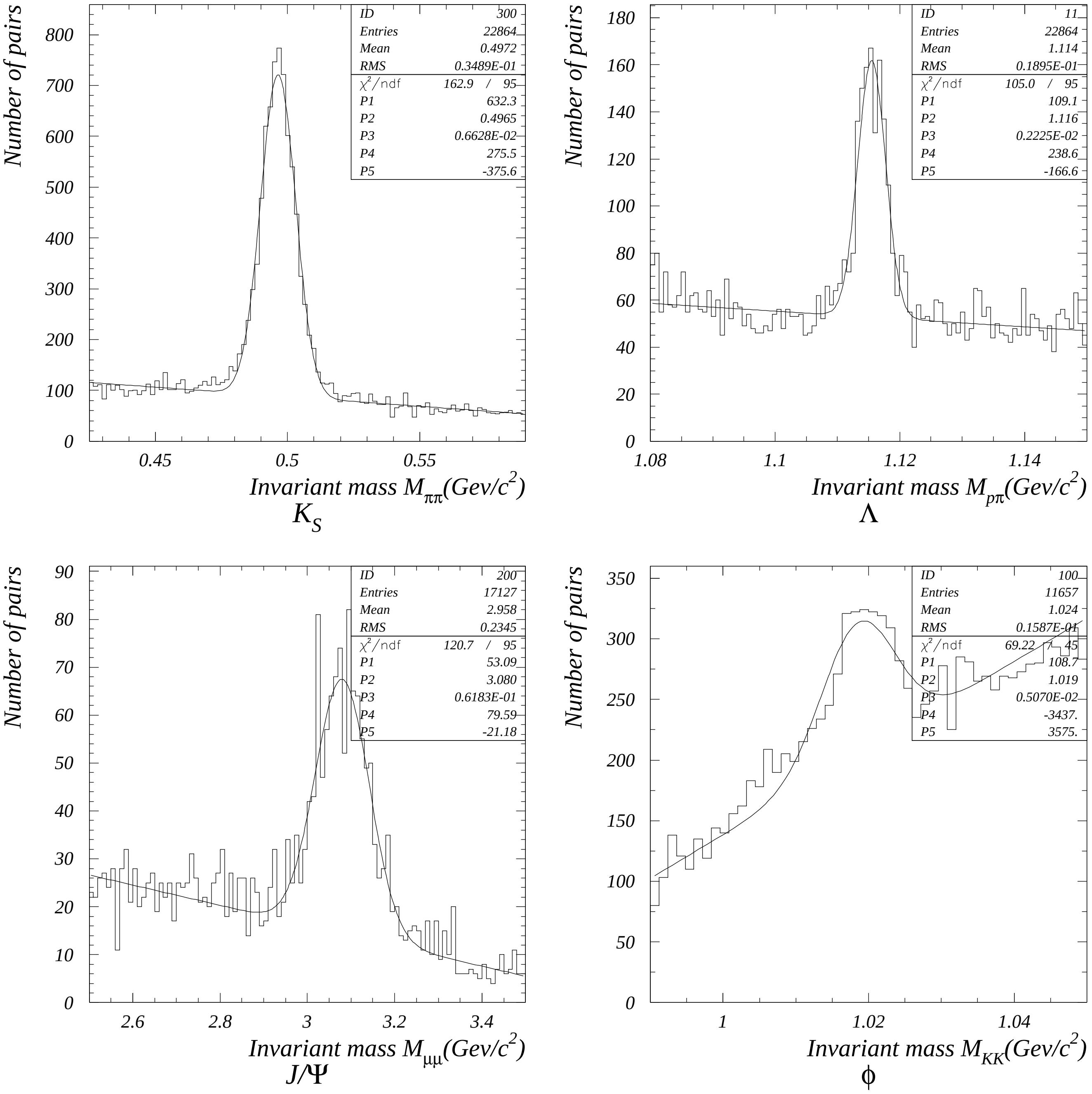

Slika 8.15: Porazdelitev po invariantni masi za različne delce. Pri vseh delcih, razen pri ϕ delcu, kjer smo zahtevali, da enega od nastalih kaonov identificiramo z zahtevo, da je njegova kaonska funkcija največje zanesljivosti večja od 0.5, smo pri izboru uporabili samo geometrijske reze. Histogrami ustrezajo delcem K_S (zgoraj levo), Λ (zgoraj desno), J/ψ (spodaj levo) in ϕ (spodaj desno).

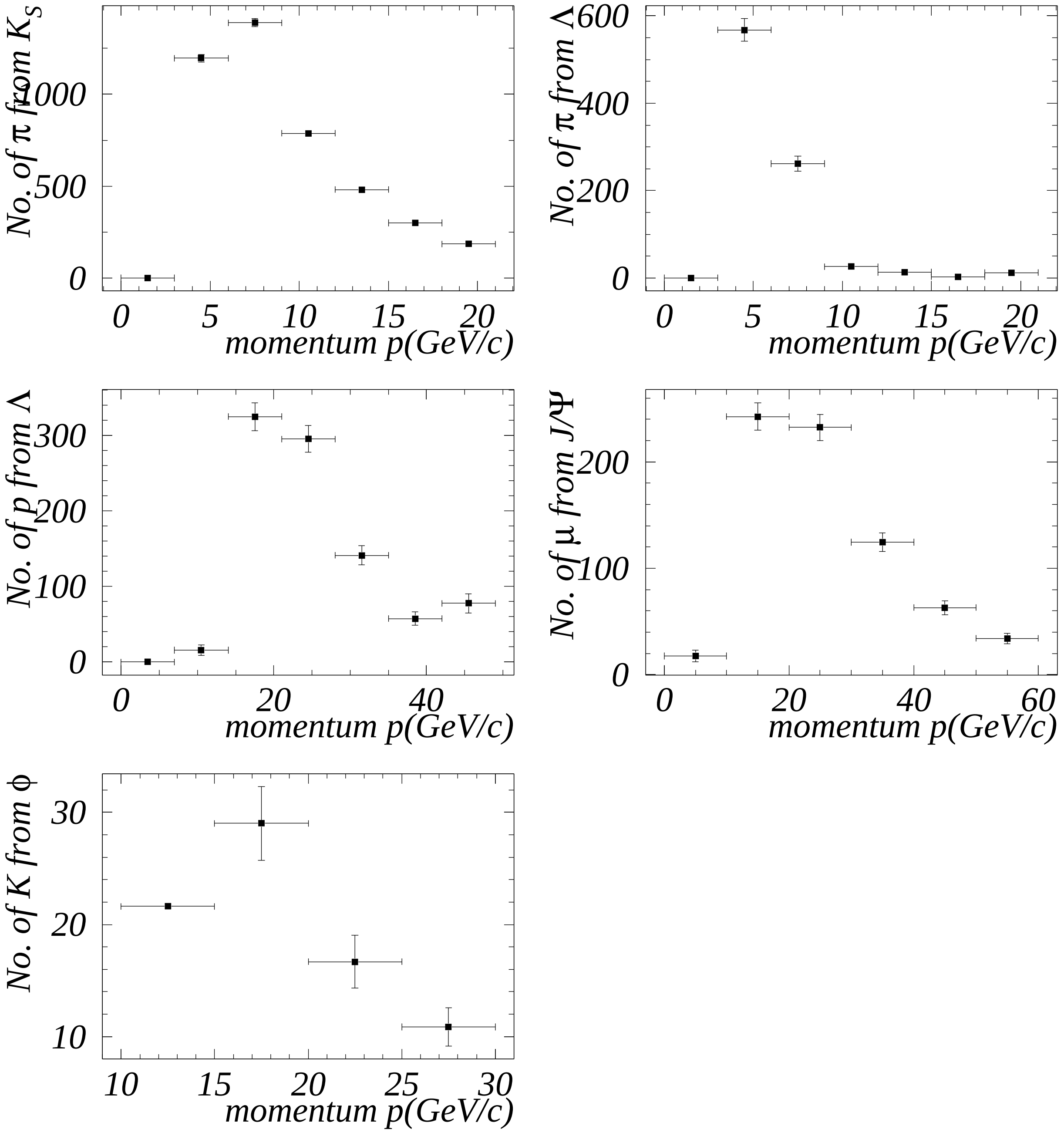

Slika 8.16: Porazdelitev po gibalni količini za pione iz K_S (zgoraj levo), pione iz Λ (zgoraj desno), protone iz Λ (sredina levo), mione iz J/ψ (sredina desno) in kaone iz ϕ (spodaj levo).

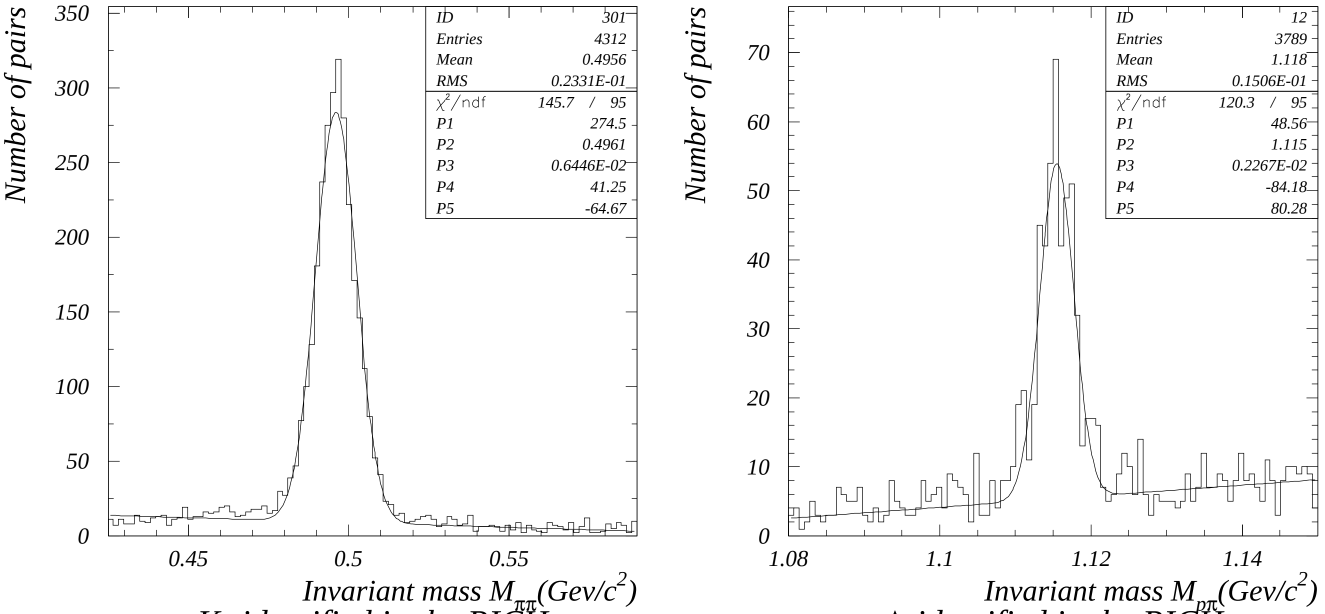

K_S identified in the RICH

Λ identified in the RICH

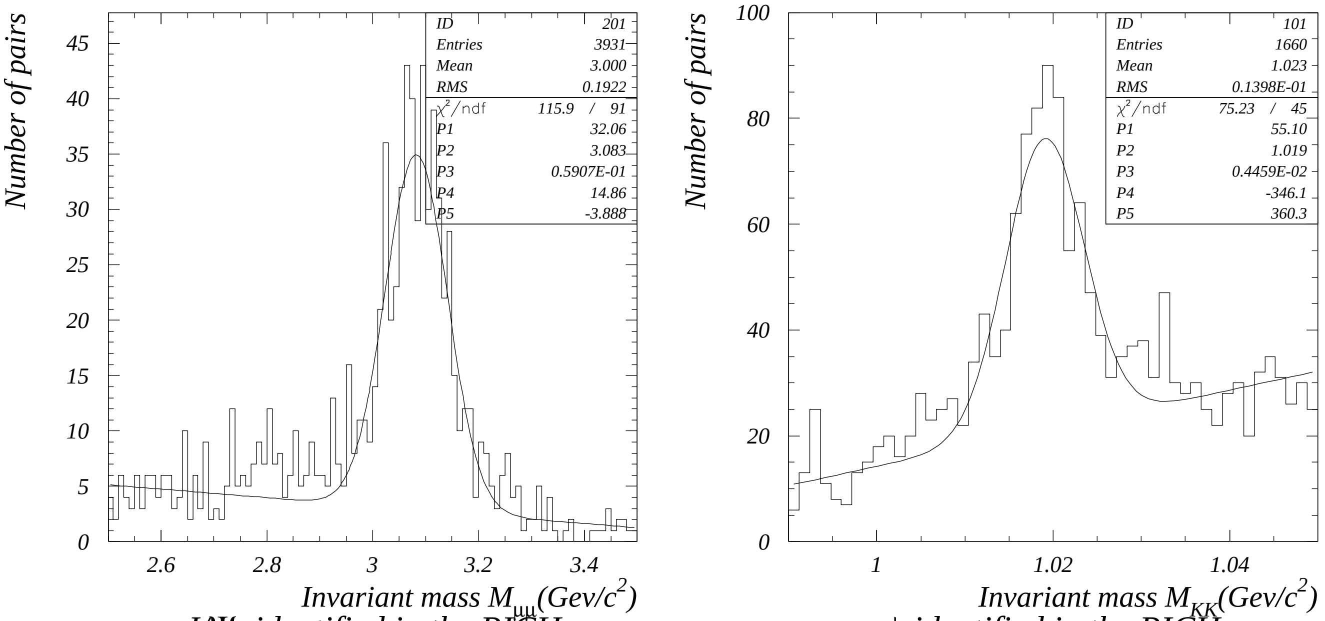

J/Ψ identified in the RICH

ϕ identified in the RICH

Slika 8.17: Porazdelitev po invariantni masi za različne delce po identifikaciji z detektorjem Čerenkovih obročev. Histogrami ustrezajo delcem K_S (zgoraj levo), Λ (zgoraj desno), J/ψ (spodaj levo) in ϕ (spodaj desno).

8.6.1 Izkoristek kot funkcija reza na funkciji maksimalne zanesljivosti.

Za izračun izkoristka smo uporabili naslednjo metodo. Najprej smo napolnili histogram z invariantno maso para sledi, če je funkcija največje zanesljivosti za ustrezno hipotezo prve sledi presegala dano vrednost. Potem smo isti histogram napolnili pri istem identifikacijskem rezu na drugi sledi. Vzporedno smo obakrat polnili še referenčni histogram brez identifikacijskega reza.

Obema histogramoma smo prilagajali vsoto Gaussove in linearne funkcije in iz števila delcev v vrhu N_{rez} in $N_{referenca}$ določili izkoristek

$$\varepsilon = \frac{N_{rez}}{N_{referenca}} \, . \tag{8.18}$$

Na ta način smo določili tako izkoristek za pravilno, kakor tudi verjetnosti za napačno identifikacijo.

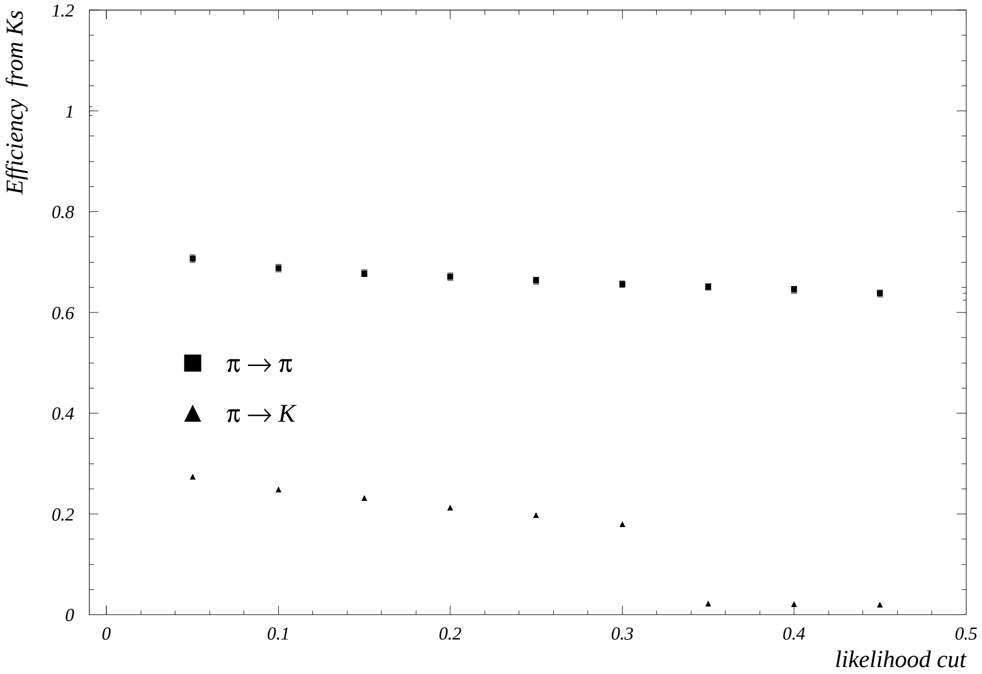

Slika 8.18: Izkoristek za identifikacijo pionov iz K_S: izkoristek za identifikacijo piona kot piona (kvadratki) in verjetnost za napačno identifikacijo piona iz K_S kot kaona (trikotniki). Pion identificiramo kot pion, če je vsota funkcij največje zanesljivosti λ^{sum} večja od izbranega reza in kot kaon, če je kaonska funkcija največje zanesljivosti večja od izbranega reza. Podatki so bili zajeti pri proženju z zaznavo enega leptona.

Na slikah 8.18 in 8.19 je prikazan izkoristek za identifikacijo pionov in mionov kot funkcija višine reza na funkciji največje zanesljivosti. Pri pionih iz K_S opazimo izrazit padec verjetnosti za napačno identifikacijo pri eni tretjini. Ker imajo za sledi, ki jim na fotonskem detektorju

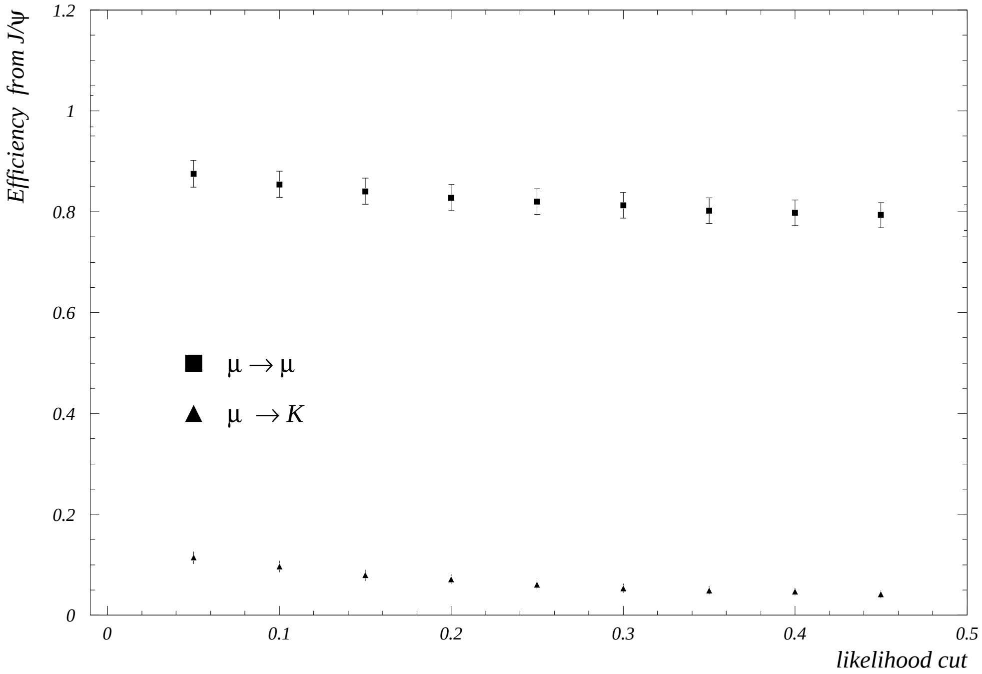

Slika 8.19: Izkoristek za identifikacijo mionov iz J/ψ: izkoristek za identifikacijo miona kot miona (kvadratki) in verjetnost za napačno identifikacijo miona iz J/ψ kot kaona (trikotniki). Mion identificiramo kot mion, če je vsota funkcij največje zanesljivosti λ^{sum} večja od izbranega reza in kot kaon, če je kaonska funkcija največje zanesljivosti večja od izbranega reza. Podatkiso rezultat izbora izmed podatkov proženih z zaznavo dveh leptonov.

ne moremo pripisati obroča, protonska, kaonska in hipoteza ozadja enako vrednost funkcije največje zanesljivosti (1/3), lahko sklepamo, da so bili pioni iz K_S napačno identificirani kot ozadje. To pomeni, da je bila smer sledi napačna za nekaj mrad, Čerenkov vrh v porazdelitvi po Čerenkovemu kotu pa se je zabrisal. Vzrok za napačne parametre sledi so nepopolna rekonstrukcija sledi in nepopolna umeritev sledilnih komor.

8.6.2 Izkoristek kot funkcija gibalne količine.

Za določitev izkoristka kot funkcija gibalne količine smo uporabili metodo, podobno zgoraj opisani, le da smo tokrat namesto reza na funkciji največje zanesljivosti spreminjali območje gibalne količine sledi, medtem ko smo rez na funkciji največje zanesljivosti postavili na izbrano vrednost (0.35). Izkoristek za pione iz K_S in za mione iz J/ψ je prikazan na sliki 8.20. Iz slike 8.21 je razvidno, da se ne spreminja zaznavno za različna obdobja in pogoje zajemanja podatkov.

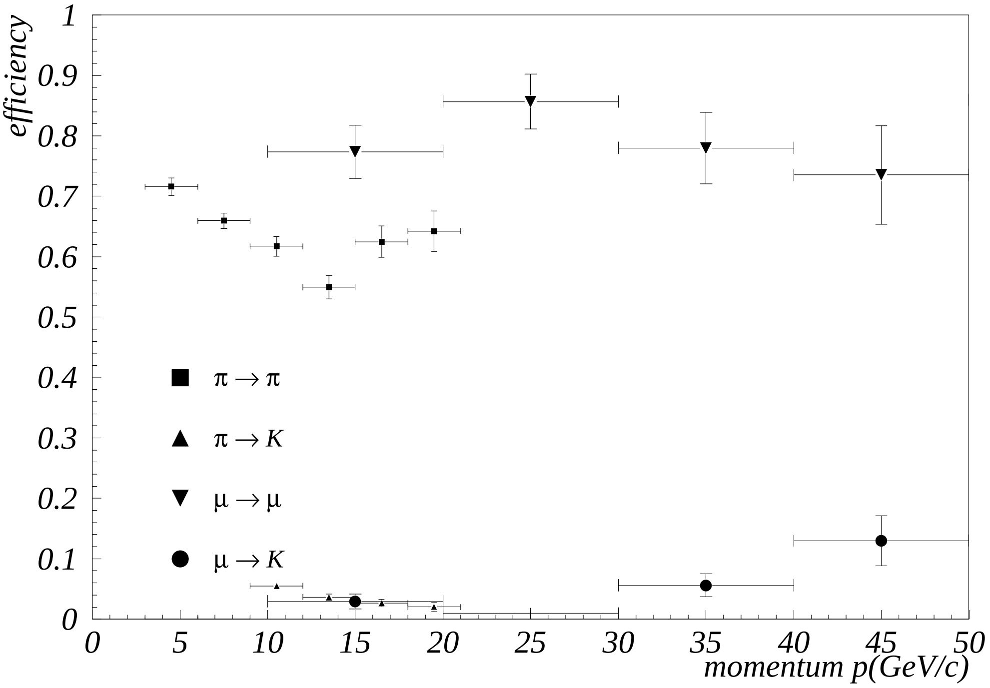

Slika 8.20: Izkoristek za identifikacijo kot funkcija gibalne količine pri rezu $\lambda^{sum} > 0.35$ za pione iz K_S in mione iz selekcije J/ψ. V območju prekrivanja pričakujemo podoben izkoristek.

Že v prejšnjem podpoglavju smo pripisali nizke izkoristke slabši rekonstrukciji sledi in slabši umeritvi sledilnih komor. To bomo sedaj prikazali še na nekaj primerih. Učinek kvalitete sledi na identifikacijo lahko opazimo na sliki 8.20, kjer je razlika v izkoristku na področju istih gibalnih količin lahko posledica različne kvalitete sledi. Za analizo so sledi urejene znotraj dogodka glede na količino Q (enačba 8.17). To pomeni, da si, ko izbiramo par delcev iz urejene tabele, najprej izberemo prvo sled, potem pa iz preostanka še drugo. Na ta način ima prva sled večji Q in torej bolje določene parametre. Na sliki 8.22 je prikazan učinek kvalitete sledi na identifikacijo.

Vpliv kvalitete sledi lahko opazimo tudi v porazdelitvi po Čerenovem kotu (slika 8.23). Za opis vrha sta potrebni dve Gaussovi porazdelitvi s širinama 1.1 mrad in 6.3 mrad. Širša od njih je lahko posledica sledi z napačno določeno smerjo. Učinek napačno določene smeri se vidi tudi na sliki 8.24, kjer je ločeno prikazana identiteta za sledi, katerih vertikalni (neukrivljeni) smeri v

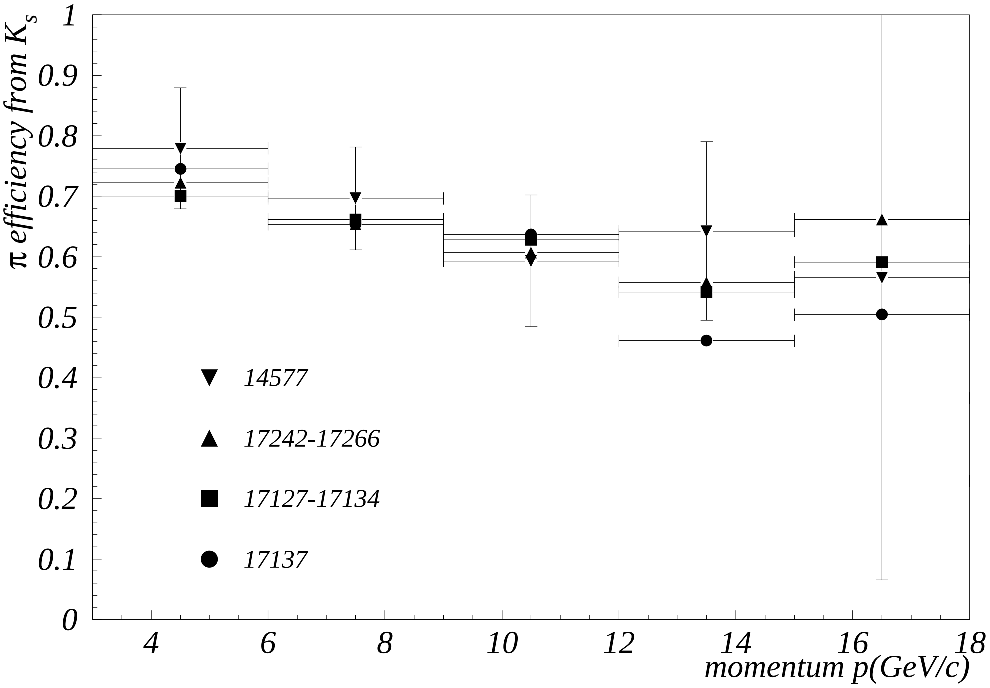

Slika 8.21: Izkoristek za identifikacijo kot funkcija gibalne količine pri rezu $\lambda^{sum} > 0.35$ za pione iz K_S za različna obdobja zajemanja podatkov.

detektorju verteksov in pred detektorjem Čerenkovih obročev se dobro oziroma slabo ujemata. Jasno se vidi, da so sledi s slabim ujemanjem večkrat identificirane kot ozadje. Pričakujemo, da se bo delež sledi, ki jih spoznamo za ozadje, z nadaljnjim razvojem metod za rekonstrukcijo sledi in z boljšo umeritvijo zmanjšal. Obe izboljšavi bi bistveno izboljšali identifikacijo delcev pod pragom.

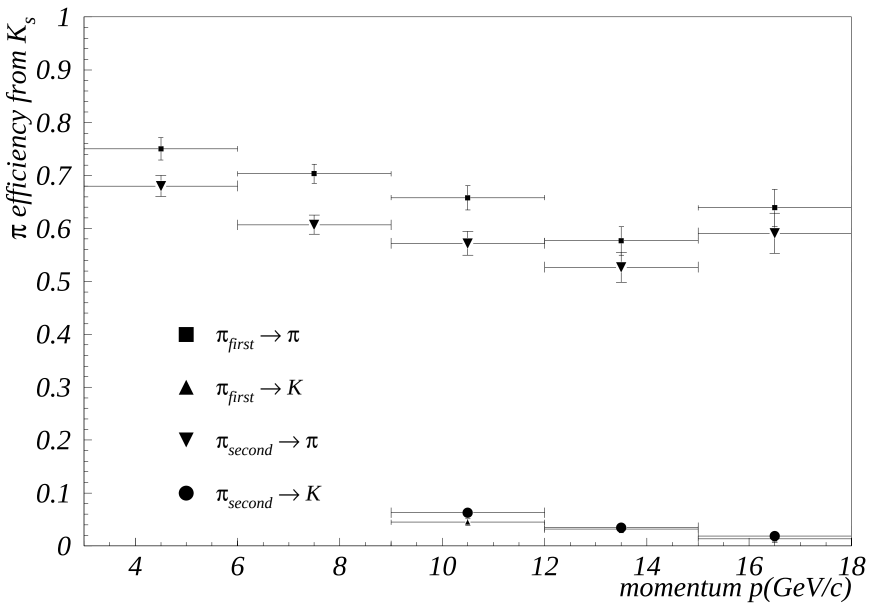

Slika 8.22: Vpliv kvalitete sledi na izkoristek identifikacije: izkoristek za identifikacijo π iz K_S kot funkcija gibalne količine, ločeno za prvo (bolj kvalitetno) in drugo sled v paru.

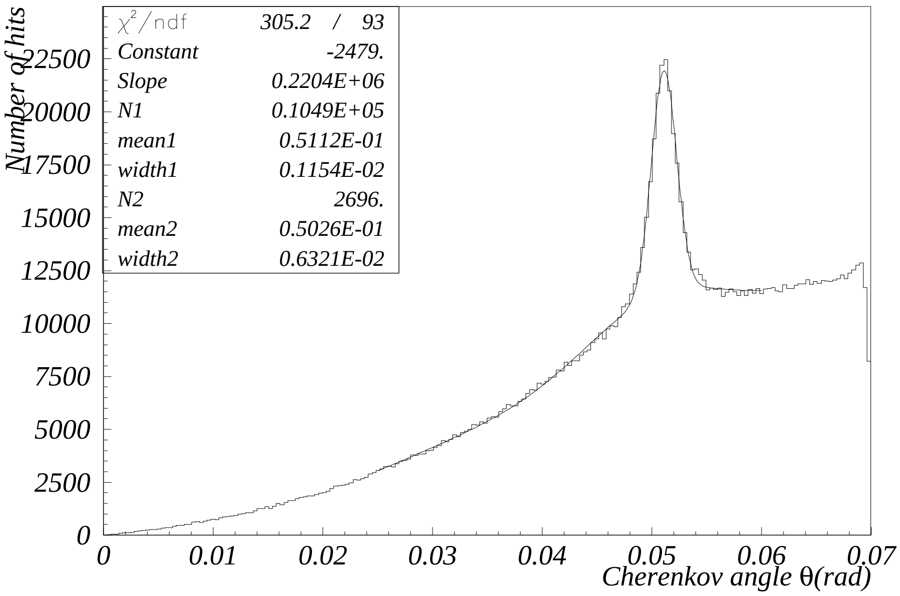

Slika 8.23: Porazdelitev po Čerenkovemu kotu za delce z gibalno količino večjo od 15 GeV/c. Za opis vrha potrebujemo dve Gaussovi funkciji s parametri $N1, mean1, width1$ in $N2, mean2, width2$.

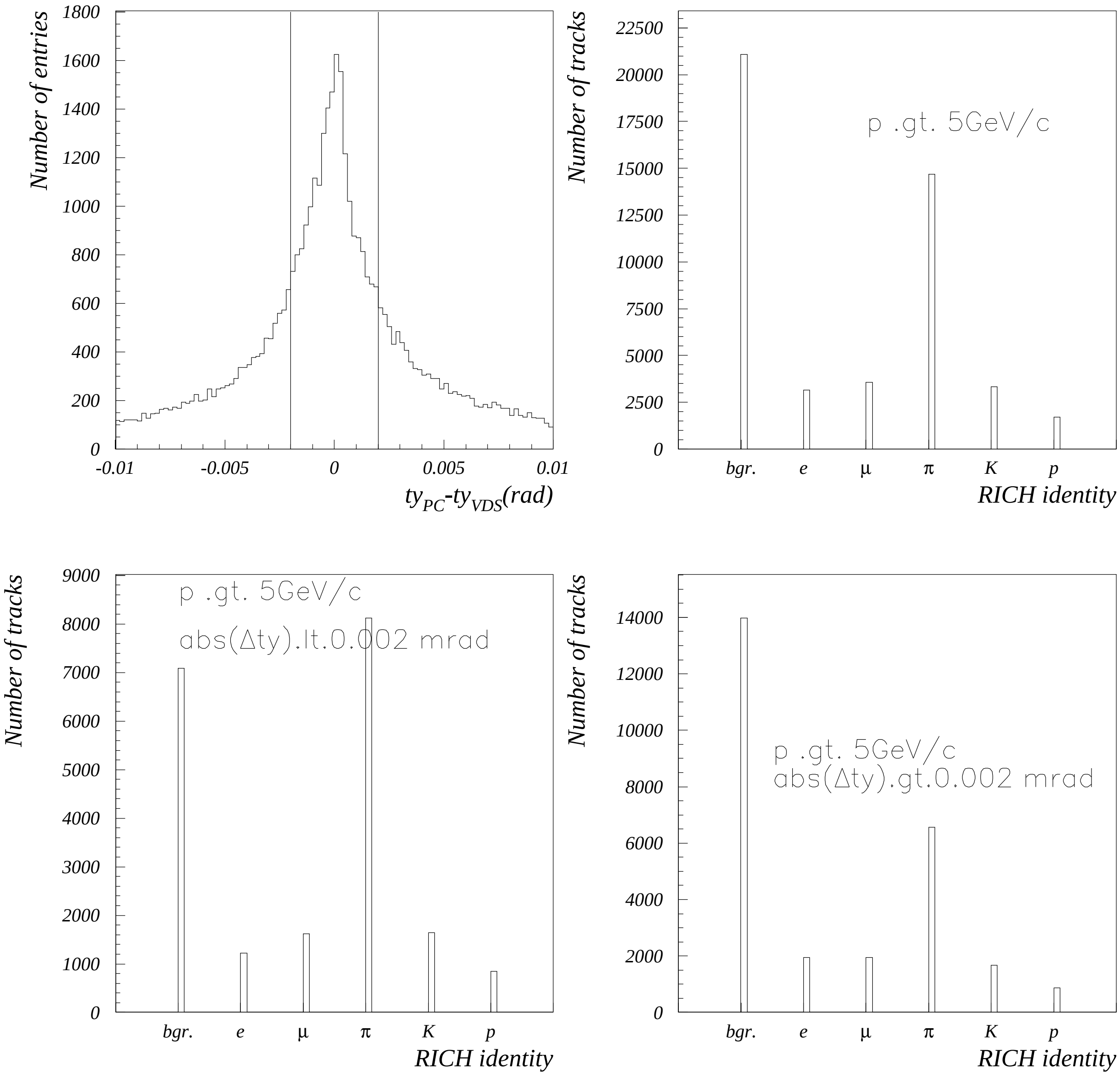

Slika 8.24: Vpliv kvalitete sledi na izkoristek identifikacije: korelacija vertikalne y (neukrivljene) smeri za rekonstruirane sledi pred detektorjem Čerenkovih obročev (ty_{PC}) in v detektorju verteksov (ty_{VDS}) (zgoraj levo). Porazdelitev rekonstruiranih sledi z gibalno količino nad 5 GeV/c, kot jih identificiramo v detektorju Čerenkovih obročev, za vse delce (zgoraj desno), delce iz srednjega dela korelacije ($|\delta ty| <$ 2 mrad) (spodaj levo) in delce iz stranskih pasov (spodaj desno). Delci so identificirani glede na najvecjo vrednost funkcije največje zanesljivosti.

8.7 Zaključek

Namen tega doktorskega dela je prispevek k razvoju metod za identifikacijo delcev v spektrometru HERA-B. Elektrone identificiramo v elektromagnetnem kalorimetru in v detektorju prehodnega sevanja, mione identificiramo v mionskem sistemu, medtem ko lahko hadrone, to je pione, kaone in protone, identificiramo le v detektorju Čerenkovih obročev. Osnovna funkcija detektorja Čerenkovih obročev je ločevanje kaonov od pionov na področju gibalnih količin od 3 GeV/c do 50 GeV/c.

Pri interakcijski pogostosti sunkov 40 MHz je gostota delcev velika in povprečna okupanca na detektoju Čerenkovih obročev nad 10%. Zaznani obroči na fotonskem detektorju se prekrivajo, kar otežuje identifikacijo hadronov. Metoda za identifikacijo delcev v detektorju Čerenkovih obročev, ki je predstavljena v tej disertaciji, uporablja iterativni pristop, pri katerem postopoma pripiše vsak zaznan foton na fotonskem detektorju tisti rekonstruirani sledi, ki ga je izsevala. Na ta način se prispevek ozadja v porazdelitvi po Čerenkovemu kotu občutno zmanjša, identifikacija delcev pa postane lažja.

Izkoristek iterativne metode za identifikacijo delcev smo najprej preverili na simuliranih dogodkih. Za izmerjene podatke smo izkoristek metode preverili na delcih, katerih identiteta je dobro določena samo s kinematičnimi in geometrijskimi rezi (pioni iz razpadov K_S in Λ, mioni iz razpadov J/ψ, kaoni iz razpadov ϕ in protoni iz razpadov Λ).

Raziskali smo napake na parametrih sledi, saj le te lahko pripeljejo do občutnega poslabšanja izkoristka identifikacije v detektorju Čerenkovih obročev. Ugotovili smo, da se napaka v smeri sledi, izračunana v programu za rekonstrukcijo sledi, razlikuje od povprečne napake, ki jo izmerimo v detektorju Čerenkovih obročev. Za rekonstrukcijo dogodkov smo zaradi tega uporabljali preskalirane vrednosti napak.

Izkoristek identifikacije smo preverili za podatke, ki smo jih zajeli od aprila do avgusta 2000 in rekonstruirali avgusta 2000. Ker smo želeli določiti povprečne vrednosti za izkoristek identifikacije, smo podatke in sledi analizirali brez posebne selekcije. Izkoristek za identifikacijo miona iz J/ψ kot lahkega delca (e,μ,π) je nad 80% do gibalnih količin 60 GeV/c. Izkoristek za identifikacijo piona iz razpada K_S in iz razpada Λ je malce nižja od pričakovane, in znaša 70% pri gibalni količini 5 GeV/c in pade na 55% pri gibalni količini okoli kaonskega praga. Izkoristek za identifikacijo protona znaša od 50% do 70%, medtem ko je činkovitost za identifikacijo kaona od 40% to 60%. Razloge za nižje izkoristke za identifikacijo od pričakovanih lahko pripišemo slabi kvaliteti rekonstruiranih sledi. Pokazali smo, da so učinkovitosti za identifikacijo za bolj kvalitetne sledi večje. Z nadaljnjim razvojem algoritmov za rekonstrukcijo sledi in z izboljšano umeritvijo sledilnih elementov lahko zato pričakujemo izboljšanje možnosti za identifikacijo v detektorju Čerenkovih obročev, še posebej v pomembnem kinematičnem področju pod protonskim pragom.

References

[1] Dirac P.A.M., Proc. R. Soc. London Ser. **A 117** 610 (1928); **118** 351 (1928)

[2] Dirac P.A.M., Proc. R. Soc. London Ser. **A 33** 60 (1930)

[3] Andreson C.D., Neddermeyer S.H., Phys.Rev **43** 1034 (1933)

[4] Lee T.D., Yang C.N., Phys.Rev. **104** 254 (1956)

[5] Wu C.S. et al., Phys.Rev. **105** 1413 (1957)

[6] Garwin R.L. et al., Phys.Rev. **105** 1415 (1957)

[7] J. H. Christenson, J. W. Cronin, V. L. Fitch, R. Turlay, Phys. Rev. Lett. **138** (1964) 13

[8] Sakharov A.D. Pisma Zh. Eksp. Teor. Fiz. **5** 32 (1967) [JETP Lett. **5** 24 (1967)]

[9] M. Kobayashi and T.Maskawa, Prog.Theor. Phys. 49, 652 (1973)

[10] C. Caso et al.,*Review of particle physics*, Eur. Phys. J. **C3** (1998) 1.

[11] Y. Nir and H. R. Quinn, *Theory of CP Violation in B Decays*, B Decays, World Scientific Publishing, 1994. (editor Sheldon Stone)

[12] H. Albrecht et al. (ARGUS Collab.) Phys. Lett. B**192** 245 (1987)

[13] A. Ali *B Decays - Introduction and Overview*, B Decays, World Scientific Publishing, 1994. (editor Sheldon Stone)

[14] T. Lohse et al., *An Experiment to Study CP Violation in the B System Using an Internal Target at the HERA Proton Ring, Proposal*, **DESY-PRC 94-02** (1994)

[15] I.Bigi, A.I.Sanda, *CP violation in heavy flavor decays, Predictions and search strategies*, Nucl. Phys., B (55 p), 1986

[16] The HERA-B collaboration, *HERA-B Physics in 2001/2002*, December 2000, DESY internal note

[17] K. Ehret,*Performance of the HERA B target and interference with HERA operation*, Near Beam Symposium Proceedings, FNAL Sept. 1997

[18] The HERA-B collaboration, *HERA-B Report on status and prospects*,**DESY-PRC 00-04**, October 2000

[19] K. T. Knöpfle, Nucl. Instr. and Methods **A368** (1995) 192.

[20] F. Sauli et al., IEEE Trans.Nucl.Sci.44,646, (1997)

[21] M. Villa,*ECAL Analysis Status update*,Hera-B note **HERA-B 99-138** (1999)

[22] D. Ressing, *DAQ architecture for HERA B* , Hera-B note

[23] T. Lohse et al., *An Experiment to Study CP Violation in the B System Using an Internal Target at the HERA Proton Ring, Design Report*, DESY-PRC 95/01 (1995)

[24] W.W.M. Allison and P.R.S. Wright, *The Physics of Charged Particle Identification*, in: Experimental Techniques in Nuclear and Particle Physics, T. Ferbel ed., World Scientific, 1991 (reprinted from: Formulae and Methods in Experimental Data Evaluation, R.K. Bock, ed., European Physical Society, 1984).

[25] P. A. Cherenkov, Phys. Rev. 52 (1937) 378.

[26] J.V. Jelley,*Cherenkov Radiation*, Pergamom Press, New York (1958)

[27] T. Ypsilantis and J. Seguinot,*Theory of ring imaging Cherenkov counters*, Nucl. Instr. and Methods **A343** (1994) 30.

[28] D.Škrk,*Calibration of the Ring Imaging Čerenkov Counter of the HERA-B experiment*, Doctoral thesis, Ljubljana **1999**

[29] 3M corporation

[30] D. Broemmelsiek, *HERA-B RICH Radiator Gas System report*, HERA-B RICH internal report

[31] D. Dujmić, K. Reeves, *Mirror Tiling for the RICH detector*, Hera-B note **HERA-B 97-182** (1997)

[32] J. Pyrlik, *Aging measurements of a TMAE-based photon detector for the HERA-B RICH*, Nucl. Instr. and Methods **A433** (1999) 92-97

[33] P. Križan et al. *Photon detectors for the HERA-B RICH*, Nucl. Instr. and Methods **A387** (1997) 146-149

[34] Hamamatsu company, *Data Sheets for R5900-M16 and R5900-M4 Photomultipliers*

[35] P. Križan et al., *Tests of a multianode PMT for the HERA-B RICH,* Nucl. Instr. and Methods **A394** (1997) 27-34

[36] Rok Pestotnik, *Večanodna fotopomnoževalka kot krajevno občutljivi detektor Čerenkovih fotonov,* Diplomsko delo, Univerza v Ljubljani, FMF, september (1996)

[37] P. Križan, IEEE 2000, *Recent Progress in Čerenkov counters*, to be published in Nucl. Instr. and Methods

[38] D.R. Broemmelsiek, *HERA-B RICH light collection system*, Nucl. Instr. and Methods **A433** (1-2) (1999) 136-142

[39] P. Križan and M. Starič, *The optimal detector surface of a fixed target RICH with a tilted mirror,* Nucl. Instr. and Methods **A394** (1997) 27-34, **A370** (1996) 124-129

[40] S.Korpar at al., *ASD8 Chip Tests with a Hamamatsu Multi-Anode PMT*, **IJS-DP7615**, Ljubljana 1997

[41] P. Križan and M. Starič, Nucl. Instr. and Methods **A379** (1996) 124

[42] W.R. Leo, *Techniques for Nuclear and Particle Physics Experiments*, Springer-Verlag, Berlin (1987).

[43] D. Dujmić, R. Eckmann, *Software for Stand-alone RICH Reconstruction*,Hera-B note **HERA-B 00-004** (2000)

[44] P. Bailon, *Cherenkov ring search using a maximum likelihood technique*, Nucl. Instr. and Methods **A238** (1985) 341-346

[45] I. Arinyo, L. Garrido, *Particle Identification with the HERA-B RICH,* Hera-B note **HERA-B 99-108** (1999)

[46] M. Starič, P. Križan, *An iterative method for the analysis of Cherenkov rings in the HERA-B RICH,* Nucl. Instr. and Methods **A433** (1999) 279-285

[47] S.Nowak, *HB GEAN*, Hera-B note **HERA-B 94-123** (1994)

[48] Application Software Group, *GEANT, Detector Description and Simulation Tool*, CERN, Geneva 1993

[49] H. Albrecht et al., *ARTE, The Event reconstruction and Analysis Tool for HERA-B experiment*, Hera-B note **HERA-B 95-065** (1995)

[50] R. Mankel, A. Spiridonov,*Ranger, a Pattern Recognition Algorithm for the HERA-B Main Tracking System*, Hera-B note **HERA-B 97-082** (1997), Hera-B note **HERA-B 98-154** (1998), Hera-B note **HERA-B 98-206** (1998), Hera-B note **HERA-B 99-111** (1999)

[51] R. Mankel, *A Concurrent Track Evolution Algorithm for Pattern Recognition in the HERA-B Main Tracking System*, Nucl. Instr. and Methods **A395** (1997) 169-184

[52] I. Kisel, S. Masciocchi, *A Cellular Automaton for Tracking in Silicon*, Hera-B note **HERA-B 99-242** (1999)

[53] O. Igonkyna, http://www-hera-b.desy.de//subgroup/software/arte/MARPLE

[54] M. Starič, P. Križan , *Alignment of RICH and ECAL with data*, **IJS-DP-8113**, Ljubljana 1999

[55] D. Dujmić, R. Eckmann and R.F. Schwitters, *Performance of the HERA-B RICH*, Hera-B note **HERA-B 00-084** (2000)

[56] Michael Schmelling, *Clone removal*, reconstruction software in ARTE, Hamburg (2000)

[57] S. Korpar et al., *The HERA-B RICH*, Nucl. Instr. and Methods **A433** (1999) 128-135

[58] P. Križan et al., *The physics potential of the HERA-B RICH*, Nucl. Instr. and Methods **A433** (1999) 357-365

Izjavljam, da je disertacija rezultat samostojnega raziskovalnega dela.

Rok Pestotnik

Ljubljana, januar 2001